Max-Planck-Institut für Kolloid- und Grenzflächenforschung
Forschungsgruppe Mechano(bio)chemie

From Single Molecules to Bulk Materials: Tuning the Viscoelastic Properties of Coiled Coil Cross-linked Hydrogels

Isabell Tunn

Dissertation
zur Erlangung des akademischen Grades
"doctor rerum naturalium"
(Dr. rer. nat.)
in der Wissenschaftsdisziplin Biochemie

eingereicht an der
Mathematisch-Naturwissenschaftlichen Fakultät
der Universität Potsdam

Potsdam, September 2020

Referees

First referee: Dr. Kerstin G. Blank

Second referee: Prof. Dr. Silke Leimkühler

Third referee: Prof. Dr. Markus Linder

https://doi.org/10.25932/publishup-47595
https://nbn-resolving.org/urn:nbn:de:kobv:517-opus4-475955

“An experiment is a question which science poses to Nature
and a measurement is the recording of Nature's answer.”

(Max Planck)

Declaration of Originality

This dissertation, submitted to the Institute of Biochemistry and Biology at the University of Potsdam, has been performed between October 2016 and March 2020 in the Mechano(bio)chemistry group of Dr. Kerstin Blank at the Max Planck Institute of Colloids and Interfaces, Germany. Hereby, I declare that this dissertation is my own work and that all resources used are specifically denoted in the text. The dissertation as a whole has not been published or submitted for any other qualification to this or any other university in the presented or similar form.

Eidesstattliche Erklärung

Die vorliegende Dissertation wurde am Institut für Biochemie und Biologie an der Universität Potsdam eingereicht. Die Dissertation wurde von mir im Zeitraum von Oktober 2016 bis März 2020 in der Arbeitsgruppe Mechano(bio)chemie unter der Leitung von Dr. Kerstin Blank am Max-Planck-Institut für Kolloid- und Grenzflächenforschung angefertigt. Hiermit versichere ich an Eides statt, dass die vorliegende Dissertation von mir eigenständig und ausschließlich unter Verwendung der zitierten Literatur und Hilfsmittel erstellt wurde. Die Dissertation wurde bisher nicht in gleicher oder ähnlicher Form einer anderen Prüfungsbehörde zur Erlangung eines akademischen Grades vorgelegt.

I. Tunn

Isabell Tunn

Potsdam, September 2020

List of publications and contributions

Publications within the scope of this thesis:

I. Tunn, M. J. Harrington, K. G. Blank, Bio-inspired histidine-Zn^{2+} coordination for tuning the mechanical properties of self-healing coiled coil-crosslinked hydrogels, *Biomimetics* **2019**, 4, 25

I. Tunn, A. S. de Léon, K. G. Blank, M. J. Harrington, Tuning coiled coil stability with histidine-metal coordination, *Nanoscale* **2018,** 48, 22725

Additional publications:

E. M. Grad, **I. Tunn**, D. Voerman, A. S. de Léon, R. Hammink, K. G. Blank; Influence of network topology on the viscoelastic properties of dynamically crosslinked hydrogels, *Frontiers in Chemistry* **2020**, 8, 536

A. E. Bergues-Pupo, M. Goktas, **I. Tunn**, P. López-García, A. Vila Verde, K. G. Blank, A. Valleriani, Goodness of fit testing in dynamic single-molecule force spectroscopy, *The Journal of Chemical Physics* **2018**, 149, 244120

Manuscripts in preparation:

P. López-García, A. D. De Araujo, **I. Tunn**, A. E. Bergues-Pupo, D. Fairlie, K. G. Blank, Fortified Coiled Coils: Enhancing Mechanical Stability with Lactam or Metal Staples, *Angew. Chem. Int. Ed., accepted*

A. S. de Léon, C. Huster, P. López-García, **I. Tunn**, M. Goktas, E. M. Grad, K. Kroy, K. G. Blank, Fracture behavior of dynamically crosslinked starPEG networks, *in preparation*

Summary

The development of bioinspired self-assembling materials, such as hydrogels, with promising applications in cell culture, tissue engineering and drug delivery is a current focus in material science. Biogenic or bioinspired proteins and peptides are frequently used as versatile building blocks for extracellular matrix (ECM) mimicking hydrogels. However, precisely controlling and reversibly tuning the properties of these building blocks and the resulting hydrogels remains challenging. Precise control over the viscoelastic properties and self-healing abilities of hydrogels are key factors for developing intelligent materials to investigate cell matrix interactions. Thus, there is a need to develop building blocks that are self-healing, tunable and self-reporting. This thesis aims at the development of α-helical peptide building blocks, called coiled coils (CCs), which integrate these desired properties. Self-healing is a direct result of the fast self-assembly of these building blocks when used as material cross-links. Tunability is realized by means of reversible histidine (His)-metal coordination bonds. Lastly, implementing a fluorescent readout, which indicates the CC assembly state, self-reporting hydrogels are obtained.

Coiled coils are abundant protein folding motifs in Nature, which often have mechanical function, such as in myosin or fibrin. Coiled coils are superhelices made up of two or more α-helices wound around each other. The assembly of CCs is based on their repetitive sequence of seven amino acids, so-called heptads (*abcdefg*). Hydrophobic amino acids in the *a* and *d* position of each heptad form the core of the CC, while charged amino acids in the *e* and *g* position form ionic interactions. The solvent-exposed positions *b, c* and *f* are excellent targets for modifications since they are more variable. His-metal coordination bonds are strong, yet reversible interactions formed between the amino acid histidine and transition metal ions (e.g. Ni^{2+}, Cu^{2+} or Zn^{2+}). His-metal coordination bonds essentially contribute to the mechanical stability of various high-performance proteinaceous materials, such as spider fangs, *Nereis* worm jaws and mussel byssal threads. Therefore, I bioengineered reversible His-metal coordination sites into a well-characterized heterodimeric CC that served as tunable material cross-link. Specifically, I took two distinct approaches facilitating either intramolecular (**Chapter 4.2**) and/or intermolecular (**Chapter 4.3**) His-metal coordination.

Previous research suggested that force-induced CC unfolding in shear geometry starts from the points of force application. In order to tune the stability of a heterodimeric CC in shear geometry, I inserted His in the *b* and *f* position at the termini of force application (**Chapter 4.2**). The spacing of His is such that intra-CC His-metal coordination bonds can form to bridge one helical turn within the same helix, but also inter-CC coordination bonds are not generally

excluded. Starting with Ni^{2+} ions, Raman spectroscopy showed that the CC maintained its helical structure and the His residues were able to coordinate Ni^{2+}. Circular dichroism (CD) spectroscopy revealed that the melting temperature of the CC increased by 4 °C in the presence of Ni^{2+}. Using atomic force microscope (AFM)-based single molecule force spectroscopy, the energy landscape parameters of the CC were characterized in the absence and the presence of Ni^{2+}. His-Ni^{2+} coordination increased the rupture force by ~10 pN, accompanied by a decrease of the dissociation rate constant. To test if this stabilizing effect can be transferred from the single molecule level to the bulk viscoelastic material properties, the CC building block was used as a non-covalent cross-link for star-shaped poly(ethylene glycol) (star-PEG) hydrogels. Shear rheology revealed a 3-fold higher relaxation time in His-Ni^{2+} coordinating hydrogels compared to the hydrogel without metal ions. This stabilizing effect was fully reversible when using an excess of the metal chelator ethylenediaminetetraacetate (EDTA). The hydrogel properties were further investigated using different metal ions, i.e. Cu^{2+}, Co^{2+} and Zn^{2+}. Overall, these results suggest that Ni^{2+}, Cu^{2+} and Co^{2+} primarily form intra-CC coordination bonds while Zn^{2+} also participates in inter-CC coordination bonds. This may be a direct result of its different coordination geometry.

Intermolecular His-metal coordination bonds in the terminal regions of the protein building blocks of mussel byssal threads are primarily formed by Zn^{2+} and were found to be intimately linked to higher-order assembly and self-healing of the thread. In the above example, the contribution of intra-CC and inter-CC His-Zn^{2+} cannot be disentangled. In **Chapter 4.3,** I redesigned the CC to prohibit the formation of intra-CC His-Zn^{2+} coordination bonds, focusing only on inter-CC interactions. Specifically, I inserted His in the solvent-exposed *f* positions of the CC to focus on the effect of metal-induced higher-order assembly of CC cross-links. Raman and CD spectroscopy revealed that this CC building block forms α-helical Zn^{2+} cross-linked aggregates. Using this CC as a cross-link for star-PEG hydrogels, I showed that the material properties can be switched from viscoelastic in the absence of Zn^{2+} to elastic-like in the presence of Zn^{2+}. Moreover, the relaxation time of the hydrogel was tunable over three orders of magnitude when using different Zn^{2+}:His ratios. This tunability is attributed to a progressive transformation of single CC cross-links into His-Zn^{2+} cross-linked aggregates, with inter-CC His-Zn^{2+} coordination bonds serving as an additional, cross-linking mode.

Rheological characterization of the hydrogels with inter-CC His-Zn^{2+} coordination raised the question whether the His-Zn^{2+} coordination bonds between CCs or also the CCs themselves rupture when shear strain is applied. In general, the amount of CC cross-links initially formed in the hydrogel as well as the amount of CC cross-links breaking under force remains to be elucidated. In order to more deeply probe these questions and monitor the state of the CC cross-links when force is applied, a fluorescent reporter system based on Förster resonance energy transfer (FRET) was introduced into the CC (**Chapter 4.4**). For this purpose, the donor-acceptor pair carboxyfluorescein and tetramethylrhodamine was used. The resulting self-reporting CC showed a FRET efficiency of 77 % in solution. Using this fluorescently labeled CC as a self-reporting, reversible cross-link in an otherwise covalently cross-linked star-PEG hydrogel enabled the detection of the FRET efficiency change under compression force. This proof-of-principle result sets the stage for implementing the fluorescently labeled CCs as molecular force sensors in non-covalently cross-linked hydrogels.

In summary, this thesis highlights that rationally designed CCs are excellent reversibly tunable, self-healing and self-reporting hydrogel cross-links with high application potential in bioengineering and biomedicine. For the first time, I demonstrated that His-metal coordination-based stabilization can be transferred from the single CC level to the bulk material with clear viscoelastic consequences. Insertion of His in specific sequence positions was used to implement a second non-covalent cross-linking mode via intermolecular His-metal coordination. This His-metal binding induced aggregation of the CCs enabled for reversibly tuning the hydrogel properties from viscoelastic to elastic-like. As a proof-of-principle to establish self-reporting CCs as material cross-links, I labeled a CC with a FRET pair. The fluorescently labelled CC acts as a molecular force sensor and first preliminary results suggest that the CC enables the detection of hydrogel cross-link failure under compression force. In the future, fluorescently labeled CC force sensors will likely not only be used as intelligent cross-links to study the failure of hydrogels but also to investigate cell-matrix interactions in 3D down to the single molecule level.

Zusammenfassung

Die Entwicklung von biomimetischen Materialien, wie Hydrogelen, zur Anwendung in der Zellkultur und der regenerativen Medizin bildet einen aktuellen Schwerpunkt der Materialwissenschaften. Häufig werden natürlich vorkommende oder neu entwickelte Proteine als biomimetische Bausteine für Hydrogele genutzt, welche die extrazelluläre Umgebung von Zellen nachahmen. Gegenwärtig bleibt es jedoch eine Herausforderung, die Eigenschaften dieser Bausteine und der daraus entwickelten Materialien genau zu kontrollieren und gezielt maßzuschneidern. Jedoch stellen präzise kontrollierbare Materialeigenschaften einen Schlüsselfaktor für die Herstellung von intelligenten Materialen für die Zellkultur dar. Das Ziel dieser Arbeit ist die Entwicklung von α-helikalen Protein-Bausteinen, so genannter Coiled Coils (CCs), mit maßgeschneiderten, reversibel veränderbaren Eigenschaften. Dazu wurden reversible Histidin (His)-Metall-Koordinationsbindungen in ein CC Heterodimer eingefügt. Des Weiteren wurden Fluoreszenz-markierte CCs entwickelt, um das Verhalten der CC-Bausteine in Hydrogelen unter Krafteinwirkung zu untersuchen.

In der Natur kommen CCs oft als Faltungsmotive in Proteinen vor, die eine mechanische Funktion haben, z.B. Myosin oder Fibrin. CCs bestehen aus zwei bis sieben α-Helices, die eine Superhelix bilden. Die Aminosäuresequenz von CCs ist hoch repetitiv und besteht aus sieben sich wiederholenden Aminosäurepositionen (*abcdefg*). In den Positionen *a* und *d* befinden sich aliphatische Aminosäuren, die den hydrophoben Kern des CCs bilden. Die Positionen *e* und *g* werden durch geladene Aminosäuren besetzt, die ionische Bindungen eingehen. In den Lösungsmittel-exponierten Positionen, können diverse Aminosäure platziert werden. Daher sind diese Positionen für Modifikationen gut geeignet. His-Metall-Koordinationsbindungen sind stabile Bindungen der Aminosäure His mit Übergangsmetallionen, wie Ni^{2+}, Cu^{2+} oder Zn^{2+}. His-Metall-Koordinationsbindungen tragen entscheidend zur mechanischen Stabilität von verschiedenen Protein-basierten Biomaterialien bei, z.B. in den Fangzähnen von Spinnen oder in Byssusfäden von Miesmuscheln. Daher wurden His-Metall-Koordinationsstellen in dieser Arbeit verwendet, um ein gut charakterisiertes CC Heterodimer zu stabilisieren. Zwei verschiedene Ansätze wurden zur Stabilisierung des CCs, und den daraus synthetisierten Materialien, genutzt. Zum einen wurden die His-Metall-Koordinationsbindungen so im CC platziert, dass primär Koordination innerhalb einer Helix stattfindet (intra-CC) (**Kapitel 4.2**). Zum anderen wurde His in Positionen eingefügt, die nur Metall-Koordinationsbindungen zwischen den CCs erlauben (inter-CC) (**Kapitel 4.3**).

Bisherige Forschungsergebnisse zur mechanischen Entfaltung von CCs in der Schergeometrie lassen vermuten, dass die Entfaltung am Angriffspunkt der Kraft beginnt. Um die Stabilität einzelner CC Heterodimere in der Schergeometrie zu erhöhen, habe ich His-Metall Koordinationsbindungen in den Positionen *b* und *f* an den Enden der CC-Peptide einfügt (intra-CC), an denen die Scherkraft angreift (**Kapitel 4.2**). Mittels Raman Spektroskopie konnte ich zeigen, dass das His-modifizierte CC α-helikal bleibt und Ni^{2+} koordiniert. Zirkulardichroismus Spektroskopie wurde genutzt, um die thermodynamische Stabilität mit und ohne Ni^{2+} zu ermitteln. Unter Zugabe von Ni^{2+} erhöhte sich die Schmelztemperatur des CCs um 4 °C. Um die Energielandschaft der Entfaltung zu untersuchen, wurde Einzelmolekülkraftspektroskopie mit dem Rasterkraftmikroskop durchgeführt. His-Ni^{2+}-Koordination führte zu einer Erhöhung der Abrisskraft um 10 pN und einer 10-fach verringerten Dissoziationskonstante. Die Koordination von Ni^{2+} führt demnach zu einer Stabilisierung des CCs. Um zu testen, ob der stabilisierende Effekt vom Einzelmolekül auf die viskoelastischen Eigenschaften von Hydrogelen übertragbar ist, wurde das CC als Vernetzungs-Baustein für sternförmiges Polyethylenglykol genutzt. Scherrheologie zeigte, dass die Relaxationszeit der CC-Hydrogele bei Zugabe von Ni^{2+} um das 3-fache erhöht ist. Dieser stabilisierende Effekt war vollkommen reversibel, wenn Metallchelatoren, wie Ethylendiamintetraessigsäure (EDTA) zugegeben wurden. Des Weiteren konnte ich zeigen, dass Cu^{2+} und Co^{2+} intra-CC Koordinationsbindungen eingehen und einen ähnlichen Effekt auf die Relaxationszeit haben wie Ni^{2+}, wohingegen Zn^{2+} auch zwischen verschiedenen CCs (inter-CC) koordiniert wurde.

Intermolekulare His-Zn^{2+}-Koordination an den Enden der Protein-Bausteine von Byssusfäden ist essentiell für deren hierarchische Struktur und Selbstheilung nach mechanischer Belastung. Im oben beschriebenen CC kann der Effekt der intra- und inter-CC His-Zn^{2+}-Koordination nicht klar voneinander getrennt werden. In **Kapitel 4.3** wurden die His daher mit größerem Abstand in das CC eingefügt, so dass nur inter-CC Zn^{2+}-Koordination möglich war. Raman und Zirkulardichroismus Spektroskopie zeigten, dass dieses CC unter Zugabe von Zn^{2+} aggregiert. Während sich die CC-Hydrogele ohne Zn^{2+} viskoelastisch verhielten, führte die Zugabe von Zn^{2+} zu annähernd elastischem Verhalten. Unter Verwendung von verschiedenen His:Zn^{2+} Verhältnissen, konnte die Relaxationszeit in einem großen Bereich gezielt verändert werden. Diese maßgeschneiderten Materialeigenschaften sind auf die schrittweise Umwandlung von einzelnen CC-Vernetzungen zu CC-Aggregaten mit inter-CC His-Zn^{2+}-Koordination zurückzuführen.

Die Rheologiemessungen mit den His-Zn^{2+}-vernetzten CC-Aggregaten werfen die Frage auf, ob die inter-CC His-Zn^{2+}-Koordinationsbindungen oder die CCs selbst brechen, wenn eine Kraft wirkt. Im Allgemeinen sind die Mechanismen der Dissoziation von Vernetzern im Hydrogel unter Krafteinwirkung größtenteils unerforscht. Um diese zu beleuchten, wurde das

CC mit einem Fluoreszenz-Reportersystem ausgestattet (**Kapitel 4.4**). Genauer gesagt, wurde ein Förster Resonanzenergietransfer (FRET) Paar (Carboxyfluorescein-Tetramethylrhodamin) an das CC gekoppelt. Die Effizienz des Energietransfers gibt in diesem System Aufschluss darüber, ob das CC assoziiert oder dissoziiert ist. Das FRET-markierte CC wurde als nicht-kovalenter, reversibler molekularer Kraftsensor in einem ansonsten kovalent vernetzten Hydrogel eingesetzt. Unter Kompression verringerte sich die FRET-Effizienz, was einen ersten Hinweise auf die Dissoziation des CCs darstellt. Dieses Ergebnis verdeutlicht, dass CCs hervorragende molekulare Kraftsensoren für biomimetische Materialien darstellen.

Diese Arbeit demonstriert, dass CCs mit maßgeschneiderten, reversibel manipulierbaren Eigenschaften exzellente Bausteine für Hydrogele sind, die in der Zellkultur und der regenerativen Medizin Verwendung finden können. Es konnte zum ersten Mal gezeigt werden, dass einzelne CCs durch His-Metall-Koordinationsbindungen reversibel stabilisiert werden können und dass diese molekulare Stabilisierung direkt auf die viskoelastischen Materialeigenschaften von Hydrogelen übertragbar ist. Durch gezieltes Einfügen von intermolekularen His-Metall-Koordinationsbindungen gelang es, CC-Hydrogele mit einem zweiten übergeordneten His-Zn^{2+} basierten Vernetzungsmodus herzustellen. So konnte die Relaxationszeit der Hydrogele über einen weiten Bereich maßgeschneidert kontrolliert werden. Um CCs als molekulare Kraftsensoren in Materialien zu etablieren, wurde das CC Heterodimer mit einem FRET-Reportersystem ausgestattet. Erste Experimente deuten darauf hin, dass die Dissoziation des CCs im Hydrogel unter Krafteinwirkung optisch verfolgt werden kann. Zukünftig können CCs mit maßgeschneiderter Stabilität nicht nur als molekulare Kraftsensoren für Materialien, sondern auch zur Erforschung von Zell-Matrix Wechselwirkungen eingesetzt werden.

Table of contents

Abbreviations

A – acceptor

ACN – acetonitrile

AFM – atomic force microscope

Ala – alanine

APDMES – 3-aminopropyl dimethyl ethoxysilane

Asp – asparagine

Boc – tert-butoxycarbonyl

CC – coiled coil

CD – circular dichroism

CF – carboxyfluorescein

CFP – cyan fluorescent protein

D – donor

DBCO – dibenzocyclooctyne

DCM – N,N Dichloromethane

DHB – 2,5-Dihydroxybenzoic acid

DIPEA – N,N-Diisopropylethylamine

DMF – N,N-Dimethylformamide

DOPA – 3,4-dihydroxyphenlyalanine

GFP – green fluorescent protein

ΔG – free energy

Δx – potential width

θ_{obs} – ellipticity

θ	– molar ellipticity
EDTA	– ethylenediaminetetraacetate
ECM	– extracellular matrix
E_L	– left-handed circularly polarized light
E_R	– right-handed circularly polarized light
EXAFS	– extended X-ray absorption fine structure
Fmoc	– fluorenylmethoxycarbonyl
FRET	– Förster resonance energy transfer
Glu	– glutamic acid
Gln	– glutamine
HCTU	– O-(6-Chlorobenzotriazol-1-yl)-N,N,N′,N′-tetramethyluronium hexafluorophosphate
His	– histidine
HPLC	– high-performance liquid chromatography
k_{off}	– unfolding rate
LVE	– linear viscoelastic range
MALDI	– matrix-assisted laser desorption/ionization
MD	– molecular dynamics
Mdeg	– millidegree
MW	– molecular weight
$N\alpha$	– α-amino group
N_2	– native state
NHS	– N-hydroxysuccinimide
NTA	– nitrilotriacetic acid
PAAm	– poly(acrylamide)

PBS – phosphate buffered saline

PEG – poly(ethylene glycol)

PIPPS – piperazine-N,N'- *bis*(3-propanesulfonic Acid)

PHPMA – N-(2-hydroxypropyl)-methacrylamide

PNIPAM – poly(N-isopropylacrylamide)

PyAOP – (7-Azabenzotriazol-1-yloxy)trispyrrolidinophosphonium hexafluorophosphate

RT – room temperature

Ser – serine

SMFS – single molecule force spectroscopy

SPPS – solid phase peptide synthesis

T – temperature

TCEP – tris(2-carboxyethyl)phospine

TEM – transmission electron microscopy

TFA – trifluoroacetic acid

Thr – threonine

TOF – time of flight

TR – tetramethylrhodamine

2U – unfolded state

UV – ultraviolet

WLC – worm-like chain

YFP – yellow fluorescent protein

XANES – X-ray absorption near edge structure

1 Introduction

The development of intelligent biomimetic hydrogels with tunable, self-healing and self-reporting cross-links is a main focus of current material research [1-3]. Biomimetic hydrogels are polymeric networks with a high water content, which are excellent candidates for bioengineering applications, such as extracellular matrix (ECM) mimics [4-7]. Proteins and peptides are often used as hydrogel building blocks, since they are modular, tunable, biocompatible and responsive to environmental changes (e.g. pH, temperature, light, electric fields) [5,8]. The exact structure and parameters controlling the formation of natural hydrogels are often poorly understood. Relating the stability of molecular building blocks to the viscoelastic properties of bulk hydrogels also remains a major challenge. Towards answering these key questions, detailed knowledge of the sequence-structure-mechanics relationships of the molecular building blocks is a prerequisite to gain control over the viscoelastic properties of hydrogels. In this work, I have developed a self-healing, reversibly tunable and precisely controllable material platform based on proteinaceous α-helical coiled coil (CC) building blocks. Specifically, I have combined a well-characterized polymer backbone with CC building blocks as cross-links. The stability of the CC was tuned by rationally designing and implementing nature-inspired non-covalent histidine (His)-metal coordination bonds at different positions. The thermodynamic stability of the CCs was investigated with optical spectroscopy (e.g. temperature-dependent circular dichroism (CD) spectroscopy), while the energy landscape parameters of the CC were characterized on the single molecule level using atomic force microscope (AFM)-based single molecule force spectroscopy (SMFS). Implementing the CC as cross-link for star-shaped poly(ethylene glycol) yielded self-healing hydrogels with precisely controllable and reversibly tunable viscoelastic properties. To shed light on material failure mechanisms, I further equipped the CC with a fluorescence-based reporter system. In this way, I have obtained a self-reporting molecular force sensor with an optical readout, which sets the stage for studying the network structure and failure of CC cross-linked hydrogels as well as for investigating cell-matrix interactions in 3D.

In the following introductory chapters, I will describe essential design principles of natural materials, characteristic features of His-metal coordination bonds and the CC protein folding motif. I will further give an overview of existing bioinspired and biomimetic CC- and His-metal coordinating hydrogels, as well as self-reporting hydrogel cross-links.

1.1 Natural design principles for protein-based materials

Nature provides a huge variety of high-performance functional materials based on proteinaceous building blocks, e.g. tendon [9], spider silk [10], mussel byssal threads (**Figure 1)** [11], *Nereis* worm jaws [12], hagfish slime [13] or whelk egg capsules [14]. The structure and resulting mechanical properties of these materials seem to be precisely tailored to fulfill specific functions. Common design principles of many biological materials are hierarchical organization, self-assembly and dynamic rearrangement of non-covalent interactions under load **(Figure 1A**). The mussel byssal threads of *Mytilus spp.* are a biological archetype for the principles described above and an inspiration for this work. Secure attachment to surfaces via strong, yet extensible byssal threads is essential for *Mytilus spp.,* which are exposed to crashing waves in costal zones. Byssal threads are self-assembled from prepepsinized collagen (preCol) proteins forming the fibrous core of the threads and mussel foot protein 1 forming the protective cuticle [15,16]. The central preCol domain is flanked by β-sheet domains and His-rich domains, which coordinate transition metal ions, such as Zn^{2+}. Under load, the His-metal coordination bonds break sacrificially and the β-sheet domains unfold, revealing the hidden length of the thread. The reversible, dynamic nature of the coordination bonds allows the byssal thread to self-heal (**Figure 1B**) [17,18].

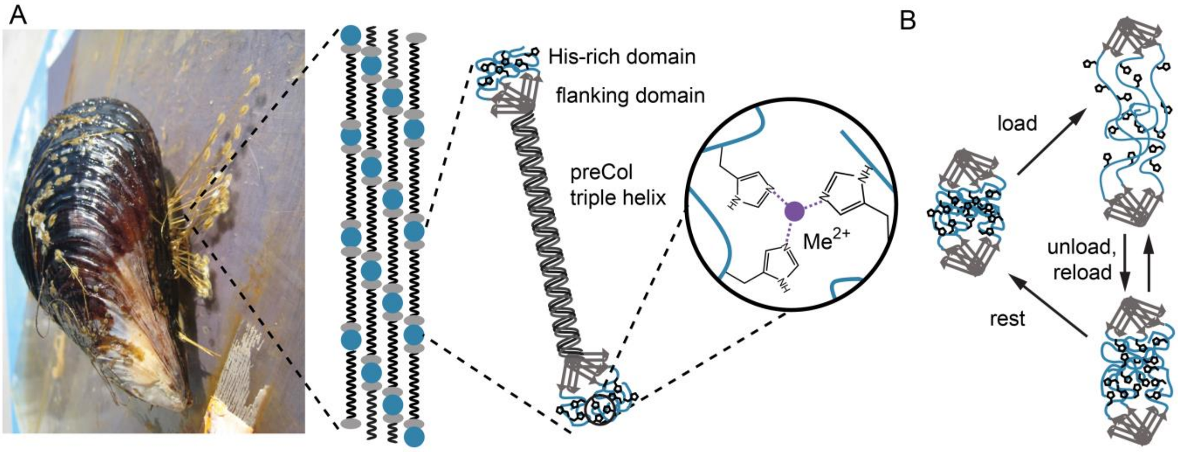

Figure 1: Mussel byssal threads: a protein-based high-performance material. A) Mussel byssus core with fibrous preCol proteins (Picture of the mussel reprinted with permission from [19], Copyright © 2014, John Wiley and Sons). The collagen-like core domain is flanked by β-sheet domains and terminal His-rich domains. The unstructured His-rich domains coordinate transition metal ions such as Zn^{2+}. B) Unfolding of the β-sheet domains and breaking of the terminal His-metal coordination bonds reveals a hidden length and allows for high energy dissipation of the thread. His-metal coordination bonds can reform after the load is released, enabling self-healing of the thread.

Other non-covalent interactions, e.g. rearrangement of hydrogen bonds in the β-sheet crystalline domains of spider silk [10] as well as structural transitions, e.g. from α-helical CCs to β-sheets in hair, whelk egg capsules and hagfish slime [20-22], also play a major role in the response of natural materials to applied force. The CC folding motif is not only found in numerous materials, but also in intra- and extracellular proteins with mechanical function (e.g. cortexillin, vimentin and fibrinogen) (**Figure 2**). This indicates that CCs are excellent building blocks for developing intelligent biomimetic materials with tunable, self-healing and self-reporting properties [23,24]. Since the sequence-structure-function relationships of CCs are well studied, they can be rationally designed with desired properties and produced by solid phase peptide synthesis or more sustainably, by recombinant gene expression. The following sections will provide background on CCs as proteinaceous building blocks in biological materials and sequence-structure relationships of CCs in general.

1.2 Coiled coils as material building blocks

In 1953, Francis Crick coined the term "coiled coil" to describe the fold of α-keratin, which was investigated independently also by Pauling and Corey [25,26]. To date, there are more than 29,000 CC structures available in the CC^+ database [27,28], illustrating the abundance of the CC folding motif in proteins. The first CC described, α-keratin, is an intermediate filament and a main component of keratinaceous materials, such as hair, scales or feathers. These materials are formed by dead cells filled with keratins and span a broad range of Young's moduli from 10 MPa in stratum corneum to 2.5 GPa in feathers [29]. Also hagfish slime, which is used by the animal as a defense against predators [30], is composed of secreted α-keratin-like proteins [31]. The egg capsules of marine snails, e.g. the whelk snail, are composed of α-helical CC proteins, that are self-assembling into filaments [14]. Furthermore, CCs are prominent folding motifs found in intracellular proteins with mechanical function (**Figure 2**). The stalk region of the motor protein myosin and also several cytoskeletal proteins such as cortexillin and vimentin are α-helical CCs [32,33]. The intermediate filament vimentin forms parallel CC dimers that assemble into staggered antiparallel tetramers and finally filaments [34]. The extracellular protein fibrinogen (**Figure 2D**) is the precursor of fibrin, which forms a mechanically stable fibrous network facilitating blood clot formation and wound closure [35]. The mechanical properties of fibrin originate from its hierarchical organization with half-staggered double stranded protofibrils that assemble into fibers and finally form a highly extensible porous filamentous network [29].

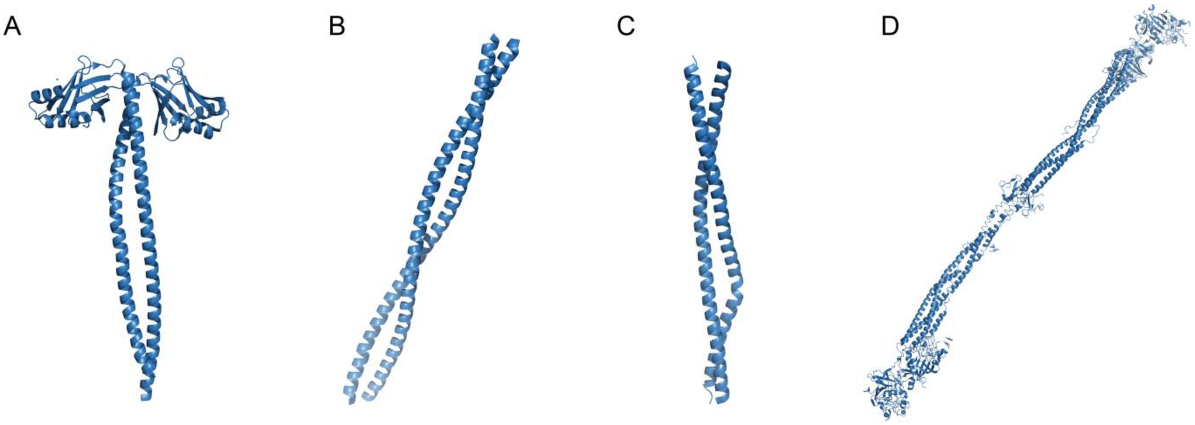

Figure 2: Coiled coils with mechanical functions. A) Molecular motor protein myosin (PBD-ID: 5CJ4) [36]. B) Actin-bundling protein cortexillin (PBD-ID: 1D7M) [33]. C) α-helical part of the intermediate filament vimentin (PDB-ID: 5WHF) [32]. D) Fibrinogen is the precursor of fibrin, which plays an important role in blood clot formation (PDB-ID: 1M1J) [37]. Figures were produced with PyMOL Molecular Graphics System, Version 2.0 Schrödinger, LLC.

Despite of their different function, all the CC materials and proteins described above show a similar characteristic three phase stress-strain response under tensile force (**Figure 3**). At low strain, the stress increases linearly (elastic response, phase I) followed by a yield plateau where hydrogen bonds stabilizing the α-helix of the CCs break and unfold with almost no stress increase (phase II).

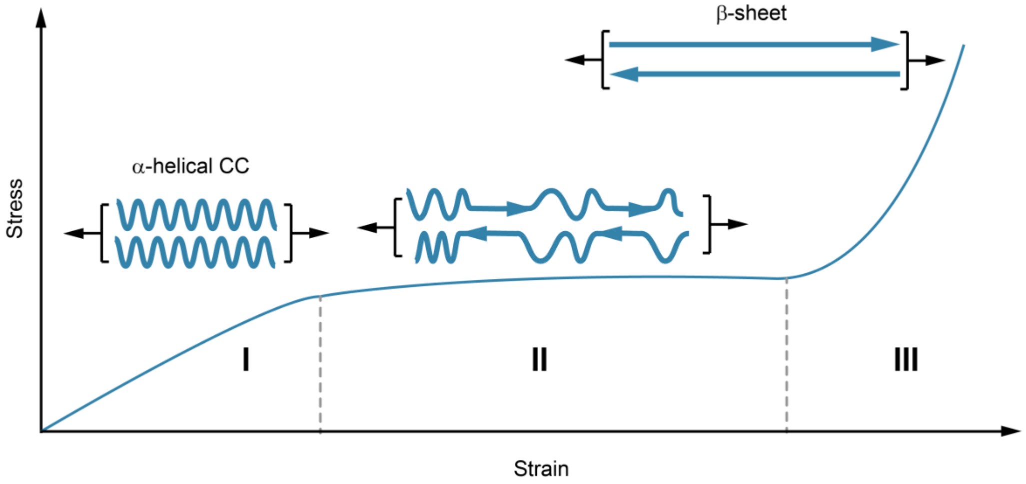

Figure 3: Characteristic stress-strain curve of coiled coil (CC) based materials. Phase I is the linear elastic response of the CC. Phase I is followed by a yield plateau (phase II) where the CC is unfolding. When the strain is released in phase I or II, the deformation is completely reversible for most CC based materials. In Phase III the CC is completely unfolded and forms mechanically more stable β-sheets.

Phase III shows the strain stiffening of the structures until final breakage [29]. The strain stiffening is caused by the α-helix to β-sheet transition of the CCs [22,38]. While the α-helix to β-sheet transition is fully reversible for whelk egg capsules even in phase III, it is only reversible at low strain values for α-keratin and fibrin [39]. The mechanical response of these biological materials is well studied at the bulk level, but the sequence-structure-mechanics relationship is less understood at the molecular level. However, molecular level understanding of the properties of CC building blocks is essential to develop intelligent, self-healing, tunable and self-reporting CC cross-linked hydrogels. The following sections will give an overview about the main sequence-structure relationships of CCs and existing work elucidating the mechanical response of CCs at the molecular level.

1.2.1 Sequence-structure relationships of coiled coil building blocks

Coiled coils are comprised of two or more self-assembling α-helices that fold into a superhelix. The sequence of CCs consists of seven amino acid repeats, forming a so-called heptad, with the residues designated as (*abcdefg*). The individual α-helices are stabilized via hydrogen bonds along the helical axis (**Figure 4A**). The superhelical self-assembly of CCs is driven by the formation of a hydrophobic core of the amino acids in *a* and *d* position that are tightly packed in a knobs-into-holes fashion (**Figure 4B**) [24]. Moreover, ionic interactions of charged amino acids in the *e* and *g* positions have been found to contribute to the direction of helix formation and stability [40]. The overall stability of the CC also depends on the helix propensity of the amino acids [41], especially in the solvent-exposed positions *b, c* and *f* [42,43]. The sequence-structure relationship of CCs has been intensively studied in the past decades, revealing a set of rules for the rational design of CCs. This allows for tuning the oligomerization state, superstructure formation, helix orientation and thermodynamic stability of CCs, which often only requires small changes in the sequence [23,44-48].

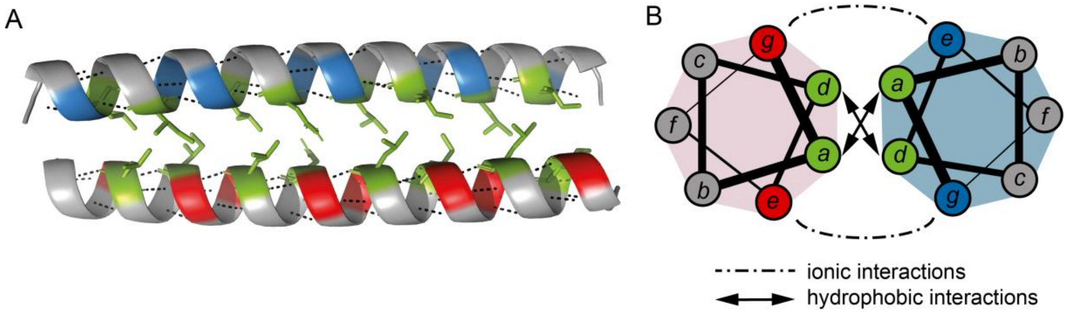

Figure 4: Structure of a heterodimeric coiled coil (CC). A) Lateral view of the structural model of the CC, dotted lines represent hydrogen bonds. The model was generated with CCBuilder 2.0 [49] and the figure produced with PyMOL Molecular Graphics System, Version 2.0 Schrödinger, LLC. B) Helical wheel model showing the heptad repeat of a dimeric CC. The hydrophobic core (*a* and *d* positions) is highlighted in green. The charged residues (*e* and *g* position) are highlighted in blue and red. Dash-dotted lines represent ionic interactions. Arrows indicate hydrophobic interactions.

Moreover, the assembly state and stability of CCs are responsive to changes of the environmental conditions, such as pH and salt concentration, which is advantageous for the development of intelligent stimuli-responsive materials [50-53]. Thus, CCs are promising intelligent building blocks for materials since they are self-assembling, self-healing and tunable via sequence modifications and environmental changes. While many aspects of the rational design of CCs are well known, the sequence-structure-mechanics relationship of CCs in different force application geometries was only investigated recently. In-depth understanding of the energy landscape parameters and unfolding mechanism of CCs in different loading geometries is essential for implementing CCs as precisely controllable and tunable building blocks into hydrogels. Therefore, the following section gives insights into recent research about the response of CCs to force.

1.2.2 Mechanical coiled coil unfolding in different loading geometries

In order to tune the viscoelastic properties of CC cross-linked materials, molecular level understanding of the energy landscape parameters and the unfolding mechanisms of CC building blocks is crucial. Currently, single molecule force spectroscopy, e.g. using optical tweezers, magnetic tweezers and the atomic force microscope (AFM), are available to gain information about the energy landscape parameters, i.e. the unfolding rate (k_{off}) and the distance from the folded to the transition state (Δx) as well as the unfolding mechanism of single molecules [54]. In this work, AFM-based single molecule force spectroscopy (SMFS) is used to study CC unfolding in the shear geometry. An AFM is composed of a cantilever with a sharp tip with a nanometer scale radius functioning as a force sensor and a piezo-table for precise sample positioning [55]. A laser is focused on the back of the cantilever and reflected back to a photodiode to detect the cantilever deflection (**Figure 5A**). This deflection signal can be converted into force taking into account the cantilever spring constant and sensitivity. The CC-forming peptides are site-specifically immobilized on the cantilever tip and the glass surface separately to apply force in shear geometry (see **Chapter 3.4**). When the cantilever is in contact with the surface, the CC forms. When the cantilever is pulled away from the surface, the CC is mechanically loaded, which leads to an increase of the detected force. The CC interaction breaks at a critical force, called the rupture force. Representative force-extension curves are shown in **Figure 5B**.

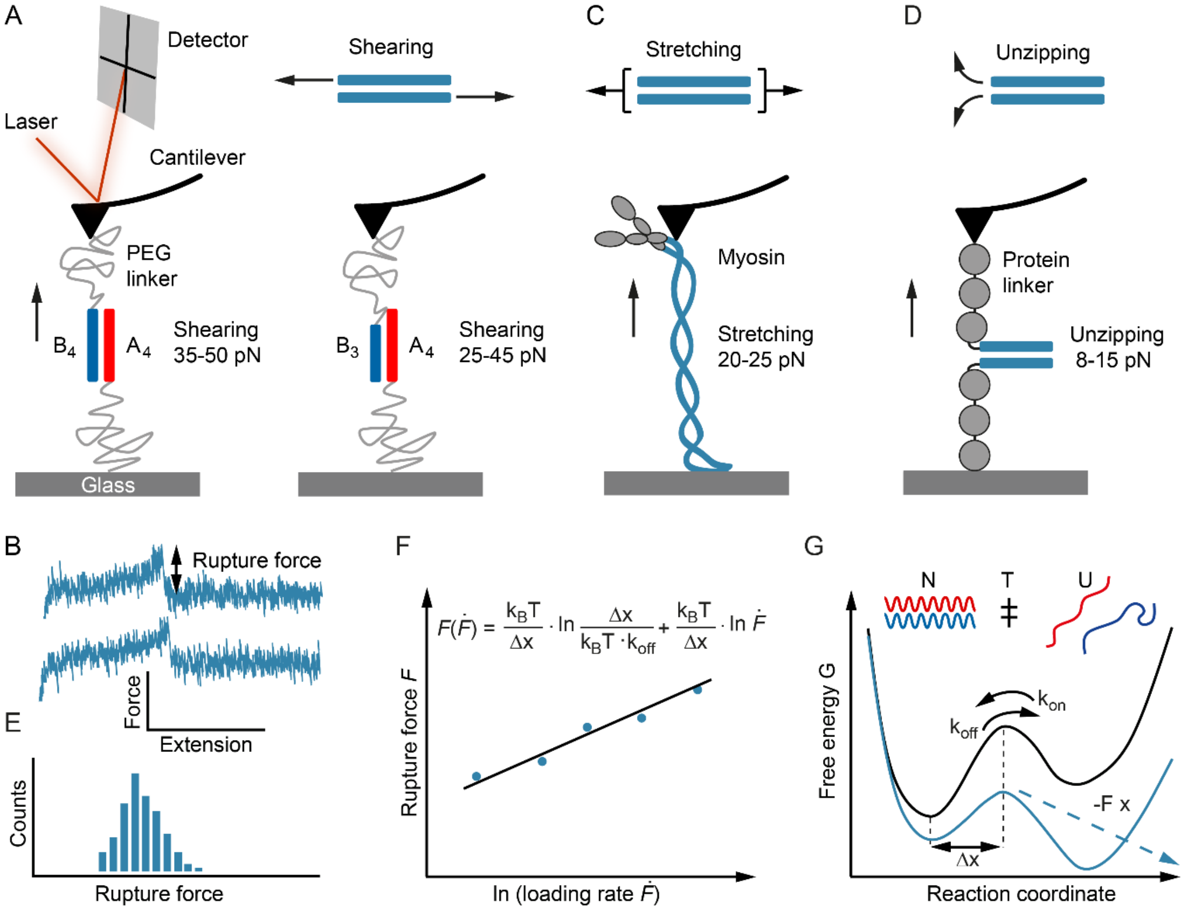

Figure 5: AFM-based single molecule force spectroscopy (SMFS) of coiled coils (CCs) in different pulling geometries. A) General measurement setup for performing AFM-SMFS of a CC in the shear geometry. In shear geometry, coiled coils consisting of 3-4 heptad repeats rupture at 25-50 pN, depending on their length [56]. B) Representative force curves of a CC in shear geometry. C) Myosin stretching results in forces of 20-25 pN [57]. D) Unzipping of a short CC at 8-15 pN [58]. E) Schematic rupture force distribution of a CC. F) Schematic plot of the loading rate (dF/dt) dependency of the rupture force. The Bell-Evans equation can be used to fit the data and extract information about the stability of the interaction and the energy landscape [59]. G) Energy landscape with the native state (N), the transition state (T) and the unfolded state (U). The rates of folding and unfolding at zero force are k_{on} and k_{off}. The distance from the native to the transition state is Δx. The energy landscape is tilted by the applied force, which promotes unfolding and chain dissociation.

The mechanical stabilities and unfolding mechanisms of CCs were found to be highly dependent on the force application geometry (e.g. shearing, stretching or unzipping) (**Figure 5**). For the shear geometry, the mechanical response was recently investigated using AFM-based SMFS and molecular dynamics (MD) simulations. Goktas et al. [56] reported rupture forces of 25-50 pN for a set of rationally designed heterodimeric CC sequences of 3-4 heptads in length (**Figure 5A**). The CC heterodimers studied were composed of a Glu-rich (acidic, A) and a Lys-rich (basic, B) peptide (A_4B_4 and A_4B_3) [46]. The 4-heptad long A_4B_4 showed a higher stability compared to the 3-heptad A_4B_3. In stretching geometry, the CC domain of the motor protein myosin reached a plateau force of 20-25 pN [57] (**Figure 5C**). In unzipping geometry, CC unfolding occurred at 8-15 pN (**Figure 5D**), which was found to be almost independent of length and sequence [58,60,61].

The mechanical response of CCs, such as the intermediate filament vimentin, strongly depends on the applied loading rate, i.e. the rate of force application (dF/dt) [34]. Using dynamic SMFS, Goktas et al. [56] also reported a loading rate dependency for the CCs studied in shear geometry. Dynamic SMFS allows one to gain information about the energy landscape parameters k_{off} and Δx. When performing dynamic SMFS, force-extension curves are collected at different cantilever retract speeds, resulting in different loading rates of the molecular interaction. The rupture force and loading rate distributions, obtained from hundreds of force-extension curves at each retract speed are plotted in histograms (**Figure 5E**) to extract the most probable values using a Gaussian fit. Plotting the obtained rupture force values semi-logarithmically against the loading rate yields a linear dependency, which can be fitted with the Bell-Evans model (**Figure 5F**) [59]. The Bell-Evans model mathematically describes the tilting of the free energy landscape when a force is applied (**Figure 5G**). The applied force favors unfolding of the CC and increases its dissociation rate. The Bell-Evans model enables extrapolation to the unfolding rate at zero force k_{off}, which is obtained from the intersection of the Bell-Evans fit with the x-axis. Δx is obtained from the slope of the fit function. Information about the energy landscape parameters k_{off} and Δx is crucial since it will allow for tuning the viscoelastic properties of CC cross-linked materials: k_{off} is expected to be directly related to the material relaxation time and Δx gives information about the deformability of the α-helices prior to failure.

Shearing the model CCs A_4B_4 and A_4B_3 in a dynamic SMFS experiment showed a 10-fold lower k_{off} ($3.2 \cdot 10^{-4}$ s^{-1}) and a higher Δx (1.29 nm) for A_4B_4 when compared to the shorter A_4B_3 (k_{off} = $6.5 \cdot 10^{-3}$ s^{-1}, Δx = 1.03 nm) [56]. Molecular dynamic (MD) simulations were used to elucidate the molecular mechanism of CC unfolding. In shear geometry, uncoiling-assisted dissociation perpendicular to the force axis was proposed as the predominant mechanism at the loading rates applied using AFM [56]. López et al. [62] studied the effect of hydrophobic core packing and helix propensity on the stability of A_4B_4. The rupture forces decreased when inserting amino acids with lower helix propensity in the solvent-exposed positions or impairing with a tight hydrophobic core packing. The effects on the energy landscape are different in both cases. While a less tight hydrophobic core packing increased Δx, a lower helix propensity resulted in a concomitant decrease of k_{off} and Δx. Taken together, these findings show that CC length, sequence and force application geometry are crucial parameters for the design of CCs as material building blocks. In this thesis, AFM-based SMFS is used to study the effect of metal ion coordination on the energy landscape of A_4B_4 in shear geometry. The next section gives background on metal coordination sites in natural proteins and rationally designed metal coordination sites for stabilizing peptides and proteins.

1.3 Stabilization of protein building blocks using metal coordination

Protein-metal coordination plays a crucial role in metabolic processes, e.g. as part of catalytic sites in enzymes, oxygen transport, nitrogen fixation, photosynthesis as well as the stabilization of proteins [63,64]. Only in the last two decades, research on biological materials revealed that protein-metal coordination also plays an important mechanical role. It is one of Nature's means to mechanically fortify materials and modulate adhesion, toughness, hardness and self-healing. Protein-metal coordination bonds have been found to contribute to the performance of mussel byssal threads (see **Chapter 1.1**), ragworm jaws, sandcastle worm glue and spider fangs, among others [19].

1.3.1 Metal coordination sites in natural proteins

Protein-metal coordination bonds are strong interactions, between specific amino acid side chains, (e.g. aspartic acid (Asp), glutamic acid, histidine, serine, threonine, phosphoserine and 3,4-dihydroxyphenlyalanine) and metal ions (e.g. Ca^{2+}, Mg^{2+}, Mn^{2+}, Fe^{3+}/Fe^{2+}, Ni^{2+}, Cu^{2+}, Co^{2+} and Zn^{2+}) [65,66]. The amino acid side chains act as ligands providing lone pair electrons to the empty orbitals of the metal ion. The mechanical stability of the resulting metal coordination bond can be up to half the stability of a covalent bond [67], while being dynamic with dissociation rate constants in the µM to pM range [68]. Histidine is the most frequent ligand for Ni^{2+}, Cu^{2+}, Co^{2+} and second most frequent ligand for Zn^{2+} [69]. The imidazole side chain moiety of His contains two nitrogen atoms (N_τ and N_π) that can form a coordination bond. The ability of His to coordinate metal ions is pH-dependent. Since the pK_a of His is ~ 6.5, the nitrogen atoms are protonated at acidic pH and unable to coordinate metal ions. At physiological pH (7.4) one nitrogen atom is deprotonated and the His side chain is able to coordinate divalent metal ions (**Figure 6**) [70,71]. At extremely basic pH, the second proton dissociates forming an imidazolate ion (pK_a ~ 14.0) [72,73], in which both nitrogen atoms can participate in coordination.

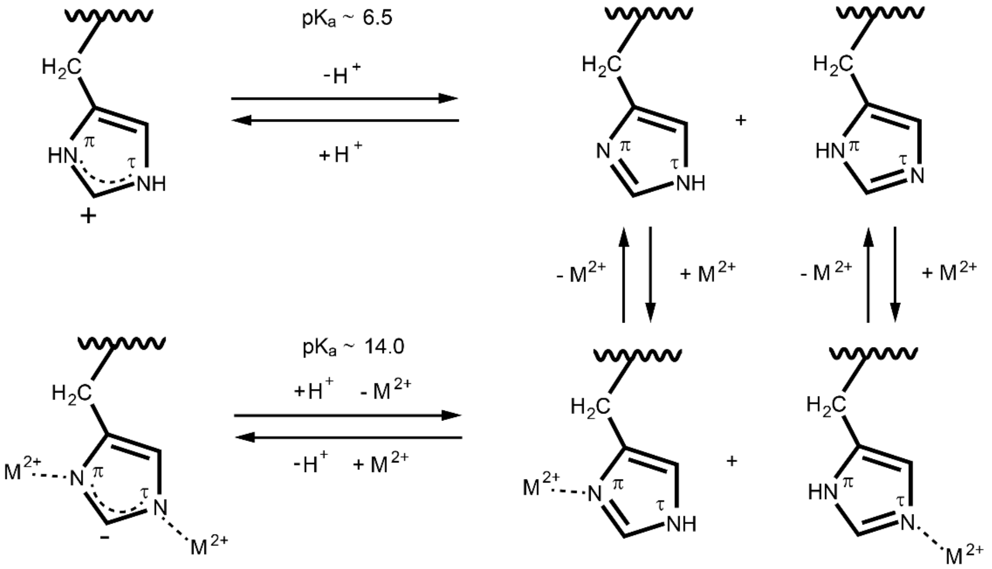

Figure 6: Histidine protonation and metal coordination states. The pK_a of His is ~ 6.5. At pH values above 6.5, one nitrogen atom gets deprotonated, which facilitates the reversible coordination of transition metal ions (M^{2+}). At high pH (pK_a ~ 14.0), the second nitrogen is deprotonated (imidazolate) and a second metal ion can be coordinated [72,73].

His-Metal coordination bonds have essential functions in enzymes, such as His-Zn^{2+} in carbonic anhydrase II and in Zn-proteases, His-Mn^{2+} in Mn-superoxide dismutase or His-Cu^{2+} in galactose oxidase [63,74,75]. Besides their physiological function, metal coordination bonds are essential for the mechanical performance of acellular biogenic materials. They are the main contributors to the abrasion resistance and hardness of the jaw of *Glycera sp.* worms and spider fangs, the adhesive properties of sandcastle worm glue (**Figure 7**) as well as the self-healing and energy dissipation of mussel byssal threads (**Figure 1**) [19].

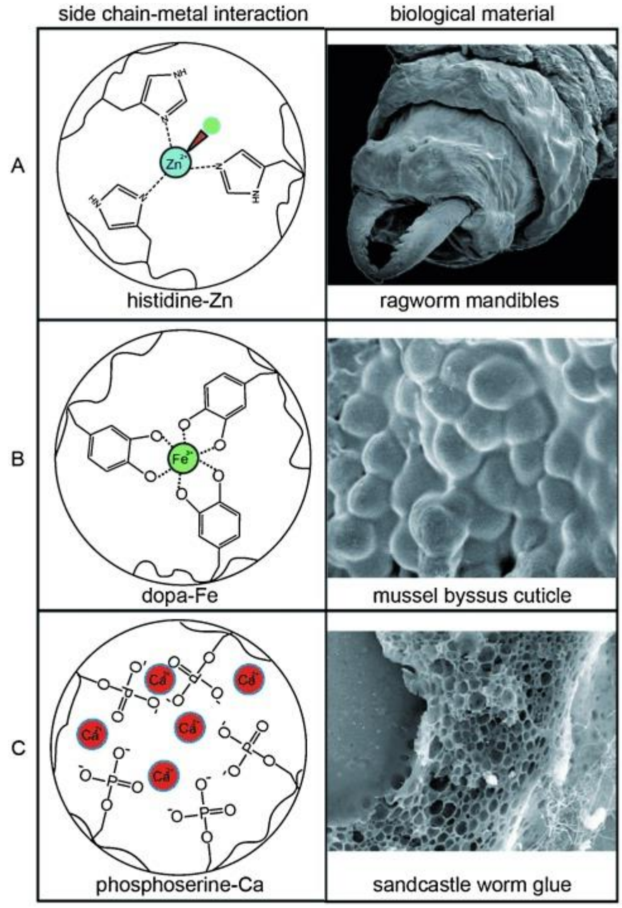

Figure 7: His-metal coordination bonds in different materials. A) Jaw of *Glycera sp.* worms with His-Zn^{2+} coordination. B) Mussel byssus cuticle fortified with DOPA-Fe^{3+}. C) Sandcastle worm glue reinforced with phosphate-Ca^{2+} bonds. (Adapted and reprinted with permission from [19], Copyright © 2014, John Wiley and Sons. SEM image of Ragworm mandibles: reprinted with permission from [76], Copyright © 2008; American Chemical Society. SEM image of the Sandcastle worm glue: reprinted with permission from [77].)

Due to their high bond strength and dynamic nature, His-metal coordination bonds have been engineered into proteins to increase their thermodynamic and mechanical stability. The stability of His-metal coordination sites is highly dependent on the spacing between the His residues and their location in the protein [78,79]. Furthermore, the stability of His-metal coordination bonds is tunable using different metal ions, since they have different preferred coordination geometries and binding affinities ($Cu^{2+} > Ni^{2+} > Co^{2+} > Zn^{2+}$) [80,81]. AFM-based SMFS studies with nitrilotriacetic acid and His_6-tag revealed that the mechanical stabilities of His-metal coordination bonds follow the order of $Cu^{2+} > Ni^{2+} > Zn^{2+} > Co^{2+}$ [82]. A brief summary on existing bioengineered His-metal coordination sites is given in the next section, since they have been used in this work for tuning the stability of CC building blocks for hydrogel applications.

1.3.2 Bioengineered His-metal coordination sites in proteins

His-metal coordination is a powerful means to increase the stability of proteins [83,84]. One of the earliest attempts to bioengineer a His-metal coordination site into a protein was the insertion of two His in the α-helix or a β-sheet of cytochrome c of *Saccharomyces cerevisiae* [85,86]. Inserted into the α-helix with an amino acid spacing of $i \rightarrow i + 4$ the bi-His-coordination site was shown to bind Cu^{2+} and stabilize the structure of the protein by 1.2 kcal mol^{-1} [85]. When inserting His in β-strands, the melting temperature of the protein was increased by 23.2 °C in the presence of Ru^{2+}(bipyridine)$_2$ [86]. This thermodynamic stabilization is based on the higher binding affinity of the metal ion to the folded state of the protein when compared to the unfolded state. The preferential self-assembly of proteins into higher-order oligomers can also be driven by His-metal coordination. Insertion of a His-Asp-metal coordination site into cytochrome *cb$_{562}$* enabled dimer formation in the presence of Cu^{2+}, whereas the addition of Ni^{2+} resulted in trimer and Zn^{2+} in tetramer formation (**Figure 8A**) [87-89]. His-metal coordination bonds have also been used to mechanically stabilize protein folds.

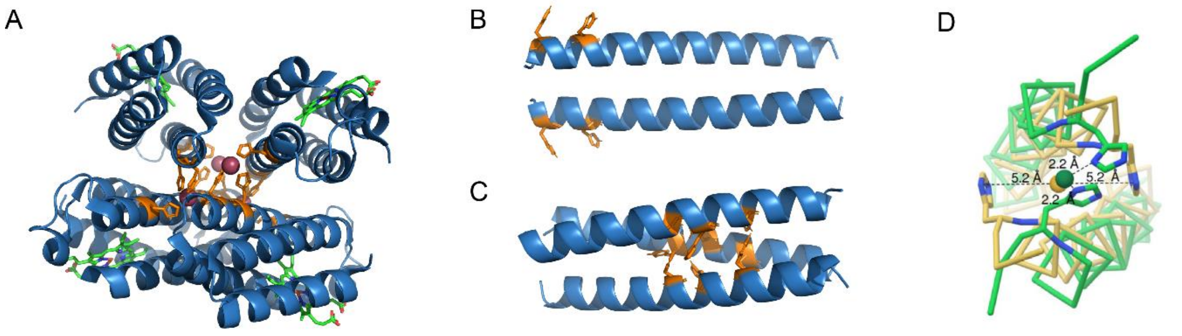

Figure 8: Structure of bio-engineered His-metal coordination sites in a cytochrome c and selected coiled coil (CC) peptides. A) Structure of cytochrome cb562 with His modifications in the presence of Zn^{2+} (red dots) (PDB-ID: 2QLA) [88]. B) Homodimeric CC with His-metal coordination sites stabilizing the N-terminus [90]. C) Homotrimeric CC designed to specifically bind two Ni^{2+} and Cu^{2+} in the hydrophobic core [91]. His residues are highlighted in orange. D) CC homodimer that folds only in the presence of Zn^{2+} or Cu^{2+} (reprinted with permission from [92], Copyright © 2018, John Wiley and Sons). Structure of B) and C) were predicted using CCBuilder 2.0 [49] Figure A-C were produced with PyMOL Molecular Graphics System, Version 2.0 Schrödinger, LLC.

For example, Cao et al. [93] investigated the stabilization of the protein GB1 when inserting two His at different positions in the sequence. AFM-based SMFS was used for studying the stability of the GB1 mutants in the presence and absence of Ni^{2+}. Introducing the His-metal coordination site in the middle of the β-sheet domain of GB1 resulted in a decrease of k_{off} from

$0.029\ s^{-1}$ to $0.007\ s^{-1}$ when compared to the wildtype protein, whereas placing His at the edges of the β-sheet did not lead to a decrease of k_{off}.

His-metal coordination bonds have not only been inserted into globular proteins, but also short natural and synthetic peptides. The optimal spacing of His in an α-helix is His-X-X-X-His ($i \rightarrow i + 4$ residues), where both His face to the same site of the helix [78,84]. In 1990, Ghadiri & Choi [94] implemented two His in the $i \rightarrow i + 4$ positions of a 20 amino acid long α-helical peptide that only folded in the presence of stabilizing His-Zn^{2+}, Cu^{2+}, Ni^{2+} or Cd^{2+} coordination. Shiga et al. [95] inserted a His-His-Glu/Asp metal-coorindation site into the hydrophobic core of a tetrameric CC, resulting in an increase of the melting temperature from 66 °C in the absence of metal ions to more than 95 °C in the presence of metal ions. Krantz & Sosnick [90] studied the heterogeneity of the folding pathway of the dimeric CC GCN4 via insertion of two His-metal coordination sites. His was placed in the solvent-exposed part at the N-terminus in the $i \rightarrow i + 4$ position (**Figure 8B**). In the presence of Co^{2+}, the nucleation and folding of the CC preferentially started at the metal ion stabilized N-terminus even though the helicity of the C-terminal region was higher [90]. This research indicates that His-metal coordination is a good means to stabilize helical turns in CC structures.

Metal-ion induced folding can also be used to control CC self-assembly. Suzuki et al. [96] and Boyle et al. [97] implemented two His in the hydrophobic core positions (*a* and *d*) of the second heptad of a homotrimeric CC. This CC only assembled in the presence of transition metal ions. Implementing His into this trimeric CC in the *a* position of the second heptad and the *a* and *d* position of the third heptad yielded a CC that specifically binds Cu^{2+} in the second heptad and Ni^{2+} in the third heptad (**Figure 8C**) [91]. Aupič et al. [92] showed that CC homodimer formation can also be controlled via insertion of a single His in the *e* position closest to the C-terminus (**Figure 8D**). The modified homodimer only formed in the presence of Zn^{2+} and Cu^{2+} but not with Ni^{2+} or Co^{2+}. This effect is based on the conformation of the His in the helix backbone and the preferred coordination of metal ions in certain conformations. His-metal coordination sites can also be used to induce conformational changes. In order to switch a β-sheet peptide to an α-helix, two His were inserted in the *b* and *e* position with $i \rightarrow i + 4$ spacing, thus promoting the formation of an α-helical CC in the presence of Zn^{2+} or Cu^{2+} [98]. The described examples highlight that His-metal coordination sites are versatile means to tune the folding, oligomerization state and stability of CCs and proteins in general [69,99-101].

1.4 Bioinspired and biomimetic coiled coil hydrogels

Hydrogels are water-swollen cross-linked polymer networks. Natural hydrogels include polysaccharide networks, such as alginate, hyaluronic acid or chitosan as well as protein-based fibrous networks, such as collagen, fibrin, elastin or hagfish slime [13,102]. In recent years, a tremendous number of biomimetic hydrogels has been developed with application potential in tissue engineering, drug delivery and for investigating cell-matrix interactions [4,5,103]. Coiled coils are promising building blocks for the development of intelligent biomimetic hydrogels since they fulfill the following requirements:

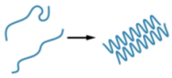

- **Self-assembly** – CC cross-linked hydrogel networks assemble without toxic chemicals under physiological conditions [102,104].

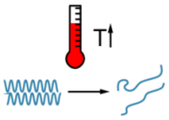

- **Stimuli-responsiveness** – The viscoelastic properties of the hydrogels are tunable via changes in sequence, pH, temperature or ionic strength [5,8].

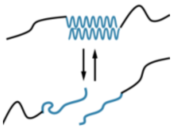

- **Self-healing** – Non-covalent cross-links are reversible and contribute to the self-healing behavior of hydrogels. This allows cells to remodel the material and migrate [4,103].

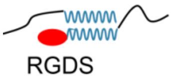

- **Biocompatibility –** The hydrogel is biocompatible and contains no immunogenic or toxic components. It allows for gas transfer and diffusion of biomolecules. Cell adhesive ligands can be easily implemented [6,103].

Coiled coils possess all the desired characteristics of the material cross-links mentioned above. They are self-assembling, self-healing, biocompatible and responsive to changes in pH, ionic strength and temperature [102,105]. Further, they can be easily equipped with cell adhesion motifs, such as RGD, to facilitate cell attachment and growth [106]. An overview of existing hydrogel networks based on CCs and CC-polymer hybrid hydrogels will be discussed in the following sections.

1.4.1 Coiled coil-based hydrogels

Most of the CC hydrogels reported in literature are based on the formation of a fibrous CC network. Since the natural ECM also contains fibrous proteins, such as collagen or fibronectin [107], CC hydrogels are well suited to mimic their natural model system. Self-assembling fibrous CC networks based on the interactions of solvent-exposed amino acids were reported by Banwell et al. [108]. Rationally engineered 4-heptad repeat CCs contained either Ala in the *b, c* and *f* positions or Gln in the *b* and *c* positions (**Figure 9A**), facilitating fiber formation via hydrophobic interactions or hydrogen bonds, respectively. Using rat adrenal tumor cells, it was shown that cell growth and differentiation was comparable with the behavior of cells when grown on the natural ECM-extract Matrigel®. Fletcher et al. [50,109] reported the formation of a pH-responsive fibrous hydrogel using a highly charged 21 amino acid long, α-helical peptide with a high number of charges the solvent-exposed *b, c* and *f* positions (**Figure 9B**).

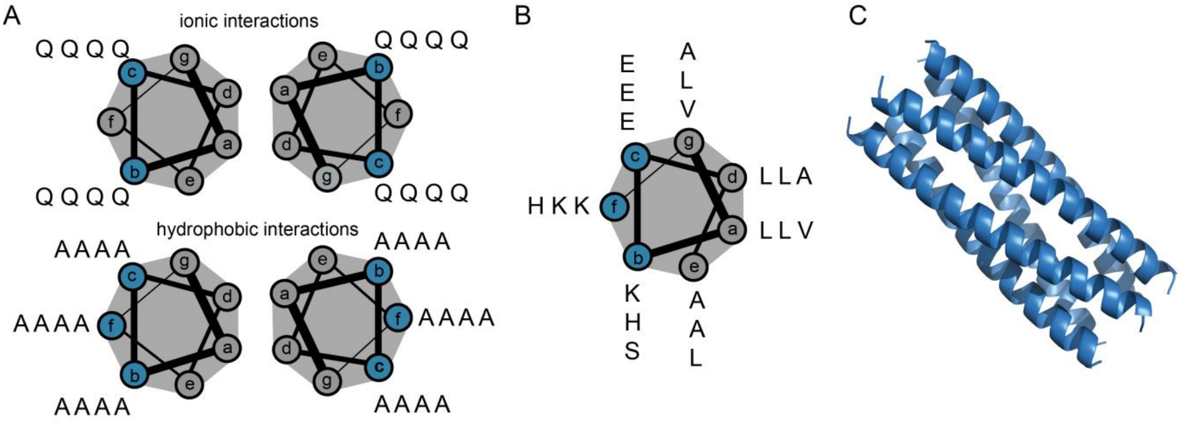

Figure 9: Design principles of fiber-forming coiled coil (CC) peptides. A) Helical wheel representation of the CC sequence used by Banwell et al. [108], B) fiber-forming CC peptides that form hydrogels based on the hydrophobic or ionic interactions [50], C) Structure of the thermosresponsive homopentameric CC [110]. The structure of CC was predicted using CCBuilder 2.0 [49] and the figure was produced with PyMOL Molecular Graphics System, Version 2.0 Schrödinger, LLC.

A thermoresponsive homopentameric CC (**Figure 9C**) was developed by Hill et al. [111]. The CC formed a porous fibrous network at 4 °C and dissolved when incubated at 37 °C. The hydrogel was able to bind and gradually release the small molecule curcumin, indicating its potential as a drug delivery system.

1.4.2 Coiled coil-polymer hybrid hydrogels

Protein-polymer hybrid hydrogels are often used for engineering biomimetic scaffolds. They combine well characterized polymers, which can be produced on large scales, with proteins or peptides that are tunable in terms of stability and responsiveness [4,112]. In CC-polymer hybrid hydrogels, CCs act as cross-links for synthetic polymers or random coil proteins. Proteinaceous hydrogels with CC cross-links were reported previously by several groups [113-115]. For example, Shen et al. [114] engineered an artificial triblock protein cross-linked with leucine-zipper end blocks that form CC tetramers and can be tuned with additional disulfide bridges. Buchberger et al. [116] combined a DNA backbone with a heterodimeric CC cross-link to assemble nanofibers.

Coiled coils are also used to cross-link synthetic polymers, such as poly(ethylene glycol) (PEG), poly(N-isopropylacrylamide) (PNIPAM) or N-(2-hydroxypropyl)-methacrylamide (PHPMA). Wang et al. [117] used the tetrameric stalk region of kinesin to cross-link PHPMA and *N',N'*-dicarboxymethylaminopropylmethacrylamide. The CC was bound to the polymer using His-Ni^{2+} coordination via the His-tag on the peptides and iminodiacetate on the polymer backbone (**Figure** 10**A**). Inspired by fibrin, Jing et al. [118] synthesized a peptide-PEG-peptide triblock that formed dimeric and tetrameric CC cross-links (**Figure 10B**). Yang et al. [119] used an antiparallel CC heterodimer as a cross-link for PHPMA, while Glassman et al. [120] described a thermoresponsive composite hydrogel made of a homopentameric CC integrated in a random coil protein with terminal PNIPAM groups (**Figure 10C**).

A system of two heterodimeric 4-heptad long CCs, characterized by different affinities, were coupled to 4-arm star-PEG (molecular weight: 10 kDa) by Dånmark et al. [121] (**Figure 10D**). It was shown that the different affinities of these CCs directly affected the viscoelastic properties, i.e. the relaxation times, of the resulting star-PEG hydrogels. The group of Tirrell further reported that single amino acid mutations in homotetrameric and homopentameric CC cross-links are sufficient to tune the relaxation time of star-PEG hydrogels over 5 orders of magnitude [122].

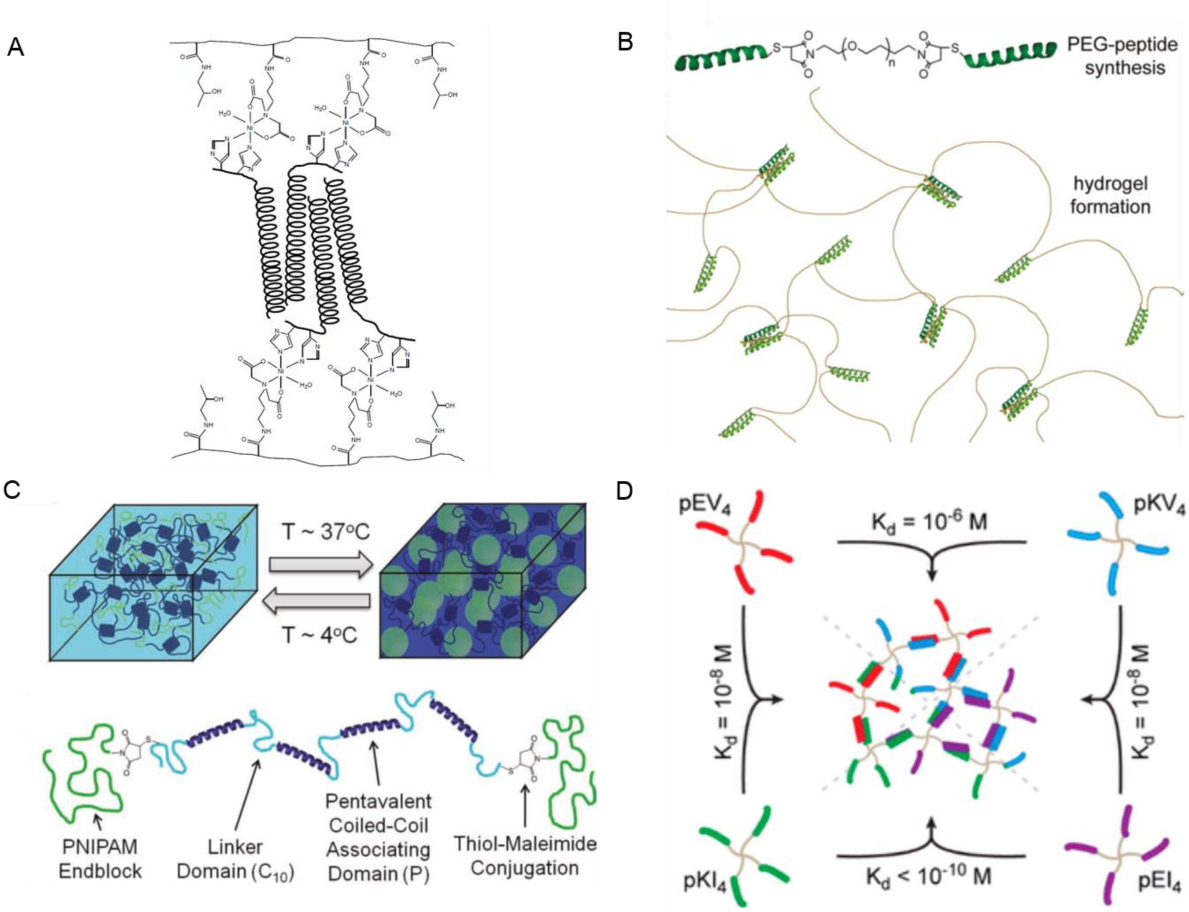

Figure 10: Coiled coil (CC) cross-linked hybrid hydrogels. A) Tetrameric stalk region of kinesin as cross-link for PHPMA and poly(*N',N'*-dicarboxymethylaminopropyl)methacrylamide. Reprinted with permission from Springer Nature: Nature, Hybrid hydrogels assembled from synthetic polymers and coiled-coil protein domains, C. Wang, R.J. Stewart, J. Kopeček, Copyright © (1999). B) Fibrin-peptide fragment, forming dimers and tetramers, used as a cross-link for linear PEG. Reprinted with permission from [118], Copyright © 2008 American Chemical Society. C) Thermo-responsive hydrogel with a pentameric CC and PNIPAM end groups. Reprinted with permission from [120]: M.J. Glassman, J. Chan, B.D. Olsen, Reinforcement of Shear Thinning Protein Hydrogels by Responsive Block Copolymer Self-Assembly, Advanced Functional Materials, Copyright © 2013 WILEY-VCH Verlag GmbH & Co. KGaA, Weinheim). D) Self-sorting heterodimeric CC system as cross-links for star-PEG. Reprinted with permission from [121], Copyright © 2016, American Chemical Society.

In combination, this shows that the viscoelastic properties of these hydrogels directly depend on the molecular properties of the CC sequence used. Moreover, the relaxation time of a polymer network is also affected by its topology. Grad et al. [123] showed that the relaxation time of the model CC A_4B_4 is two orders of magnitude lower when used as a cross-link in fiber-like poly(isocyanopeptide) (PIC) hydrogels when compared to star-PEG hydrogels. This reveals that relaxation of hydrogel networks depends not only on the molecular properties of the cross-link, but also on the hierarchical organization of the polymer backbone.

1.5 Metal-coordination cross-linked hydrogels

Inspired by mussel byssal threads and other metal coordinating materials, hybrid hydrogels with metal coordination cross-links emerged [124]. As coordinating amino acid ligands, not only His, but also Cys, DOPA, Tyrosine or Phenylalanine can be used, yielding redox-active, stimuli-responsive and self-healing hydrogels [125,126].

pH-responsive Fe^{3+}-coordinating star-PEG-DOPA hydrogels have first been reported by Holten-Andersen et al. [127]. The catechol moieties of the DOPA residues were able to form stable Fe^{3+} complexes at basic pH and had self-healing properties. The mechanical properties were further tuned when changing the dynamics of the catechol cross-links via pH or oxidation. Li et al. [128] showed that the relaxation time of star-PEG-DOPA gels is tunable over orders of magnitude when using multivalent DOPA-Fe^{3+}-nanoparticle coordination compared to single DOPA-Fe^{3+} cross-links (**Figure 11A**). Star-PEG with terminal His residues was reported to form hydrogels in the presence of Ni^{2+}, Cu^{2+}, Co^{2+} or Zn^{2+} (**Figure 11B**). The relaxation time of the hydrogels was found to be correlated with the dissociation rate constants of the metal ion used [129]. It was demonstrated by Grindy et al. [130] that the viscoelastic properties of star-PEG-His hydrogels were tunable when using mixtures of different metal ions. Using the redox-active Co^{2+}/Co^{3+} system, the properties of the star-PEG-His hydrogels switched from viscoelastic liquid-like with Co^{2+} to elastic-solid like after conversion to Co^{3+} (**Figure 11C**) [131,132].

His-metal-coordination cross-links were also implemented in protein-based hydrogels. An elastin-like polypeptide was equipped with His-metal coordination sites and formed tough stretchable hydrogels in the presence of Zn^{2+} [133]. Kong et al. [134] tuned the stability of the protein system GL5HH-I27, which displays mutually exclusive folding, through insertion of two His residues in the β–sheet domain of GL5HH. GL5HH was folded in the presence of Ni^{2+}, while I27 was folded in the absence of Ni^{2+}. Integrated into a resilin network, the Young's modulus, resilience and swelling of the resulting hydrogel was controllable through Ni^{2+} in a continuous and reversible fashion.

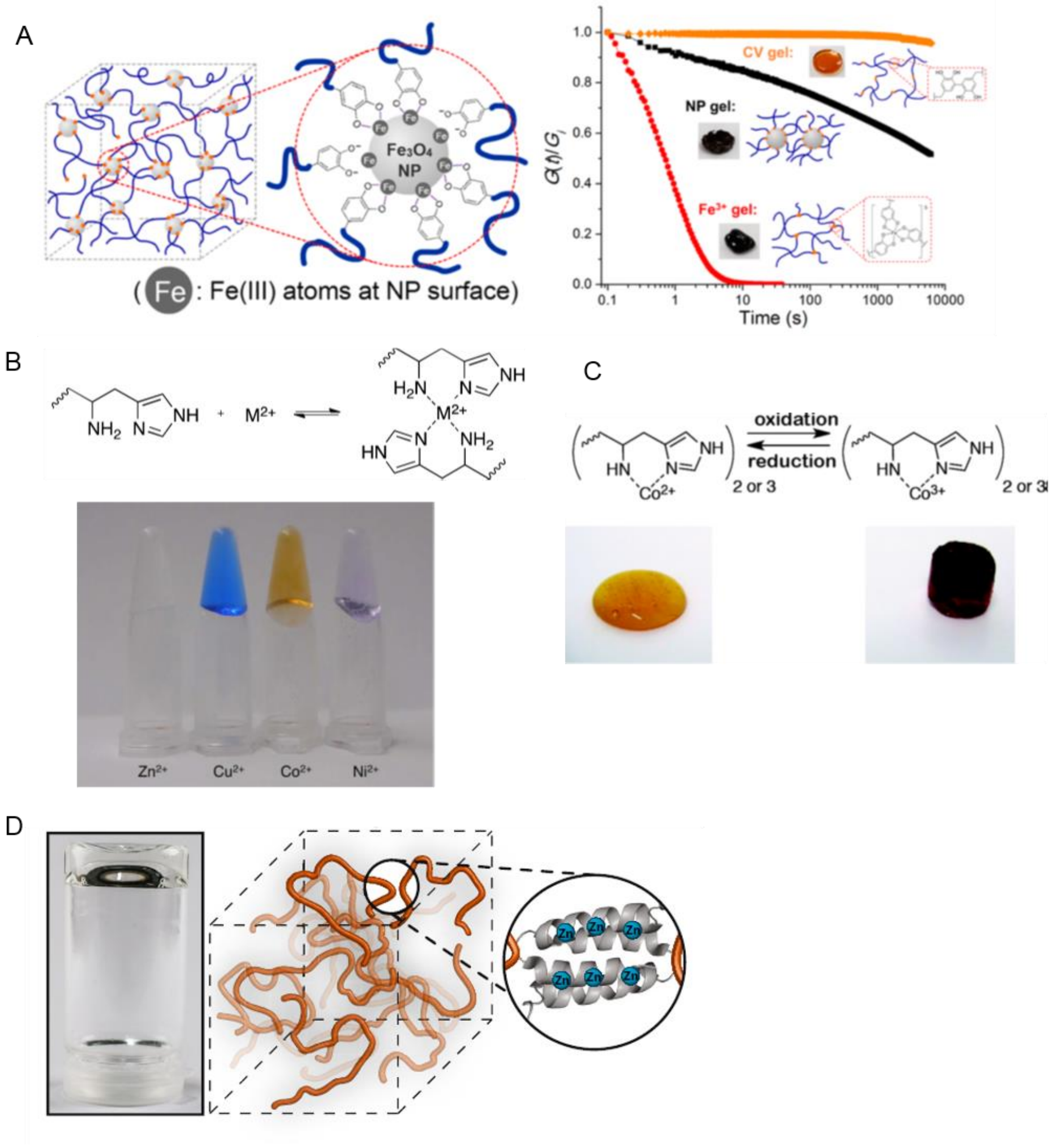

Figure 11: Hydrogels cross-linked *via* metal coordination. A) Scheme of a PEG hydrogel cross-linked with DOPA-iron nanoparticles (left) and the stress relaxation of the PEG-DOPA hydrogel in different cross-linking modes. Reprinted with permission from [128], Copyright © 2016 American Chemical Society. B) Star-PEG-histidine (His) cross-links with different metal ions. Reprinted with permission from [129], Copyright © 2013 American Chemical Society. C) Star-PEG-His hydrogel properties change drastically when using Co^{3+} instead of Co^{2+}. Reprinted with permission from [131], Copyright © 2016 American Chemical Society. D) Hyaluronic acid hydrogel cross-linked with a Glu-rich helix-loop-helix motif that only forms in the presence of Zn^{2+}. Reprinted from [135], Copyright © 2017 Springer Nature.

A soft hydrogel with a Zn^{2+}-coordinating α-helical helix-loop-helix motif (**Figure 11D**) was developed in the group of Aili [135]. Cross-linked to hyaluronic acid, the building block formed Zn^{2+}-responsive hydrogels, which disassemble rapidly in the presence of chelators, such as ethylenediaminetetraacetate (EDTA). To the best of my knowledge, this is the only report of a metal coordinating CC used as a hydrogel cross-link.

1.6 Self-reporting cross-links for studying network structure and material failure

When hydrogels are stretched, compressed or otherwise deformed they undergo changes at the molecular level ultimately leading to bulk material failure. In order to study material failure mechanisms in real-time and detect damage before catastrophic failure, self-reporting molecular force sensors, with an optical readout (mechanophores) have been developed [136]. The optical readout can be based on luminescence, fluorescence or Förster resonance energy transfer (FRET). One of the first mechanofluorescent material building block reported is spiropyrane, which undergoes a force-induced reaction to merocyanine (**Figure 12A**) [137]. Also other organic fluorophores, such as rhodamine have been implemented in polymeric materials to monitor material failure [138-141]. Mechanoluminescence imaging of covalently cross-linked materials damaged by osmotic stress was reported by Clough et al. [142]. Here, the covalent non-fluorescent cross-link bis(adamantly)-1,2-dioxetane transformed to a lumninescent species when ruptured.

Many mechanophores are small, hydrophobic molecules that cannot self-heal and only report mechanical damage once. Therefore, the number of reversible and self-reporting fluorescent force sensors currently available for hydrogels is limited. A covalently cross-linked hydrogel with quenched rhodamine embedded in micelles was reported by Wang et al. [143]. When force was applied, water entered the micelles and the fluorescence signal increased. Rapp et al. [144] monitored the chain dynamics of a proteinaceous hydrogels with a linker domain flanked by CC domains that formed a pentamer cross-link. The linker domain was labeled with fluorescein and the chain dynamics in the hydrogel network was monitored using fluorescence recovery after photobleaching. Further, using CC pentamers with different thermodynamic stability, the dynamics of the polymer chains was altered and, as a result, also the viscoelastic properties of the hydrogel. Furthermore, changes in the spatial organization of alginate hydrogels labeled with the FRET pair fluorescein and rhodamine were reported by Kong et al. [145]. They monitored conformational changes in the polymer chains and intermolecular association of the chains using changes in the FRET efficiency. Drawbacks of this study are that no site-specific labeling of the alginate was possible to ensure a regular spacing of the FRET pair. Nevertheless, the results imply that fluorescence reporter systems are a useful means to study the state of hydrogel cross-links under applied force.

Recently, more water-soluble and photostable fluorophores, such as Alexa Fluor®488 and Alexa Fluor®555, have been implemented as FRET pairs into PEG and fibronectin-PNIPAM hydrogels [146,147]. Fluorescent proteins, such as the cyan, green or yellow fluorescent protein were also used to report damage in hydrogels (**Figure 12B**) [148,149]. However, the fluorescent proteins did not act as active cross-links contributing to the network.

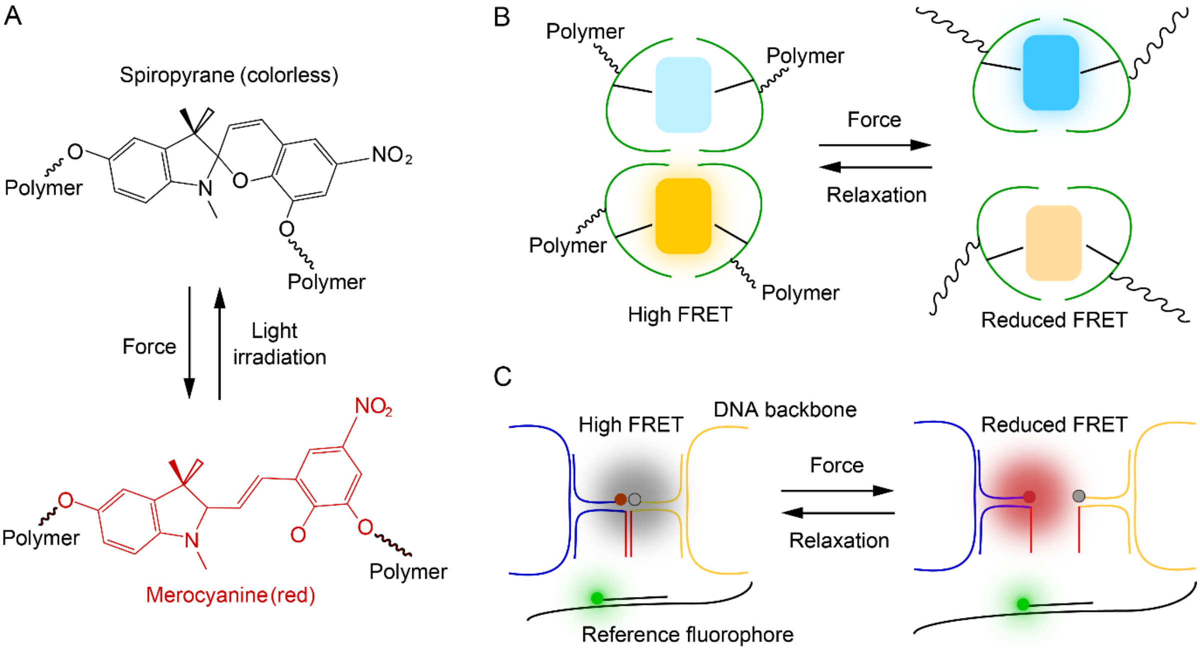

Figure 12: Mechanoresponsive fluorescent reporters to monitor material failure. A) The colorless spriopyrane undergoes a force-induced transition to the red merocyanine [137]. B) Protein cage with the FRET pair cyan fluorescent protein (CFP) and yellow fluorescent protein (YFP) integrated into a covalently cross-linked polymer network [148]. C) DNA hydrogel with a mechanofluorescent fluorophore-quencher pair and a reference fluorophore (green). When the hydrogel is stretched the DNA cross-link breaks and the red fluorescence increases [150].

A self-healing DNA hydrogel was reported by Merindol et al. [150]. The cross-links in this hydrogel consisted of a short double-stranded stretch of DNA mechanically loaded in unzipping geometry and labeled with a fluorophore-quencher system (**Figure 12C**). Hydrogel failure was studied using tensile testing and showed a drastic increase in the fluorescence when force was applied.

Currently, mechanically calibrated and fluorescently labeled DNA molecules are also used as molecular force sensors to study cell adhesion; however, they are not naturally occurring in the ECM and display a rather small range of rupture forces ranging from 12 to 56 pN [151-154]. Cell-matrix interactions are essential for cell adhesion, migration and differentiation [155]. Cells are constantly probing their extracellular matrix mechanically and integrate the feedback into their signaling cascades, a process called mechanotransduction [156]. Recently, many key players of the molecular machinery involved in this process have been identified [157]. However, up to this point, it is not possible to resolve the forces acting across individual receptor molecules (e.g. integrins). Furthermore, cell-matrix interactions are often studied in 2D. Naturally most cells are located in a 3D environment [155], and the bulk viscoelastic properties of the extracellular environment are crucial for the spreading, proliferation and differentiation of cells [158-160]. Overall, fluorescently labeled CCs are excellent candidates to replace DNA force sensors and serve as tunable self-reporting force sensors for studying hydrogel network structure as well as cell-matrix interactions in 3D at the single molecule level.

2 Scope of this thesis

Coiled coils (CCs) are α-helical protein folding motifs with mechanical function. They occur in proteinaceous acellular materials, such as hagfish slime and are further highly abundant in mammalian tissues, e.g. as part of the proteins myosin and fibrin. Since CCs are native components of the ECM, they have been used as building blocks for biomimetic hydrogels [105]. However, precisely controlling and reversibly tuning the viscoelastic properties of CC cross-linked hydrogels has remained challenging. The goal of this work was to develop reversibly tunable, self-healing and self-reporting CC cross-links and to test their application potential as intelligent material building blocks. Towards this goal, I investigated the following three aspects:

1. **Can individual CC building blocks and the resulting CC cross-linked hydrogels be tuned with bioinspired His-metal coordination bonds?**

   In order to tune the molecular properties of individual CCs, I implemented His-metal coordination sites into solvent-exposed residues of a synthetic heterodimeric CC ($A_{4H||}B_{4H||}$). Specifically, I investigated whether the reversible nature of His-metal coordination can be utilized for tuning the stability of the CC and, as a result, the viscoelastic properties of CC cross-linked hydrogels. It is known that the terminal heptads are more dynamic and contribute less to the overall thermodynamic stability of the CC when compared to internal heptads [161]. Molecular dynamics (MD) simulations further predict that the dominant pathway of force-induced chain separation is unfolding-assisted dissociation in the range of loading rates applied in AFM-SMFS. Importantly, unfolding appears to start from the termini where the force is applied [56]. In a first series of experiments (**Chapter 4.2)**, I thus implemented His-metal coordination sites in the terminal heptads of the same helix (intra-CC) in order to stabilize the respective heptads against unfolding. This strategy is expected to experimentally verify the proposed mechanism of force-induced dissociation, while at the same time providing a reversibly tunable material building block. The structure and ability of the CC to bind metal ions was assessed using Raman spectroscopy (**Chapter 4.2.1**). The effect of His-metal coordination on the thermodynamic stability and the underlying energy landscape parameters k_{off} and Δx of the CC were studied using circular dichroism (CD) spectroscopy and AFM-SMFS in the absence and presence of Ni^{2+} (**Chapter 4.2.1** and **4.2.2**).

Using this molecularly characterized CC, I further investigated if the expected stabilization is transferable from the single molecule to the bulk hydrogel level. In order to answer this question, I used the His-modified CC as a cross-link for star-PEG (**Chapter 4.2.3)**. The viscoelastic properties (i.e. the relaxation time) of the CC-star-PEG hybrid hydrogel were studied using shear rheology in the presence and absence of Ni^{2+}. Further, the reversibility of the His-metal stabilization effect was investigated using metal chelators, such as EDTA. The coordination of transition metal ions is strongly dependent on the conformation of the His residues in the protein backbone and the preferred coordination geometries of the metal ions used [89,99,162]. It was thus anticipated that different metal ions lead to different degrees of CC stabilization and, therefore, also affect the hydrogel viscoelastic properties. To prove this hypothesis, I studied the ability of additional ions (Cu^{2+}, Co^{2+} and Zn^{2+}) to coordinate His in the CC as well as their effect on the properties of the resulting hydrogels (**Chapter 4.2.4**).

2. What is the effect of His-metal coordination induced higher-order CC assembly on the viscoelastic properties of the hydrogel?

The implementation of hydrophobic amino acids in the solvent-exposed positions of CCs has been shown to induce aggregation and fiber formation [108,163]. His-metal coordination bonds play a crucial role in the higher-order self-assembly and self-healing of mussel byssal threads as well as their mechanical response under load [17,164,165]. In order to introduce and precisely control higher-order self-assembly, I relocated the His residues to favor inter-CC ($A_{4H\perp}B_{4H\perp}$) over intra-CC His-metal coordination (**Chapter 4.3**). Hierarchical assembly of polyisocyanopeptide (PIC) fibers cross-linked with structurally similar CC heterodimers showed a large effect on the viscoelastic properties of the resulting hydrogel [123]. The relaxation time of the PIC hydrogel was shifted to longer time scales when compared to the relaxation time of a star-PEG hydrogel cross-linked with the same CC. In my work, the goal was to cross-link star-PEG hydrogels with a CC that is able to form His-metal bonds between CCs, thus facilitating the higher-order assembly of CC cross-links within the hydrogel network. The formation and effect of such higher-order cross-links was studied using Zn^{2+}, since it is the most prominent metal ion in the core of byssal threads.

In addition to tuning the viscoelastic properties of CC cross-linked hydrogels with His-metal coordination, another key goal of this work was the development of self-reporting CC building blocks to monitor the state of CC cross-links (associated vs. dissociated) in the hydrogel network. For dynamically cross-linked hydrogels it is still a significant challenge to determine the number of cross-links initially formed as well as the network structure and the material failure mechanism. Currently available methods for studying network defects and chain dynamics are, for example, multiple quantum-nuclear magnetic resonance spectroscopy and dielectric spectroscopy; however, these methods are only available in highly specialized labs and do not allow for studying the network in the presence of mechanical deformation [166,167].

3. Is it possible to monitor CC cross-link failure in the hydrogel using an optical readout?

Mechanoresponsive fluorescence reporters are a promising avenue for understanding hydrogel network mechanics at the molecular level. The goal of this work was to set up a fluorescent reporter system that ultimately allows for determining how the rupture of CC cross-links relates to bulk material failure. To obtain a proof-of-principle, I have equipped a CC heterodimer with a fluorescence reporter system that provides information about the CC state. Specifically, a carboxyfluorescein (CF)–tetramethylrhodamine (TR) FRET pair was used to distinguish the associated (active) and dissociated (inactive) state of each CC cross-link in the hydrogel network. The CC $A4_{CF}B4_{TR}$ was characterized using CD and fluorescence spectroscopy and, subsequently, used as a dynamic cross-link in an otherwise covalently cross-linked star-PEG hydrogel. The failure of the hydrogel was assessed following changes in FRET efficiency under compression force. For this purpose, a rheometer coupled with a fluorescence microscope was used.

Overall, I envision that this work will yield a versatile material platform, consisting of a molecular toolkit of reversibly tunable, self-healing and self-reporting CCs. These will not only serve as intelligent material cross-links but also as molecular force sensors with high application potential in materials research and cell biology.

3 Materials and methods

This section describes the chemicals and buffers used. It further gives a brief theoretical background for each method as well as a detailed description of the experimental procedure.

3.1 Chemicals and buffers

All chemicals used had per analysis quality. The buffer solutions (**Table 1**) were prepared with ultrapure water (Ultra clear^{TM} Intregra UV UF, Siemens) and sterile filtered (0.2 µm pore size). The non-coordinating buffer piperazine-1,4-bis(propanesulfoinc acid) (PIPPS) was used for all measurements performed with the His-metal coordinating CCs. The measurement buffer used for studying the fluorescently labeled CCs was phosphate buffered saline (PBS) since it is a physiological standard buffer. Sodium borate buffer and coupling buffer were used to prepare the surfaces and cantilevers for AFM-SMFS.

Table 1: Composition of the buffers used. The buffer components had per analysis grade. Buffers were prepared with ultrapure water and the pH was adjusted with NaOH, if necessary. The buffers where sterile filtered.

Name	Composition		pH	Experiment
PIPPS	10 mM 137 mM 2.7 mM	PIPPS NaCl KCl	8.1	AFM-SMFS, rheology, CD spectroscopy
PBS	10 mM 2 mM 137 mM 2.7 mM	Na_2HPO_4 KH_2PO_4 NaCl KCl	7.4	measurements with the fluorescently labeled CC
Sodium borate buffer	50 mM	$H_3BO_3/Na_2B_4O_7$	8.5	AFM-SMFS
Coupling buffer	50 mM 50 mM 10 mM	Na_2HPO_4 NaCl EDTA	7.2	AFM-SMFS

3.2 Peptides

The peptides A_4, $A_{4H\parallel}$, B_4 and $B_{4H\parallel}$ were purchased from a commercial supplier (Centic Biotech) with >95 % purity. The peptides $A_{4H\perp}$ and $B_{4H\perp}$ were prepared in house with solid phase peptide synthesis (SPPS). The fluorescently labeled peptides A_{4CF} and B_{4TR} were purchased from a commercial supplier (Proteogenix) with >95 % purity.

3.2.1 Solid phase peptide synthesis and purification of peptides

Proteins and peptides are naturally synthesized in the ribosomes of cells. However, many bioengineered peptides are not obtained via expression of recombinant genes in host organisms, e.g. *Escherichia coli*, but with a chemical synthesis protocol on a solid support.

Theoretical background

The concept of SPPS was first published by Bruce Merrifield in 1963 [168]. While Merrifield used tert-butoxycarbonyl (Boc)/benzyl chemistry for the protection of reactive sites, today fluorenylmethoxycarbonyl (Fmoc)/t-butyl SPPS is a standard method for the synthesis of peptides [169]. Fmoc-based SPPS can be automatized and was quickly adapted by non-chemists, since it does not require highly toxic hydrogen fluoride as the original protocol [170]. The general steps in Fmoc-based SPPS are described in the following paragraph.

In SPPS, peptides are generally synthesized on a solid support from the C-terminus to the N-terminus. To increase the biological stability of synthetic peptides against proteases and to obtain uncharged termini, the C-terminus is often amidated and the N-terminus is acetylated [171]. The amino acids used carry an Fmoc-protecting group at the α-amino group ($N\alpha$) and an orthogonal protecting group, such as t-butyl or triphenylmethyl, at the side chain residue, if necessary. As a solid support, polystyrene, polyamide or PEG-polystyrene resins are commercially available with different linkers, such as H-rink amide, Pal or Sieber, which all allow for the amidation of the C-terminus [172]. The resin is first swollen in N,N-dimethylformamide (DMF) and then the first Fmoc-protected amino acid is coupled to the linker (**Figure 13**). In general, all amino acids are coupled with a 2-10 times excess to the amount of linker on the resin to ensure the effective completion of the reaction [172]. For the activation of the coupling reaction, 2-(6-chlor-1*H*-benzotriazol-1-yl)-1,1,3,3-tetramethylaminium-hexafluorphosphate (HCTU) or (7-Azabenzotriazol-1-yloxy)trispyrrolidinophosphonium hexafluorophosphate (PyAOP) are commonly used in the presence of N,N-diisopropylethylamine (DIPEA) as an organic base.

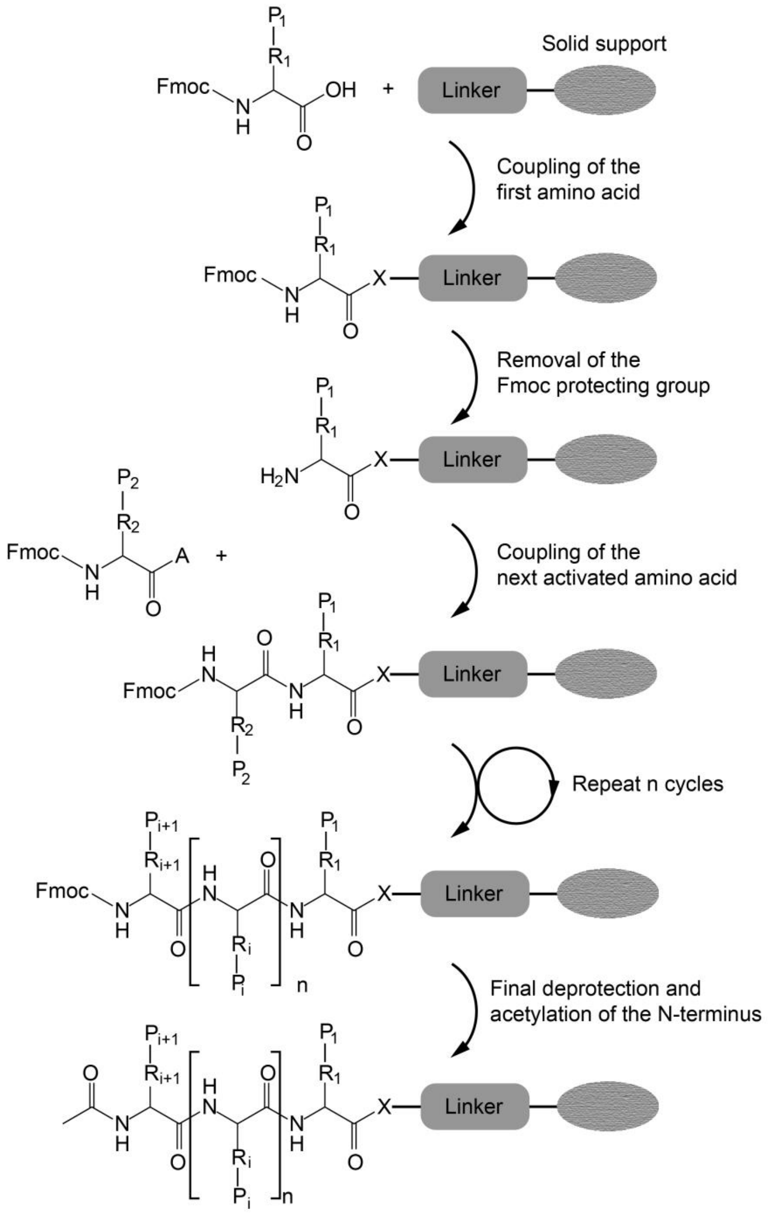

Figure 13: Scheme of standard Fmoc-based solid phase peptide synthesis after Amblard et al. [172]. The first amino acid is coupled to the linker on the solid support (resin) via its free C-terminus. The Fmoc protecting group is removed with 20% piperidine in DMF. Then the second activated amino acid is coupled to the free N-terminus of the growing peptide chain. These two steps are repeated n cycles until the final deprotection and acetylation of the N-terminus. A = activator group, P = protecting group, R = side chain residue.

After each coupling cycle, the Nα-atom of the amino acid is deprotected using 20:80 % (v/v) piperidine:DMF. The successful removal of the Fmoc-group can be monitored with UV spectroscopy, since the resulting dibenzo-fulvene-piperidine adduct absorbs UV light (302 nm) [173]. After deprotection, the next amino acid is added to the resin together with the activator and base. This cycle is repeated until the N-terminal amino acid is reached. The N-terminus is acetylated with 1:1:3 acetic anhydride:pyridine:DMF after deprotection of Fmoc. Finally, the resin is washed with DCM and dried under nitrogen flow.

The cleavage of the peptide from the resin and the removal of the side chain protecting groups is performed with a cocktail of 92.5:2.5:2.5:2.5 % trifluoroacetic acid (TFA):triisopropylsilane:ethanedithiol:water. Triisopropylsilane, ethanedithiol and water act as scavengers to prevent reaction of emerging carbocations with electron-rich side chain residues of the peptide, such as cysteine. Precipitation of the crude peptide is performed with ice cold diethyl ether, followed by drying and dissolving in 20 % acetonitrile (ACN):water with 0.1 % TFA. For purification, the crude peptide is separated with reversed phase high-performance liquid chromatography (HPLC) using a hydrophobic C_{18}-column. The elution is performed with an increasing gradient of ACN. After lyophilization, the mass identity of the purified peptide fractions is determined with mass spectrometry using matrix-assisted laser desorption/ionization (MALDI), combined with a time-of-flight (TOF) detector. First, the peptide is mixed with the a large excess of laser-sensitive matrix and allowed to dry on a target plate [174]. The MALDI-TOF spectrometer operates under vacuum and is equipped with a laser for ionization. During ionization, the matrix molecules decompose and the peptides are released into the gas phase as charged ions [175]. The ions are subsequently accelerated using an electric field. The velocity of the ions is proportional to their mass to charge ratio (m/z). Then the ions travel a region without an electric field, where they separate according to their mass. Finally the ions hit the detector as a function of time, yielding a TOF mass spectrum [175].

Experimental procedure

Peptide synthesis was performed using a Tribute peptide synthesizer (Gyros Protein Technologies, Inc.). The synthesis was performed at room temperature (RT) at a 100 µmol scale using standard Fmoc-based SPPS with a 5x excess of amino acids and HCTU as coupling agent (Merck) as well as a 2.5x excess of DIPEA. H-rink amide ChemMatrix® was used as a resin (Sigma Aldrich) to obtain an amidated C-terminus. The N-terminus of the peptide was acetylated with 1:1:3 acetic anhydride:pyridine:DMF. The peptides were cleaved from the resin using a cleavage cocktail for 2 h at RT. The composition of the cleavage cocktail was 92.5:2.5:2.5:2.5 % TFA:triisopropylsilane:ethandithiol:water. Ice-cold diethyl ether was used to precipitate the crude peptides. The precipitate was centrifuged at 4,700 g for 15 min at 4 °C and washed three times with cold diethyl ether. The precipitate was dried under nitrogen flow and dissolved in 10 % ($B_{4H\perp}$) and 20 % ($A_{4H\perp}$) acetonitrile in ultrapure water, respectively.

3.2.2 High-performance liquid chromatography

Experimental procedure

The peptides were purified with reversed phase HPLC (LC-20A Prominence, Shimadzu Corporation). A preparative C_{18}-column (Macherery Nagel) was used for purification with a linear gradient of water (solution A: water with 0.1 % TFA) and acetonitrile (solution B: ACN with 0.1 % TFA). The gradient was applied from 10 % (respectively 20 %) solution A to 80 % (respectively 100 %) solution B in 30 min at a constant flow rate of 25 ml min^{-1}. The eluted peptide fractions were collected based on the UV absorbance at 220 nm and lyophilized. The chromatograms for all peptides can be found in the appendix (**Figure S1, Figure S2**). MALDI-TOF mass spectrometry (Autoflex Speed, Bruker) was used to confirm the mass identity and purity of the peptides. As a matrix 2,5-dihydrobenzoic acid (DHB) was used. The mass spectra of the peptides can be found in the appendix (**Figure S3, Figure S4**).

3.3 Peptide characterization

The structure of proteins and peptides is frequently investigated with a range of different optical spectroscopy techniques. In this work, CD spectroscopy, Raman spectroscopy and fluorescence spectroscopy were used to characterize the CCs.

3.3.1 Circular dichroism spectroscopy

CD spectroscopy is frequently used to study the secondary structure and thermal stability of proteins and peptides. Here, the α-helical structure and thermal unfolding of the CC peptides were studied in the absence and presence of metal ions.

Theoretical background

The principle of CD spectroscopy is based on the phenomenon that chiral molecules absorb left-handed and right-handed circularly polarized light differently [176]. Circular polarized light is obtained from monochromatic light using a modulator, which shifts the linear component of the light one half relative to its orthogonal linear component. The oscillation of the electric field component of the circular polarized light is described by two vectors either rotating clockwise (E_R) or counterclockwise (E_L) (**Figure 14A**). Proteins and peptides, which contain chiral amide bonds, absorb E_L and E_R to different extents, resulting in an elliptic polarization of the light [177]. This ellipticity θ_{obs} is measured with a photomultiplier detector and is usually given in millidegrees (mdeg). From θ_{obs}, the molar ellipticity θ [deg cm^2 dmol^{-1}] is calculated with the path length d [cm] and the molar concentration of the sample c [dmol l^{-1}] using the following equation

$$\theta = \frac{\theta_{obs}}{d \cdot c} \qquad (1)$$

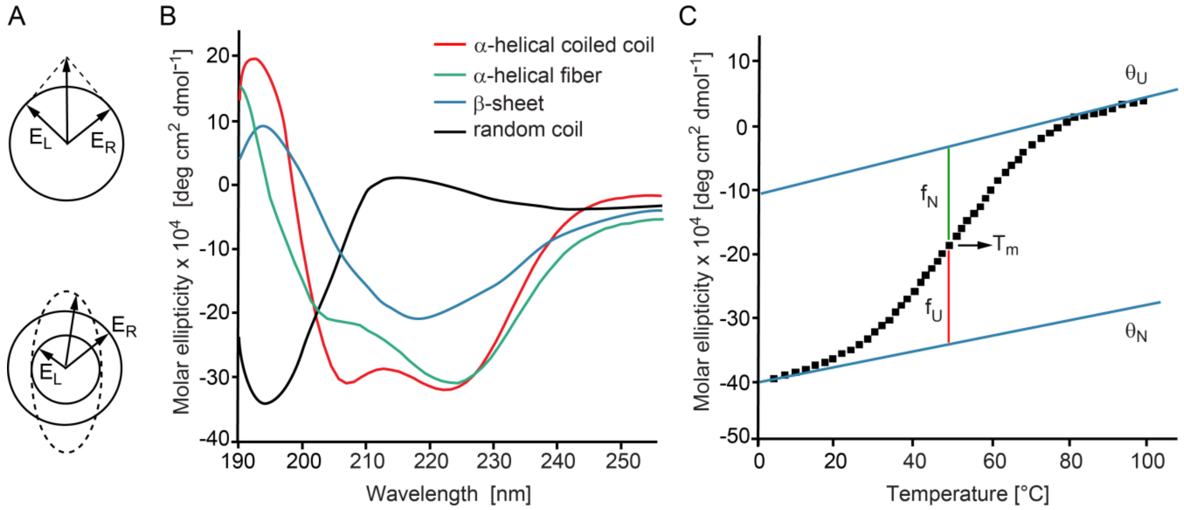

Figure 14: Circular dichroism spectroscopy of proteins and peptides. A) Scheme of the E-vector of plane polarized light, which can be split into a left-handed (E_L) and right-handed (E_R) component with the same phase and amplitude. A CD-active sample absorbs one type of circularly polarized light stronger than the other. The resulting vector describes an ellipse. B) CD-signal of protein secondary structures. C) Thermal denaturation curve of a protein or peptide. The pre- and post-transition baselines of θ_N and θ_U are marked in blue. The melting temperature T_m is the mid-point of the transition where $f_N = f_U = 0.5$.

The secondary structures of proteins and peptides yield distinct signatures in CD spectroscopy (**Figure 14B**). For β-sheet conformations, a maximum at 195 nm and a minimum at 218 nm are observed. Random coils show a minimum at 195 nm and a low intensity maximum at 210 nm. The α-helical conformation results in a maximum at 193 nm and two minima at 208 and 222 nm [178]. The ratio between the minima ($r_{222/208}$) is used to estimate CC formation [179,180]. A $r_{222/208}$ ratio close to 1 or higher indicates a well-defined CC. Formation of CC-fibers or aggregates results in a decrease of the minimum at 208 nm while the second minimum is shifted to 225 nm [163,181,182].

Coupled to a heating element, CD spectroscopy is also used to determine the thermal stability of peptides and proteins [178]. Formation of single α-helices and dimerization was found to be a cooperative two-state process for most dimeric CCs. When a native CC (N_2) is heated in a suitable temperature range, the loss of the α-helical secondary structure and the concomitant increase of unfolded random coil peptides (2U) can be monitored.

$$N_2 \overset{\Delta T}{\rightleftharpoons} 2U$$

The melting temperature (T_m) is obtained from the resulting sigmoidal unfolding curve and is defined as the temperature where half of the CC is folded and half is unfolded (**Figure 14C**). The CD spectrometer used in this thesis is equipped with an analysis program (Global3) that yields T_m based on a global fit to a series of spectra measured at different temperatures. It is based on equilibrium thermodynamics and assumes a two-state model for each transition as described by Greenfield [178]. The free energy (*ΔG*) of the transition is given as

$$\Delta G = -RT \ln K \qquad (2)$$

where R is the gas constant, T is the temperature in Kelvin and K is the equilibrium constant. It can also be defined as

$$K = \frac{[N_2]}{2[U]} \qquad (3).$$

The fraction of folded CC *f* at a given temperature is

$$f = \frac{[N_2]}{[N_2] + 2[U]} = \frac{(\theta_t - \theta_U)}{(\theta_N - \theta_U)} \qquad (4)$$

where θ_t is the CD signal of the sample at a given temperature, θ_N is the CD signal of the completely folded CC and θ_U is the CD signal of the fully unfolded CC. When *f* equals 0.5, the melting temperature T_m is reached. The **Equations 2, 3** and **4** are combined and rearranged to yield

$$\theta_t = \frac{(\theta_N - \theta_U)}{[1 + e^{(\Delta G/RT)}]} + \theta_U \qquad (5).$$

The free energy can also be calculated with the Gibbs-Helmholtz equation, where ΔC_p is the change in the heat capacity as follows

$$\Delta G = \Delta H\left(1 - \frac{T}{T_m}\right) - \Delta C_p((T_m - T) + T \ln(\frac{T}{T_m})) \qquad (6).$$

Since for most proteins and peptides ΔC_p is much lower than ΔH, ΔC_p is assumed to be zero [183]. Considering this, inserting **Equation 6** into **Equation 5** gives

$$\theta_t = \frac{(\theta_N - \theta_U)}{\left[1 + e^{\left((\Delta H/R)(\frac{1}{T} - \frac{1}{T_m})\right)}\right]} + \theta_U \qquad (7).$$

Equation 7 yields a 4-paramter model (ΔH, T_m, θ_N, θ_U) for fitting θ_t at each wavelength measured. Global3 allows for baseline correction of the pre- and post-transition baselines of unfolding. The fitting algorithm uses the first derivative of the sigmoidal melting curves to obtain initial parameters for T_m and ΔH. The derivative is a normal distribution where the maximum equals T_m and the width determines ΔH. The parameters are then optimized until the fit converges with the data [183].

Experimental procedure

Peptide stock solutions (5 mg ml^{-1}) were mixed in a 1:1 molar ratio and diluted with PIPPS to a final CC concentration of 25 µM for $A_{4H\parallel}B_{4H\parallel}$ and 30 µM for $A_{4H\perp}B_{4H\perp}$. For measurements in the presence of metal ions, 100 mM $NiCl_2$, $CuCl_2$, $CoCl_2$, $ZnCl_2$ or $CaCl_2$ stock solutions were added to the peptide solution to yield the desired ratio of M^{2+}:His prior to dilution with PIPPS. For $A_{4H\parallel}B_{4H\parallel}$, peptides without the terminal Cys were used for CD spectroscopy. For $A_{4H\perp}B_{4H\perp}$, Cys disulfide bridges were kept in the reduced state by adding 50 mM tris(2-carboxyethyl)phospine (TCEP) to a final concentration of 300 µM. A Chirascan qCD spectrometer (Applied Photophysics) was used to acquire the CD spectra of the peptides using a quartz cuvette (Hellma Analytics) with a path length of 1 mm. The spectra were recorded in the wavelength range from 200-250 nm with a bandwidth of 1 nm, a step resolution of 1 nm and an integration time of 1 s. A buffer spectrum, recorded with the same settings, was subtracted from the peptide and CC spectra for baseline correction. All single spectra were recorded at 20 °C with three accumulations and averaged. The molar ellipticity θ [deg cm^2 dmol^{-1}] was calculated from the ellipticity according to **Equation 1**.

The thermal unfolding experiments were performed from 4-90 °C with a heating rate of 1 °C min^{-1}, in 1 °C steps with an integration time of 0.7 s. All thermal unfolding measurements were performed in triplicate unless stated otherwise. To determine the melting temperature, a global fit of the spectra (range from 205-250 nm) was performed using Global3 (Applied Photophysics). A single transition was assumed and the pre- and post-baseline correction was applied. The mean ($\bar{x}$) melting temperature was obtained from three independent measurements and the standard error of the mean (SEM) (**Equation 8**) was calculated

$$SEM = \frac{\sqrt{\frac{\sum_{i=1}^{n}(\bar{x} - x_i)^2}{n-1}}}{\sqrt{n}} \qquad (8)$$

with the number of measurements n = 3 [184].

3.3.2 Raman spectroscopy

Raman spectroscopy is a vibrational spectroscopy technique. It is based on the interaction of light with matter. It was discovered by Raman and Krishnan in 1928 [185]. Since Raman spectroscopy has a high reproducibility, is non-destructive and requires small amounts of sample, it is often used to characterize the structure and conformation of biological materials [186].

Theoretical Background

In contrast to infrared spectroscopy, where infrared radiation is absorbed by the molecule, Raman spectroscopy is based on inelastic scattering of monochromatic light [187]. The energy of the incident photons is higher than the distinct vibrational energy state of the molecule or molecular groups, resulting in the polarization/distortion of the electron clouds. This elevates the molecule into a virtual energy state (**Figure 15**). The molecule returns to the ground state through one of three different scattering mechanisms: The most probable type is elastic or Rayleigh scattering with the energy of the incident light equal to the energy of the scattered light. Stokes and anti-Stokes Raman scattering are inelastic and less probable [187]. Stokes scattering occurs when a molecule is excited from a ground vibrational state to a virtual state, returning to the first exited vibrational ground state. This results in a red-shift of the scattered photon. In anti-Stokes Raman scattering, the molecule is elevated from the first excited ground state to a virtual energy state and goes back to the lowest vibrational ground state. Therefore, the energy of the scattered light is higher than the energy of the incident light (i.e. the photon is blue-shifted). In a typical Raman spectroscopy experiment, the energy shift of Stokes Raman scattered photons (Raman shift) is used to obtain information about distinct vibrational modes of molecular groups. Anti-Stokes Raman spectroscopy is also possible; however, as the majority of molecules under ambient condition are in the ground state, the effect is much weaker than Stokes scattering. The Raman shift is displayed in wavenumbers [cm^{-1}].

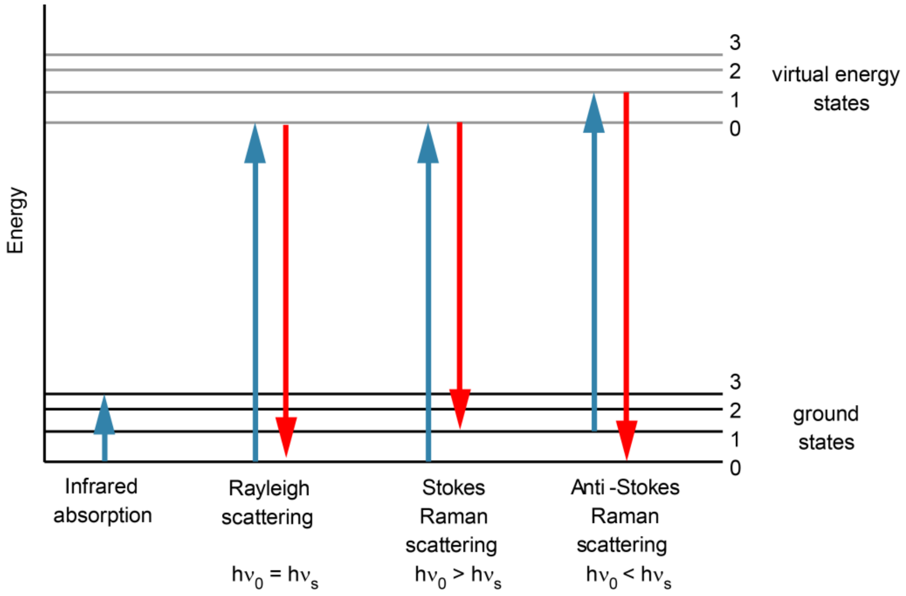

Figure 15: Schematic representation of vibrational energy states in infrared absorption and Raman scattering. Absorbance of infrared light brings the molecule to a higher vibrational energy state. In elastic Rayleigh scattering, the energy elevating the molecule to a higher virtual energy state equals the scattered energy ($h\nu_0 = h\nu_s$). Here, h is the Planck's constant and ν is the frequency. Stokes and anti-Stokes Raman scattering are inelastic. In Stokes Raman scattering, the energy of scattered light is smaller than the energy of the incident light ($h\nu_0 > h\nu_s$). Anti-Stokes Raman is the least probable scattering since the molecule goes from a higher vibrational ground state to a higher virtual energy level and back to the lowest energy ground state ($h\nu_0 < h\nu_s$).

The polypeptide backbone of proteins and many side chain residues are Raman active and display distinct peaks for different secondary structures. The amide I (1634-1676 cm^{-1}) and the amide III (1100-1375 cm^{-1}) bands are the most prominent Raman bands giving information about the secondary structure of peptides and proteins [186]. The amide I band is primarily based on stretching of the C=O in the protein backbone while the amide III band originates from in plane N-H bending in combination with C-N stretching [188]. For α-helical peptides and proteins, the amide I band possesses maxima that are typically located between 1645-1658 cm^{-1} and an amide III band between 1280-1320 cm^{-1} [22,189]. Moreover, many amino acid side chains are Raman active [190]. In the case of His, changes of the protonation and metal coordination state of the five-membered imidazole side chain can be monitored in the region from 1520-1640 cm^{-1} [71]. The bands originate from the stretching vibration of the C_4=C_5 double bond of imidazole and shift to distinct regions if metal ions are bound in a specific configuration (**Figure 16**). In order to study the vibrational modes of His using Raman spectroscopy, it is advantageous if the sample contains low amounts of aromatic amino acids since their peaks partially overlap with His peaks [71].

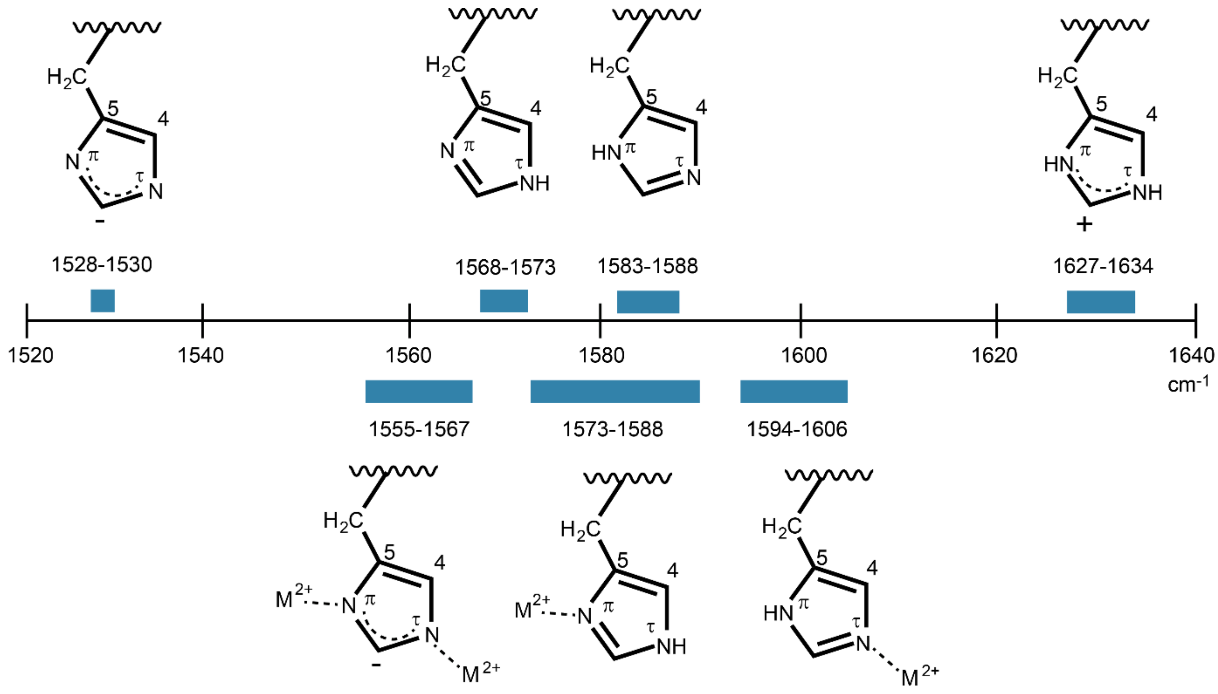

Figure 16: Protonation and coordination bands of His after Takeuchi. [71] For the imidazolate ion, a band at 1528-1530 cm^{-1} is observed. Deprotonated His exists in two tautomers, showing different Raman bands at 1568-1573 cm^{-1} or 1583-1588 cm^{-1}, respectively. Metal coordination bands are observed at 1573-1588 cm^{-1} or 1594-1606 cm^{-1}, depending on which nitrogen-atom coordinates a metal ion. If both nitrogen atoms are deprotonated, two metal ions can be coordinated. This results in a band at 1555-1567 cm^{-1} (bridging mode).

At acidic pH (<6.5), both nitrogen atoms (Nτ and Nπ) of the imidazole ring are protonated (1627-1634 cm^{-1}) (**Figure 16**). Histidine has two pKa values in the basic pH range. The first pK$_a$ of His is around pH 6.5 and can shift slightly depending on the neighboring amino acids [70]. In this case, His can tautomerize with either the hydrogen bound to the Nπ (1583-1588 cm^{-1}) or Nτ-atom (1568-1573 cm^{-1}). The nitrogen atom carrying a free electron pair can form coordination bonds with transition metal ions (see **Chapter 1.3**). Coordination of metal ions to the Nτ-atom leads to a band at 1594-1606 cm^{-1}, while coordination to the Nπ-atom results in a band at 1573-1588 cm^{-1} [191]. The exact position of the peaks also depends on the metal ion coordinated. The second pK$_a$ of His is around pH 14.0 where His forms a imidazolate ion (1528-1530 cm^{-1}) which is able to coordinate two metal ions (bridging) with a band at 1555-1567 cm^{-1} [71]. In this thesis, the coordination of metal ions, such as Ni^{2+}, Cu^{2+}, Co^{2+} and Zn^{2+}, with the His-modified CCs will be studied using the procedure described below.

Experimental procedure

The peptide stock solutions (5 mg ml^{-1}) were mixed in a 1:1 molar ratio. The respective metal ion was added from a stock solution (20 mM) and the sample was diluted to obtain a final concentration of 0.5 mM $A_{4H\parallel}B_{4H\parallel}$ (1:2 M^{2+}:His ratio) or 1 mM $A_{4H\perp}B_{4H\perp}$ (1:1 M^{2+}:His ratio). Then, the pH was raised to ~ 8 using 1 µl 50 mM NaOH. To obtain a pH of ~4, 4 µl 50 mM HCl was added. The sample solution was dried on a quartz glass slide to obtain a peptide film. The measurement was performed using a confocal Raman microscope (alpha 300, WITec). The microscope was equipped with a linearly polarized laser (λ = 532 nm, Oxxius) and a 50x objective (numerical aperture 0.6, Nikon). The samples were measured with 0° polarization and no filter in the light path. A thermoelectrically cooled CCD detector (DU401A-BV, Andor) was used to detect the Raman scattered light with an integration time of 2 s and 30 accumulations for $A_{4H\parallel}B_{4H\parallel}$ or, alternatively, 10 s integration time with 6 accumulations for $A_{4H\perp}B_{4H\perp}$. Spectra from at least 3 different positions of the peptide film were collected and averaged with the measurement software (ScanCtrlSpectroscopyPlus 1.38 WITec) and Project FOUR (4.1, WITec). For further analysis, OPUS 7.0 (Bruker) was used. Specifically, the baseline was corrected (rubberband method, linear, 1 pt), the spectra were smoothed (Savitzky-Golay algorithm, 9 pt) and normalized to the maximum of the amide I peak with OriginPro 2015 (OriginLab Corporation).

3.3.3 Fluorescence spectroscopy

Fluorescence is the emission of a photon from an electronically excited state of a molecule, while the molecule returns to the ground state. The molecule is promoted when absorbing a photon, which is supplied by an external light source. Fluorescence is widely used in research and industry, e.g. in flow cytometry, DNA sequencing [192], microscale thermophoresis [193], biomedical screenings, imaging of biological materials and detection of proteins using fluorescently labeled antibodies or recombinant protein expression with fluorescent fusion proteins [194]. In this thesis, I labeled a heterodimeric CC with a pair of fluorescent dyes (carboxyfluorescein and tetramethylrhodamine) in order to study the state of the CC cross-link in star-PEG hydrogels. Specifically, the state of the CC was monitored using Förster resonance energy transfer (FRET). The following paragraphs will describe fluorescence, FRET and fluorescence spectroscopy in more detail.

Theoretical Background

Fluorescence occurs in aromatic molecules with conjugated electrons systems, e.g. fluorescein or the chromophore in green fluorescent protein (GFP) (**Figure 17**), as well as quantum dots and elements, such as europium [195].

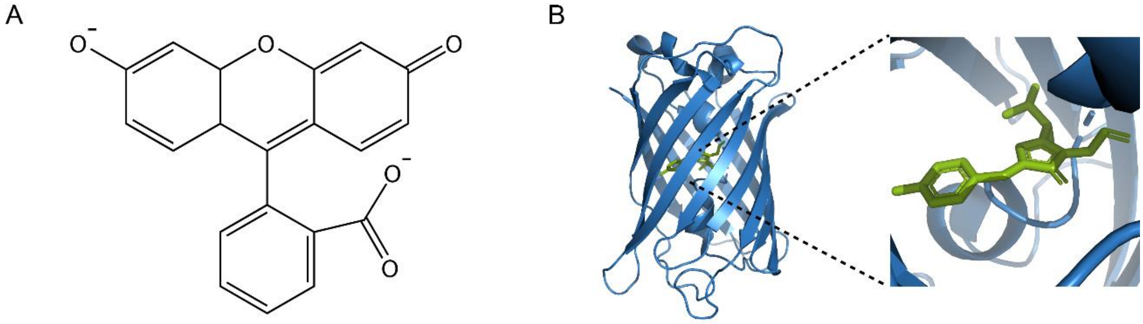

Figure 17: Structure of selected fluorophores. A) Fluorescein. B) Green fluorescent protein (GFP) (PDB-ID: 4KW8). The figure was produced with PyMOL Molecular Graphics System, Version 2.0 Schrödinger, LLC.

The Jablonski diagram describes the processes of photon absorption and emission. Molecules are promoted from the electronic ground state (S_0) to an excited electronic state (S_1, S_2) within 10^{-15} s of absorbing a photon of specific energy (i.e. wavelength) (**Figure 18**) [195]. In the excited state, internal conversion, solvent interactions and FRET can occur. Internal conversion is the relaxation of a molecule in the excited state to the lowest vibrational energy level of S_1. Fluorescence is the emission of a photon when the molecule returns from S_1 to the ground state S_0 after 1-10 ns. The energy of the emitted photon is lower than the energy of the absorbed photon (Stokes shift) due to internal conversion and the fact that many molecules do not return to the lowest vibrational energy level of the ground state. Photon emission competes with intersystem crossing to the triplet state (phosphorescence), non-radiative relaxation modes as well as quenching, which may originate from solvent interactions or FRET. FRET is the non-radiative transfer of energy from a donor (D) to an acceptor (A) molecule and allows the donor to relax to the ground state without emitting a photon. Instead, the acceptor is lifted to an excited state and emits a photon when returning to its ground state.

In order for FRET to occur, the donor and the acceptor molecules (FRET pair) have to be coupled by dipole-dipole interactions and the emission spectrum of the donor has to overlap with the excitation spectrum of the acceptor. The extent of energy transfer is further influenced by the lifetime of the donor and the distance between the donor and the acceptor. The efficiency of the energy transfer (E_{th}) of a FRET pair at a specific distance is defined as

$$E_{FRET} = \frac{R_0^6}{r^6 + R_0^6} \qquad (9)$$

where R_0 is the Förster radius. The Förster radius is the distance between the donor and the acceptor at a FRET efficiency of 50 %.

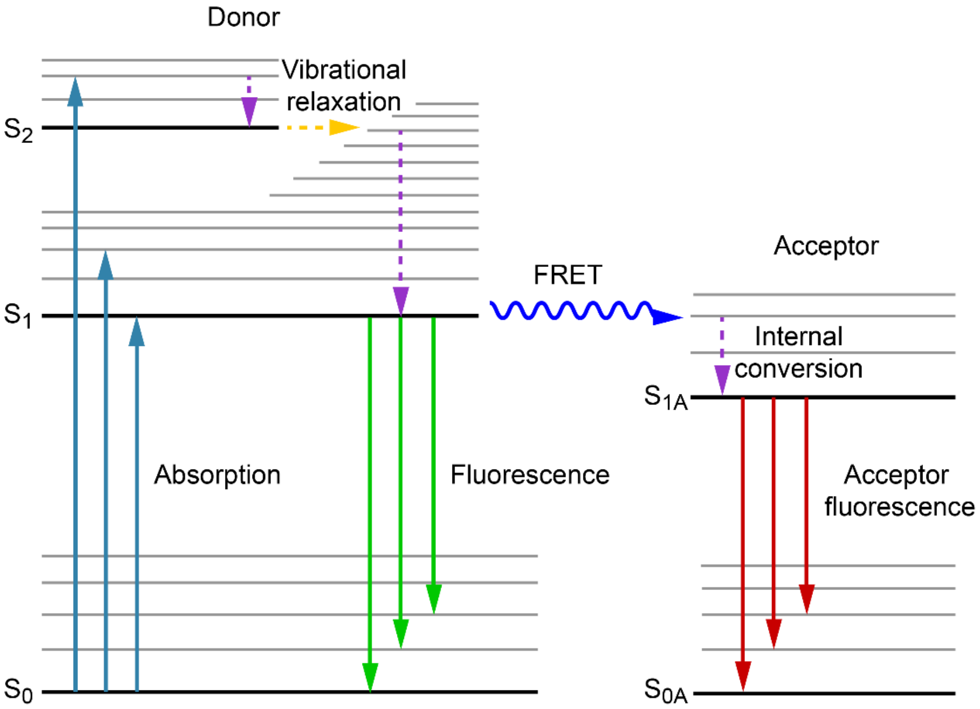

Figure 18: Jablonski-diagram. Shown are the ground state S_0 and electronically excited states S_1 and S_2 with vibrational sublevels. Absorption of a photon promotes the fluorophore to a higher energy state. The fluorophore relaxes to the lowest excited electronic state of S_1 due to vibrational relaxation and internal conversion. The fluorophore emits a photon when returning to any of the vibrational energy levels of the ground state (fluorescence). In the presence of an acceptor fluorophore with an excitation spectrum overlapping with the emission spectrum of the fluorophore (donor), the energy is transferred from the donor to the acceptor without the emission of light (FRET). Instead, the excited acceptor emits a photon to go back to the ground state.

Experimentally, the FRET efficiency is often determined from measuring the emitted fluorescence intensity of the donor in the presence (I_{DA}) and the absence of the acceptor (I_D) using the following equation

$$E = 1 - \frac{I_{DA}}{I_D} \qquad (10)$$

Fluorescence measurements are frequently performed using a fluorescence spectrometer. A simplified setup of a fluorescence spectrometer is shown in **Figure 19**. It is equipped with a light source (e.g. Xenon arc/flash lamp) and motorized excitation and emission monochromators to select and scan the wavelength and allow the acquisition of emission and excitation spectra. The excitation light hits the sample cuvette and is detected in a 90° angle. After passing the emission monochromator, the emitted photons are detected with a photomultiplier tube and the signal is amplified and saved.

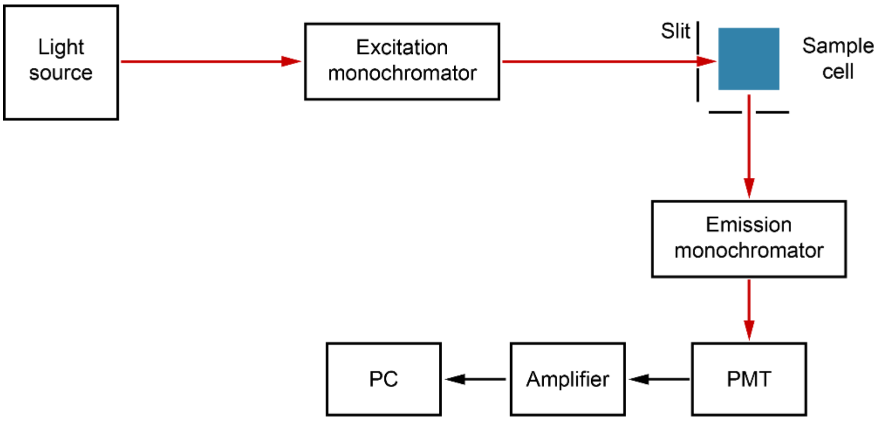

Figure 19: Schematic setup of a fluorescence spectrometer. The excitation light passes the sample cell and is detected in a 90°angle.

Experimental procedure

The fluorescence spectra of the FRET-labeled CC (A_4 with carboxyfluorescein (CF), A_{4CF}, and B_4 with tetramethylrhodamine (TR), B_{4TR}) were obtained using a FluoroMax 4 fluorescence spectrometer (Horiba). Here, the CF donor and the TR acceptor form a FRET pair when the CC is folded. The measurement was performed in a quartz glass cuvette (d = 1 cm, Hellma Analytics) at RT. Before performing the fluorescence measurements, the concentration of the fluorescent CC peptides was determined using absorbance spectroscopy (Lambert-Beer-Law, $\varepsilon_{CF} = 68000\ M^{-1}\ cm^{-1}$ and $\varepsilon_{TR} = 65000\ M^{-1}\ cm^{-1}$). For collecting fluorescence spectra, the CC peptides were mixed in a 1:1 molar ratio to yield 5 µM $A_{4CF}B_{4TR}$ in PBS. TCEP (50 µM) was added to prevent the formation of disulfide bridges. Also, the individual peptides were measured with 50 µM TCEP. Further, a competition assay with a non-labeled CC was performed. Here, a 400x excess of A_4B_4 was added to the $A_{4CF}B_{4TR}$ sample and the decrease of the FRET efficiency was monitored over 3 h.

The samples were excited at 475 nm (CF, donor) with a slit width of 1 nm and the emission spectra were collected from 500-650 nm with a slit width of 1 nm and an integration time of 0.05 s. The obtained spectra were normalized to the emission maximum of CF in the A_{4CF} sample at 523 nm and the FRET efficiency was obtained according to **Equation 10**. The spectra were collected in triplicate to obtain the mean and the SEM. To ensure that all samples contained the same amount of acceptor, the emission spectrum of the acceptor was also collected (excited at 530 nm, slit width: 1 nm) from 560-700 nm (slit width: 1 nm, integration time: 0.05 s).

3.4 Atomic force microscope-based single molecule force spectroscopy

In order to engineer biomimetic hydrogels with precisely tunable viscoelastic properties, knowledge about the unfolding mechanism, thermodynamic stability and energy landscape parameters of its cross-links is crucial. Single molecule force spectroscopy (SMFS) is a powerful method to obtain information about the unfolding rate k_{off} as well as the width of the binding potential Δx. The most common SMFS techniques are magnetic tweezers [196], optical tweezers [197] and the atomic force microscope (AFM) [198]. While magnetic and optical tweezers allow for measuring forces in the range from 10^{-3}-100 pN, AFM spans a force range from 10-10^4 pN [54]. AFM-SMFS is an ideal tool to determine the energy landscape parameters of stable molecular interactions, because of fast sample preparation, adaptable immobilization chemistry and measurements in near-physiological conditions.

Theoretical Background

The AFM was initially invented for imaging surfaces and biological samples with nanometer resolution [55,199]. Since AFM has a force resolution in the pN-range, it is also frequently used as a versatile tool to determine the unfolding mechanisms of single biomolecules and to study the kinetics of bond rupture processes [200]. The basic components of an AFM are a piezo-scanner to ensure the accurate nanometer positioning of the sample and a cantilever with a sharp nanometer sized tip as a flexible force sensor (**Figure 20A**). A laser is focused on the back of the cantilever, which is coated with a reflective layer (e.g. gold). In a typical SMFS measurement, the cantilever moves towards and away from the surface (z-direction). The interaction of the cantilever with a surface (or with molecules immobilized on the surface) causes the cantilever to bend, resulting in a laser deflection signal as a function of the piezo displacement. These raw data then need to be converted into so-called force-extension curves that display the force versus the true tip-sample separation. The laser deflection signal is recorded on a segmented photodiode in the form of a voltage signal. The voltage signal can then be transformed into force (F) [N], using the so-called inverted optical lever sensitivity (invOLS) and the spring constant of the cantilever. The invOLS [nm V^{-1}] is determined from pushing the cantilever onto a hard surface (e.g., glass) at high contact forces. In this setup, the deflection of the cantilever (Δz_c) equals the displacement of the piezo scanner (Δz_p). From the slope of the deflection difference (ΔV) plotted against Δz_p, the invOLS can be obtained. As the cantilever behaves like an elastic spring, the cantilever deflection can subsequently be converted into force using Hookes law:

$$F = -k_s \Delta z_c \qquad (11)$$

with the cantilever spring constant k_s [pN nm^{-1}] and the cantilever deflection [nm V^{-1}] in the z-direction (Δz_c). In this thesis, the spring constant of the cantilever was experimentally determined using the thermal noise method.[201] In the last step, the piezo displacement is converted into the tip-sample separation, subtracting the cantilever deflection from the piezo displacement.

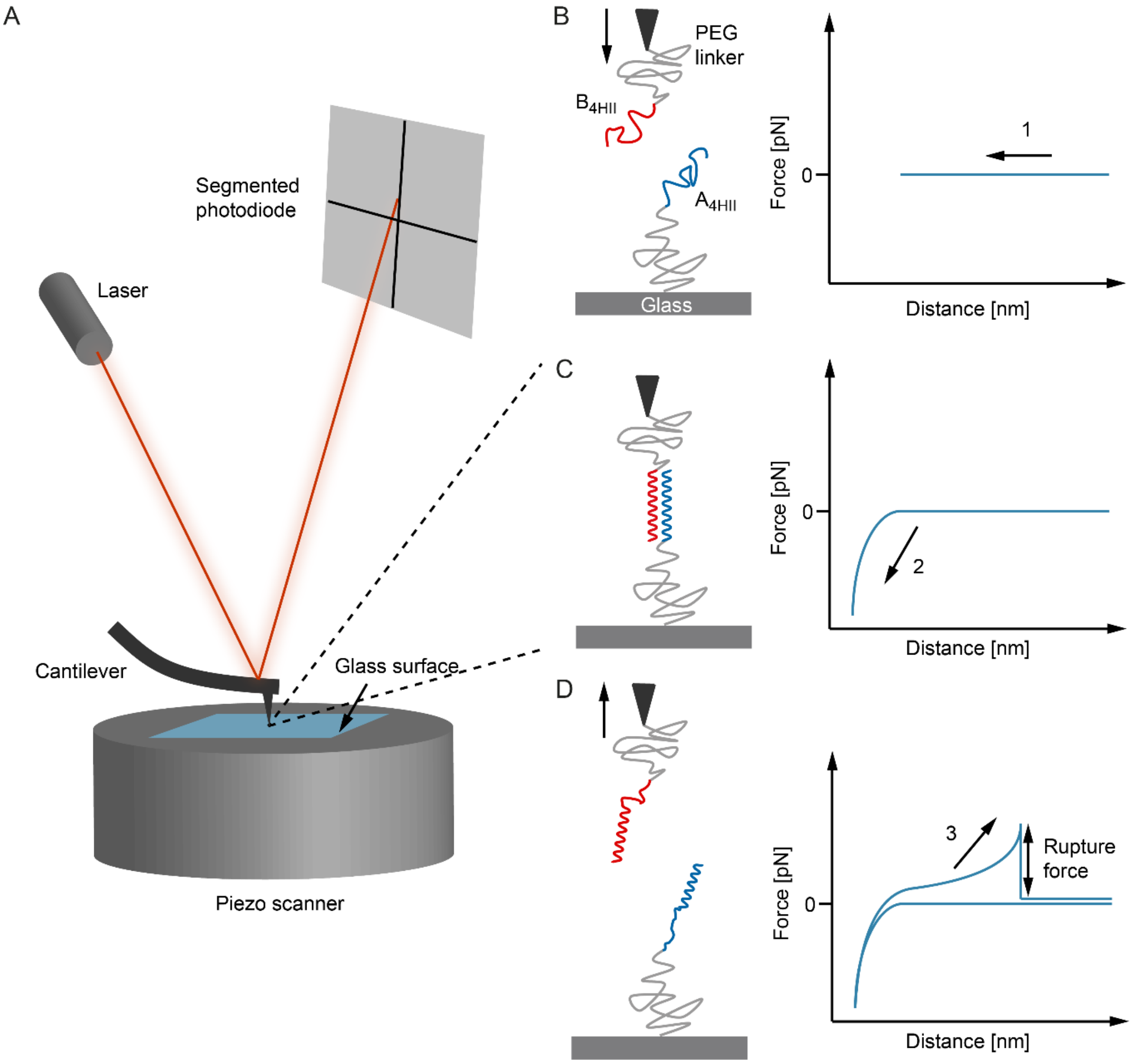

Figure 20: Basic principle of atomic force microscope (AFM)-based single molecule force spectroscopy (SMFS). A) Experimental setup. A glass surface, functionalized with one CC-forming peptide, is mounted on a piezo scanner. The second CC-forming peptide is coupled to the cantilever. The deflection of the cantilever during each approach-retract cycle is detected using a laser, which is focused on the back of the cantilever. B) The functionalized cantilever tip is approaching the surface. The force detected is 0 pN at the baseline level. C) The cantilever bends slightly backwards upon contact with the surface and the CC forms. D) The cantilever is retracted from the surface and the CC is mechanically loaded in the shear geometry. The force acting on the CC is increasing and it partially unfolds before it ruptures. After rupture of the CC interaction, the force returns to the baseline level.

In order to study the force-induced unfolding of a CC, one CC-forming peptide is immobilized on the cantilever tip and the other one on the surface. The particular surface functionalization used for the immobilization of the CCs is described in the experimental section below. In a typical SFMS experiment, the cantilever first approaches the surface (**Figure 20B**), and slightly bends upward when contact with the surface is established, which is indicated by a negative force (**Figure 20C**). During this contact period, the CC can form and is subsequently ruptured when the cantilever is retracted from the surface. As a result of the increasing force, the CC starts unfolding and finally dissociates at a critical rupture force (F_R), resulting in the drop of the force back to the baseline (**Figure 20D**). The described approach and retract cycle is repeated at different positions of the sample thousands of times until several hundreds of single molecule force-extension curves have been collected.

On average, only 5-20 % of the force curves contain single rupture events, which have to be distinguished from non-specific interactions and rare multiple events. The PEG linkers used as spacers between the CC and the surface/cantilever tip serve as an internal control for selecting single rupture events since they have a characteristic non-linear force-extension behavior, which originates from stretching the polymer against entropic forces. The force-extension curves can be fitted with the worm-like chain (WLC) model [202]

$$F(x) = \frac{k_B T}{l_p}\left(\frac{1}{4\left[1-\frac{x}{l_c}\right]^2} - \frac{1}{4} + \frac{x}{l_c}\right) \qquad (12)$$

with the persistence length l_p, the contour length l_c, the end-to-end distance of the polymer chain x, the Boltzmann constant k_B and the temperature T (**Figure 21A**). The total length of the two extended PEG linkers is approximately 130 nm [203] and the length of the CC is 4 nm. The applied loading rate $\dot{F}$ ($\dot{F} = dF/dt$) [pN s^{-1}] is determined from the slope of the force curve at the detachment point of the CC multiplied by the retract speed of the cantilever.

At ambient temperature, the CC fluctuates around the bound state, which leads to a distribution of rupture forces (**Figure 21B**). A Gaussian distribution is fitted to the histograms to obtain the most probable values for the rupture force and the loading rate. The obtained rupture force is not an intrinsic property of the CC, but depends on the applied loading rate and the temperature. The simplest model to describe the force-induced unbinding of a dimeric CC is a two-state model where the bound state (N_2) and the unfolded state (2U) are separated by a transition state (T) (**Figure 22A**).

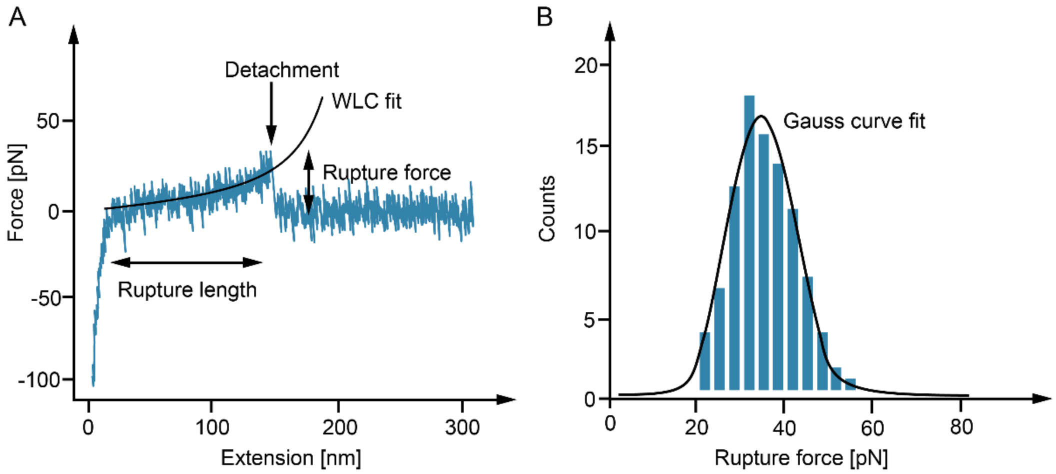

Figure 21: Analysis of force-extension curves. A) Representative force-extension curve of a CC. The rupture force and loading rate are extracted after fitting the force-extension curve with the worm-like chain model [202]. B) Several hundreds of force-extension curves are evaluated and the rupture force distribution is plotted. The data is fitted with a Gaussian distribution to obtain the most probable value. The same type of fit is used to obtain the most probable loading rate from the loading rate distribution.

The unbinding transition is characterized by the height of the free energy barrier, related to the thermal unfolding rate at zero force k_{off}, as well as the distance from the bound to the transition state (Δx). The unfolding rate k_{off} depends exponentially on the height of the free energy barrier (ΔG_{off}) [204]

$$k_{off} = v \cdot e^{-\frac{\Delta G_{off}}{k_B T}} \qquad (13)$$

with the attempt frequency ν and the Boltzmann constant k_B [205]. When a force is applied, the energy landscape is tilted, decreasing ΔG_{off} (**Equation 14**).

$$k_{off}(F) = v \cdot e^{-\frac{\Delta G_{off} - F\Delta x}{k_B T}} \qquad (14)$$

If the loading rate applied in SMFS is on the same time scale as the thermal transition, the CC is at equilibrium and the rupture force is independent of the loading rate. If the loading rate applied is faster than the thermal transition between the states, the force-induced transition occurs out of equilibrium and is loading rate dependent [206]. To obtain force-extension curves at different loading rates, the retract speed of the cantilever is varied. The Bell-Evans model (**Equation 15**) is widely used to describe the loading rate dependent unfolding/dissociation of biomolecular interactions [59,207].

$$F(\dot{F}) = \frac{k_B T}{\Delta x} \cdot \ln \frac{\Delta x}{k_B T\, k_{off}} + \frac{k_B\, T}{\Delta x} \cdot \ln \dot{F} \qquad (15)$$

Plotting the most probable values of the rupture force against the logarithm of the corresponding loading rate yields a linear correlation, which is fitted with the Bell-Evans model (**Figure 22B**). The Bell-Evans model assumes that Δx is independent of the force applied. The k_{off} at zero force is obtained from the intercept with the x-axis and Δx is determined from the slope (**Equation 15**).

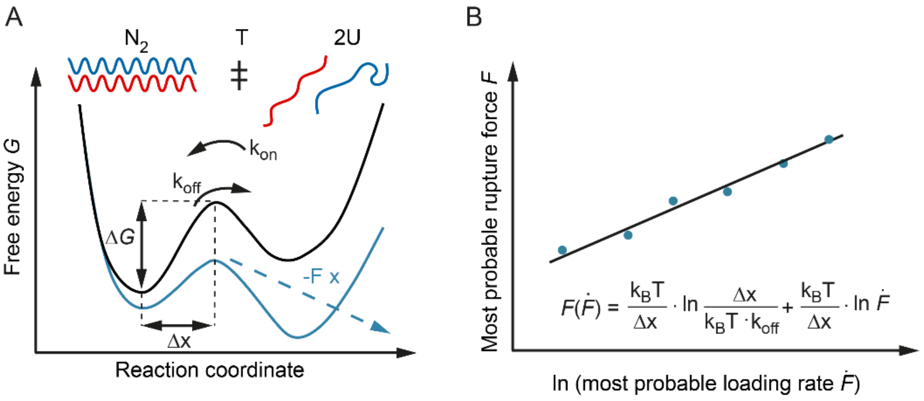

Figure 22: Mechanical characterization of CCs under applied force. A) Schematic energy landscape of the CC with the bound state (N_2) the transition state (T) and the unfolded state (2U). When a force is applied, the energy landscape is tilted and the energy barrier between the bound state N_2 and the transition state T is decreased, which promotes CC unfolding. B) Bell-Evans fit for the loading rate depended unfolding of the CC in non-equilibrium conditions. The most probable values for the rupture force and the loading rate were obtained from the respective distribution at each retract speed. The unfolding rate at zero force (k_{off}) and the distance to the transition state (Δx) can be determined from the Bell-Evans fit [59,207].

Cantilever and surface functionalization

Cantilevers and glass coverslips were prepared according to Zimmermann et al. [208]. First, cantilevers (MLCT, Bruker) were cleaned using a UV-ozone cleaner (BioForce, Nanoscience) for 20 min. Second, the cantilevers were submerged in pure 3-aminopropyldimethylethoxysilane (APDMES) (abcr) for amino-silanization for 10 min at RT. After washing with isopropanol and ultrapure water, the amino-functionalized cantilevers were dried and cured for 30 min at 80 °C. The coverslips (Menzel Gläser, Ø 24 mm) were sonicated for 10 min in isopropanol and 3x 5 min in water. After 15 min UV-ozone cleaning, amino-silanization was performed in a 1 % (v/v) solution of APDMES in absolute ethanol for 1 h (**Figure 23A**). Then, the coverslips were washed 3x with isopropanol and water, followed by curing in the oven at 80 °C for 1 h. For the next steps, the coverslips and the cantilevers were treated in parallel. In the first step, a heterobifunctional NHS-poly(ethylene glycol)-maleimide (MW = 10 kDa, Rapp Polymere) was coupled to the amino-functionalized surface via the NHS-ester (**Figure 23B).** Specifically, the PEG was dissolved in sodium borate buffer to 30 mM and incubated on the surface for 1 h at RT in a humidity chamber. Second, the surfaces were washed thoroughly with water and dried under nitrogen flow. Third, the peptides were dissolved in coupling buffer to 0.5 mM and incubated on the surfaces for 1 h at 4 °C in a humidity chamber (**Figure 23C**). The B-peptide (B_{4HII}) was coupled to the cantilever and the A-peptide (A_{4HII}) to the coverslip. Then, the surfaces were washed intensively with PIPPS to remove the unbound peptides.

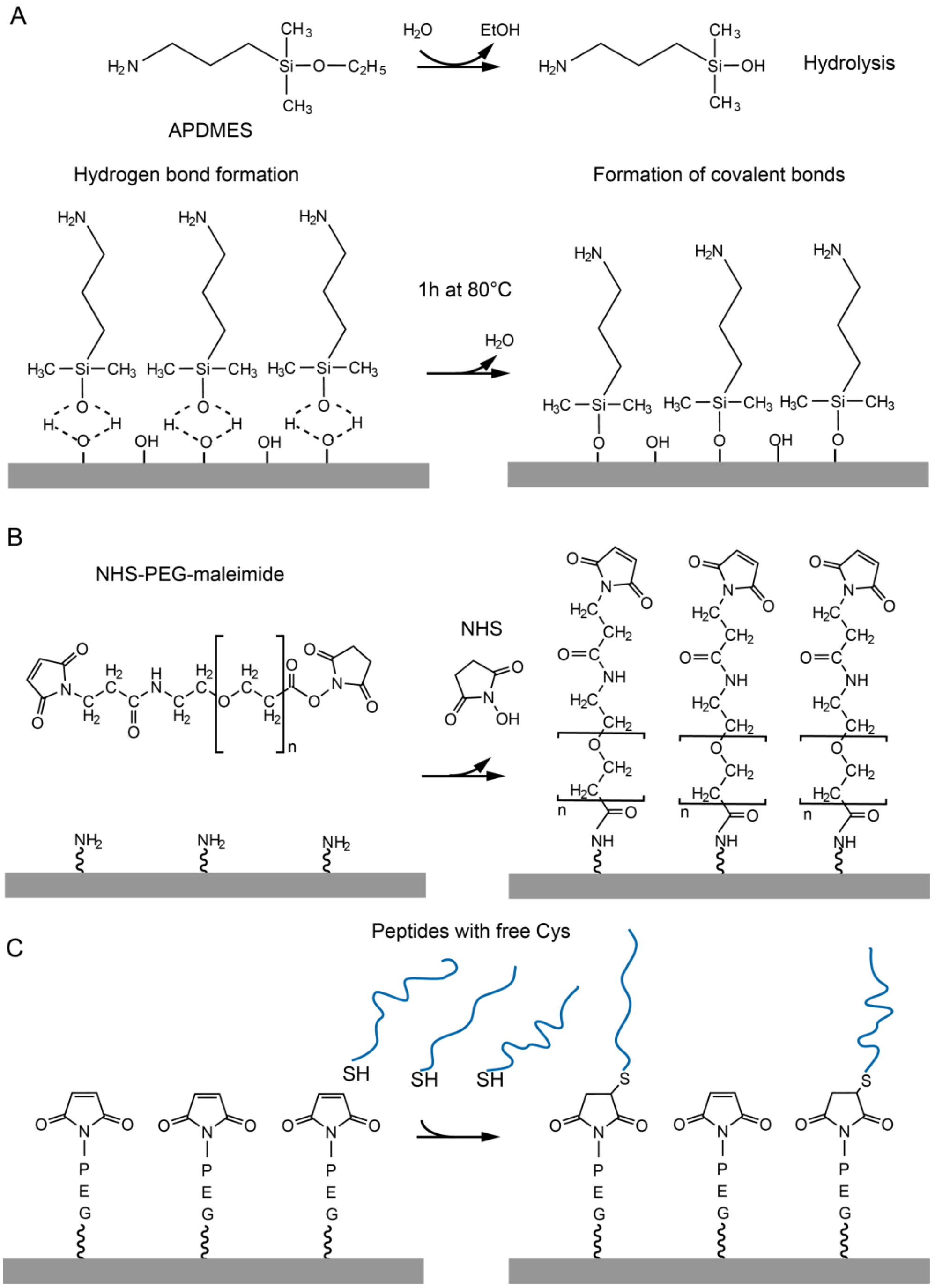

Figure 23: Schematic of the surface functionalization steps after Zimmermann et al. [208]. A) Silanization of the surface with 3-aminopropyldimethylethoxysilane (APDMES). B) Coupling of NHS-PEG-maleimide to the surface via the NHS-ester. C) Immobilization of the peptide on the surface. The free cysteine (Cys) at the terminus of the peptide is reacting with the maleimide group of the PEG.

Force spectroscopy and data analysis

A Force Robot 300 (JPK Instruments) was used to perform the SMFS measurements at RT in PIPPS. The MLTC cantilever C with a nominal spring constant of 0.01 N m^{-1} was used. To preserve the surface functionalization, the nominal values for the spring constant and the sensitivity were initially used to collect the force-extension curves and the calibration was performed after the measurements. The thermal noise method [201] was used to calibrate the cantilevers. The obtained spring constant values range from 0.013-0.025 N m^{-1} (**Table S1**). Dynamic SMFS was performed at six different retract speeds (50, 200, 400, 1000, 2500, 5000 nm s^{-1}), collecting several thousands of force-extension curves at each retract speed. The set-point force was 80 pN and a 10 x 10 µm grid with 8 x 8 points was used to obtain force-extension curves from different positions on the surface.

The effect of His-metal coordination on CC stability was investigated adding 1 mM $NiCl_2$ in PIPPS buffer. For each experimental condition, three independent measurements with new cantilevers and coverslips was performed and data was collected at the six different retract speeds. The measurements of $A_{4H\perp}B_{4H\perp}$ in the presence of metal ions were not possible because of the formation of insoluble aggregates on the coverslip. The JPKSPM data processing software V5.0.68 (JPK Instruments) was used to analyze the obtained force-extension curves. The PEG linkers used served as an internal control. The force curves show a characteristic force-extension behavior of PEG that can be fitted using the WLC model (**Equation 12**). Only the force-extension curves displaying a single rupture event (visual inspection) and a contour length larger than 90 nm were considered for further analysis, taking into account the polydispersity of the PEG. Using these criteria, force-extension curves displaying non-specific rupture events are eliminated, since they cannot be fitted with the WLC model and/or possess shorter contour lengths.

For each retract speed, the rupture forces and the loading rates obtained were plotted in histograms using IGOR Pro 6.37 (Wavemetrics). The most probable rupture force and the most probable loading rate were determined fitting a Gaussian distribution to the histograms (a logarithmic plot is displayed for $\dot{F}$) (**Table S2**). For each of the independent measurements, the values of the most probable rupture force were plotted against the logarithm of the most probable loading rate. The Bell-Evans model [209] (**Equation 15**) was used to fit the data in order to obtain the unfolding rate at zero force (k_{off}) and the potential width (Δx) at $T = 25\ °C = 298.15\ K$.

3.5 Rheology

Rheology (greek: "*rhein*" = to flow) characterizes the deformation of solids and the flow behavior of liquids under shear force [210]. The shear behavior of materials ranges from ideally viscous (e.g. low viscosity oils) to ideally elastic (e.g. a steel ball). Most materials, such as plastics, toothpaste, paintings, hand cream, hydrogels or cheese have viscous and elastic components – they are viscoelastic.

Theoretical background

The viscoelastic properties of biomimetic hydrogels are reported to affect cell signaling and differentiation [159]. Therefore, it is highly desirable to control and precisely tune these properties when applying hydrogels as scaffolds in cell culture or tissue engineering. Shear rheology is the method of choice to characterize the viscoelastic properties of hydrogels [211]. In shear rheology, the hydrogel is mounted on a static bottom plate and shear force is applied with the measurement tool (**Figure 24A**). Frequently used measurement setups employ a plate-plate or cone-plate geometry. Cone-plate systems are beneficial for the measurement of hydrogels since the shear rate applied to the sample is equal over the entire radius of the tool. The measurement tool can be moved in a rotating or oscillating fashion.

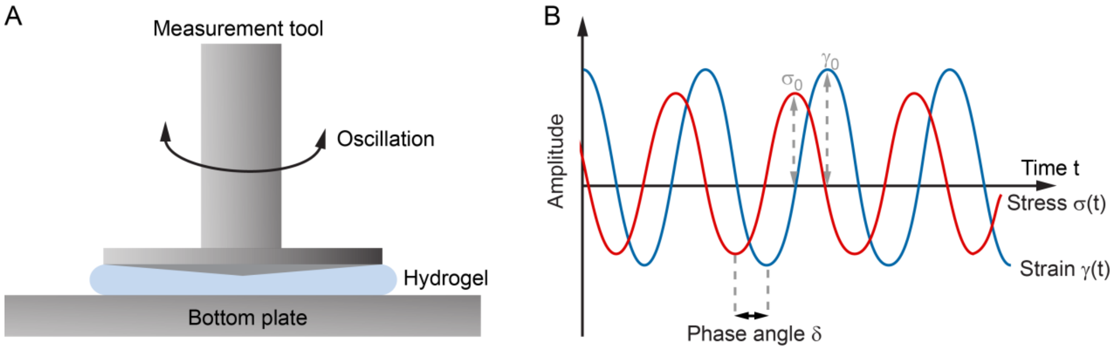

Figure 24: Oscillatory shear rheology. A) Schematic measurement setup with the hydrogel being located between a static bottom plate and an oscillating cone-tool. B) Time-dependent oscillation of strain and stress with a strain amplitude of γ_0 and a stress amplitude of σ_0. The two curves show a phase shift δ.

Rheometers can be operated in a strain-controlled or stress-controlled mode. When a controlled shear stress σ is applied in a sinusoidal fashion, the obtained shear strain γ can be phase shifted by the phase angle δ (**Figure 24B**) [210].

$$\gamma(t) = \gamma_0 \sin(\omega t) \qquad (16)$$

$$\sigma(t) = \sigma_0 \sin(\omega t + \delta) \qquad (17)$$

The angular frequency of the sine wave is ω [rad s^{-1}]. For ideally elastic materials, there is no phase shift and $\delta = 0$ °. In contrast, ideally viscous materials, show a phase shift of $\delta = 90$ ° and viscoelastic materials have a phase shift of $0° < \delta < 90°$. The complex shear modulus G*(t) [Pa] is defined as

$$G^*(t) = \frac{\sigma(t)}{\gamma\,(t)} = G' + iG'' \qquad (18)$$

with the real/elastic modulus *G'* and the imaginary/viscous modulus *G"*. In terms of material behavior, G' is the deformation energy stored and *G"* is the deformation energy dissipated by the material.

$$G' = \frac{\sigma_0}{\gamma_0} \cdot \cos\delta \qquad (19) \qquad\qquad G'' = \frac{\sigma_0}{\gamma_0} \cdot \sin\delta \qquad (20)$$

Intact hydrogel networks behave like viscoelastic solids in which *G'* is higher than *G"*. The effective cross-link density d_c of the hydrogel can be estimated with

$$d_c = \frac{G'}{R \cdot T} \qquad (21)$$

where R is the gas constant and T is the temperature [212]. To obtain quantitative mechanical properties, measurements are performed at small deformations in the linear viscoelastic (LVE) range of the hydrogel. This is essential to ensure that the properties are independent of the applied stress or strain [210]. The LVE range is determined with an amplitude sweep in which the strain amplitude is varied over a large range and the angular frequency is kept constant (**Figure 25A**). When the cross-links break at high strain amplitudes, a crossover of *G'* and *G"* is observed. The relaxation time τ is a characteristic property of non-covalently cross-linked viscoelastic hydrogels and depends on the thermal stability and kinetics of the cross-links as well as the network topology (**Figure 25B**) [128,213]. Experimentally, the relaxation time of a material can be determined from a frequency sweep based on the Maxwell model [210] or from a stress relaxation test (**Figure 25C**).

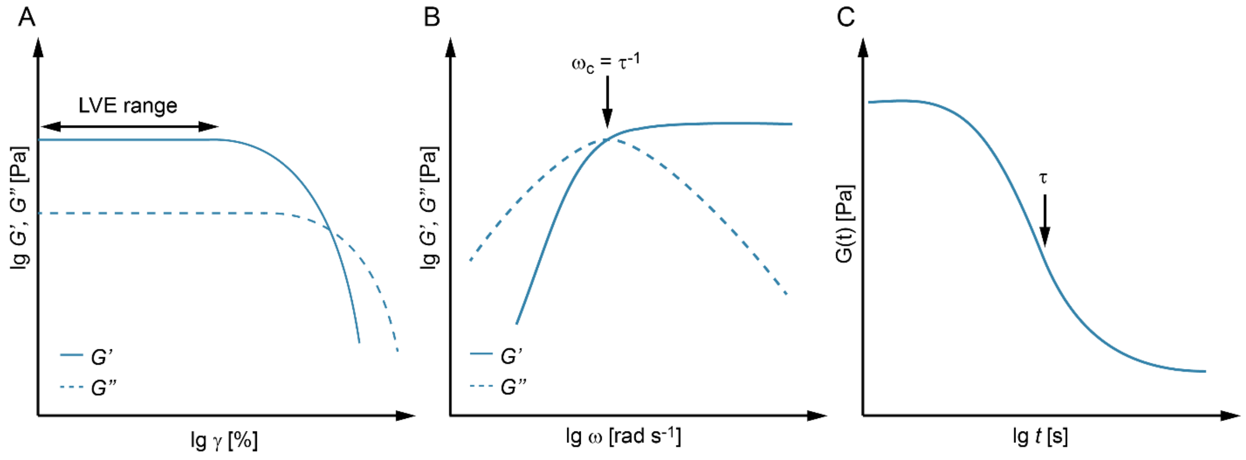

Figure 25: Hydrogel characterization using shear rheology. A) Strain amplitude sweep at constant angular frequency to determine the linear viscoelastic (LVE) range of the hydrogel. B) Frequency sweep at a constant amplitude in the LVE range to determine the relaxation time τ. C) Stress relaxation can also be determined with a step-strain experiment, where the time evolution of the relaxation modulus is followed. A fit of the data to Kohlrausch's stretched exponential relaxation model yields the relaxation time [214].

The Maxwell model describes a viscoelastic material using a combination of dashpot and spring in serial connection (**Figure 26A**). The spring describes the elastic behavior and the dashpot the viscous behavior of the sample. The deflection of both parts is independent of each other. When a constant load is applied, the spring deforms immediately until it reaches a constant deflection value (**Figure 26B**). The piston of the dashpot moves continuously as long as force is applied (**Figure 26C**). The result is a time-dependent deformation function. Once the load is removed, the spring moves back elastically to its initial position, while the state of the dashpot remains unchanged (**Figure 26C**).

The Maxwell model assumes that the total deformation is the sum of the individual deformations (γ_v and γ_e) or the two components of the shear stress (σ_v and σ_e), respectively [215].

$$\gamma = \gamma_v + \gamma_e \qquad (22)$$

$$\sigma = \sigma_v + \sigma_e \qquad (23)$$

Newtons's law applies to the viscous component

$$\dot{\gamma}_v = \frac{\sigma_v}{\eta} \qquad (24)$$

with the viscosity η. Hooke's law describes the elastic component

$$\dot{\gamma}_e = \frac{\dot{\sigma}_e}{G} \qquad (25).$$

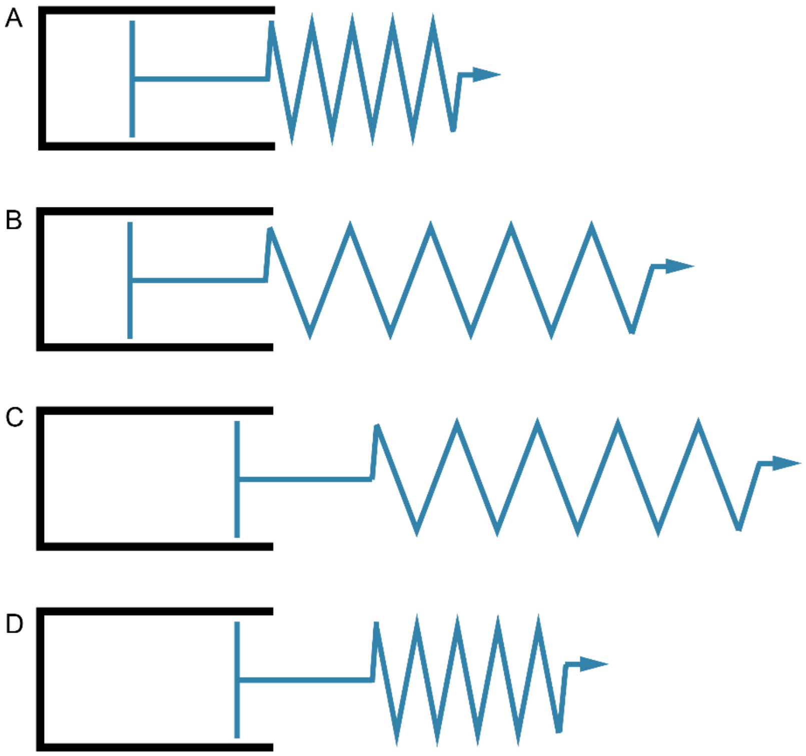

Figure 26: Deformation behavior of viscoelastic solids according to the Maxwell model. A) Initial state of the dashpot and the spring. B) Load is applied to the sample and the elastic spring stretches. C) Once the spring is fully stretched, the piston of the dashpot starts to move continuously as long as force is applied. D) When the load is removed, the spring goes back to its initial position instantly, while the piston stays in its position.

The differential equation of the sum of the shear rates is described as

$$\dot{\gamma} = \dot{\gamma}_v + \dot{\gamma}_e = \frac{\sigma_v}{\eta} + \frac{\dot{\sigma}_e}{G} = \frac{\sigma}{\eta} + \frac{\dot{\sigma}}{G} \qquad (26)$$

with $\dot{\gamma}$ = dγ/dt and $\dot{\sigma}$ = dσ/dt. Since the relaxation time τ of viscoelastic materials is

$$\tau = \frac{\eta}{G} \qquad (27)$$

the Maxwell model can also be written as

$$\dot{\gamma} \cdot \eta = \sigma + \tau \cdot \dot{\sigma} \qquad (28)$$

In frequency sweeps, the angular frequency is varied while a constant strain amplitude in the LVE range is applied. For materials that behave according to the Maxwell model, the relaxation time is obtained from the frequency ω_c where *G'* and *G"* cross each other (**Equation 29**).

$$\tau_{fs} = \frac{1}{\omega_c} \qquad (29)$$

If the relaxation time of the material is too long to be in the measurable range of a frequency sweep, a stress relaxation test can be performed. First, a low pre-strain (e.g. 0.1 %) is applied for a short time. Then, an instant step to a constant higher strain value in the LVE range is performed. The relaxation modulus G(t) of the hydrogel is monitored over time. The Kohlrausch stretched exponential relaxation model describes the relaxation behavior of many non-covalently cross-linked polymeric hydrogels [214].

$$G(t) = G_0 \, exp(-(\frac{t}{\tau_{sr}})^{\alpha}) \qquad (30)$$

G_0 is the initial plateau modulus and τ_{sr} is the relaxation time. The fitting parameter α is governed by the physical properties of the hydrogel and usually ranges from $0 \leq \alpha \leq 1$ [214,216].

Hydrogel preparation

For hydrogel preparation, the CC peptides were coupled to maleimide-terminated 4-arm star-shaped PEG (star-PEG, Jenkem) (**Figure 27**).

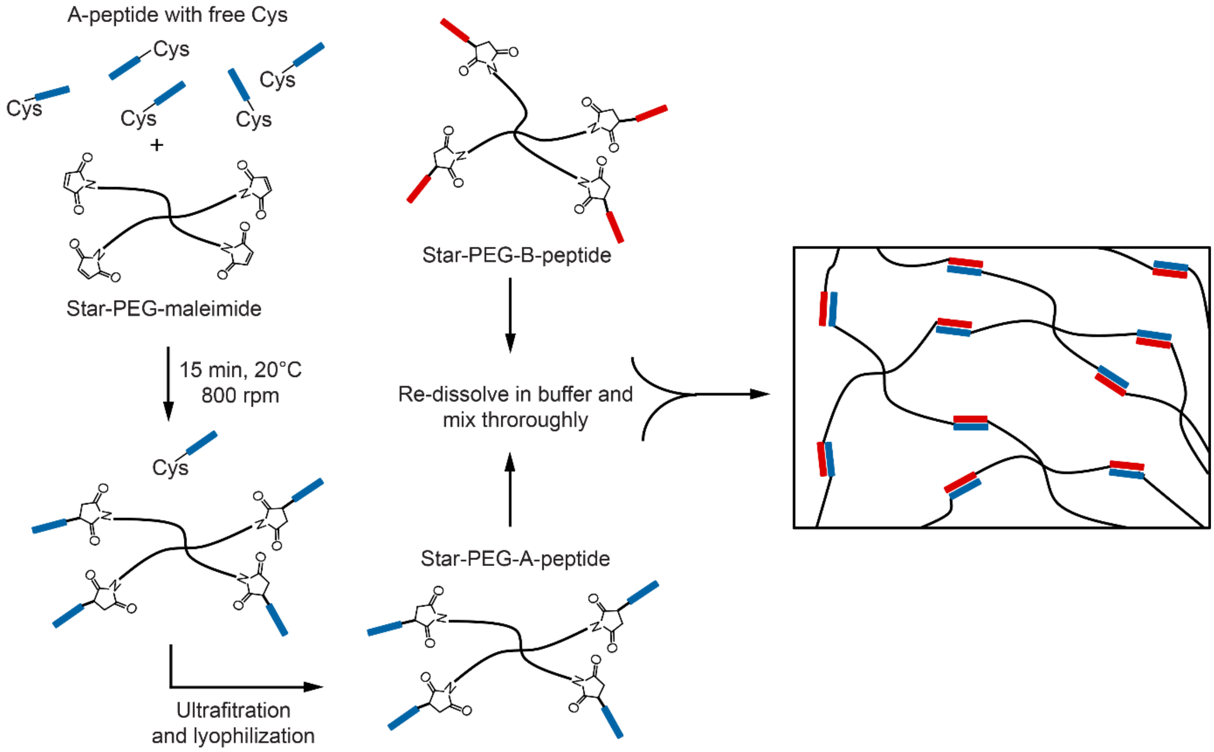

Figure 27: Hydrogel preparation. The reduced A-peptides with free Cys are coupled to star-PEG-maleimide in PBS. An excess of A-peptide is used to ensure that all arms of the star-PEG are functionalized. The excess of peptide and the buffer salts are removed using ultrafiltration. Subsequently, the star-PEG-peptide conjugate is lyophilized. The same procedure is followed for the B-peptides. The star-PEG-A-peptide and star-PEG-B-peptide conjugates are re-dissolved in the measurement buffer and mixed thoroughly in a 1:1 ratio.

First, the CC peptides were dissolved in PBS in a concentration of 10 mg ml^{-1}. Possible disulfide bonds formed between the terminal Cys of the peptides were reduced using Pierce™ Immobilized TCEP Disulfide Reducing Gel (Thermo Fisher Scientific) for 1.5 h at 4 °C on a mixer (2000 rpm). Second, the concentration of free Cys was determined with Ellman's reagent (Thermo Fisher Scientific). When reacting with free Cys, Ellman's reagent forms a chromophore that can be quantified via its absorbance at 412 nm. Third, the reduced peptides were incubated with 4-arm star-PEG-maleimide separately, yielding star-PEG-$A_{4H\parallel}$ ($A_{4H\perp}$) and star-PEG-$B_{4H\parallel}$ ($B_{4H\perp}$). To ensure that all star-PEG molecules are functionalized, a 1.2-fold excess of free Cys was used for the coupling reaction. The reaction mixture was incubated for 15 min at RT on a mixer (800 rpm). Ultrafiltration (Amicon® Ultra, 10 kDa cut-off, Merck) was used to remove the excess of peptide and to exchange PBS to ultrapure water (5x washing, 14,000 *g*, 10 min). The obtained star-PEG-peptide conjugates were freeze dried and stored at -20 °C until usage. The hydrogels were prepared through thoroughly mixing the re-dissolved star-PEG-$A_{4H\parallel}$ ($A_{4H\perp}$) and star-PEG-$B_{4H\parallel}$ ($B_{4H\perp}$) conjugates (0.5 mM in PIPPS) in a stoichiometric ratio of 1:1. The hydrogels formed in less than 1 min. Entrapped air bubbles were removed by centrifugation for 2 min at 2,000 *g*. Different metal ions were added from 100 mM stock solutions right after forming the hydrogel and mixed thoroughly. A 2.5-fold to 4-fold excess of the chelating agent EDTA was used to study the reversibility of metal ion coordination. To allow equilibration, hydrogels with $A_{4H\perp}B_{4H\perp}$ were incubated at least 4 h at 4 °C before the measurement.

Covalently cross-linked hydrogels with a low amount of $A_{4CF}B_{4TR}$ were formed in PBS in a round metal mold (height: 1 mm) using the following protocol: The CC-forming peptides A_{4CF} and B_{4TR} (final concentration 5 µM) were mixed with 10 mM of the covalent cross-link SH-PEG-SH (2 kDa, Rapp Polymere) (final concentration 2mM). Then, 2 mM star-PEG was added and thoroughly mixed, yielding a final concentration 1 mM star-PEG. To complete the bond formation, the hydrogels were incubated for 1 h at RT in a humid atmosphere. As controls, hydrogels containing only the donor peptide A_{4CF} or the acceptor peptide B_{4TR} were prepared following the same protocol.

Hydrogel characterization using shear rheology

All hydrogels were characterized using stress-controlled oscillatory shear rheology (MCR 301 or MCR 302, Anton Paar) using a cone-plate geometry with 12 mm diameter (CP-12, 0.02 mm gap, 1° angle, Anton Paar). The measurements were performed at 25 °C with a temperature-controlled hood, preventing evaporation of the sample.

Amplitude sweeps were conducted to determine the LVE range of the hydrogel. Strain amplitudes from 0.1 % ($A_{4H\perp}B_{4H\perp}$) or 1 %-1000 % were applied to the sample at a constant angular frequency of 10 rad s^{-1}. Directly after the first amplitude sweep, another amplitude sweep was performed from 1000 %-1 % or 0.1 % ($A_{4H\perp}B_{4H\perp}$) shear strain.

A step strain test was performed, applying alternating shear strain of 0.1 % ($A_{4H\perp}B_{4H\perp}$) or 1 % ($A_{4H\parallel}B_{4H\parallel}$) and 1000 % at a constant angular frequency of 10 rad s^{-1} to test for self-healing of the hydrogels. The time intervals of the applied strain were 5 min for $A_{4H\parallel}B_{4H\parallel}$ in the absence of metal ions and 20 min for $A_{4H\parallel}B_{4H\parallel}$ in the presence of 1:1 His:Ni^{2+} as well as $A_{4H\perp}B_{4H\perp}$ in the absence and presence of 1:1 His:Zn^{2+}.

Frequency sweeps were performed from 100-0.001 rad s^{-1} at constant strain amplitude of 1 %, which is in the LVE range of the hydrogels. The relaxation time τ_{fs} of the CC cross-links was obtained from the cross-over frequency ω_c of G' and G'' in the frequency sweeps using **Equation 29**. All samples were measured in triplicate in order to obtain a mean relaxation time (± SEM).

For the $A_{4H\perp}B_{4H\perp}$ hydrogels, stress relaxation tests were performed in addition to the frequency sweeps. This was necessary as no cross-over of G' and G'' was observed in the measurable frequency range for hydrogels containing a high Zn^{2+} concentration. Specifically, a 10 % step-strain was applied to the hydrogel and the relaxation modulus G(t) of the materials was monitored. Kohlrausch's stretched exponential relaxation model (**Equation 30**) was used to describe the relaxation behavior of the CC cross-linked hydrogel. The fit was performed in Origin Pro 2015 using the Levenberg-Marquardt iteration method. For the fit, G_0 was fixed to the value of G' obtained during an amplitude sweep performed before the relaxation test (LVE range).

For hydrogels containing the FRET reporter system, the fluorescently labeled CC was used at low concentration while the majority of the cross-links were covalent (SH-PEG-SH). Only low concentrations of the FRET-labeled CC can be used to avoid undesired self-quenching effects. For compression tests, the hydrogels were formed in a mold and transferred to the base plate of the rheometer carefully. The rheometer was equipped with a transparent base plate and a fluorescence microscope (MCR 302, Anton Paar). The microscope consisted of a long-distance 10x objective (Apo Plan,∞ / NA 0.28, Mitutoyo), a light source (SugarCUBE™ Ultra, Ushio America Inc.) and a CCD camera (Lumenera LM165C, TELEDYNE Lumenera). For detecting carboxyfluorescein, the following filters were used: 470/22 nm excitation filter (Semrock), a dual band pass dichroic mirror (Semrock FF493/574) and a 514/30 nm emission filter (Semrock). The hydrogels were compressed between the base plate and a plate measurement tool (12 mm diameter) and the carboxyfluorescein signal was recorded at 1 mm (initial height) and 0.1 mm gap width. The camera was set to an exposure time of 50 ms, a gain of 18 and a green gain of 4. The red and blue gains were set to 1. Images were collected for 10 hydrogels containing $A_{4CF}B_{4TR}$ and 10 hydrogels containing only A_{4CF}. Tetramethylrhodamine fluorescence was collected using a 556/20 nm excitation filter (Semrock) and a 617/73 nm emission filter (Semrock). For this control experiment, 4 hydrogels of $A_{4CF}B_{4TR}$ and only B_{4TR} were measured (red gain = 1.24, blue and green gain = 1) to show that the concentration of B_{4TR} was comparable in the hydrogels.

For all images, the mean intensities of carboxyfluorescein or tetramethylrhodamine were obtained using imageJ 1.47 [217] and the FRET efficiency was calculated using **Equation 10**. The mean intensities are given in **Table S6** and **Table S7**.

4 Results

4.1 Experimental design

Coiled coils are prominent protein folding motifs in proteinaceous materials and naturally occur in the ECM of mammalian tissues. As a result, they are frequently used as biocompatible building blocks for biomimetic hydrogels (see **Chapter 1.4**). It has remained a significant challenge to precisely control and reversibly tune the viscoelastic properties of dynamically cross-linked hydrogels. The scope of this thesis was to develop reversibly tunable, self-healing and self-reporting CC building blocks. In order to achieve this goal, I bioengineered His-metal coordination sites into the well-characterized model CC A_4B_4. This heterodimeric CC is 4-heptads long and composed of an acidic peptide (A_4) with Glu in *e* and *g* positions and a basic peptide (B_4) with Lys in *e* and *g* positions (**Table 2**) [46]. The hydrophobic core of A_4B_4 is formed by Ile and Leu, which allow for tight knobs-into-holes packing (**Figure 4**). An Asp inserted in the third heptad ensures heterodimer formation in a non-staggered fashion. The solvent-exposed positions *b* and *c* are occupied by Ala, since it has the highest helix propensity. Gln and Lys are used in the *f* positions to enhance solubility. The aromatic amino acids Trp and Tyr were used to measure the peptide concentration in the original sequence. In this thesis, Trp and Tyr were exchanged to Gln in some CC designs since peaks of aromatic amino acids overlap with peaks for His-metal coordination in Raman spectroscopy [71].

The thermodynamic stability of A_4B_4 is well-characterized with a melting temperature of 81.0 °C and a picomolar dissociation constant [46]. The energy landscape parameters of A_4B_4 were recently determined with AFM-SMFS applying the force in shear geometry [56]. Depending on the loading rate, the rupture force of A_4B_4 ranged from 35-50 pN with $k_{off} = 3.2 \cdot 10^{-4}$ s^{-1} and $\Delta x = 1.29$ nm (see **Chapter 1.2.2**). In shear geometry, the dominant mechanism of CC chain separation is suggested to be a combination of unfolding from the termini of force application and dissociation of the CC. Insertion of less helical amino acids in the solvent-exposed positions or amino acids with a less tight hydrophobic core packing decreased both the melting temperature and the dynamic rupture forces [62]. The first question to be addressed within the scope of this thesis was:

1. Can individual CC building blocks and the resulting CC cross-liked hydrogel be reversibly tuned with bioinspired His-metal coordination bonds?

To answer this question, I inserted two His residues into the solvent-exposed positions *b* and *f* in the terminal heptads of the CC ($A_{4H\parallel}B_{4H\parallel}$) with an *i* → *i* + *4* spacing (**Table 2, Figure** 28**A**). The *i* → *i* + *4* spacing places the His residues on the same face of the helix and is thus optimal for His-metal coordination [78,94]. The insertion of His led to a reduced helix propensity of the CC peptides; however, it allowed for the formation of stabilizing His-metal coordination bonds parallel to the main helical axis of the CC, i.e. bridging two helical turns. The folding of the CC in the absence of metal ions was investigated using Raman and CD spectroscopy (**Chapter 4.2.1**). Ni^{2+} was used as a coordinating metal ion since it is flexible in terms of the number of coordination partners and also accepts low coordination numbers [69,101]. Intramolecular His-Ni^{2+} coordination was thus expected to function as an additional bond parallel (∥) to the helical axis. The stabilization effect of His-Ni^{2+} coordination was investigated using CD spectroscopy and AFM-SMFS. This further allowed me to experimentally test the proposed mechanism of CC unfolding from the ends of force application under shear force (**Chapter 4.2.2**).

Table 2: Peptide sequences studied in this work. Heterodimeric 4-heptad CC sequences with the heptad register indicated in the first row. Histidine (His, H) modifications are indicated in bold. The terminal Cys (C) are inserted for site-specific immobilization in AFM-SMFS and hydrogel preparation. As fluorescent label, carboxyfluorescein (CF) was coupled to the Lys in A_4 and tetramethylrhodamine (TR) was coupled to the N-terminus of B_4.

Name	Sequence	MW* [g mol^{-1}]	HC$^{\#}$
	gabcdef gabcdef gabcdef gabcdef		
A_4	**C**GG EIAALEQ EIAALEK ENAALEQ EIAALEQ GG	3411	5.55
B_4	GG KIAALKQ KIAALKQ KNAALKK KIAALKQ GG**C**	3403	11.70
$A_{4H\parallel}$	**C**GG EI**H**ALE**H** EIAALEK ENAALEQ EIAALEQ GG	3486	3.25
$B_{4H\parallel}$	GG KIAALKQ KIAALKQ KNAALKK KI**H**ALK**H** GG**C**	3478	8.50
$A_{4H\perp}$	**C**GG EIAALE**H** EIAALE**H** ENAALE**H** EIAALEQ GG	3438	2.36
$B_{4H\perp}$	GG KIAALK**H** KIAALK**H** KNAALK**H** KIAALKQ GG**C**	3430	4.90
A_{4CF}	**C**GG EIAALEQ EIAALEK(CF) ENAALEW EIAALEQ GG	3827	-
B_{4TR}	(TR)GG KIAALKQ KIAALKY KNAALKK KIAALKQ GG**C**	3809	-

* MW – molecular weight; # HC – helical content, calculated with AGADIR [218] (T = 25 °C, pH = 7.4., ionic strength = 0.14 M).

Once characterized, I implemented the His-metal coordinating CC as cross-link in star-PEG-based hydrogels (**Chapter 4.2.3**). Specifically, I studied if the thermodynamic stabilization effect is transferable from the single molecule to the bulk material level using shear rheology. Frequency sweeps were used to determine the relaxation time of the hydrogel in the presence and absence of Ni^{2+}. Using the metal chelator EDTA, I tested if the His-Ni^{2+} coordination effect was reversible. To extend the tunable range of the hydrogel, I investigated the effect of Cu^{2+}, Co^{2+} and Zn^{2+}-coordination on the stability of $A_{4H\parallel}B_{4H\parallel}$. It was expected that the metal ions differ in their stabilizing effect according to the Irving-Williams series [81] and can be used to further tune the viscoelastic properties of the CC cross-linked hydrogel (**Chapter 4.2.4**).

His-metal coordination is a major factor for the higher-order self-assembly and the self-healing of mussel byssal threads as well as their mechanical response under load. The second question proposed in this thesis focused on inter-CC metal coordination (**Chapter 4.3**).

2. What is the effect of His-metal coordination induced higher-order CC assembly on the viscoelastic properties of the hydrogel?

To investigate if higher-order assembly of CCs can be induced using His-metal coordination, His residues were inserted in the *f* positions of the CC peptides $A_{4H\perp}$ and $B_{4H\perp}$ (**Table 2, Figure 28B**). In this design, the His residues are spaced by one heptad, which corresponds to 10.8 Å along the helical axis [219]. The optimal bond length for His-metal coordination is 2.1 Å [220]. Thus, the spacing prohibited the formation of coordination bonds along the helical axis and promoted the formation of coordination bonds with other CCs perpendicular ($\perp$) to the helical axis. This design, utilizing inter-CC His-metal coordination, is thus expected to favor the formation of higher-order CC-assemblies (**Chapter 4.3**). Specifically, I studied how the viscoelastic properties of the CC cross-linked hydrogel change in the presence of different concentrations of Zn^{2+}, which is the most prominent metal ion in the core of self-assembling byssal threads [17].

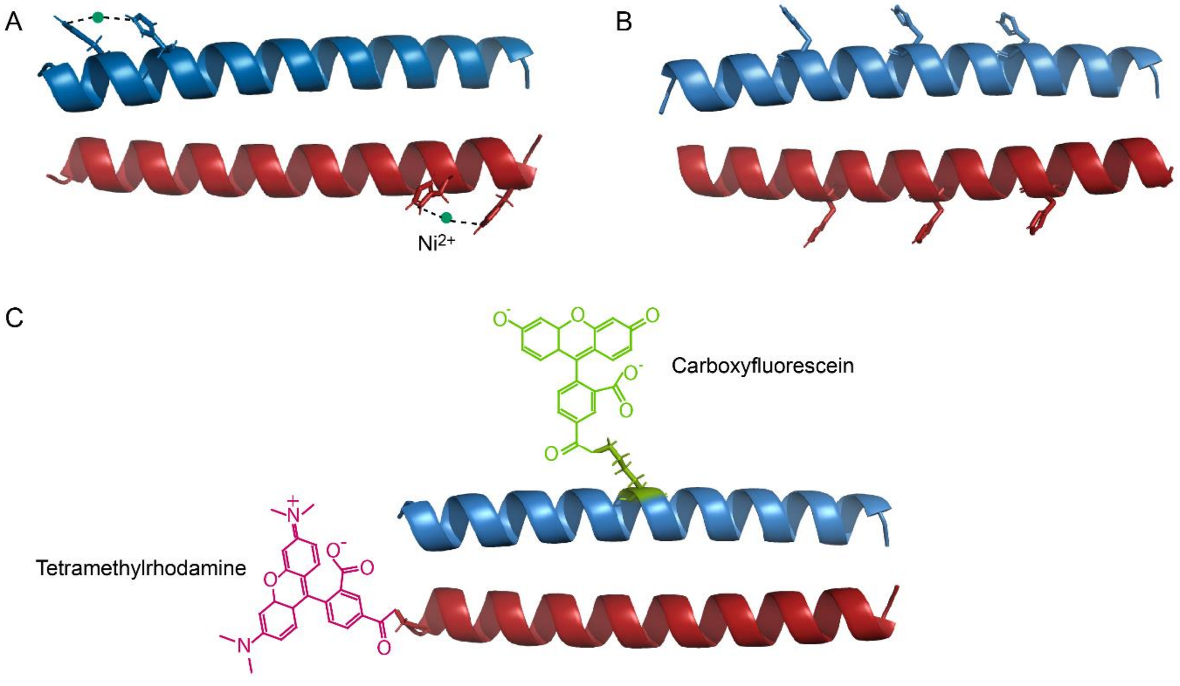

Figure 28: Schematic representation of the coiled coils (CCs) used in this thesis. A) CC with His in the terminal heptads where the shear force is applied. His-Ni^{2+} coordination is expected to function as an additional bond stabilizing the CC parallel to the helical axis ($A_{4H\parallel}$ $B_{4H\parallel}$). B) His-metal coordination sites are inserted in the *f* position of the CC to promote inter-CC metal coordination and higher-order assembly. His-metal coordination bonds are expected to form perpendicular to the helical axis of $A_{4H\perp}$ $B_{4H\perp}$. C) Fluorescently labeled CC $A_{4CF}B_{4TR}$. When the CC is formed, carboxyfluorescein and tetramethylrhodamine are in proximity to each other, which allows for FRET. When the CC dissociates, FRET is disrupted. Models were predicted using CC-builder2.0 [49]. The figures were produced with PyMOL Molecular Graphics System, Version 2.0 Schrödinger, LLC.

Understanding the network structure as well as the failure of CC cross-links in hydrogels is the basis for implementing CCs as self-reporting molecular force sensors in ECM mimicking hydrogels. Within the scope of this thesis, I developed a fluorescently labeled CC to answer the following question:

3. Is it possible to monitor CC cross-link failure in the hydrogel using an optical readout?

In order to determine whether the state of the CC cross-link A_4B_4 can be monitored when force is applied to the hydrogel, I equipped the CC with a FRET-based reporter system (**Table 2, Figure 28C**). Specifically, A_4 was labeled with carboxyfluorescein (CF) on the Lys in the second heptad (A_{4CF}). The N-terminus of B_4 was labeled with tetramethylrhodamine (TR) yielding B_{4TR}. CD spectroscopy was used to study the effect of the labeling on the folding and thermodynamic stability of the CC (**Chapter 4.4.1**). When the CC formed, the fluorophores were in close proximity to each other enabling FRET from carboxyfluorescein to tetramethylrhodamine. Using fluorescence spectroscopy, I determined the FRET efficiency of the CC (**Chapter 4.4.2**). As a proof-of-principle experiment, I introduced a low concentration of FRET-labeled CCs into a covalently cross-linked star-PEG hydrogel. Only a low amount of fluorescently labeled CC cross-links was used to prevent undesired self-quenching of the fluorophores in the hydrogel (**Figure 29A**), while the majority of the cross-links were formed by linear SH-PEG-SH (**Figure 29B**).

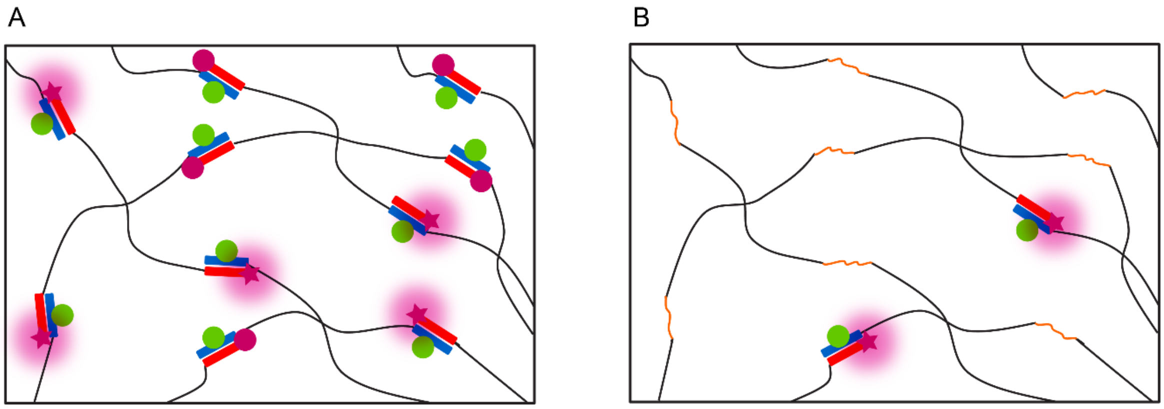

Figure 29: Experimental design of self-reporting coiled coil (CC) cross-linked hydrogels. A) Star-PEG hydrogel containing only fluorescently labeled CC cross-links. The high concentration of the fluorophores will lead to self-quenching effects. B) Star-PEG hydrogel containing covalent SH-PEG-SH cross-links (orange) and a low amount of FRET-labeled non-covalent CC cross-links.

To test the mechanoresponsiveness of the hydrogel, a rheometer combined with a fluorescence microscope was used to compress the $A_{4CF}B_{4TR}$ containing hydrogel. Specifically, the carboxyfluorescein signal was measured at different gap widths to determine the state of the self-reporting CC cross-links as a function of deformation.

4.2 Tuning coiled coil stability with His-metal coordination

In order to tune the stability of individual A_4B_4 CCs in the shear geometry, His-metal coordination sites were inserted in the *b* and *f* position of the terminal heptads, where the force was applied. His-Ni^{2+} coordination was expected to stabilize the terminal heptads of $A_{4H\parallel}B_{4H\parallel}$ parallel to the helical axis and the direction of force application (intra-CC). This allowed to experimentally test if the dominant unfolding mechanism is uncoiling-assisted dissociation of the CC, starting from the termini of force application as suggested by MD simulations [56]. Once characterized, the His-modified CC was implemented as a cross-link in star-PEG hydrogels to investigate if the molecular stabilization effect is transferred to the bulk viscoelastic properties of the hydrogel. The peptides A_4, B_4, $A_{4H\parallel}$ and $B_{4H\parallel}$ with and without terminal Cys were purchased from Centic Biotech and structurally characterized using CD and Raman spectroscopy prior to mechanical characterization using AFM-SMFS. All measurements were performed in the non-coordinating PIPPS buffer to ensure optimal coordination conditions.

4.2.1 Effect of intramolecular His-Ni^{2+} coordination on the thermodynamic stability of $A_{4H\parallel}B_{4H\parallel}$

The insertion of two His residues in the peptides $A_{4H\parallel}$ and $B_{4H\parallel}$ leads to a reduced helix propensity (**Table 2**) and might therefore alter the structure and stability of the CC. Raman and CD spectroscopy were used to investigate the secondary structure and thermal stability of the His-modified CC $A_{4H\parallel}B_{4H\parallel}$. Raman spectroscopy was also used to study the ability of the His residues to coordinate Ni^{2+}. The position of the amide I band is characteristic for the secondary structure of proteins and peptides and is based on stretching of the C=O in the protein backbone. The bands originating from the C_4=C_5 vibration of the imidazole side chain of His are extremely sensitive to changes in the protonation and coordination state and allow to investigate metal coordination. The Raman spectrum of $A_{4H\parallel}B_{4H\parallel}$ shows an amide I peak at 1654 cm^{-1}, which is assigned to α-helical secondary structure (**Figure 30**) [186]. At pH 8.0, the spectrum shows an additional peak at 1571 cm^{-1}, which is assigned to deprotonated His [71]. The addition of 1:2 Ni^{2+}:His leads to a shift of the peak to 1604 cm^{-1}, indicating Ni^{2+}-coordination by the Nτ-atom of His (**Figure 16**), while the amide I peak remains at 1654 cm^{-1}. This demonstrates that Ni^{2+}-coordination does not change the secondary structure of the CC. At acidic pH, the His is protonated (1629 cm^{-1}) and not able to coordinate Ni^{2+}.

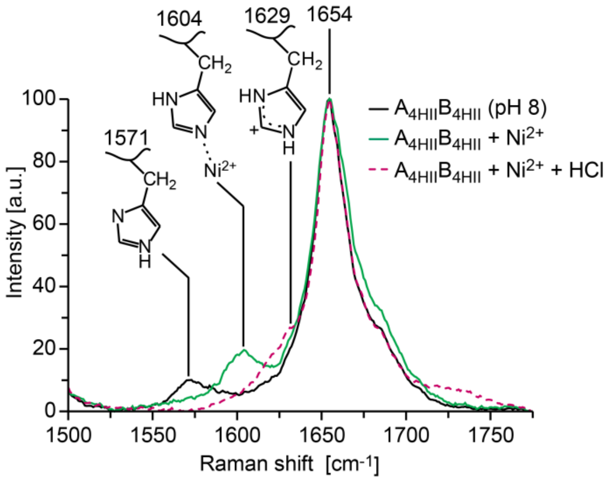

Figure 30: Raman spectroscopy of $A_{4HII}B_{4HII}$ Peptides without terminal Cys were used. The pH was adjusted to ~8 with NaOH. For metal coordination, $NiCl_2$ was added at a 1:2 Ni^{2+}:His ratio. Samples were prepared in solution and dried on a quartz glass slide. The spectra were normalized to the maximum of the amide I band. (Adapted and reproduced with permission from ref. [221], published in 2018 by the Royal Society of Chemistry.)

CD spectroscopy was used to confirm the α-helical secondary structure of $A_{4HII}B_{4HII}$. The CD spectra of in the individual peptides as well as the CC, measured in the presence and absence of Ni^{2+}, are shown in **Figure 31A**. $A_{4HII}B_{4HII}$ had a characteristic α-helical signature with two minima at 222 nm and 208 nm. The ratio of the two minima $r_{222/208}$ was 1.02, indicating a well-folded CC structure [179,180]. In the presence of Ni^{2+}, the intensity of the minima slightly increased and $r_{222/208}$ was 1.05.

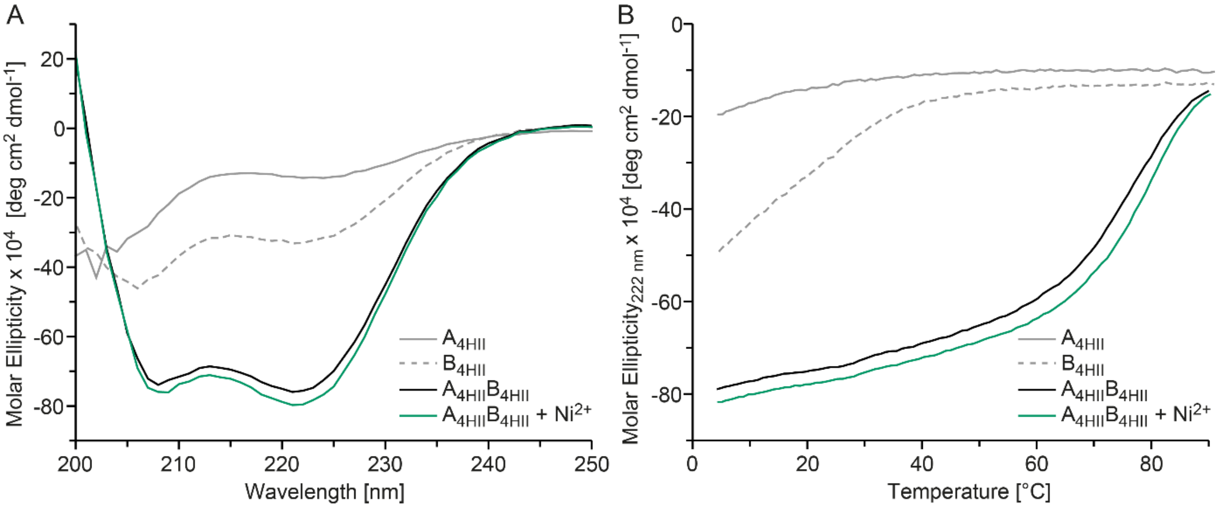

Figure 31: Circular dichroism spectra of the coiled coil (CC) $A_{4HII}B_{4HII}$ A) Spectra of the CC-forming peptides and the CC in the presence and absence of Ni^{2+} (3:1 Ni^{2+}:His) at 20 °C in PIPPS buffer. B) Thermal unfolding of the individual peptides and the folded CC followed at 222 nm. The peptide concentration was 50 μM. The molar ellipticity was calculated using **Equation 1**. The individual peptides were measured once, while the CCs were measured in triplicate. The average melting temperature is shown in **Table 3**. (Adapted and reproduced with permission from ref. [221], published in 2018 by the Royal Society of Chemistry.)

The individual peptides A_{4HII} and B_{4HII} were largely unfolded, showing a low intensity minimum at 222 nm or a minimum of higher intensity at 200 nm-206 nm, respectively. The thermodynamic stability of the CC was studied in the absence and presence of Ni^{2+} using thermal unfolding experiments (**Figure 31B**). While the individual peptides showed no sigmoidal unfolding curve, and exhibited a melting temperature <4 °C, the CC displayed a sigmoidal unfolding transition. All measurements were performed in triplicate and the data was fitted using Global3 to obtain the melting temperature T_m (**Table 3**). The T_m of $A_{4HII}B_{4HII}$ increased from 76.4 °C to 80.2 °C in the presence of Ni^{2+} (3:1 Ni^{2+}:His). The reference CC A_4B_4 has a T_m of 83.8 °C in PIPPS in the absence of Ni^{2+}, which does not increase when Ni^{2+} is added (**Figure S5**). This shows that the insertion of His into $A_{4HII}B_{4HII}$ decreases the thermal stability by 7 °C compared to the reference CC A_4B_4. This lower thermal stability likely originates from the fact that His has a lower helix propensity when compared to the replaced Ala and Gln residue [41]. Nevertheless, His-Ni^{2+} coordination stabilized the CC thermodynamically and led to a 4 °C increase of T_m.

Table 3: Melting temperature of the coiled coils in the presence and absence of Ni^{2+}. The melting temperature [°C] was obtained from the thermal unfolding curves using Global3. The standard error of the mean (SEM) was calculated using **Equation 8**.

Sample	**$A_{4HII}B_{4HII}$**	**$A_{4HII}B_{4HII}$ +3:1 Ni^{2+}:His**	**A_4B_4**	**A_4B_4 +3:1 Ni^{2+}:His**
		Melting temperature T_m [°C]		
1	75.8	80.1	83.6	85.3
2	75.3	81.2	83.4	85.0
3	78.1	79.2	84.5	84.5
Mean ± SEM	**76.4 ± 0.6**	**80.2 ± 0.9**	**83.8 ± 0.3**	**85.0 ± 0.1**

4.2.2 Mechanical stability of $A_{4HII}B_{4HII}$ at the single molecule level in the presence and the absence of Ni^{2+}

The effect of His-Ni^{2+} coordination was further investigated using AFM-SMFS to determine changes in the energy landscape of $A_{4HII}B_{4HII}$. The individual peptides A_{4HII} and B_{4HII} were immobilized to the cantilever tip or the glass surface via a PEG-linker using the Michael addition reaction between Cys and maleimide (see **Figure 20**). Hundreds of single molecule force-extension curves were obtained from repeated approach and retract cycles at different positions of the A_{4HII}-functionalized the surface. Representative force-extension curves of $A_{4HII}B_{4HII}$, measured in the absence and presence of Ni^{2+} and after washing with EDTA, are shown in **Figure** 32. The rupture force increased by ~10 pN in the presence of 1 mM $NiCl_2$.

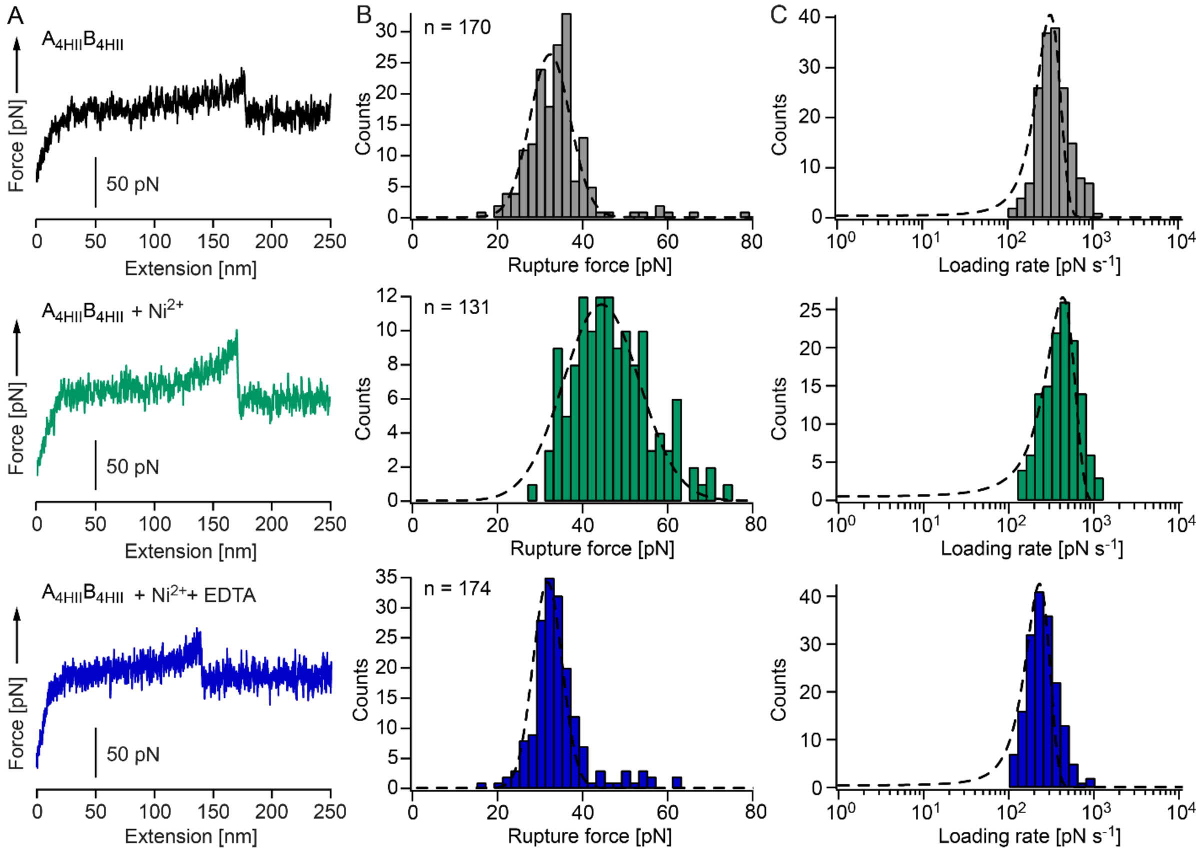

Figure 32: Single molecule force spectroscopy of $A_{4HII}B_{4HII}$. A) Representative force-extension curves of the CC, measured in the absence and presence of 1 mM Ni^{2+} and after washing with 10 mM ethylenediaminetetraacetate (EDTA). All measurements were performed in PIPPS buffer. B) Rupture force histograms, obtained at a retract speed of 400 nm s^{-1}. C) Loading rate histograms for a retract speed of 400 nm s^{-1}. The most probable rupture force and the most probable loading rate were obtained from a Gaussian fit to the histograms (dashed line). The number of force curves included in each histogram is n. (Adapted and reproduced with permission from ref. [221], published in 2018 by the Royal Society of Chemistry.)

The WLC model was fitted to the obtained force-extension curves to ensure that only single molecule pulling events are evaluated (see **Chapter 3.4**). The rupture force F_R and loading rate $\dot{F}$ histograms were fitted with a Gaussian distribution. At a retract speed of 400 nm s^{-1}, the most probable F_R was 32.3 pN in the absence of Ni^{2+} and 44.4 pN in the presence of 1 mM $NiCl_2$. This proves that the CC is stabilized against unfolding through the His-Ni^{2+} coordination bonds in the terminal heptads, as predicted for a shear loading geometry from MD simulations. The broadening of the F_R histogram in the presence of Ni^{2+} indicates that a mixture of CCs with 0, 1 or 2 Ni^{2+} coordinated might be probed in the measurement. Further increasing the $NiCl_2$

concentration did, however not increase the rupture force (**Figure S6**). Therefore, dynamic binding and unbinding of Ni^{2+} to His might lead to a distribution of CCs rupturing with 0, 1 or 2 Ni^{2+} coordinated. After washing with an excess of the metal chelating agent EDTA, the most probable F_R was reduced to 31.7 pN, indicating that the stabilization effect was fully reversible.

Dynamic SMFS provided information about the effect of His-Ni^{2+} coordination on the energy landscape of the CC. Measurements were performed at six different cantilever retract speeds and the most probable values for F_R and $\dot{F}$ were extracted (**Figure S7, Figure S8**, **Table** S2). **Figure** 33 shows a linear dependency of the most probable F_R on the logarithm of the most probable $\dot{F}$.

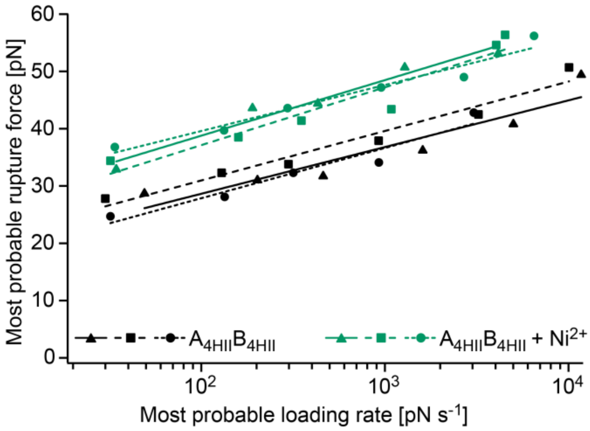

Figure 33: Dynamic single molecule force spectroscopy of $A_{4HII}B_{4HII}$. The most probable rupture forces were plotted versus the logarithm of the corresponding loading rates, collected at six different retract speeds. Three independent data sets were obtained in the absence and the presence of 1 mM Ni^{2+}, each with three different cantilevers and surfaces. The Bell-Evans model was fitted to the data (lines). The parameters for k_{off} and Δx are given in **Table 4**. (Adapted and reproduced with permission from ref. [221], published in 2018 by the Royal Society of Chemistry.)

The Bell-Evans model was fitted to three independent data sets of $A_{4HII}B_{4HII}$, collected in the absence and the presence of Ni^{2+}, and the unfolding rate at zero force k_{off} and the distance to the transition state Δx were determined (**Table 4**). In the presence of Ni^{2+}, the average k_{off} was almost 10 times lower ($2.5 \cdot 10^{-3}$ s^{-1}) than in the absence of Ni^{2+} ($11.0 \cdot 10^{-3}$ s^{-1}). This suggests that the barrier height to the transition state increased when Ni^{2+} was bound. However, there was no notable difference in the potential width Δx, when comparing the data measured in the absence (1.11 nm) and presence of Ni^{2+} (1.03 nm). This suggests that the dissociation pathway of the CC was not altered. Overall, these results show that introducing His-Ni^{2+} coordination into the terminal heptads under load stabilizes the CC thermodynamically and mechanically.

Table 4: Results of the Bell-Evans fit for $A_{4HII}B_{4HII}$, measured in the presence and absence of Ni^{2+}. Three independent measurements were performed and fitted separately. The obtained mean values for k_{off} and Δx and the standard error of the mean (SEM) are given. (Adapted and reproduced with permission from ref. [221], published in 2018 by the Royal Society of Chemistry.)

Sample	**$A_{4HII}B_{4HII}$**		**$A_{4HII}B_{4HII}$ + 1 mM Ni^{2+}**	
Parameter	k_{off} [s^{-1}]	Δx [nm]	k_{off} [s^{-1}]	Δx [nm]
Cantilever 1	$6.9 \cdot 10^{-3}$	1.10	$4.8 \cdot 10^{-3}$	0.94
Cantilever 2	$8.7 \cdot 10^{-3}$	1.16	$2.4 \cdot 10^{-3}$	0.98
Cantilever 3	$17.5 \cdot 10^{-3}$	1.08	$0.3 \cdot 10^{-3}$	1.18
Mean ± SEM	**$(11.0 \pm 3.3) \cdot 10^{-3}$**	**1.11 ± 0.02**	**$(2.5 \pm 1.3) \cdot 10^{-3}$**	**1.03 ± 0.07**

4.2.3 Reversibly tuning the stability of $A_{4HII}B_{4HII}$ cross-linked star-PEG hydrogels

To investigate if the molecular stabilization effect of His-Ni^{2+} coordination is transferred to the bulk viscoelastic properties of CC cross-linked hydrogels, $A_{4HII}B_{4HII}$ was used to assemble a polymer-peptide hybrid hydrogel. In this hydrogel, the CC acted as a self-assembling, self-healing and reversibly tunable cross-link. For hydrogel formation, the peptides A_{4HII} and B_{4HII} were coupled separately to 4-arm star-PEG-maleimide via their terminal Cys and the resulting peptide-PEG conjugates were mixed in a 1:1 ratio (see **Chapter 3.5**). Oscillatory shear rheology was used to study the viscoelastic properties of the hydrogel in the absence and the presence of Ni^{2+} (1:1 Ni^{2+}:His) and after adding an excess of EDTA. First, amplitude sweeps were performed from 1-1000 % strain to determine the LVE range of the hydrogels (**Figure S9**). The elastic storage modulus *G'* decreased at strains above 100 % while the viscous loss modulus *G"* increased, indicating cross-link rupture in all three conditions. The mechanical properties of the hydrogels fully recovered once the strain was lowered again to 1 %, suggesting that the dynamic non-covalent CC cross-links were self-healing. To prove the self-healing properties of the hydrogel in the absence and the presence of Ni^{2+}, repeated step train tests were performed (**Figure 34**). A low strain in the LVE range (1 %) was applied, followed by an instant strain-step to 1000 %. *G'* was high at low strain, indicating an intact hydrogel network. In contrast, *G*' decreased 10 times at high strain, demonstrating the failure of CC cross-links.

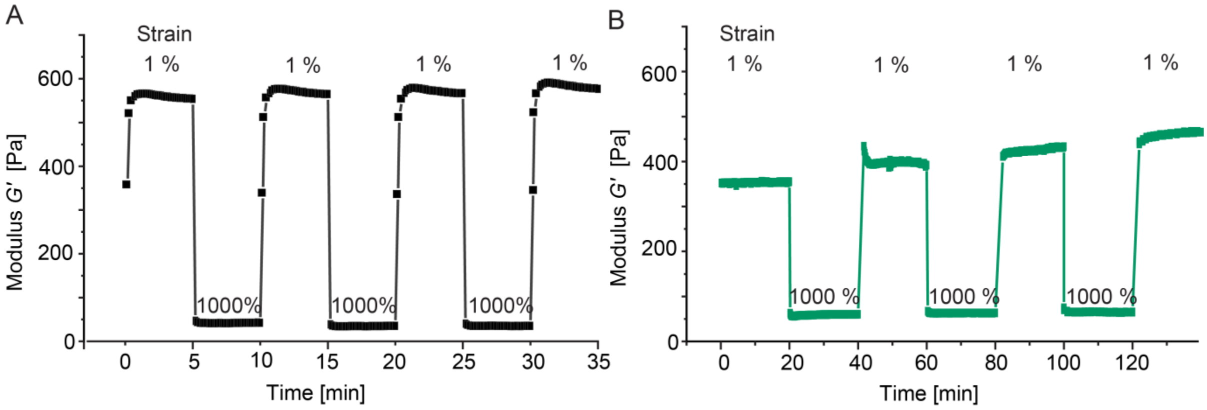

Figure 34: Self-healing test of $A_{4HII}B_{4HII}$ cross-linked hydrogels. A) Hydrogel without metal ions. B) Hydrogel with 1:1 Ni^{2+}:His. The elastic storage modulus *G'* was initially measured at 1 % strain amplitude. In the following, alternating strain steps of 1000 % and 1% strain amplitude were applied at a constant angular frequency of 10 rad s^{-1}. PIPPS buffer was used for both hydrogels. Measurements were performed at 25 °C.

The initial *G'* values recovered when the stain was lowered again to 1 % demonstrating the self-healing of the hydrogel. The cycle of cross-link failure and self-healing was repeated four times. In the presence of Ni^{2+}, *G'* slightly increased with each cycle. This phenomenon can originate from an unequal distribution of Ni^{2+} in the hydrogel, which was added after formation of the hydrogel. Each cycle at high strain amplitude, where the network was not intact, could lead to a better mixing of Ni^{2+} in the hydrogel, enabling more His-Ni^{2+} coordinating CCs to form.

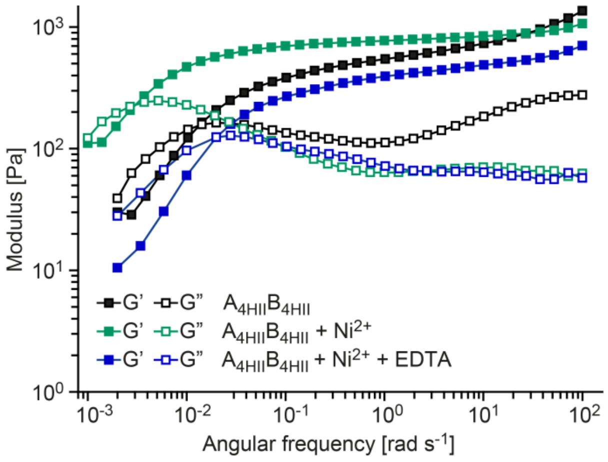

Figure 35: Frequency sweeps of $A_{4HII}B_{4HII}$ cross-linked hydrogels. Measurements were performed at a constant strain amplitude of 1 % in PIPPS buffer in the absence of metal ions, in the presence of 1:1 Ni^{2+}:His and with 1:1 Ni^{2+}:His + 10 mM ethylenediaminetetraacetate (EDTA). The relaxation time τ was calculated from the crossover frequency (ω_c) of the elastic storage modulus *G'* and the viscous loss modulus G'' ($\tau = 1/\omega_c$). Measurements were performed at 25 °C. (Adapted and reproduced with permission from ref. [221], published in 2018 by the Royal Society of Chemistry.)

Frequency sweeps, performed at a constant strain amplitude of 1 % provided insights into the dynamic behavior of the hydrogel (**Figure 35**). The relaxation time τ_{fs} of the hydrogel, measured in the absence and presence of Ni^{2+} and after adding an excess of EDTA was determined from the crossover frequency ω_c where *G'* and *G"* intersect (see **Equation 29**). It provides information about the average lifetime of the CC cross-links in the hydrogel. Without metal ions, the relaxation time was 92 s. A three-fold increase in τ_{fs} was observed in the presence of Ni^{2+} (258 s), following the same trend as k_{off} in AFM-SMFS.

Table 5: Relaxation times of $A_{4HII}B_{4HII}$ cross-linked hydrogels. Shown are the values obtained from three independent frequency sweeps (**Figure 35**, **Figure S10**), including the mean ± standard error of the mean (SEM). (Adapted and reproduced with permission from ref. [221], published in 2018 by the Royal Society of Chemistry.)

Sample	**$A_{4HII}B_{4HII}$**	**$A_{4HII}B_{4HII}$ + 1:1 Ni^{2+}:His**	**$A_{4HII}B_{4HII}$ + Ni^{2+} + EDTA**
		Relaxation time τ_{fs} [s]	
Hydrogel 1	72	270	50
Hydrogel 2	135	286	33
Hydrogel 3	70	217	48
Mean ± SEM	**92 ± 12**	**258 ± 36**	**44 ± 4**

Furthermore, the stabilizing effect was fully reversible when adding EDTA (44 s) and the relaxation time was even reduced to half of the initial relaxation time of $A_{4HII}B_{4HII}$. A reason might be impurities of transition metal ions, originating from the synthesis of the hydrogel or the buffer components. Traces of metal ions can bind to a fraction of the CCs and increase the relaxation time of the hydrogel without adding further metal ions. In summary, stabilizing single CCs with His-Ni^{2+} coordination bonds directly translates into tunable viscoelastic properties of the bulk hydrogel.

4.2.4 Tuning hydrogel relaxation time with different metal ions

In order to expand the tunable range of relaxation times, I tested the effect of Cu^{2+}, Co^{2+} and Zn^{2+}-coordination on the hydrogel properties. Since metal ions differ in their preferred coordination number, coordination geometry [99,101] and binding constants [81], I investigated the metal ion coordination mode and the effect on the structure of $A_{4HII}B_{4HII}$ using Raman and CD spectroscopy (**Figure 36**).

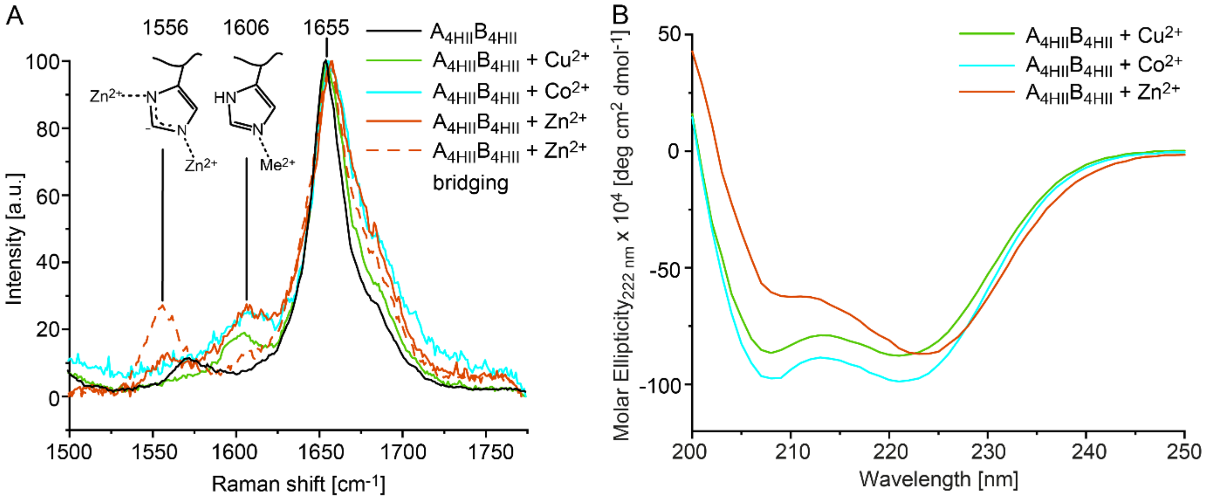

Figure 36: Spectroscopic characterization of $A_{4HII}B_{4HII}$ in the presence of Cu^{2+}, Co^{2+} and Zn^{2+}. A) Raman spectra of the CC in the presence of different metal ions (1:2 M^{2+}:His). For this measurement, CC-forming peptides with terminal Cys residues were used. The samples were prepared in solution and dried on a quartz glass slide. The pH was adjusted to ~8 with NaOH before the metal ions were added. B) Circular dichroism spectra of the CC (no terminal Cys) in the presence of different metal ions (3:1 M^{2+}:His). The measurements were performed at 20 °C in PIPPS buffer. The peptide concentration was 50 µM. The molar ellipticity was calculated using **Equation 1**.

The Raman spectra of the CC, measured in the presence of Cu^{2+}, Co^{2+} or Zn^{2+}, showed an amide I peak at 1655 cm^{-1}. This peak is assigned to α-helical secondary structure. In the presence of Cu^{2+} or Co^{2+}, the His-M^{2+} coordination peak at 1606 cm^{-1} was comparable to the peak in the presence of Ni^{2+} (1604 cm^{-1}). In the presence of Zn^{2+}, the amide I peak was shifted to 1657 cm^{-1}, which is also assigned to α-helices. For Zn^{2+}-coordination, an additional peak was observed at 1556 cm^{-1}, which is assigned to His coordinating two metal ions in a 'bridging' conformation (**Figure 36A**) [71]. In some areas of the Zn^{2+}-containing peptide-film the bridging peak was the most prominent peak. This shows that Ni^{2+}, Cu^{2+} and Co^{2+} are coordinated in a similar geometry, while Zn^{2+}-coordination can also occur in the bridging mode. Bridging has been found previously in mussel byssus-derived peptide films [222].

CD spectroscopy of $A_{4HII}B_{4HII}$ revealed that coordination of Cu^{2+} or Co^{2+} did not alter the secondary structure of the CC (**Figure 36B**). In contrast, the minimum at 222 nm shifted to 225 nm and the intensity of the second minimum at 208 nm decreased in intensity when Zn^{2+} was coordinated. Similar CD spectra have been observed for CC-forming fibers [163,181,223] or α-helical aggregates [224,225]. The thermal unfolding curves (**Figure S11**) revealed a T_m of 78.9 °C for Co^{2+}-coordination, which is 2.5 °C higher than the T_m in the absence of metal ions (**Table 3**). In the presence of Cu^{2+} or Zn^{2+}, T_m decreased to 47.9 °C and 41.0 °C, respectively. In both samples, the solution was slightly opaque. This suggests the formation of aggregates or fibers, which impaired the proper analysis of the thermal unfolding experiments.

Amplitude sweeps of $A_{4HII}B_{4HII}$ cross-linked hydrogels showed that the LVE range did not change in the presence of Cu^{2+} and Co^{2+} (1-100 %); however, in the presence of Zn^{2+} it only spanned a range of 1-50 % (**Figure S12**). Frequency sweeps revealed that Cu^{2+} (τ_{fs} = 189 s) and Co^{2+}-coordination (τ_{fs} = 139 s) increased the relaxation time of the CC cross-link compared to the hydrogel without metal ions (τ_{fs} = 92 s), but the effect was smaller when compared to Ni^{2+} (τ_{fs} = 258 s) (**Figure 37**). When Zn^{2+} was added to the hydrogel, a 6-fold increase in the storage modulus was observed and the hydrogel could no longer be described with the Maxwell model (no cross-over of *G'* and *G"* at the maximum of *G"*). Aggregation is expected to introduce additional cross-links, which may further cause changes in network topology. Even though the cross-over in *G'* and *G"* is absent, a maximum in *G"* is still visible at 10^{-2} rad s^{-1}. This may indicate the presence of cross-links that relax on a similar timescale as the cross-links formed in the Cu^{2+} and Co^{2+}-coordinating hydrogels. The second maximum at 10 rad s^{-1}, seen for Zn^{2+} (and also for Co^{2+}) coordinating hydrogels likely originates from the formation of B_{4HII} homodimers, which were previously observed in hydrogels without metal ions.

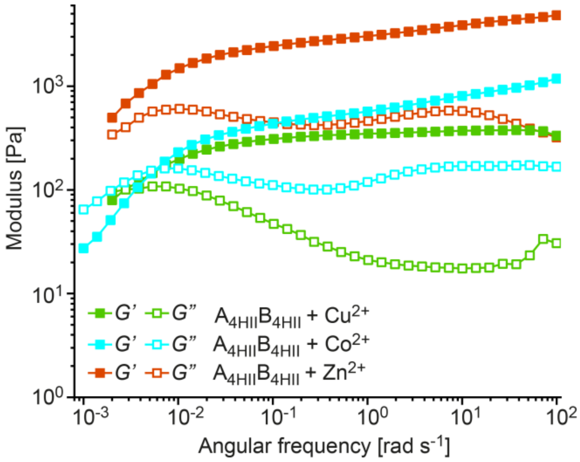

Figure 37: Frequency sweep of $A_{4HII}B_{4HII}$ cross-linked hydrogels in the presence of Cu^{2+}, Co^{2+} or Zn^{2+}. Measurements were performed at 25 °C in PIPPS buffer at a constant strain amplitude of 1 % with 1:1 M^{2+}:His. The relaxation time τ was calculated from the crossover frequency (ω_c) where the elastic storage modulus *G'* and the viscous loss modulus *G"* intersect ($\tau = \omega_c^{-1}$).

Taken together, Cu^{2+} and Co^{2+}-coordination exhibit a smaller stabilization effect when compared to Ni^{2+}-coordination. In contrast, Zn^{2+}-coordination seems to promote interactions between CCs (inter-CC). This may cause CC assembly in to higher-order structures and a concomitant increase of *G'*. Similarly, recent investigations on mussel byssal threads revealed that intermolecular His-Zn^{2+} coordination is essential for self-assembly and self-healing [165].

4.3 Intermolecular His-metal coordination to induce higher-order coiled coil assembly

His-Zn^{2+} coordination was found to induce the aggregation of the CC $A_{4H\parallel}B_{4H\parallel}$ most probably via the promotion of inter-CC interactions. The higher-order assembly of $A_{4H\parallel}B_{4H\parallel}$ in the presence of Zn^{2+} had a significant effect on the relaxation time of the hydrogels, which is useful to increase the tunable range of viscoelastic properties. To decouple the effects of intramolecular and intermolecular His-Zn^{2+} coordination, I bioengineered three His into the solvent-exposed *f* positions of A_4B_4. This was expected to promote His-Zn^{2+} coordination between CCs perpendicular (⊥) to their helical axis (**Table 2**). The peptides $A_{4H\perp}$ and $B_{4H\perp}$ were prepared in house using SPPS. The results of the analytical HPLC as well as the MALDI spectra are presented in the appendix (**Figure S1** to **Figure S4**).

4.3.1 His-Zn^{2+} coordination mediated higher-order assembly of $A_{4H\perp}B_{4H\perp}$

To investigate the secondary structure of CC $A_{4H\perp}B_{4H\perp}$ and the effect of His-Zn^{2+} coordination, CD spectra were obtained. $A_{4H\perp}B_{4H\perp}$ shows a typical α-helical structure in the absence of metal ions. The spectrum displays two minima at 222 nm and 208 nm and a $r_{222/208}$ of 1.10 (**Figure 39**). In the absence of metal ions, the melting temperature of $A_{4H\perp}B_{4H\perp}$ was 64.7 °C (**Table S3**). In the presence of Zn^{2+}, a shift of the minimum from 222 nm to 225 nm was observed, while the minimum at 208 nm decreased in intensity.

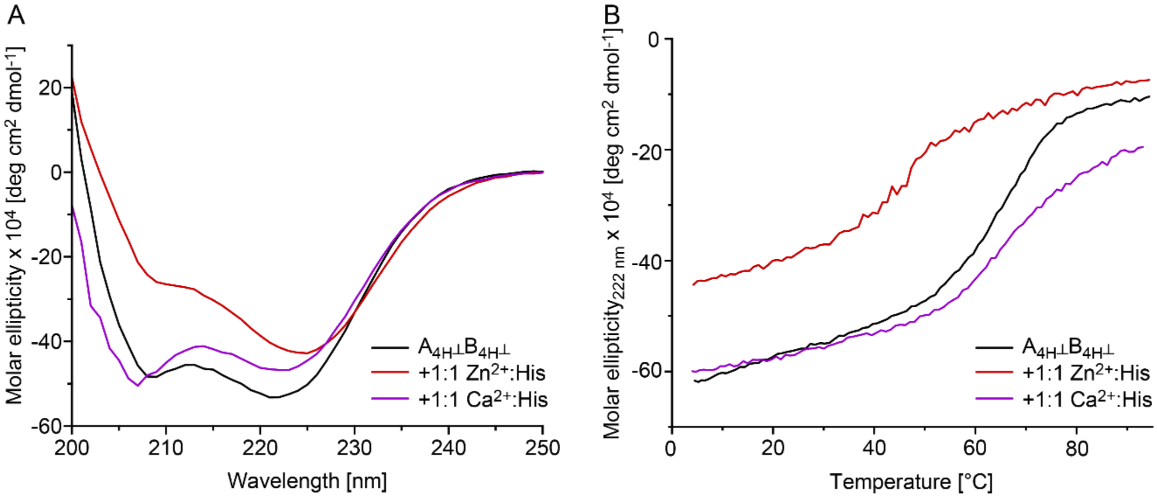

Figure 38: Circular dichroism spectra of $A_{4H\perp}B_{4H\perp}$. A) Spectra of the CC, measured in the presence and absence of Zn^{2+} and Ca^{2+} (1:1 M^{2+}:His) at 20 °C in PIPPS buffer. B) Thermal unfolding of the CC followed at 222 nm. The peptide concentration was 50 µM. The molar ellipticity was calculated using **Equation 1**. The mean melting temperature can be found in **Table S3**. (Figure 38A was adapted and reproduced from ref. [226].)

Exactly the same effect was also found for $A_{4H\parallel}B_{4H\parallel}$, when the CC was measured in the presence of 1:1 Zn^{2+}:His. This is a first confirmation that Zn^{2+} favors the formation of inter-CC interactions, which leads to the formation of α-helical aggregates or fibers [181,223,224]. In the presence of Zn^{2+}, the melting temperature (44.4 °C) could not be determined properly since the sample turned slightly opaque. To investigate if other divalent ions can also induce higher-order assembly, 1:1 Ca^{2+}:His was added as a negative control since it only interacts weakly with His [227]. The CC maintained an α-helical secondary structure in the presence of Ca^{2+}; however, the minimum at 208 nm shifted to 206 nm and $r_{222/208}$ decreased to 0.97. This small destabilizing effect might result from the interaction of Ca^{2+} with Glu in $A_{4H\perp}$, interfering with the ionic interactions between Glu and Lys in the *e* and *g* positions. Despite this possible interaction, the melting temperature did not change in the presence of Ca^{2+} (63.1 °C).

The individual peptides showed a random coil structure in the absence of metal ions and with 1:1 Ca^{2+}:His (**Figure S13**). In the presence of 1:1 Zn^{2+}:His, α-helical assemblies were observed for both peptides. Therefore, it is not possible to unambiguously conclude if Zn^{2+} cross-linked CC assemblies or aggregated mixtures of individual peptides form in the $A_{4H\perp}B_{4H\perp}$ sample. However, the second possibility requires the dissociation of the thermostable CC induced by Zn^{2+}-coordination, which is considered unlikely.

The secondary structure of the CC and the His-metal coordination modes were further investigated using Raman spectroscopy (**Figure 39**). The amide I band showed that the CC has an α-helical secondary structure. In the presence of Zn^{2+}, the amide I peak shifted slightly to 1654 cm^{-1} and a shoulder appeared at 1680 cm^{-1}. This shoulder was observed previously in keratin, the predominantly α-helical CC building block of hair, where it was assigned to β-sheets or unordered structures [22,228]. I propose that this change in the spectrum originated from the distortion of the helices upon aggregation. Similar to $A_{4H\parallel}B_{4H\parallel}$, two peaks at 1556 and 1605 cm^{-1} are present after adding Zn^{2+} to $A_{4H\perp}B_{4H\perp}$. This reveals that Zn^{2+} was coordinated by one or both nitrogen atoms of the imidazole side chain of His. The addition of Ca^{2+} did not result in a shift of the peak for deprotonated His at 1574 cm^{-1} and only a small additional peak appeared at 1594 cm^{-1}. This showed that only a small amount of Ca^{2+} was weakly coordinated and most of the His was free.

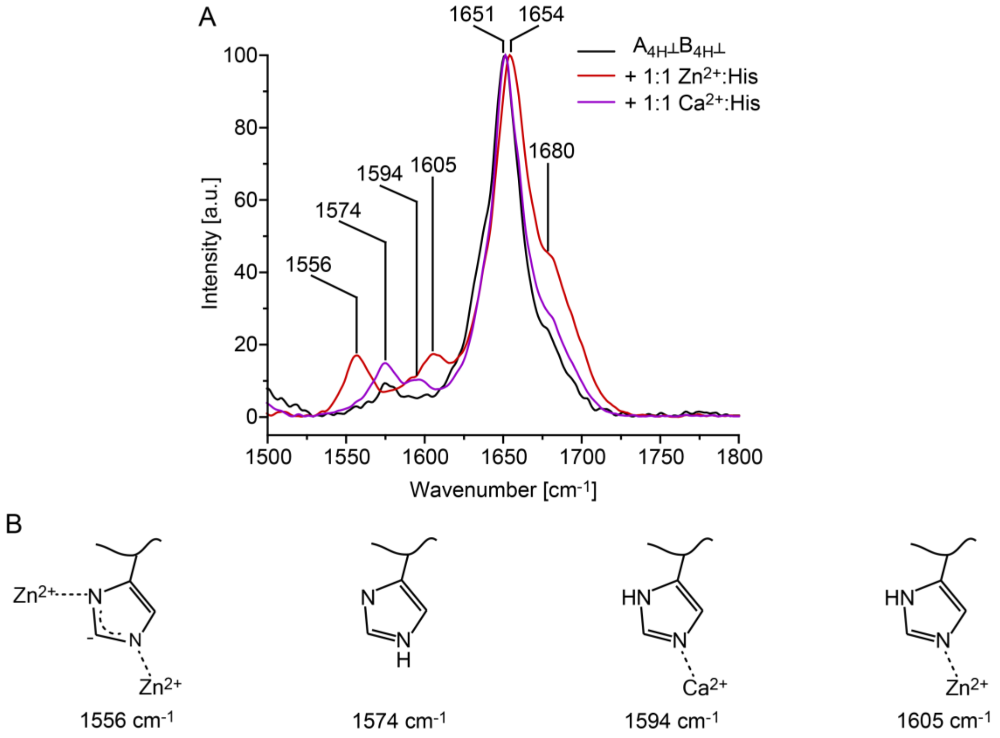

Figure 39: Raman spectroscopy of $A_{4H}\perp B_{4H}\perp$. A) Raman spectra. The pH was adjusted to ~8 with NaOH. For metal coordination, $ZnCl_2$ or $CaCl_2$ was added in a 1:1 M^{2+}:His ratio. Samples were prepared in solution and dried on a quartz glass slide. The spectra were normalized to the maximum of the amide I band. B) His peaks assigned to the different protonation or coordination states. (This figure was adapted and reproduced from ref. [226].)

In order to gain more detailed insight into the structure of the CC assemblies in the presence of Zn^{2+}, wide-angle X-ray scattering was performed on $A_{4H}\perp B_{4H}\perp$ lyophilized with and without 1:1 Zn^{2+}:His (prepared at pH 7.4). No structural information could be obtained from the solid samples, however, probably due to the lack of periodicity in the sample. The Zn^{2+} cross-linked aggregates are thus expected to be random and lack regularly aligned a-helices. To account for a possible change in the structure of the CC assemblies during lyophilization, measurements in the fully hydrated state (>95 % water) were considered, but turned out to be too challenging.

4.3.2 Tuning hydrogel properties with intermolecular His-Zn^{2+} coordination as a second cross-linking mode

The formation of hierarchically self-assembled materials with self-healing properties is a principle often found in Nature. Reminiscent of the His-rich termini of the building blocks in byssal threads, the CC $A_{4H}\perp B_{4H}\perp$ formed higher-order aggregates via intermolecular His-Zn^{2+} coordination. It was reported previously that the relaxation time of a hydrogel is not solely determined by the cross-link used. It also depends on the higher-order structure of the polymer network [123]. Here, I investigated how the higher-order assembly of the CC cross-links affects the viscoelastic properties of a star-PEG hydrogel. Interestingly, when adding 1:1 Zn^{2+}:His, the hydrogel expelled some water, giving a first indication of a change in the network structure. To allow the structure to equilibrate, the hydrogels were incubated for 4 h at 4 °C before any rheology experiments were started. The viscoelastic properties of the CC cross-linked hydrogel were studied in the presence of different His-Zn^{2+} ratios and with 1:1 Ca^{2+}:His as a negative control. First, the self-healing ability of the $A_{4H\perp}B_{4H\perp}$ cross-linked hydrogel was tested in the absence and presence of 1:1 Zn^{2+}:His (**Figure 40**). The initial *G'* (0.1 % strain) of the hydrogel containing 1:1 Zn^{2+}:His was more than seven times (~4000 Pa) higher when compared to the hydrogel without metal ions (~500 Pa). This suggests that the effective cross-link density increased from 0.2 mol m^{-3} to 1.6 mol m^{-3} in the presence of Zn^{2+}. In the absence of metal ions, *G'* fully recovered after hydrogel failure at 1000 % strain. In contrast, *G'* only partially recovered in the presence of 1:1 Zn^{2+}:His. The part of the cross-links that self-healed after the first high-strain interval also reformed when the strain protocol was repeated (**Figure 40B**).

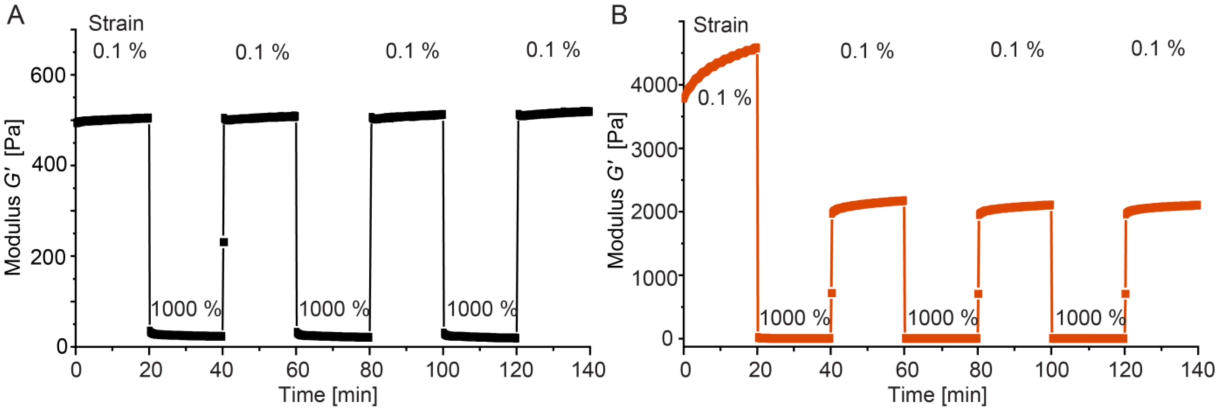

Figure 40: Self-healing test of the $A_{4H\perp}B_{4H\perp}$ cross-linked hydrogel. A) Hydrogel without metal ions. B) Hydrogel with 1:1 Zn^{2+}:His. The elastic shear modulus *G'* was initially measured at 0.1 % strain amplitude. Then alternating strain steps of 1000 % and 0.1% strain amplitude were applied at a constant angular frequency of 10 rad s^{-1}.Measurements were performed at 25°C in PIPPS buffer.

To investigate time-dependent self-healing in more detail, amplitude sweeps were performed four times in the absence and the presence 1:1 Zn^{2+}:His. These measurements showed a LVE range from 0.1-100 % and 0.1-50 %, respectively (**Figure S14**). The time-dependent self-healing of the hydrogel in the presence of Zn^{2+} is displayed in **Figure 41**. The hydrogel only recovered ~80 % of the initial *G'* after the first amplitude sweep. When allowed to rest for 1 h at 25 °C, more cross-links reformed and ~90 % of the initial *G'* recovered: This suggests that a constant fraction of the intermolecular cross-links reformed small aggregates quickly;

however, the growth of bigger Zn^{2+} cross-linked aggregates was time-dependent. A similar time-dependent self-healing behavior was also reported for mussel byssal threads [17]. Amplitude sweeps further revealed that Zn^{2+}-induced aggregation is fully reversible when adding an excess of EDTA. Aggregation is further entirely absent when adding 1:1 Ca^{2+}:His (**Figure S15**).

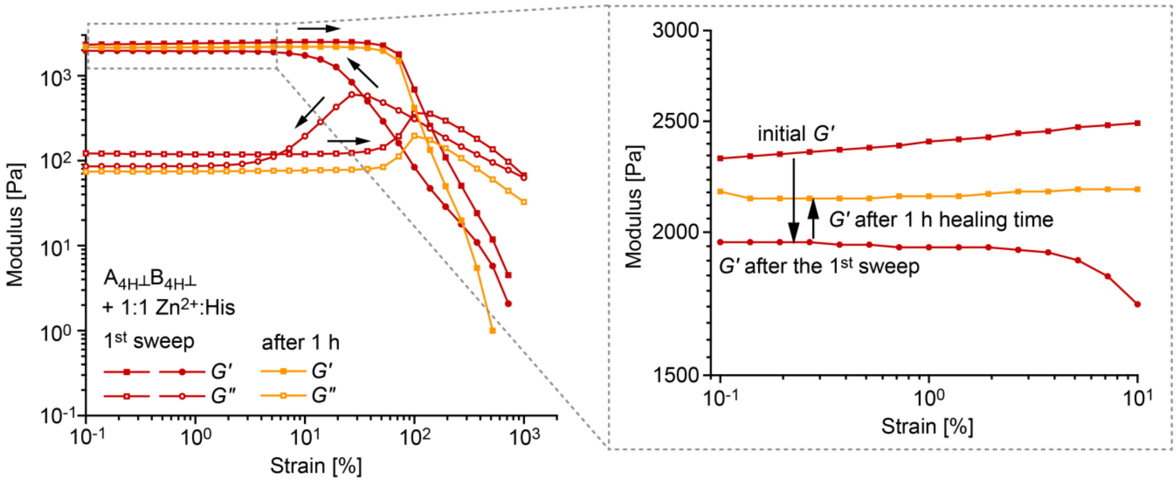

Figure 41: Amplitude sweep of the $A_{4H}{\perp}B_{4H}{\perp}$ hydrogel with 1:1 Zn^{2+}:His. Amplitude sweeps were performed at a constant angular frequency of 10 rad s^{-1}, changing the strain amplitude from 0.1 to 1000 % and vice versa. After the first amplitude sweep, the hydrogel only recovered ~80 % of its initial *G'*. The hydrogel was allowed to rest for 1 h after four amplitude sweeps had been performed (**Figure S13**). Then, an additional amplitude sweep was performed and revealed the recovery of *G'* to ~90% of the initial value. Measurements were performed at 25 °C in PIPPS buffer. (This figure was adapted and reproduced from ref. [226].)

Frequency sweeps were used to study the dynamic mechanical properties of the $A_{4H}{\perp}B_{4H}{\perp}$ cross-linked hydrogels. In the absence of metal ions, the mean relaxation time of the hydrogel was 11.2 s (**Figure 42A, Figure S16, Table 6**). When adding Zn^{2+} at a ratio of 1:1 Zn^{2+}:His, the hydrogel was elastic-like over the whole frequency range measured, without a crossover of *G'* and *G"* (τ_{fs} > 1000 s). Thus, the hydrogel properties can be switched from viscoelastic to elastic-like when implementing inter-CC His-Zn^{2+} coordination bonds. Also in this experiment, the formation of the Zn^{2+} cross-linked aggregates was fully reversible when adding an excess EDTA (τ_{fs} = 5.9 s). The relaxation time of the hydrogel containing 1:1 Ca^{2+}:His (τ_{fs} = 4.7 s) was comparable to the hydrogel without metal ions.

To assess if His-Zn^{2+} coordination can be used to precisely tune the relaxation time, $A_{4H}{\perp}B_{4H}{\perp}$ hydrogels with different His-Zn^{2+} ratios were prepared. The hydrogel behaved elastic-like at a ratio of 1:1 Zn^{2+}:His. Also, at 1:2 Zn^{2+}:His and 1:10 Zn^{2+}:His no crossover of *G'* and *G"* was observed, but a small maximum at ~0.02 rad s^{-1} emerged (**Figure 42B**). Lowering the ratio to 1:20 Zn^{2+}:His, yielded a clear intersection of *G'* and *G"* (τ_{fs} = 51.8 s). When the Zn^{2+}:His ratio was lowered to 1:100, the relaxation time was 10 s, which was comparable to the relaxation time of the hydrogel without metal ions. Further frequency sweeps at ratios of 1:5, 1:15 and 1:50 Zn^{2+}:His revealed that the relaxation time of the hydrogel can be controlled in a precise stepwise manner (**Figure S18A**). In contrast, the effect of the Zn^{2+}:His ratio on the LVE range of the hydrogels was much smaller (**Figure S17, Figure S18**).

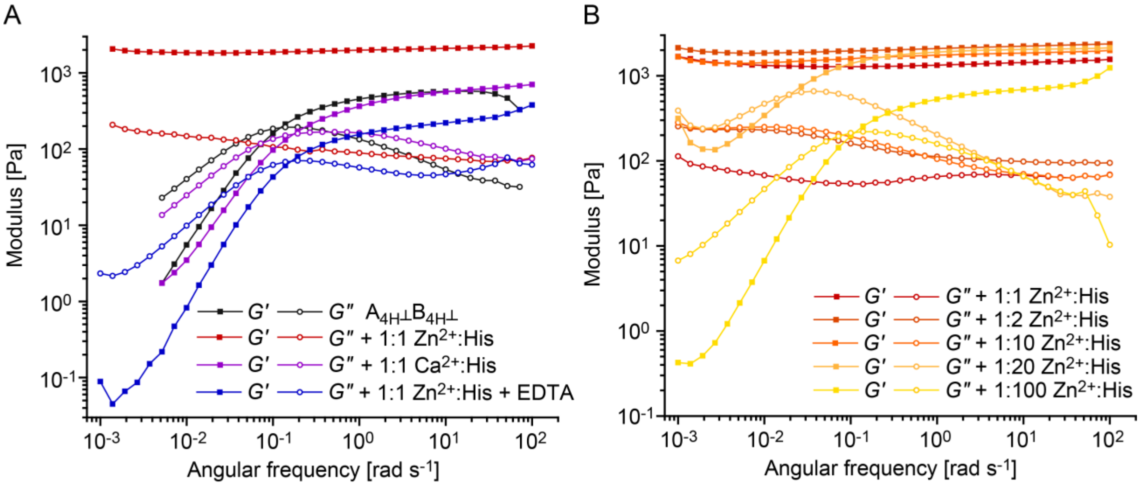

Figure 42: Frequency sweeps of $A_{4H\perp}B_{4H\perp}$ cross-linked hydrogels. A) Measurements in the absence of metal ions, in the presence of 1:1 Zn^{2+}:His, 1:1 Ca^{2+}:His and with 1:1 Zn^{2+}:His + 10 mM ethylenediaminetetraacetate (EDTA). B) Measurements in the presence of different Zn^{2+}:His ratios. All measurements were performed in PIPPS buffer at 25 °C. The relaxation time τ was calculated from the crossover frequency (ω_c) where the elastic storage modulus *G′* and the viscous loss modulus *G″* intersect ($\tau = \omega_c^{-1}$). (This figure was adapted and reproduced from ref. [226].)

The CD spectra of the individual peptides $A_{4H\perp}$ and $B_{4H\perp}$ showed aggregate formation in the presence of Zn^{2+}. It was thus tested if Zn^{2+} cross-linked hydrogels also form with the individual star-PEG-$A_{4H\perp}$ and star-PEG-$B_{4H\perp}$ conjugates. Hydrogel formation was successful when incubating star-PEG-$A_{4H\perp}$ and star-PEG-$B_{4H\perp}$ with 1:1 Zn^{2+}:His ratio. In contrast to the $A_{4H\perp}B_{4H\perp}$ cross-linked hydrogels, no hydrogels formed when lowering the ratio to 1:10 for star-PEG-$A_{4H\perp}$ and 1:5 for star-PEG-$B_{4H\perp}$ (**Figure S19**). In the Glu-rich $A_{4H\perp}$, Zn^{2+}-coordination seemed to induce α-helix formation, an effect that was also described for a helix-loop-helix motif introduced by Selengard et al. [135]. Based on these results, it can be concluded that the contribution of the CC as a cross-link and rigid backbone for intermolecular His-Zn^{2+} coordination is essential for hydrogel formation. Intermolecular His-Zn^{2+} coordination acts as a second cross-linking mode, which requires the presence of $A_{4H\perp}B_{4H\perp}$. CC cross-links and their controlled higher-order assembly thus form the basis for switching the hydrogel properties from viscoelastic to elastic-like in a stepwise fashion.

Table 6: Relaxation times obtained for $A_{4H}{\perp}B_{4H}{\perp}$ hydrogels. Shown are the values obtained from three independent frequency sweeps, including the mean ± standard error of the mean (SEM). (This table was adapted and reproduced from ref. [226].)

Sample	**$A_{4H}{\perp}B_{4H}{\perp}$**	**$A_{4H}{\perp}B_{4H}{\perp}$ + 1:1 Zn^{2+}:His**	**$A_{4H}{\perp}B_{4H}{\perp}$ + 1:1 Ca^{2+}:His**	**$A_{4H}{\perp}B_{4H}{\perp}$ + 1:1 Zn^{2+}:His + EDTA**
		Relaxation time τ_{fs} [s]		
Hydrogel 1	7.2	>1000	5.2	5.2
Hydrogel 2	7.2	>1000	5.2	7.2
Hydrogel 3	19.3	>1000	3.7	5.2
Mean ± SEM	**11.2 ± 4.0**	**-**	**4.7 ± 0.5**	**5.9 ± 0.7**

Stress-relaxation experiments were performed for the hydrogels in the presence of 1:1, 1:10 and 1:20 Zn^{2+}:His to obtain the relaxation time. This was not accessible in the frequency sweeps, as drying of the hydrogel did not allow for extension of the measurement time to reach lower frequencies. A step-strain of 10 % was applied to the hydrogel and the relaxation of the sample was monitored over time. **Figure 43** reveals that the metal-free hydrogel fully relaxed in 100 s, while the hydrogel with 1:20 Zn^{2+}:His only relaxed after 10,000 s. The hydrogels with 1:10 Zn^{2+}:His and 1:1 Zn^{2+}:His did not fully relax on the timescale of the experiment.

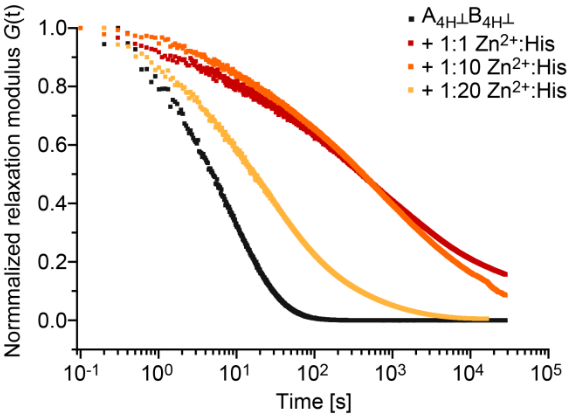

Figure 43: Stress relaxation of $A_{4H}{\perp}B_{4H}{\perp}$ hydrogels. After applying a step strain of 10 %, stress relaxation was measured for hydrogels prepared in the absence of metal ions and with 1:1, 1:10 and 1:20 Zn^{2+}:His. The fitted curves are plotted in **Figure S20**. Measurements were performed at 25 °C in PIPPS buffer. (This figure was adapted and reproduced from ref. [226].)

Kohlrausch's stretched exponential relaxation model (**Equation 30**) was fitted to the relaxation curves (**Figure S20**). From the fit, a relaxation time of τ_{sr} = 6.6 s was obtained for the hydrogel without metal ions, while τ_{sr} = 34.4 s for the hydrogel prepared with 1:20 Zn^{2+}:His. Both values are highly similar to the relaxation times obtained from the frequency sweeps (**Table S4**). In the presence of 1:10 and 1:1 Zn^{2+}:His, τ_{sr} was 1272 s and 1244 s, respectively.

Materials with physically constrained cross-links are often described with Kohlrausch's stretched exponential relaxation model. The shape of the fit is governed by the parameter α, which decreases from 0.59 in the hydrogel without metal ions to 0.24 in the hydrogel with 1:1 Zn^{2+}:His. The relationship between α and the relaxation process of the hydrogel is not fully understood. The two current hypotheses to explain the underlying molecular processes are:

1. For hydrogels with one distinct relaxation time, α = 1 (single exponential). For hydrogels with several relaxation times α decreases and the relaxation curve is described with a stretched exponential ($0 < \alpha \leq 1$).

2. At the molecular level the relaxation of the hydrogel always follows a stretched exponential, since there are cooperative molecular motions and network entanglements present [229].

If the first hypothesis holds, α is expected to be 1 in the metal-free $A_{4H\perp}B_{4H\perp}$ cross-linked hydrogel, since only single CC cross-links with a distinct relaxation time are expected to be present. The observation that α = 0.59 indicates that cooperative molecular motions and entanglements played a role even if only well-defined single CC cross-links should be present. The α-value deceased to 0.24 with increasing Zn^{2+}:His ratio, showing that the distribution of relaxation timescales increased even further. This effect can be caused by the formation of Zn^{2+} cross-linked CC aggregates, varying in size and number of metal coordination bonds. In the case of Zn^{2+} cross-linked aggregates, the relaxation and reformation of cross-links is restricted by the network architecture and the PEG chain length. This may cause additional heterogeneities in the hydrogel network and both processes are assumed to contribute to the parameter α.

It remains to be investigated if higher-order His-metal metal coordination bonds or the CC cross-links themselves break when strain was applied. SMFS experiments could not be used to study the mechanical stability of these different interactions as the CC peptides aggregated on the surface in the presence of Zn^{2+}. A rupture force of 28 pN was reported for Zn^{2+}:His at a loading rate of 500 nm s^{-1} [82]. This is in the same range where the characterized $A_{4H\parallel}B_{4H\parallel}$ ruptured. To study the failure mechanism of the hydrogel in the absence and presence of Zn^{2+}, the CC could be equipped with a fluorescent-label to self-report its state in the hydrogel (CC formed vs. free CC-forming peptides).

4.4 Monitoring the state of coiled coil cross-links with a FRET-based reporter system

The development of reversibly tunable, self-reporting molecular force sensors is of high interest for monitoring the structure and failure of cross-links in hydrogels as well as for investigating cell-matrix interactions. Coiled coils are excellent candidates for the development of force sensors, since they are mechanically and thermodynamically tunable and occur in a wide range of natural biomaterials. In order to optically monitor the state of the well-characterized model CC A_4B_4, a FRET pair was introduced [46,56]. As a first approach, the Lys of A_4 was labeled with carboxyfluorescein (A_{4CF}) and the N-terminus of B_4 was labeled with tetramethylrhodamine (B_{4TR}) (**Chapter 2**). FRET between the carboxyfluorescein donor and the tetramethylrhodamine acceptor was intended to facilitate the optical readout of the CC state, since FRET can only occur in the folded CC. The labeled peptides were purchased from a commercial supplier with a purity >95 % (Proteogenix). In the following paragraph, the secondary structure and the melting temperature of $A_{4CF}B_{4TR}$ was investigated with CD spectroscopy.

4.4.1 Thermodynamic stability of the fluorescently labeled $A_{4CF}B_{4TR}$

It is described in the literature that fluorescence labeling can alter CC stability or even induce aggregation [230]. I used CD spectroscopy to investigate if fluorophore attachment affected the secondary structure and thermodynamic stability of the CC. The spectrum of $A_{4CF}B_{4TR}$ showed a typical α-helical signature with two minima at 222 nm and 208 nm and $r_{222/208} = 1.06$, indicating that the peptides form a CC (**Figure 44**). The individual A_{4CF} peptide showed a random coil secondary structure, while B_{4TR} also exhibited the typical minima for α-helical structure. The reported melting temperature of A_4B_4 is 80.5 °C [56]. The mean melting temperature of $A_{4CF}B_{4TR}$ was determined to be 80.0 °C (**Figure 44, Table S5**), proving that the fluorophore labeling did not interfere with CC formation. Interestingly, coupling of tetramethylrhodamine increased the T_m of B_{4TR} from 25.3 °C [46] to 45.3 °C, while the T_m of A_{4CF} was <4 °C with and without carboxyfluorescein. The weak B_{4TR} homodimer might be stabilized as a result of stacking interactions between tetramethylrhodamine molecules, which are coupled at the N-terminus of B_{4TR} [231].

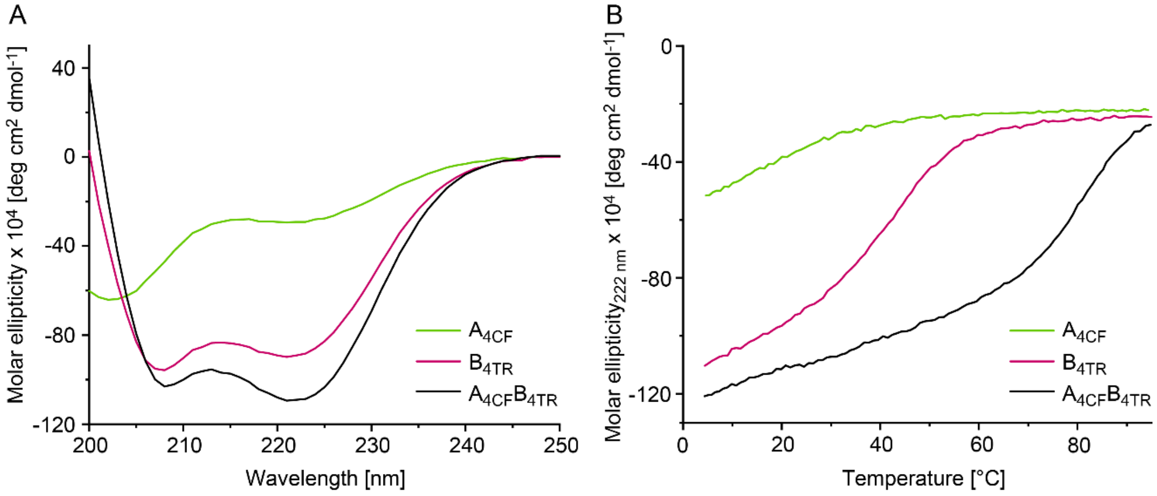

Figure 44: Circular dichroism spectra of the fluorescently labeled $A_{4CF}B_{4TR}$. A) Spectra of A_{4CF}, B_{4TR} and the CC, measured at 20 °C in PBS. B) Thermal unfolding of the CC and the individual CC-forming peptides followed at 222 nm. The peptide concentration was 50 µM. The molar ellipticity was calculated using **Equation 1**. Individual peptides were measured once. The CC was measured three times and the mean melting temperature is shown in **Table S5**.

In summary, the results show that the fluorophores did not affect the secondary structure and the thermodynamic stability of the CC. Therefore, it is assumed that the fluorophores do not significantly influence the energy landscape of the previously characterized CC A_4B_4 [56].

4.4.2 Förster resonance energy transfer (FRET) efficiency of $A_{4CF}B_{4TR}$

In order to monitor the state of CC cross-links in hydrogels with a fluorescent readout, A_4B_4 was labeled with the FRET pair carboxyfluorescein and tetramethylrhodamine. The theoretical FRET efficiency E_{FRET} of the fluorophores was calculated according to **Equation 9** with a Förster radius of 55 Å at pH 7 [145,232]. The distance between the fluorophores was approximated from the labeling positions of the fluorophores in the CC structure, which was predicted using CC-builder 2.0 [49]. Since the molecular structure of the predicted CC did not include the fluorophores, the distance r between the attachment points of the FRET pair was measured in Pymol (r = 25.7 Å). Inserted into **Equation 9**, the theoretical FRET efficiency E_{FRET} in the native CC should be 99 %. However, the distance between the centers of the fluorophore molecules is certainly higher than 25.7 Å as the linkers between the fluorophores and the CC were not considered. Further, the rotational flexibility of the fluorophores is unknown. Thus, the FRET real efficiency is expected to be lower than 99 %.

Experimentally, the FRET efficiency was determined from fluorescence emission spectra of the donor (CF, excited at 475 nm) in the presence and absence of the acceptor. **Figure 45A** shows the fluorescence emission spectra of A_{4CF}, B_{4TR} and the CC $A_{4CF}B_{4TR}$ in PBS, when the samples were excited at 475 nm. A_{4CF} showed the expected strong emission with a maximum at 523 nm. The B_{4TR} sample was only weakly fluorescent when excited at 475 nm, indicating weak acceptor excitation. In the CC sample, the intensity of carboxyfluorescein decreased when compared to A_{4CF} while the intensity of tetramethylrhodamine increased (emission maximum at 584 nm).

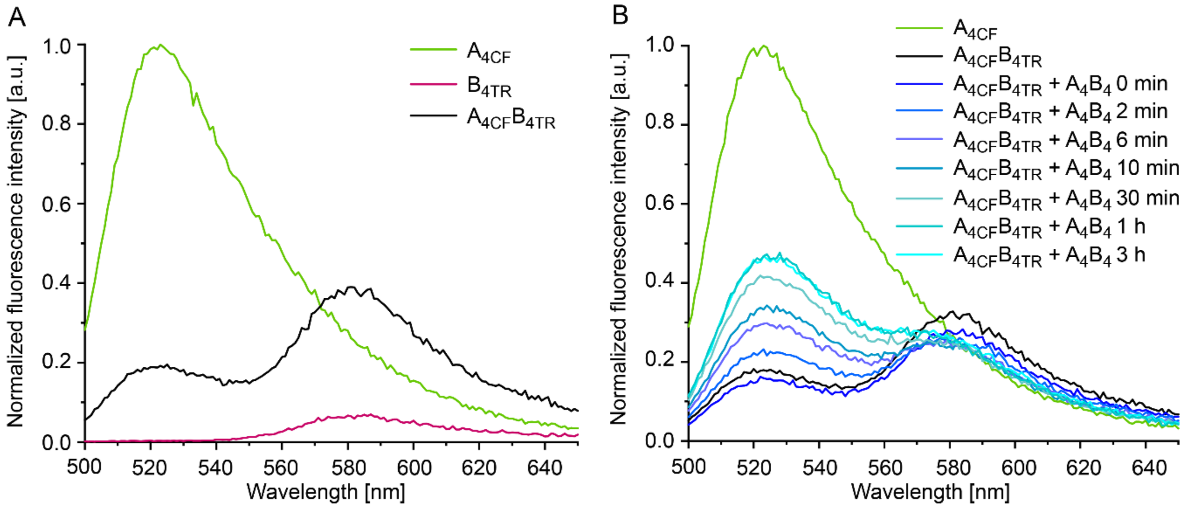

Figure 45: Determination of the FRET efficiency and competition test with A_4B_4. A) The FRET efficiency (E) was determined from the intensity at the donor (A_{4CF}) emission maximum at 523 nm in the presence and the absence of the acceptor (B_{4TR}) using **Equation 10** (excitation of the donor at 475 nm). The emission spectrum of B_{4TR} after excitation at 475 nm was collected in addition. B) Competition test with 2 mM (400-fold excess) of non-labeled A_4B_4. The non-labeled peptides compete for binding to the labeled $A_{4CF}B_{4TR}$. The FRET efficiency was decreased to 53 % when compared to $A_{4CF}B_{4TR}$ after 1 h. The concentration of A_{4CF} and B_{4TR} was 5 µM in PBS. Measurements were performed at RT.

The FRET efficiency was calculated from $A_{4CF}B_{4TR}$ and A_{4CF} (**Equation 10**), using the intensity at the carboxyfluorescein emission maximum. The mean FRET efficiency of $A_{4CF}B_{4TR}$ was 77 % (**Table S5**). Inserting the obtained FRET efficiency into **Equation 9** yielded a fluorophore distance of 45 Å. In order to avoid self-quenching and intermolecular FRET in the hydrogel, the fraction of fluorophore labeled CC needs to be low (e.g. 5 µM as used for the fluorescence spectra). However, a minimum cross-link concentration of 2 mM is required for hydrogel formation. One possible strategy to address this problem is to mix $A_{4CF}B_{4TR}$ with non-labeled A_4B_4. Monitoring the time evolution of the $A_{4CF}B_{4TR}$ FRET efficiency after adding 2 mM A_4B_4 shows a decrease from 84 % to 59 % in the first 30 min and to 53 % after 1 h (**Figure 45B**). In hydrogels containing a low fraction of labeled $A_{4CF}B_{4TR}$ and a high fraction of A_4B_4, the high excess of non-labeled CC will thus lead to a fast decrease of the FRET efficiency because the FRET-labeled CCs dissociate and re-associate with non-labeled peptides. Therefore, $A_{4CF}B_{4TR}$

should not be implemented into an A_4B_4 cross-linked hydrogel, and a thermodynamically more stable interaction should be used to cross-link the hydrogel (e.g. a covalent cross-link).

4.4.3 Monitoring fluorescently labeled coiled coil cross-links in hydrogels under compression force

As a first proof-of-principle for the employment of fluorescently labeled CCs as molecular force sensors, I implemented the reversible $A_{4CF}B_{4RT}$ cross-link at low concentration (5 μM) into an otherwise covalently cross-linked star-PEG hydrogel. As a covalent cross-link, I used SH-PEG-SH (2 kDa). Monitoring the FRET efficiency of the self-reporting CC, enabled me to draw conclusions on the state of the CC in the bulk hydrogel. Since the thiol-maleimide reaction and thus cross-link formation was very fast, it was very challenging to obtain a homogeneous distribution of the fluorescently-labeled CC on the molecular scale. To monitor the failure of CC cross-links in the bulk hydrogel, a compression force was applied with a rheometer. The rheometer was coupled with a fluorescence microscope, allowing for the direct observation of the CC response while the force was applied. The carboxyfluorescein intensity was recorded at the initial height of the sample (1 mm) and after compression to 0.1 mm (**Figure 46**). Following the same procedure, also hydrogels containing only the donor (A_{4CF}) or the acceptor (B_{4TR}) were measured. The mean intensity was obtained for all images and the FRET efficiency was calculated according to **Equation 10**, using the $A_{4CF}B_{4TR}$ and A_{4CF} containing hydrogels. All intensity values are given in **Table S6.** At the initial sample height, the FRET efficiency in the $A_{4CF}B_{4TR}$ hydrogels was 66 % (n = 10). This is about 10 % lower, when compared to the FRET efficiency of $A_{4CF}B_{4TR}$ in solution (77 %). The FRET efficiency decreased to 36 % (n = 10) when decreasing the gap height to 0.1 mm (**Figure 46A and B**). The decrease in FRET efficiency indicated that a certain number of CCs ruptured upon compression and that the CC indeed self-reported its state. When increasing the gap height back to 1 mm, the fluorescence intensity of carboxyfluorescein recovered to an average value of 85 % of the initial intensity ($A_{4CF}B_{4TR}$ hydrogel). Also in the hydrogel containing only A_{4CF}, the fluorescence intensity of carboxyfluorescein showed only 78 % recovery. The loss in fluorescence intensity might thus be the result of photobleaching. Overall, the results suggest that the non-covalent CC cross-links break upon compression and reform when the force is released. As the mechanical stability of the thiol-maleimide bond exceeds the stability of the CC, it is anticipated that the covalent cross-links stay mostly intact.

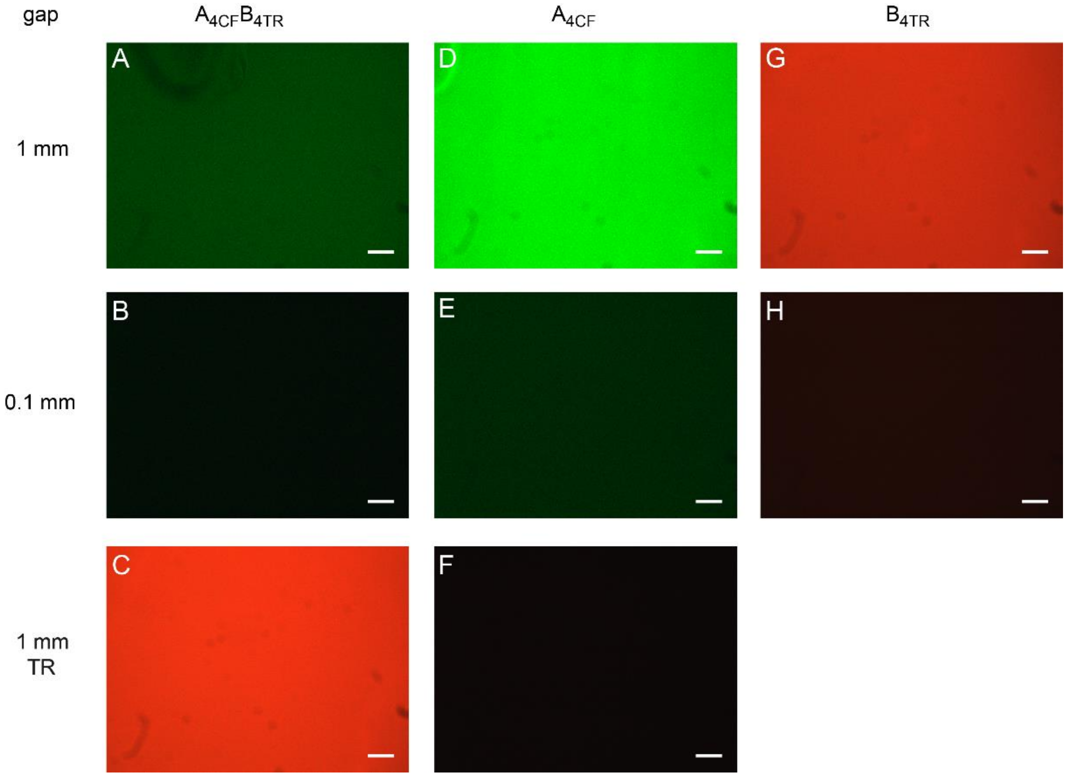

Figure 46: Fluorescence images of the star-PEG hydrogel with covalent SH-PEG-SH cross-links and $A_{4CF}B_{4TR}$ as molecular force sensor. The $A_{4CF}B_{4TR}$ concentration was 5 µM. Control hydrogels were prepared containing only the donor A_{4CF} or the acceptor B_{4TR}. The hydrogels had an initial height of 1 mm and were compressed to 0.1 mm. A, B, E, D) Fluorescence signal of carboxyfluorescein. C, F, G, H) Fluorescence signal of tetramethylrhodamine. Scale bar = 20 µm.

Measuring fluorescence intensity-based intermolecular FRET using wide-field microscopy requires a high number of internal controls. To investigate whether the concentration of the acceptor tetramethylrhodamine was similar in all hydrogels, fluorescence images were taken for $A_{4CF}B_{4TR}$ and B_{4TR} hydrogels (**Figure 46C and G)**. The mean intensity of tetramethylrhodamine was 90 counts in $A_{4CF}B_{4TR}$ (n = 4) and 80 counts in B_{4TR} hydrogels (n = 4) (**Table S7**). The higher intensity in the hydrogels with $A_{4CF}B_{4TR}$ is attributed to the presence of A_{4CF}, which showed a low intensity of 10 counts in the tetramethylrhodamine detection channel (**Figure 46F**).

In summary, the presented proof-of-principle experiments revealed that the force applied to a hydrogel can be monitored using fluorescently labeled self-reporting CCs. Future work needs to focus on the development of strategies for implementing low amounts of labeled CCs into non-covalently cross-linked hydrogels, for forming homogeneous hydrogels and for monitoring the failure of self-healing hydrogels. Once this is achieved, more elaborate techniques, such as micro-rheology or AFM-based nanoindentation, can be utilized to obtain quantitative force-response relationships, ideally with molecular level resolution.

5 Discussion

Coiled coils are abundant building blocks in natural materials, which have been rationally engineered and implemented as self-assembling and self-healing cross-links in a number of biomimetic hydrogels. Tunability and precise control over the viscoelastic properties of hydrogels are key factors for their application in cell biology and biomedicine, since the viscoelastic properties of ECM mimics were shown to influence cell signaling and differentiation [159]. In spite of their extensive use, none of the CC building blocks used in previously reported hydrogels was characterized at the single molecule level, even though information about the energy landscape parameters is critical for tuning the viscoelastic properties. This work provides the first report of a calibrated and tunable CC building block used as a hydrogel cross-link. I showed that the stability of individual CCs is reversibly tunable at the single molecule level when rationally engineered with His-metal coordination sites. The metal-dependent stabilization effect was directly transferred to the bulk hydrogel level, when using the CC as a cross-link for star-PEG. Thereby, I clearly demonstrated that the relaxation time of the hydrogel is reversibly tunable. Moreover, controlling the specific location of His residues, I was also able to produce CCs that form intermolecular cross-links. Intermolecular His-metal coordination sites in the CC provided a second cross-linking mode, which enabled me to reversibly tune the storage modulus and relaxation time of the hydrogel from viscoelastic to elastic-like in a stepwise manner. In order to monitor the state (bound vs. unbound) of the CC cross-links in the hydrogel, I equipped the CC with a FRET pair. This self-reporting CC was introduced in a covalently cross-linked star-PEG hydrogel. I showed that the FRET efficiency deceased to half when compressing the hydrogel to one tenth of its initial height.

5.1 Tuning the stability of coiled coil building blocks using His-metal coordination

Precise control over the kinetic and thermodynamic properties of CC building blocks is crucial to develop self-healing and self-reporting hydrogels with well-defined tunable viscoelastic properties for applications in tissue engineering or cell culture. In order to achieve this goal, it is essential to gain a precise understanding of the connection between the sequence of the CC, the molecular energy landscape parameters, the dissociation mechanism under force, and the relationship of these behaviors with the bulk viscoelastic properties of CC cross-linked hydrogels. The sequence-structure-mechanics relationship of CC shearing was investigated using AFM-SMFS and MD simulations [56,62]. Unfolding-assisted dissociation perpendicular to the force axis was proposed as the predominant chain separation mechanism at loading rates applied in AFM-SMFS. MD simulations suggest that unfolding predominantly occurs from the termini of force application. With the goal to develop a CC building block with reversibly tunable stability, I introduced His-metal coordination sites into the solvent-exposed *b* and *f* position of A_4B_4. Specifically, these coordination sites were located in the terminal heptads under load ($A_{4HII}B_{4HII}$). In order to experimentally validate this approach and to understand the effect of this modification on the energy landscape parameters of the CC, SMFS of the CC was performed in the presence and absence of Ni^{2+}. The experimental design further allowed for investigating if mechanical unfolding of the CC indeed starts from the termini of force application, as predicted by MD simulations.

Molecularly understanding the effect of His-metal coordination on CC stability is essential for tuning the bulk viscoelastic properties of CC cross-linked hydrogels. Here, I will discuss the effect of His-Ni^{2+} coordination on the energy landscape and the unfolding pathway of single $A_{4HII}B_{4HII}$ molecules. The rupture force range of $A_{4HII}B_{4HII}$ was 25-45 pN depending on the loading rate applied and increased to 35-55 pN in the presence of His-Ni^{2+} coordination bonds. This increase in the rupture force was completely reversible when adding an excess of EDTA to chelate the Ni^{2+}. Dynamic SMFS revealed that His-Ni^{2+} coordination to $A_{4HII}B_{4HII}$ lowered the k_{off} by a factor of 10, while the distance to the transition state Δx did not change. Since Δx was not affected by His-Ni^{2+} coordination it is assumed that only the energy barrier height is increased while the general unfolding pathway of the CC is not altered (**Figure 47A**). Krantz & Sosnick [90] described a similar thermodynamic stabilization effect on the energy landscape of a CC homodimer with N-terminal His-metal coordination sites (**Figure 8B**). The α-helical structure of the metal coordinating heptads was stabilized in the presence of metal ions, increasing both the free energy of the equilibrium state and the free energy of folding (2.5 kcal mol^{-1}). A similar effect on k_{off} and Δx has been reported by Cao et al. [93] for a His-Ni^{2+} stabilized GB1 protein. Introducing a His-metal coordination site in the middle of the β-sheet domain of GB1 decreased the k_{off} by an order of magnitude from 0.029 s^{-1} to 0.0071 s^{-1} whereas placing the His at the edges of the β-sheet only led to a 5-fold decrease of the unfolding rate. This highlights that the stabilizing effect of the His-Ni^{2+} bridge is highly dependent on its position in the native structure of the protein and the unfolding pathway followed by the protein when force is applied.

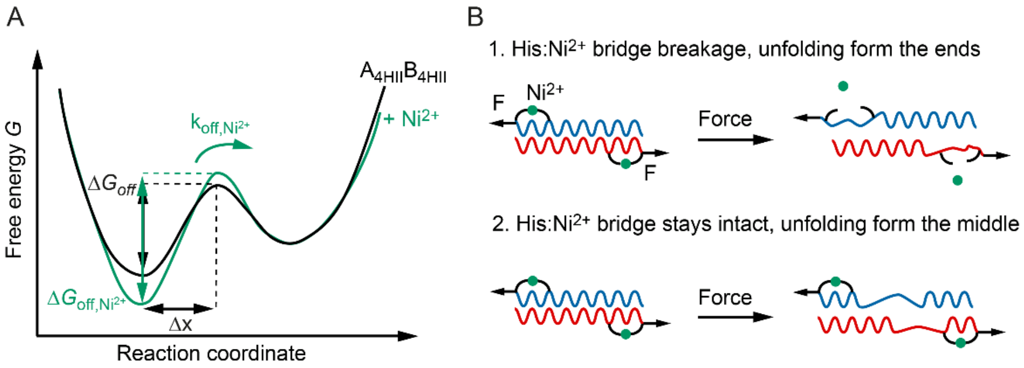

Figure 47: Energy landscape and proposed unfolding mechanism of $A_{4HII}B_{4HII}$ in the presence of Ni^{2+}. A) The free energy barrier to the transition state is increased when the CC is stabilized against mechanical unfolding via a His-Ni^{2+} bridge. The unfolding rate k_{off} is reduced in the presence of Ni^{2+}, while the distance to the transition state Δx is not changed. B) Possible effect of Ni^{2+} on the chain dissociation mechanism. 1. The CC unfolds from the termini of force application after rupture of the His-Ni^{2+} bridge. 2. The His-Ni^{2+} bridge stays intact and the CC starts unfolding form a more central heptad.

The results obtained here verify the rational approach to use His-metal coordination sites for stabilizing the CC building block against initial unfolding. Furthermore, these results provide a better mechanistic understanding of single CC mechanics. They represent the first experimental proof that the termini of force application are mechanically weak points in the structure, as predicted by MD simulations. His-Ni^{2+} coordination bonds act as a reversible bridge, preferentially binding to the folded CC and reducing the conformational freedom of heptads loaded parallel to force vector [78,233]. This effect is synergistically transferred via the hydrophobic core and functions to stabilize the whole CC. However, the results do not allow for unambiguously discriminating between two possible unfolding mechanisms that both explain the stabilization of the native CC and the decrease of k_{off} (**Figure 47B**):

1. His-Ni^{2+} coordination increases the energy barrier for unfolding the first heptad under load. Once a critical force is reached, the transient His-Ni^{2+} coordination bonds open and, as a result, the helix-stabilizing hydrogen bonds as well as the hydrophobic interactions break.

2. His-Ni^{2+} stabilized heptads remain folded during the whole SMFS experiment. The CC starts unfolding at internal heptads. As internal heptads are stabilized by a larger number of hydrogen bonds and hydrophobic interactions, the energy barrier of unfolding and subsequent chain dissociation is increased.

The rupture forces reported for His-Ni^{2+} bonds are in the range of 40-300 pN [82,234], which is overlapping with the rupture force of $A_{4HII}B_{4HII}$. The bond lifetime of a His_6-tag bound to Ni^{2+}-nitrilotriacetate (NTA) was determined to be 15 s at zero force and 15 ms at 150 pN load [235], which is in the timescale (80 ms to 8 s) required to collect a force-extension curve at the different retract speeds. The kinetics of the His_6-tag-Ni^{2+} bond might be different from the unbinding kinetics of the His-Ni^{2+} coordination bonds in the CC and no information about the unbinding kinetics of single His-Ni^{2+} coordination bonds is currently available. It is thus not possible to unambiguously conclude which unfolding mechanism is predominant in the presence of the reversible His-Ni^{2+} bond.

To further investigate the uncoiling-assisted dissociation mechanism of CCs in shear geometry, the His-metal coordination sites could be shifted to the terminal heptads that are not directly loaded. Since the terminal heptads of CCs are generally more flexible when compared to internal heptads [161], the thermodynamic stabilization effect of the His-metal coordination on the CC should be similar. However, the effect on the mechanical unfolding pathway might be small if the force is not applied directly to the stabilized heptads. Alternatively, a metal ion with a longer bond lifetime, such as Co^{3+} or Ru^{3+} could be used. If the hypothesis that the terminal heptads break first was true, the stronger metal coordination would lead to a stabilization of the terminal heptad against unfolding and result in a decrease of k_{off}. An irreversible bond, i.e. a covalent staple, was used by Patricia Lopéz García to study the unfolding mechanism in more detail [236]. The covalent staple led to a large decrease in k_{off} and Δx. In comparison, the His-Ni^{2+} bridge only led to a decreased k_{off}, suggesting that the His-Ni^{2+} bonds opened under load and the CC unfolded from the termini, while the covalent staple stayed intact and the CC unfolded from internal positions. Nevertheless, the transient properties of the His-Ni^{2+} coordination bonds are beneficial in star-PEG-based hydrogels, since they allow for reversibly tuning the viscoelastic properties.

With the knowledge about the effect of reversible His-metal coordination on the energy landscape of single CCs at hand, I studied if this effect was transferable to the bulk hydrogel level. The ability to reversibly tune the viscoelastic properties of biomimetic hydrogels is highly desirable for applications in biomedical engineering and cell biology. Even though CCs have been used as building blocks for bioengineering numerous hydrogels [50,103,108,113-115,118,121], reversibly tuning the viscoelastic properties of CC cross-linked hydrogel *in situ* using small molecules, such as metal ions, has not been considered. Here, I report the first star-PEG hydrogel cross-linked with a His-Ni^{2+} coordinating CC. The metal coordination mediated stabilization of single CCs was directly transferable to the viscoelastic properties of the bulk hydrogel (**Figure 48A**). Specifically, the relaxation time of the hydrogel was intimately linked to the stability of the CC. In the presence of Ni^{2+}, the relaxation time was 3-fold slower than in the absence of metal ions. This effect originates from the stabilization of the terminal heptads of the CC in the presence of Ni^{2+}, since it was fully reversible when EDTA was added. To the best of my knowledge, a hydrogel with metal coordinating CC cross-links has only been reported previously by Selengard et al. [135]. A helix-loop-helix motif, which only folded in the presence of Zn^{2+}, was used as a cross-link and allowed for forming and dissolving the hydrogel in an on-off fashion. However, tuning the viscoelastic properties via the stability of the CC was not possible. In contrast, the CC cross-linked hydrogels developed in this thesis are stable without metal ions present, but their stability is tunable with metal ion coordination. Another hydrogel that is tunable with metal ion coordination was published recently [134]. It was based on an engineered fusion of the proteins GL5 and I27, which displayed mutually exclusive folding. The proteins were linked in a conformation that only allows the more stable I27 to fold, while GL5 is unfolded. When equipped with a His-metal coordination site, the resulting GL5HH was stabilized in the presence of Ni^{2+} and folded, while I27 was forced to unfold. This led to a change in the effective cross-link density of a covalently cross-linked hydrogel, since GL5HH and I27 have different contour lengths.

To expand the tunable range of the CC cross-linked hydrogel, I investigated the effect of different transition metal ions. I showed that the relaxation time of the $A_{4HII}B_{4HII}$ cross-linked hydrogel followed the order $Zn^{2+} > Ni^{2+} > Cu^{2+} \approx Co^{2+}$, but the changes observed are relatively small for Ni^{2+}, Cu^{2+} and Co^{2+}. Comparably small differences in the mechanical properties of byssal threads occur, even though the metal ions implemented by the mussel strongly vary according to their availability in the environment [237,238]. Thus, the CC developed here is flexible in terms of which metal ion is coordinated. The relaxation time of star-PEG hydrogels cross-linked solely via His-metal coordination was previously reported by the group of Messersmith. The properties of these hydrogels were tunable over several orders of magnitude when using different metal ions, such as Ni^{2+}, Cu^{2+}, Co^{2+} or Zn^{2+} [129,130]. In this work, the observed stability trend for the relaxation time of the His-metal coordinating CC does neither follow the Irving-Williams series of His-metal binding affinities ($Cu^{2+} > Ni^{2+} > Co^{2+} > Zn^{2+}$) [80,81] nor the rupture forces reported for His_6-tag-metal coordination bonds ($Cu^{2+} > Ni^{2+} > Zn^{2+} > Co^{2+}$) [82].

The stabilization of proteins and peptides via metal ion coordination is not directly comparable to the properties of hydrogels cross-linked via individual His-metal coordination bonds. In proteins, metal coordination strongly depends on the identity and 3D conformation of the coordinating amino acids as well as the secondary, tertiary and quaternary structure of the protein-scaffold [84]. Therefore, the thermodynamic, kinetic [84] and mechanical [93] stabilization effect of metal ion coordination strongly varies according to the spatial organization and configuration of the coordinating amino acids [239]. In case of $A_{4HII}B_{4HII}$, the coordination geometry was restricted by the rigid backbone of the CC, resulting in similar Raman bands and relaxation times for Ni^{2+}, Cu^{2+} and Co^{2+}.

The presence of Zn^{2+}-induced the formation of higher-order CC assemblies as additional cross-links, changing the cross-link density and the hydrogel network architecture. This led to a change in the viscoelastic properties of the CC cross-linked hydrogel, illustrated by a 6-fold increase of the storage modulus and deviation from the Maxwell model (see **Figure 37**). Gupta et al. [240] reported a hydrogel based on a His-rich protein from the jaw of *Nereis virens* that also showed the biggest modulus increase in the presence of Zn^{2+}, while Co^{2+}, Ni^{2+} and Cu^{2+} showed almost no effect on the modulus. Raman spectroscopy of $A_{4HII}B_{4HII}$ revealed differences in the coordination mode of Ni^{2+}, Cu^{2+} and Co^{2+} compared to Zn^{2+}, which was partially coordinated by His in the bridging mode. Since the full deprotonation of His (imidazolate ion) occurs at high pH (pK_a ~14.0), it was unusual to observe a bridging coordination peak at the pH used in this work (8.1). Coordination of imidazole to haemoproteins (Fe^{3+}) was found to decrease the second pK_a of imidazole from 14.0 to 10.4, which promoted formation of the imidazolate ion [73,241,242]. George et al. [73] assumed this was caused by electrostatic effects of Fe^{3+} on imidazole, which led to an enthalpy decrease for imidazolate ion formation. Once completely deprotonated, His was able to coordinate two metal ions. Bridging coordination modes of His-Zn^{2+} were also obtained for byssus-derived His-rich β-sheet peptide films and hydrogels as well as the amyloid peptide $A\beta_{1\text{-}16}$ [222,243,244]. This suggests that several peptides exist where the coordination of one Zn^{2+} might decrease the pK_a of His to enable imidazolate formation and concomitant coordination of a second Zn^{2+}. To gain detailed insights into the coordination geometry of the metal ions in the hydrogel and confirm the presence of the bridging coordination of Zn^{2+}, extended X-ray absorption fine structures (EXAFS) and X-ray absorption near edge spectra (XANES) could be obtained. However, the high water content of the hydrogels (~ 95 %) would be a challenge for reliable data collection.

5.2 Tuning the higher-order assembly of coiled coils via His-metal coordination

Inspired by the Zn^{2+}-induced higher-order assembly of the CC $A_{4H\parallel}B_{4H\parallel}$, I decoupled the effect of intra- and intermolecular His-Zn^{2+} coordination. Specifically, I bioengineered a CC with a larger spacing of His residues so that only inter-CC Zn^{2+}-coordination ($A_{4H\perp}B_{4H\perp}$) was possible (**Figure 48B**). Zn^{2+}-induced CC-aggregation acted as a second cross-linking mode and caused a dramatic change in the viscoelastic properties of the hydrogel. In the presence of 1:1 Zn^{2+}:His, *G'* was seven times higher when compared to the hydrogel without metal ion, indicating a higher degree of cross-linking and a change in network connectivity [245]. The CC $A_{4H\perp}B_{4H\perp}$ provided a rigid backbone conformation that defined a set of possible coordination geometries as well as a specific environment for secondary ligand interactions. From a structural and mechanical point of view, the addition of Zn^{2+} induced the formation of rigid Zn^{2+}-coordinating CC clusters interspaced with more flexible PEG chains that connect the clusters. The re-organization of cross-links into clusters (**Figure 48B**) altered the network topology and increased the modulus. The altered topology might also be responsible for the decreased LVE range of the hydrogel in the presence of Zn^{2+}. A comparable reinforcement was reported for a hydrogel containing the His-rich jaw protein of *Nereis virens,* which showed an increase in stiffness from 360 kPa to more than 10 MPa in the presence of Zn^{2+} [240]. In general, the spatial organization of His-metal coordination sites on multiple length scales significantly influenced the thermodynamics and kinetics of metal ion binding to peptides [79,246] and proteins [78,94] as well as the mechanical response of proteins [93] and proteinaceous materials, such as byssal threads. In short, unstructured His-rich peptides, the spacing of the His residues allowed stable metal ion coordination, which was relatively flexible in terms of the metal ion coordinated. However, different stabilization effects were observed in more stable structural frameworks, for example, seen when comparing the coordination of Zn^{2+} to $(HAAH)_3$ or to a His_6-tag [246].

The long His-rich domains of the preCol proteins of mussel byssus threads were also thought to be largely unstructured; however, MD simulations suggest that the 3D distribution of the His residues still plays a significant role in the mechanical response [164,239]. Reinecke et al. [247] revealed that the His-rich peptides of the preCol form antiparallel amyloid-like β-sheets at basic pH (pH 8). Folding of the His-rich peptides resulted in defined conformations of the His residues and allowed for His-M^{2+} coordination mediated fortification of the β-sheets. This has also been observed when using these peptides as material building blocks in peptide thin films or as cross-links in star-PEG hydrogels [222,243]. His-M^{2+} coordination was shown to have a significant effect on the structure and mechanical properties of these materials. This indicates that the metal coordination geometry and structure of the building blocks is tightly interrelated with their mechanical properties. Immobilized on a surface and probed with peptide coated beads, the His-rich peptides revealed adhesion forces up to 4 nN in the presence of Ni^{2+} [164]. The adhesion forces were higher than the forces of individual His-metal bonds (40-300 pN) and were tunable with pH and metal ion concentration. This indicated that the stability of peptides that coordinate multiple metal ions was tunable over a wide range when using different metal ion concentrations. Similarly, the relaxation time of the aggregate-forming CC cross-linked hydrogel was tunable when using different His:Zn^{2+} ratios.

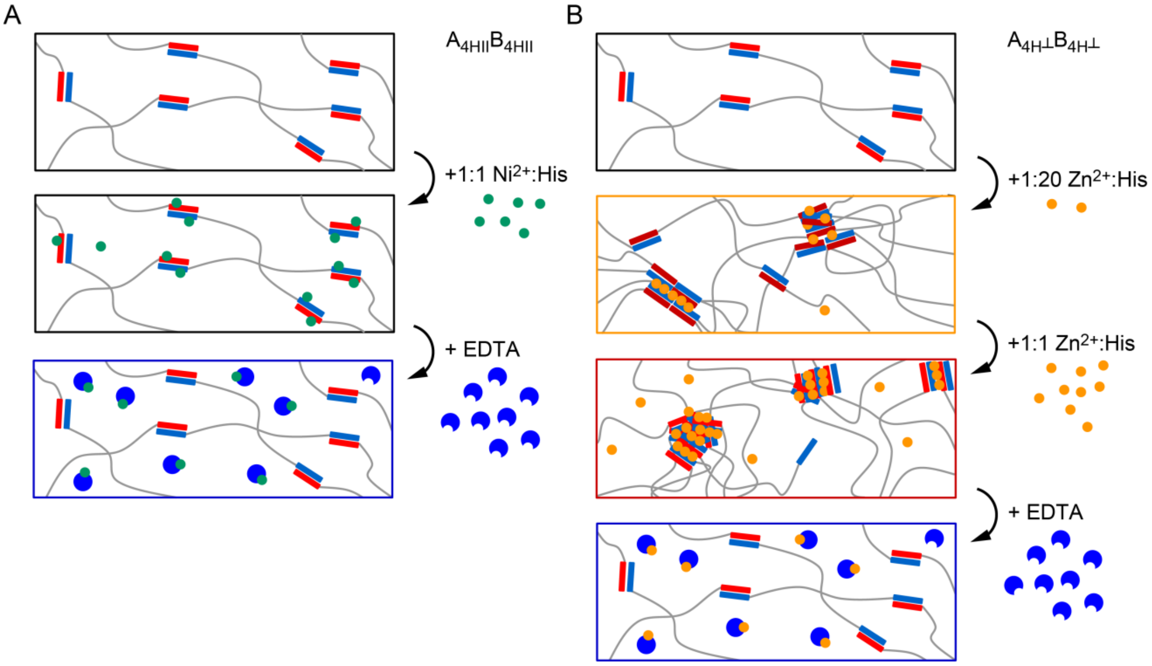

Figure 48: Scheme of the coiled coil (CC) cross-linked hydrogel in the absence and presence of metal ions. A) His-Ni^{2+} coordination in $A_{4H\parallel}B_{4H\parallel}$ results in mechanical stabilization of single cross-links. B) His-Zn^{2+} coordination induces the formation of Zn^{2+} cross-linked CC aggregates in $A_{4H\perp}B_{4H\perp}$ hydrogels. His-metal coordination is reversible in both hydrogel systems when an excess of ethylenediaminetetraacetate (EDTA) is added.

The Zn^{2+}-induced CC aggregation facilitated the switch of the hydrogel from viscoelastic (no metal) to elastic-like (1:1 Zn^{2+}:His) and back to viscoelastic when adding EDTA (**Figure 48B**). Different Zn^{2+}:His ratios allowed for tuning the relaxation time over three orders of magnitude (~10-1000 s) in a stepwise manner. A catechol functionalized star-PEG hydrogel, with similarly switchable viscoelastic properties was reported previously. When cross-linked via single Fe^{3+}-catechol complexes, the hydrogel was viscoelastic, while it transitioned to elastic-like when using Fe_3O_4 nanoparticles as cross-links [128]. The relaxation time of the hydrogel was dependent on the size of the nanoparticles and thereby the number of polymer chains bound to the nanoparticle. Bigger nanoparticles increasingly promoted multivalent interactions, which led to an increase of the hydrogel relaxation time. The same trend was observed with increasing Zn^{2+}-His ratios in the hydrogel reported here, supporting the claim that secondary His-Zn^{2+} cross-linked CC aggregates govern the relaxation time of the hydrogel.

Additional evidence that the network topology affects the viscoelastic properties of CC cross-linked hydrogels is provided by Grad et al. [123]. The CC A_4B_4 was used as a non-covalent cross-link for star-PEG and a fiber-forming polyisocyanopeptide (PIC). The relaxation time of the PIC hydrogel was about two orders of magnitude slower when compared to the star-PEG hydrogel. Thus, the relaxation of the hydrogel was not only determined by cross-link stability, but also the topology of the network, which included multivalent CC interactions within the polymer fibers.

Similar to the metal-free $A_{4H\perp}B_{4H\perp}$ cross-linked hydrogels, the hydrogel systems characterized by Li et al. [128] and Zhang et al. [248] showed complete self-healing after applying a high shear strain. In contrast, the formation of Zn^{2+} cross-linked CC aggregates lead to a time-dependent self-healing of the hydrogel, with *G*' recovering only 80 % of the initial value after the first amplitude sweep. When allowed to self-heal for 1 h, the hydrogel recovered 90 % of the initial modulus. On the molecular scale, this suggests that small aggregates recovered quickly, while the aggregates appear to grow with extended incubation time. The strong stretched exponential behavior of the hydrogel with 1:1 Zn^{2+}:His supports this observation. The small value for α of 0.24 indicates a healing process that spans broad timescales of many orders of magnitude. Remarkably, the observed time-dependent self-healing of the Zn^{2+}-aggregate hydrogel is reminiscent of mussel byssal threads, which also require extended resting periods to recover up to 90 % of their initial material properties [15,18]. The self-healing behavior of the byssal threads is predominantly associated with the reformation of a complex network of intermolecular metal coordination bonds in the His-rich end blocks of the preCol proteins. The β-sheet framework, which is connected via the reversible His-metal bonds, provides hidden length when the His-metal bonds break [165]. For the His-rich peptides, healing was proposed to originate from the thermal dissociation and reformation of metal coordination bonds, gradually moving towards a network topology with higher mechanical stability. This was supported by the increased healing rate at higher temperatures [15,17]. The activation energy for the healing process was calculated to be 20.8 kcal mol^{-1}, which is similar to the energy of a metal coordination bond. In summary, the results showed that His-metal coordination is not only useful for tuning the relaxation time and the modulus, but also the self-healing behavior of hydrogels.

5.3 Monitoring coiled coil cross-link failure using Förster resonance energy transfer

Currently, little information is available about the formation, network structure and failure of CC cross-linked hydrogels on the molecular level. However, detailed understanding is crucial for applications of CC cross-linked hydrogels as ECM mimics in cell culture and tissue engineering. Driven by the question of whether the failure of CCs can be monitored using an optical readout, I developed the fluorescently labeled CC $A_{4CF}B_{4TR}$ using carboxyfluorescein and tetramethylrhodamine. The obtained FRET-based CC is the first mechanoresponsive CC cross-link that self-reports its state in bulk hydrogels. The limitations of the tested approach as well as strategies for improving hydrogels synthesis are discussed in the following paragraphs.

The attachment of fluorophores to CC dimers can affect the thermodynamic stability of the CC or even induce aggregation of the peptide-fluorophore conjugates [230]. Therefore, I first investigated the thermodynamic stability of the fluorescently labeled $A_{4CF}B_{4TR}$. The melting temperature was not impaired by fluorophore attachment, showing that the used labeling positions are well suited. In solution, the FRET efficiency was 77 %. A higher FRET efficiency of about 90 % would be beneficial for future designs to increase the sensitivity towards detecting individual cross-links. To increase the FRET efficiency, the distance between the fluorophores needs to be decreased, e.g. labeling both CC-forming peptides close to the N-terminus. However, this could lead to undesired stacking, self-quenching and aggregation effects if fluorophores with a similar structure, such as carboxyfluorescein and tetramethylrhodamine, are used [249].

The fluorescently labeled, self-reporting CC developed here was subsequently used as a molecular force senor in a covalently cross-linked star-PEG hydrogel. A low amount of FRET-labeled CC cross-links was inserted into a covalently cross-linked hydrogel to prevent self-quenching effects of the fluorophores. The formation of covalently cross-linked hydrogels using star-PEG-maleimide and linear SH-PEG-SH was challenging, since the fast kinetics of the thiol-maleimide reaction prevented homogeneous mixing of the components. Even though the hydrogels developed here cannot be considered homogeneous at the molecular level, changes in the FRET efficiency were studied at the bulk hydrogel level using a rheometer equipped with a fluorescence microscope. The hydrogels were compressed with a plate tool and the change in FRET efficiency was monitored (**Figure 49**). When a compression force was applied, the non-covalent CC cross-link was expected to break before the covalent cross-link. Indeed, The FRET efficiency decreased almost to half when the hydrogel was compressed from 1 mm to 0.1 mm, indicating that the fluorescently labeled CCs self-reported on their cross-link state. When releasing the compression force, about 80% of the initial fluorescence intensity was recovered, indicating cross-link self-healing. To ultimately prove the functionality of the developed FRET-labeled CC force sensor, control measurements of the CC force sensor in the absence of a hydrogel network with the CCs freely diffusing in solution (absence of force) are still required.

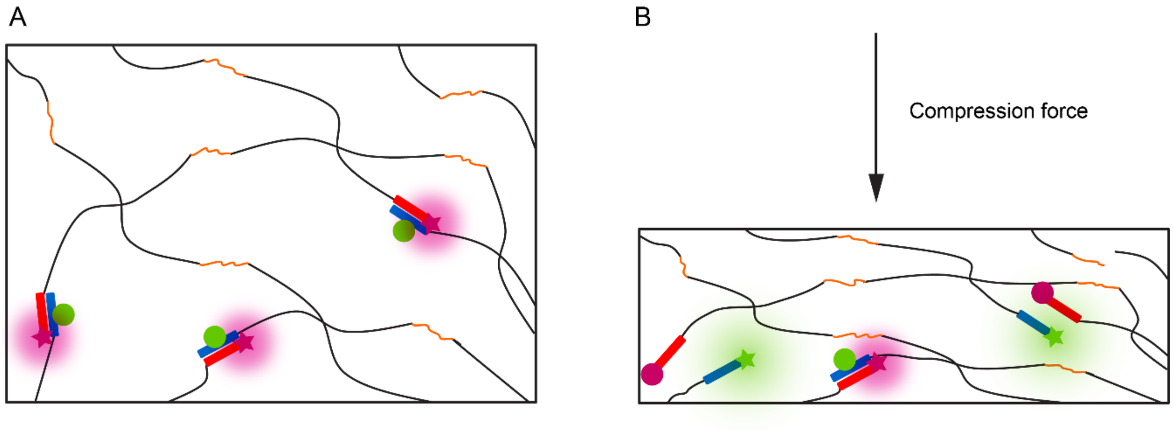

Figure 49: Scheme of the covalently cross-linked star-PEG hydrogel with $A_{4CF}B_{4TR}$. A) Star-PEG hydrogel covalently cross-linked with SH-PEG-SH bonds (orange) and a low amount of FRET-labeled $A_{4CF}B_{4TR}$. The FRET efficiency is high in the formed hydrogel. B) Compressed hydrogel network. The compression force leads to failure of some CC cross-links, which leads to a decrease in the FRET efficiency. Also, part of the covalent bonds may fail under compression force; however, to a much smaller extent.

The number of previously reported hydrogels with a FRET-based reporter system are limited. Merindol et al. [150] reported a fluorophore-quencher FRET pair implemented in a DNA-based hydrogel. Using FRET-labeled DNA force sensors with different thermodynamic stability, it was shown that stress relaxation can be monitored using the fluorescence signal. However, DNA is not a natural ECM component, which makes this hydrogel less suitable as an intelligent ECM mimic. In contrast, CCs naturally occur in the ECM and their stability is rationally tunable over a wide range. Thus, CCs are excellent candidates to replace DNA force sensors in mechanoresponsive hydrogels.

In order to apply the self-reporting CC as a molecular force sensor in biomimetic hydrogels and to obtain a more homogeneous hydrogel, it will be beneficial to implement the fluorescently labeled CC at low concentration in the background of a non-covalently cross-linked hydrogel. However, using the same CC building block (A_4B_4) as the non-labeled cross-link was not possible due to the insufficient thermodynamic stability of this CC. As a result, the FRET-labeled $A_{4CF}B_{4TR}$ dissociated over time and reformed with non-labeled A_4B_4 (2 mM), required to form the star-PEG hydrogel. It is anticipated that the dissociation of the labeled CC may even be promoted when forces are applied during mixing of hydrogel components.

A fluorescently-labeled CC was previously used to study the chain dynamics of a CC cross-linked protein hydrogel by Rapp et al. [144]. Specifically, the CC was used for studying the mobility and dynamics of the polymer chains using fluorescence recovery after photobleaching. Similar measurement setups could be used to investigate the star-PEG hydrogel in future studies. To develop a non-covalently cross-linked star-PEG hydrogel, a second CC cross-link, which does not interact with the fluorescently labeled $A_{4CF}B_{4TR}$ is a highly promising approach (orthogonal CC). Several orthogonal CC sequences are described in the literature [250-252]. Using two orthogonal CCs, fluorescently labelling the thermodynamically and mechanically less stable CC will allow for monitoring its failure under applied force. A specific suggestion for an orthogonal CC system is described in the future directions of this thesis (**Chapter 6**).

In summary, I developed two CC cross-linked hydrogels with reversibly tunable relaxation time based on His-metal coordination. In the presence of Ni^{2+}, the $A_{4H\parallel}B_{4H\parallel}$ hydrogel self-healed immediately in the absence and presence of metal ions. In contrast, the presence of Zn^{2+} cross-linked aggregates, specifically in the $A_{4H\perp}B_{4H\perp}$ hydrogel, led to a time-dependent self-healing resembling the natural model system, the byssal thread. Both hydrogels self-assemble fast under physiological conditions and their relaxation time is tunable *in situ* using metal ions as small soluble additives . Equipped with a FRET pair, CCs have the potential to be used as self-reporting non-covalent cross-link, as exemplary shown here in a covalently cross-linked hydrogel. This highlights the application potential of CCs as molecular force sensors in biomimetic materials.

6 Conclusions and future directions

Using His-metal coordinating CCs, this work demonstrated for the first time that tuning the stability of individual CCs yields star-PEG hydrogels with reversibly tunable viscoelastic properties. The results revealed that the relaxation time of $A_{4HII}B_{4HII}$ was tunable using different metal ions and the metal chelator EDTA. The developed CC cross-links are therefore promising building blocks for use in ECM mimicking hydrogels and extend the A_4B_4-based CC library developed in the Mechano(bio)chemistry group [56,62]. The unfolding rate k_{off} of $A_{4HII}B_{4HII}$ was reduced by one order of magnitude when adding Ni^{2+} ($2.5 \cdot 10^{-3}$ s^{-1}); however, this value is still 10-times higher than the k_{off} reported for the reference CC A_4B_4 ($3.2 \cdot 10^{-4}$ s^{-1}) [56]. For studying cell-matrix interactions, increasing the tunable range of dissociation rates or hydrogel relaxation times would be beneficial, since cells have been reported to respond to the viscoelastic properties of the surrounding matrix [158,159]. In order to further tune the stability of CCs, Lopez et al. implemented a covalent staple in the least stable terminal heptads of A_4B_4 [236]. Also for this CC, the reported k_{off} did not decrease beyond the value measured for A_4B_4. This indicates that CC uncoiling can also start from central heptads and that the helices cannot be stabilized beyond a given maximum value for heterodimeric CCs.

To increase the tunable range, CCs with a higher oligomerization state, such as timers or tetramers may be used. MD simulations of a trimeric CC revealed higher rupture forces and increased toughness when compared to a dimeric CC [253]. In order to study the energy landscape and guarantee reproducible, homogeneous hydrogel formation, a heterotrimeric CC is clearly an interesting addition to the CC toolkit. Currently, no truly heterotrimeric CC sequence is available in the literature. However, a His-metal coordination site could solve this problem, demonstrating the versatility of His-metal coordination once more. When inserted in the hydrophobic core, His-metal coordination sites were reported to induce CC homotrimer formation via metal binding [91,95,97]. An example for a metal binding trimer sequence is given in **Table 7** [91]. Trimer formation is induced in the presence of Ni^{2+} or Cu^{2+}. Furthermore, literature about specific heterotetrameric CCs (AABB) indicates that they are also promising candidates to expand the stability range of the CC library (**Table 7**) [254,255].

In order to use CCs as force sensors in ECM-mimicking hydrogels, it is not only important to elucidate the stability of CCs on the single molecule level. Knowledge about the relationship of the mechanical and thermodynamic properties of the CCs and the bulk material response is of utmost importance. In this thesis, I revealed that stabilizing individual CCs with His-metal coordination bonds directly results in an increased relaxation time of the hydrogel. The oscillatory measurements conducted here, yield information related to the thermal stability of the CC. To gain insights into the relationship between single CC mechanics and the mechanical response of CC cross-linked hydrogels, non-linear, rotatory rheology experiments were performed in the Mechano(bio)chemistry group [256]. Rotatory sweeps yield stress-strain curves similar to the data obtained from tensile tests. Performing rotatory sweeps at different strain rates allowed gaining loading rate dependencies for the CC cross-links in the hydrogel. Currently, a theoretical model based on the Bell-Evans equation is developed in collaboration with Prof. Kroy (University Leipzig) to obtain k_{off} and Δx from the rheology data. If successful, this research will promote the use of CCs as molecular force sensors in star-PEG hydrogels for cell culture applications. It may further allow for extracting the characteristic parameters k_{off} and Δx for specific molecular interactions directly from rheology. This can be beneficial since AFM-SMFS is more time consuming than rotatory rheology measurements.

Table 7: Potential coiled coil (CC) sequences for future studies. Approaches to increase the mechanical stability of CC cross-links could be: a metal-coordinating homotrimer binding Ni^{2+} or Cu^{2+} from [91] or a heterotetramer in the form of AABB from [254]. The orthogonal CC C_4D_4, designed after principles described in [250], can be labeled with more photostable fluorophores in the same positions as $A_{4CF}B_{4TR}$ and used as a force sensor in A_4B_4 cross-linked hydrogels. A Lysine (**K**) with an orthogonal protecting group and an azidohomoalanine (**Z**) are shown as possible coupling sites for the fluorophores.

Name	**Sequence**
	`gabcdef gabcdef gabcdef gabcdef gabcdef`
Metal coordinating homotrimer [91]	**C**GG IEK KIEAIEK K**H**EA**H**EK K**H**EAIEK KIEA GG
	GG IEK KIEAIEK K**H**EA**H**EK K**H**EAIEK KIEA GG
	GG IEK KIEAIEK K**H**EA**H**EK K**H**EAIEK KIEA GG**C**
Heterotetrameric CC [254]	**C**GG MK**E**I**E**D KLE**E**I**E**S KLY**E**I**E**N ELA**E**I**E**K L GG
	GG MK**E**I**E**D KLE**E**I**E**S KLY**E**I**E**N ELA**E**I**E**K L GG
	GG MK**K**I**K**D KLE**K**I**K**S KLY**K**I**K**N ELA**K**I**K**K L GG**C**
	GG MK**K**I**K**D KLE**K**I**K**S KLY**K**I**K**N ELA**K**I**K**K L GG
Orthogonal CC C_4D_4	**C**GG EIAALEQ ENAALEK **K**NAALKQ KIAALKQ GG
	ZGG KIAALKQ KNAALKQ ENAALEK EIAALEQ GG**C**

Using intermolecular His-metal coordinating CCs as cross-links, the star-PEG hydrogel was tunable from viscoelastic to elastic-like in a stepwise fashion, using different His:Zn^{2+} ratios. This change in the viscoelastic properties of the hydrogel was attributed to the formation of a second type of cross-linking: higher-order Zn^{2+} cross-linked CC aggregates. However, it remains to be elucidated whether only the inter-CC His-Zn^{2+} coordination bonds or also the CCs themselves break when the hydrogel is loaded mechanically. Furthermore, also information about the molecular structure and the failure of CC cross-linked hydrogels under load is currently unavailable. In order to study hydrogel formation and failure, I integrated a FRET-based reporter system into A_4B_4. This new CC-based molecular force sensor was tested in the background of a covalently cross-linked hydrogel. This strategy eliminated the need for a second, orthogonal CC to dilute the FRET-labeled CC. Dilution is required to avoid self-quenching and intermolecular FRET. In future experiments, the use of a second reversible cross-link should be preferred as more homogenous hydrogels are expected.

A possible orthogonal CC sequence is C_4D_4 (**Table 7**). The orthogonality originates from the additional Asn in the second heptad and the changed charge pattern. According to related sequences reported by Gradišar and Jerala [250], the melting temperature of C_4D_4 should be 65 °C. C_4D_4 is thus expected to be less stable than A_4B_4. Inserted into a hydrogel predominantly cross-linked with A_4B_4, the orthogonal and FRET-labelled CC C_4D_4 will then allow for studying hydrogel failure. In addition, more photostable fluorophores such as Alexa Fluor$^{©}$488 and Alexa Fluor$^{©}$555 can be implemented. To do so, azidohomoalanine (Z) can be introduced at the N-terminus of the D_4 to enable coupling of the fluorophore in a strain promoted azide-alkyne cycloaddition reaction. Further, Lys with an orthogonal protecting group can be used to couple fluorophores carrying an N-hydroxysuccinimide ester.

With the perspective to develop sustainable, easily biodegradable ECM mimics, the star-PEG backbone of the hydrogel can be replaced with a random coil protein backbone, such as elastin-like peptides [257,258]. This would allow for the recombinant production of purely proteinaceous hydrogel building blocks, e.g. elastin-like peptides terminated with CC cross-links. The resulting protein-based building blocks will have a polydispersity of one and in addition allow for precisely tuning the length of the protein backbone.

In summary, this work shed light on the outstanding application potential of self-healing, tunable and self-reporting CC cross-linked hydrogels in materials science. The growing library of mechanically calibrated CCs and sustainable production of purely protein-based CC-cross-linked hydrogels sets the stage for the application of precisely tunable self-healing and self-reporting CC cross-linked hydrogels in cell culture and biomedical engineering.

References

1. K. Ariga, T. Mori and J. P. Hill, Mechanical Control of Nanomaterials and Nanosystems. *Adv. Mater.* **2012,** 24 (2), 158-176.

2. V. A. Ganesh, A. Baji and S. Ramakrishna, Smart Functional Polymers – A New Route Towards Creating a Sustainable Environment. *RSC Adv.* **2014,** 4 (95), 53352-53364.

3. H. Zhao, K. Xu, P. Zhu, C. Wang and Q. Chi, Smart Hydrogels with High Tunability of Stiffness as a Biomimetic Cell Carrier. *Cell Biol. Int.* **2019,** 43 (2), 84-97.

4. E. Radvar and H. S. Azevedo, Supramolecular Peptide/Polymer Hybrid Hydrogels for Biomedical Applications. *Macromol. Biosci.* **2019,** 19 (1), 1800221.

5. X. Li and X. Su, Multifunctional Smart Hydrogels: Potential in Tissue Engineering and Cancer Therapy. *J. Mater. Chem. B* **2018,** 6 (29), 4714-4730.

6. M. W. Tibbitt and K. S. Anseth, Hydrogels as Extracellular Matrix Mimics for 3D Cell Culture. *Biotechnol. Bioeng.* **2009,** 103 (4), 655-663.

7. X. Li, Q. Sun, Q. Li, N. Kawazoe and G. Chen, Functional Hydrogels With Tunable Structures and Properties for Tissue Engineering Applications. *Front. Chem.* **2018,** 6, 499.

8. H. L. Lim, Y. Hwang, M. Kar and S. Varghese, Smart Hydrogels as Functional Biomimetic Systems. *Biomater. Sci.* **2014,** 2 (5), 603-618.

9. P. Fratzl, K. Misof, I. Zizak, G. Rapp, H. Amenitsch and S. Bernstorff, Fibrillar Structure and Mechanical Properties of Collagen. *J. Struc. Biol.* **1998,** 122 (1), 119-122.

10. J. M. Gosline, M. E. DeMont and M. W. Denny, The Structure and Properties of Spider Silk. *Endeavour* **1986,** 10 (1), 37-43.

11. J. H. Waite, X. X. Qin and K. J. Coyne, The Peculiar Collagens of Mussel Byssus. *Matrix Biol.* **1998,** 17 (2), 93-106.

12. C. C. Broomell, R. K. Khan, D. N. Moses, A. Miserez, M. G. Pontin, G. D. Stucky, F. W. Zok and J. H. Waite, Mineral Minimization in Nature's Alternative Teeth. *J. R. Soc., Interface* **2007,** 4 (12), 19-31.

13. D. S. Fudge, K. H. Gardner, V. T. Forsyth, C. Riekel and J. M. Gosline, The Mechanical Properties of Hydrated Intermediate Filaments: Insights from Hagfish Slime Threads. *Biophys. J.* **2003,** 85 (3), 2015-2027.

14. S. S. Wasko, G. Tay, A. Schwaighofer, C. Nowak, J. H. Waite and A. Miserez, Structural Proteins from Whelk Egg Capsule with Long Range Elasticity Associated with a Solid-state Phase Transition. *Biomacromolecules* **2014,** 15 (1), 30-42.

15. M. J. Harrington, H. S. Gupta, P. Fratzl and J. H. Waite, Collagen Insulated from Tensile Damage by Domains that Unfold Reversibly: In Situ X-ray Investigation of Mechanical Yield and Damage Repair in the Mussel Byssus. *J. Struct. Biol.* **2009,** 167 (1), 47-54.

16. N. Holten-Andersen, T. E. Mates, M. S. Toprak, G. D. Stucky, F. W. Zok and J. H. Waite, Metals and the Integrity of a Biological Coating: The Cuticle of Mussel Byssus. *Langmuir* **2009,** 25 (6), 3323-3326.

17. C. N. Z. Schmitt, Y. Politi, A. Reinecke and M. J. Harrington, Role of Sacrificial Protein–Metal Bond Exchange in Mussel Byssal Thread Self-Healing. *Biomacromolecules* **2015,** 16 (9), 2852-2861.

18. E. Carrington and J. M. Gosline, Mechanical Design of Mussel Byssus: Load Cycle and Strain Rate Dependence. *Am. Malacol. Bull.* **2004,** 18, 135-142.

19. E. Degtyar, M. J. Harrington, Y. Politi and P. Fratzl, The Mechanical Role of Metal Ions in Biogenic Protein-Based Materials. *Angew. Chem. Int. Ed.* **2014,** 53 (45), 12026-12044.

20. M. J. Harrington, S. S. Wasko, A. Masic, F. D. Fischer, H. S. Gupta and P. Fratzl, Pseudoelastic Behaviour of a Natural Material is Achieved via Reversible Changes in Protein Backbone Conformation. *J. R. Soc., Interface* **2012,** 9 (76), 2911-2922.

21. J. Fu, P. A. Guerette and A. Miserez, Self-Assembly of Recombinant Hagfish Thread Keratins Amenable to a Strain-Induced α-Helix to β-Sheet Transition. *Biomacromolecules* **2015,** 16 (8), 2327-2339.

22. R. Paquin and P. Colomban, Nanomechanics of Single Keratin Fibres: A Raman Study of the α-helix →β-sheet Transition and the Effect of Water. *J. Raman Spectrosc.* **2007,** 38 (5), 504-514.

23. A. N. Lupas and J. Bassler, Coiled Coils - A Model System for the 21st Century. *Trends Biochem. Sci.* **2017,** 42 (2), 130-140.

24. B. Apostolovic, M. Danial and H.-A. Klok, Coiled Coils: Attractive Protein Folding Motifs for the Fabrication of Self-assembled, Responsive and Bioactive Materials. *Chem. Soc. Rev.* **2010,** 39 (9), 3541-3575.

25. F. Crick, The Fourier Transform of a Coiled-Coil. *Acta Crystallogr.* **1953,** 6 (8-9), 685-689.

26. L. Pauling and R. B. Corey, Compound Helical Configurations of Polypeptide Chains: Structure of Proteins of the α-Keratin Type. *Nature* **1953,** 171 (4341), 59-61.

27. E. Moutevelis and D. N. Woolfson, A Periodic Table of Coiled-Coil Protein Structures. *J. Mol. Biol.* **2009,** 385 (3), 726-732.

28. O. D. Testa, E. Moutevelis and D. N. Woolfson, CC+: A Relational Database of Coiled-coil Structures. *Nucleic acids res.* **2009,** 37 (Database issue), D315-D322.

29. B. Wang, W. Yang, J. McKittrick and M. A. Meyers, Keratin: Structure, Mechanical Properties, Occurrence in Biological Organisms, and Efforts at Bioinspiration. *Prog. Mater. Sci.* **2016,** 76, 229-318.

30. J. Lim, D. S. Fudge, N. Levy and J. M. Gosline, Hagfish Slime Ecomechanics: Testing the Gill-clogging Hypothesis. *J. Exp. Biol.* **2006,** 209 (4), 702-710.

31. E. A. Koch, R. H. Spitzer, R. B. Pithawalla and D. A. Parry, An Unusual Intermediate Filament Subunit from the Cytoskeletal Biopolymer Released Extracellularly into Seawater by the Primitive Hagfish (Eptatretus stouti). *J. Cell Sci.* **1994,** 107 (11), 3133-3144.

32. A. H. Pang, J. M. Obiero, A. W. Kulczyk, V. M. Sviripa and O. V. Tsodikov, A Crystal Structure of Coil 1B of Vimentin in the Filamentous form Provides a Model of a High-order Assembly of a Vimentin Filament. *FEBS J.* **2018**, 285, 2888-2899.

33. P. Burkhard, R. A. Kammerer, M. O. Steinmetz, G. P. Bourenkov and U. Aebi, The Coiled-coil Trigger Site of the Rod Domain of Cortexillin I Unveils a Distinct Network of Interhelical and Intrahelical Salt Bridges. *Structure* **2000,** 8 (3), 223-230.

34. J. Block, H. Witt, A. Candelli, E. J. G. Peterman, G. J. L. Wuite, A. Janshoff and S. Köster, Nonlinear Loading-Rate-Dependent Force Response of Individual Vimentin Intermediate Filaments to Applied Strain. *Phys. Rev. Lett.* **2017,** 118 (4), 048101.

35. J. W. Weisel and R. I. Litvinov, Fibrin Formation, Structure and Properties. *Subcell. Biochem.* **2017,** 82, 405-456.

36. E. N. Korkmaz, K. C. Taylor, M. P. Andreas, G. Ajay, N. T. Heinze, Q. Cui and I. Rayment, A Composite Approach Towards a Complete Model of the Myosin Rod. *Proteins* **2016,** 84 (1), 172-189.

37. Z. Yang, J. M. Kollman, L. Pandi and R. F. Doolittle, Crystal Structure of Native Chicken Fbrinogen at 2.7 A Resolution. *Biochemistry* **2001,** 40 (42), 12515-12523.

38. Z. Qin and M. J. Buehler, Molecular Dynamics Simulation of the α-Helix to β-Sheet Transition in Coiled Protein Filaments: Evidence for a Critical Filament Length Scale. *Phys. Rev. Lett.* **2010,** 104 (19), 198304.

39. A. Miserez and P. A. Guerette, Phase Transition-induced Elasticity of α-helical Bioelastomeric Fibres and Networks. *Chem. Soc. Rev.* **2013,** 42 (5), 1973-1995.

40. J. M. Mason, U. B. Hagemann and K. M. Arndt, Role of Hydrophobic and Electrostatic Interactions in Coiled Coil Stability and Specificity. *Biochemistry* **2009,** 48 (43), 10380-10388.

41. C. N. Pace and J. M. Scholtz, A Helix Propensity Scale Based on Experimental Studies of Peptides and Proteins. *Biophys. J.* **1998,** 75 (1), 422-427.

42. J. R. Litowski and R. S. Hodges, Designing Heterodimeric Two-stranded α-Helical Coiled-coils: Effects of Hydrophobicity and α-Propentity on Protein Folding, Stability and Specificity. *J. Biol. Chem.* **2002,** 277 (40), 37272-37279.

43. B. I. Dahiyat, D. Benjamin Gordon and S. L. Mayo, Automated Design of the Surface Positions of Protein Helices. *Protein Sci.* **1997,** 6 (6), 1333-1337.

44. J. M. Fletcher, A. L. Boyle, M. Bruning, G. J. Bartlett, T. L. Vincent, N. R. Zaccai, C. T. Armstrong, E. H. C. Bromley, P. J. Booth, R. L. Brady, A. R. Thomson and D. N. Woolfson, A Basis Set of de Novo Coiled-Coil Peptide Oligomers for Rational Protein Design and Synthetic Biology. *ACS Synth. Biol.* **2012,** 1 (6), 240-250.

45. M. K. Yadav, L. J. Leman, D. J. Price, C. L. Brooks, C. D. Stout and M. R. Ghadiri, Coiled Coils at the Edge of Configurational Heterogeneity. Structural Analyses of Parallel and Antiparallel Homotetrameric Coiled Coils Reveal Configurational Sensitivity to a Single Solvent-Exposed Amino Acid Substitution. *Biochemistry* **2006,** 45 (14), 4463-4473.

46. F. Thomas, A. L. Boyle, A. J. Burton and D. N. Woolfson, A Set of *de novo* Designed Parallel Heterodimeric Coiled Coils with Quantified Dissociation Constants in the Micromolar to Sub-nanomolar Regime. *J. Am. Chem. Soc.* **2013,** 135 (13), 5161-5166.

47. G. De Crescenzo, J. R. Litowski, R. S. Hodges and M. D. O'Connor-McCourt, Real-time Monitoring of the Interactions of Two-stranded *de novo* Designed Coiled-coils: Effect of Chain Length on the Kinetic and Thermodynamic Constants of Binding. *Biochemistry* **2003,** 42 (6), 1754-1763.

48. C. Aronsson, S. Dånmark, F. Zhou, P. Öberg, K. Enander, H. Su and D. Aili, Self-sorting Heterodimeric Coiled Coil Peptides with Defined and Tuneable Self-assembly Properties. *Sci. Rep.* **2015,** 5, 14063.

49. C. W. Wood and D. N. Woolfson, CCBuilder 2.0: Powerful and Accessible Coiled-coil Modeling. *Protein Sci.* **2018,** 27 (1), 103-111.

50. N. L. Fletcher, C. V. Lockett and A. F. Dexter, A pH-responsive Coiled-coil Peptide Hydrogel. *Soft Matter* **2011,** 7 (21), 10210-10218.

51. I. Jelesarov, E. Dürr, R. M. Thomas and H. R. Bosshard, Salt Effects on Hydrophobic Interaction and Charge Screening in the Folding of a Negatively Charged Peptide to a Coiled Coil (Leucine Zipper). *Biochemistry* **1998,** 37 (20), 7539-7550.

52. H. Wendt, L. Leder, H. Härmä, I. Jelesarov, A. Baici and H. R. Bosshard, Very Rapid, Ionic Strength-dependent Association and Folding of a Heterodimeric Leucine Zipper. *Biochemistry* **1997,** 36 (1), 204-213.

53. B. Apostolovic and H.-A. Klok, pH-Sensitivity of the E3/K3 Heterodimeric Coiled Coil. *Biomacromolecules* **2008,** 9 (11), 3173-3180.

54. K. C. Neuman and A. Nagy, Single-Molecule Force Spectroscopy: Optical Tweezers, Magnetic Tweezers and Atomic Force Microscopy. *Nat. Methods* **2008,** 5 (6), 491-505.

55. G. Binnig, C. F. Quate and C. Gerber, Atomic Force Microscope. *Phys. Rev. Lett.* **1986,** 56 (9), 930-933.

56. M. Goktas, C. Luo, R. M. A. Sullan, A. E. Bergues-Pupo, R. Lipowsky, A. Vila Verde and K. G. Blank, Molecular Mechanics of Coiled Coils Loaded in the Shear Geometry. *Chem. Sci.* **2018,** 9 (20), 4610-4621.

57. I. Schwaiger, C. Sattler, D. R. Hostetter and M. Rief, The Myosin Coiled-coil is a Truly Elastic Protein Structure. *Nat. Mater.* **2002,** 1 (4), 232-235.

58. T. Bornschlögl and M. Rief, Single Molecule Unzipping of Coiled Coils: Sequence Resolved Stability Profiles. *Phys. Rev. Lett.* **2006,** 96 (11), 118102.

59. E. Evans and K. Ritchie, Dynamic Strength of Molecular Adhesion Bonds. *Biophys. J.* **1997,** 72 (4), 1541-1555.

60. Z. Xi, Y. Gao, G. Sirinakis, H. Guo and Y. Zhang, Single-molecule Observation of Helix Staggering, Sliding, and Coiled Coil Misfolding. *Proc. Natl. Acad. Sci. U. S. A.* **2012,** 109 (15), 5711-5716.

61. B. Ramm, J. Stigler, M. Hinczewski, D. Thirumalai, H. Herrmann, G. Woehlke and M. Rief, Sequence-resolved Free Energy Profiles of Stress-bearing Vimentin Intermediate Filaments. *Proc. Natl. Acad. Sci. U. S. A.* **2014,** 111 (31), 11359-11364.

62. P. López-García, M. Goktas, A. E. Bergues-Pupo, B. Koksch, D. Varón Silva and K. G. Blank, Structural Determinants of Coiled Coil Mechanics. *Phys. Chem. Chem. Phys.* **2019,** 21 (18), 9145-9149.

63. T. Lovell, F. Himo, W.-G. Han and L. Noodleman, Density Functional Methods Applied to Metalloenzymes. *Coord. Chem. Rev.* **2003,** 238–239, 211-232.

64. T. Dudev and C. Lim, Metal Binding Affinity and Selectivity in Metalloproteins: Insights from Computational Studies. *Annu. Rev. Biophys.* **2008,** 37, 97-116.

65. Z. Xu, Mechanics of Metal-Catecholate Complexes: The Roles of Coordination State and Metal Types. *Sci. Rep.* **2013,** 3, 2914-2914.

66. W. N. Lipscomb and N. Sträter, Recent Advances in Zinc Enzymology. *Chem. Rev.* **1996,** 96 (7), 2375-2434.

67. H. Lee, N. F. Scherer and P. B. Messersmith, Single-Molecule Mechanics of Mussel Adhesion. *Proc. Natl. Acad. Sci. U. S. A.* **2006,** 103 (35), 12999-13003.

68. Z. Xiao and A. G. Wedd, The Challenges of Determining Metal–Protein Affinities. *Nat. Prod. Rep.* **2010,** 27 (5), 768-789.

69. I. Dokmanić, M. Sikić and S. Tomić, Metals in Proteins: Correlation Between the Metal-ion Type, Coordination Number and the Amino-acid Residues Involved in the Coordination. *Acta Crystallogr., Sect. D: Biol. Crystallogr.* **2008,** 64 (Pt 3), 257-263.

70. S. P. Edgcomb and K. P. Murphy, Variability in the pKa of Histidine Side-chains Correlates with Burial within Proteins. *Proteins* **2002,** 49 (1), 1-6.

71. H. Takeuchi, Raman Structural Markers of Tryptophan and Histidine Side Chains in Proteins. *Biopolymers* **2003,** 72 (5), 305-317.

72. A. Barth, The Infrared Absorption of Amino Acid Side Chains. *Progr. Biophys. Mol. Biol.* **2000,** 74 (3), 141-173.

73. P. George, G. I. H. Hanania, D. H. Irvine and I. Abu-Issa, 1090. The Effect of Co-ordination on Ionization. Part IV. Imidazole and Its Ferrimyoglobin Complex. *J. Chem. Soc.* **1964**, 5689-5694.

74. S. Lindskog, Structure and Mechanism of Carbonic Anhydrase. *Pharmacol. Ther.* **1997,** 74 (1), 1-20.

75. G. Kurisu, Y. Kai and S. Harada, Structure of the Zinc-binding Site in the Crystal Structure of a Zinc Endoprotease from Streptomyces Caespitosus at 1 Å Resolution. *J. Inorg. Biochem.* **2000,** 82 (1), 225-228.

76. C. C. Broomell, S. F. Chase, T. Laue and J. H. Waite, Cutting Edge Structural Protein from the Jaws of Nereis virens. *Biomacromolecules* **2008,** 9 (6), 1669-1677.

77. R. J. Stewart, J. C. Weaver, D. E. Morse and J. H. Waite, The Tube Cement of *Phragmatopoma californica*: A Solid Foam. *J. Exp. Biol.* **2004,** 207 (26), 4727-4734.

78. F. H. Arnold and B. L. Haymore, Engineered Metal-binding Proteins: Purification to Protein Folding. *Science* **1991,** 252 (5014), 1796-1797.

79. S. Knecht, D. Ricklin, A. N. Eberle and B. Ernst, Oligohis-tags: Mechanisms of Binding to Ni2+-NTA Surfaces. *J. Mol. Recognit.* **2009,** 22 (4), 270-279.

80. S. Sjöberg, Critical Evaluation of Stability Constants of Metal-imidazole and Metal-histamine Systems (Technical Report). *Pure Appl. Chem.* **1997,** 69 (7), 1549-1570.

81. H. Irving and R. J. P. Williams, 637. The Stability of Transition-metal Complexes. *J. Chem. Soc.* **1953,** (0), 3192-3210.

82. L. Schmitt, M. Ludwig, H. E. Gaub and R. Tampé, A Metal-chelating Microscopy Tip as a New Toolbox for Single-Molecule Experiments by Atomic Force Microscopy. *Biophys. J.* **2000,** 78 (6), 3275-3285.

83. S.-S. Suh, B. L. Haymore and F. H. Arnold, Characterization of His-X3-His Sites in α-helices of Synthetic Metal-Binding Bovine Somatotropin. *Protein Eng.* **1991,** 4 (3), 301-305.

84. F. H. Arnold and J. H. Zhang, Metal-mediated Protein Stabilization. *Trends Biotechnol.* **1994,** 12 (5), 189-192.

85. J. T. Kellis, R. J. Todd and F. H. Arnold, Protein Stabilization by Engineered Metal Chelation. *Nat. Biotechnol.* **1991,** 9 (10), 994-995.

86. A. Muheim, R. J. Todd, D. R. Casimiro, H. B. Gray and F. H. Arnold, Ruthenium-mediated Protein Cross-linking and Stabilization. *J. Am. Chem. Soc.* **1993,** 115 (12), 5312-5313.

87. E. N. Salgado, J. Faraone-Mennella and F. A. Tezcan, Controlling Protein−Protein Interactions through Metal Coordination: Assembly of a 16-Helix Bundle Protein. *J. Am. Chem. Soc.* **2007,** 129 (44), 13374-13375.

88. E. N. Salgado, R. A. Lewis, J. Faraone-Mennella and F. A. Tezcan, Metal Mediated Self-Assembly of Protein Superstructures: Influence of Secondary Interactions on Protein Oligomerization and Aggregation. *J. Am. Chem. Soc.* **2008,** 130 (19), 6082-6084.

89. E. N. Salgado, R. A. Lewis, S. Mossin, A. L. Rheingold and F. A. Tezcan, Control of Protein Oligomerization Symmetry by Metal Coordination – C(2) and C(3) Symmetrical Assemblies through Cu(II) and Ni(II) Coordination. *Inorg. Chem.* **2009,** 48 (7), 2726-2728.

90. B. A. Krantz and T. R. Sosnick, Engineered Metal Binding Sites Map the Heterogeneous Folding Landscape of a Coiled Coil. *Nat. Struct. Biol.* **2001,** 8 (12), 1042-1047.

91. T. Tanaka, T. Mizuno, S. Fukui, H. Hiroaki, J.-i. Oku, K. Kanaori, K. Tajima and M. Shirakawa, Two-Metal Ion, Ni(II) and Cu(II), Binding α-Helical Coiled Coil Peptide. *J. Am. Chem. Soc.* **2004,** 126 (43), 14023-14028.

92. J. Aupič, F. Lapenta and R. Jerala, SwitCCh: Metal-Site Design for Controlling the Assembly of a Coiled-Coil Homodimer. *ChemBioChem* **2018,** 19 (23), 2453-2457.

93. Y. Cao, T. Yoo and H. Li, Single Molecule Force Spectroscopy Reveals Engineered Metal Chelation is a General Approach to Enhance Mechanical Stability of Proteins. *Proc. Natl. Acad. Sci. U. S. A.* **2008,** 105 (32), 11152-11157.

94. M. R. Ghadiri and C. Choi, Secondary Structure Nucleation in Peptides. Transition Metal Ion Stabilized alpha-helices. *J. Am. Chem. Soc.* **1990,** 112 (4), 1630-1632.

95. D. Shiga, D. Nakane, T. Inomata, H. Masuda, M. Oda, M. Noda, S. Uchiyama, K. Fukui, Y. Takano, H. Nakamura, T. Mizuno and T. Tanaka, The Effect of the Side Chain Length of Asp and Glu on Coordination Ctructure of Cu2+ in a *de novo* Designed Protein. *Biopolymers* **2009,** 91 (11), 907-916.

96. K. Suzuki, H. Hiroaki, D. Kohda, H. Nakamura and T. Tanaka, Metal Ion Induced Self-Assembly of a Designed Peptide into a Triple-Stranded α-Helical Bundle: A Novel Metal Binding Site in the Hydrophobic Core. *J. Am. Chem. Soc.* **1998,** 120 (50), 13008-13015.

97. A. L. Boyle, M. Rabe, N. S. A. Crone, G. G. Rhys, N. Soler, P. Voskamp, N. S. Pannu and A. Kros, Selective Coordination of Three Transition Metal Ions within a Coiled-coil Peptide Scaffold. *Chem. Sci.* **2019,** 10 (31), 7456-7465.

98. K. Pagel, S. C. Wagner, R. Rezaei Araghi, H. von Berlepsch, C. Böttcher and B. Koksch, Intramolecular Charge Interactions as a Tool to Control the Coiled-coil-to-amyloid Transformation. *Chem. - Eur. J.* **2008,** 14 (36), 11442-11451.

99. M. Harding, The Geometry of Metal-ligand Interactions Relevant to Proteins. II. Angles at the Metal Atom, Additional Weak Metal-donor Interactions. *Acta Crystallogr. Sect. D* **2000,** 56 (7), 857-867.

100. P. Chakrabarti, Geometry of Interaction of Metal Ions with Histidine Residues in Protein Structures. *Protein Eng., Des. Sel.* **1990,** 4 (1), 57-63.

101. S. Barber-Zucker, B. Shaanan and R. Zarivach, Transition Metal Binding Selectivity in Proteins and its Correlation with the Phylogenomic Classification of the Cation Diffusion Facilitator Protein Family. *Sci. Rep.* **2017,** 7 (1), 16381.

102. H. K. Lau and K. L. Kiick, Opportunities for Multicomponent Hybrid Hydrogels in Biomedical Applications. *Biomacromolecules* **2015,** 16 (1), 28-42.

103. H. Wang and S. C. Heilshorn, Adaptable Hydrogel Networks with Reversible Linkages for Tissue Engineering. *Adv. Mater.* **2015,** 27 (25), 3717-3736.

104. G. W. M. Vandermeulen and H.-A. Klok, Peptide/Protein Hybrid Materials: Enhanced Control of Structure and Improved Performance through Conjugation of Biological and Synthetic Polymers. *Macromol. Biosci.* **2004,** 4 (4), 383-398.

105. J. Kopeček, Hydrogel Biomaterials: A Smart Future? *Biomaterials* **2007,** 28 (34), 5185-5192.

106. S. E. D'Souza, M. H. Ginsberg and E. F. Plow, Arginyl-glycyl-aspartic Acid (RGD): A Cell Adhesion Motif. *Trends Biochem. Sci.* **1991,** 16, 246-250.

107. E. Prince and E. Kumacheva, Design and Applications of Man-made Biomimetic Fibrillar Hydrogels. *Nat. Rev. Mater.* **2019,** 4 (2), 99-115.

108. E. F. Banwell, E. S. Abelardo, D. J. Adams, M. A. Birchall, A. Corrigan, A. M. Donald, M. Kirkland, L. C. Serpell, M. F. Butler and D. N. Woolfson, Rational Design and Application of Responsive α-helical Peptide Hydrogels. *Nat. Mater.* **2009,** 8 (7), 596-600.

109. A. F. Dexter, N. L. Fletcher, R. G. Creasey, F. Filardo, M. W. Boehm and K. S. Jack, Fabrication and Characterization of Hydrogels Formed from Designer Coiled-coil Fibril-forming Peptides. *RSC Adv.* **2017,** 7 (44), 27260-27271.

110. J. Hume, J. Sun, R. Jacquet, P. D. Renfrew, J. A. Martin, R. Bonneau, M. L. Gilchrist and J. K. Montclare, Engineered Coiled-Coil Protein Microfibers. *Biomacromolecules* **2014,** 15 (10), 3503-3510.

111. L. K. Hill, M. Meleties, P. Katyal, X. Xie, E. Delgado-Fukushima, T. Jihad, C.-F. Liu, S. O’Neill, R. S. Tu, P. D. Renfrew, R. Bonneau, Y. Z. Wadghiri and J. K. Montclare,

Thermoresponsive Protein-Engineered Coiled-Coil Hydrogel for Sustained Small Molecule Release. *Biomacromolecules* **2019,** 20 (9), 3340-3351.

112. J. Kopeček and J. Yang, Smart Self-assembled Hybrid Hydrogel Biomaterials. *Angew. Chem., Int. Ed. Engl.* **2012,** 51 (30), 7396-7417.

113. C. Xu and J. J. Kopeček, Genetically Engineered Block Copolymers: Influence of the Length and Structure of the Coiled-Coil Blocks on Hydrogel Self-Assembly. *Pharm. Res.* **2008,** 25 (3), 674-682.

114. W. Shen, R. G. H. Lammertink, J. K. Sakata, J. A. Kornfield and D. A. Tirrell, Assembly of an Artificial Protein Hydrogel through Leucine Zipper Aggregation and Disulfide Bond Formation. *Macromolecules* **2005,** 38 (9), 3909-3916.

115. W. A. Petka, J. L. Harden, K. P. McGrath, D. Wirtz and D. A. Tirrell, Reversible Hydrogels from Self-Assembling Artificial Proteins. *Science* **1998,** 281 (5375), 389-392.

116. A. Buchberger, C. Simmons, N. Fahmi, R. Freeman and N. Stephanopoulos, Hierarchical Assembly of DNA Origami Nanostructures Using Coiled-coil Peptides. *J. Am. Chem. Soc.* **2020,** 142, 3, 1406–1416.

117. C. Wang, R. J. Stewart and J. Kopeček, Hybrid Hydrogels Assembled from Synthetic Polymers and Coiled-coil Protein Domains. *Nature* **1999,** 397 (6718), 417-420.

118. P. Jing, J. S. Rudra, A. B. Herr and J. H. Collier, Self-Assembling Peptide-Polymer Hydrogels Designed From the Coiled Coil Region of Fibrin. *Biomacromolecules* **2008,** 9 (9), 2438-2446.

119. J. Yang, C. Xu, C. Wang and J. Kopeček, Refolding Hydrogels Self-Assembled from N-(2-Hydroxypropyl)methacrylamide Graft Copolymers by Antiparallel Coiled-Coil Formation. *Biomacromolecules* **2006,** 7 (4), 1187-1195.

120. M. J. Glassman, J. Chan and B. D. Olsen, Reinforcement of Shear Thinning Protein Hydrogels by Responsive Block Copolymer Self-Assembly. *Adv. Funct. Mater.* **2013,** 23 (9), 1182-1193.

121. S. Dånmark, C. Aronsson and D. Aili, Tailoring Supramolecular Peptide–Poly(ethylene glycol) Hydrogels by Coiled Coil Self-Assembly and Self-Sorting. *Biomacromolecules* **2016,** 17 (6), 2260-2267.

122. L. J. Dooling and D. A. Tirrell, Engineering the Dynamic Properties of Protein Networks through Sequence Variation. *ACS Cent. Sci.* **2016,** 2 (11), 812-819.

123. E. M. Grad, I. Tunn, D. Voerman, A. S. de Léon, R. Hammink and K. G. Blank, Influence of Network Topology on the Viscoelastic Properties of Dynamically Crosslinked Hydrogels. *Frontiers in Chemistry* **2020,** 8, 536.

124. S. Zechel, M. D. Hager, T. Priemel and M. J. Harrington, Healing through Histidine: Bioinspired Pathways to Self-Healing Polymers via Imidazole–Metal Coordination. *Biomimetics* **2019,** 4 (1), 20.

125. H. Li, P. Yang, P. Pageni and C. Tang, Recent Advances in Metal-Containing Polymer Hydrogels. *Macromol. Rapid Commun.* **2017,** 38 (14), 1700109.

126. S. Basak, I. Singh, A. Banerjee and H.-B. Kraatz, Amino Acid-based Amphiphilic Hydrogels: Metal Ion Induced Tuning of Mechanical and Thermal Stability. *RSC Adv.* **2017,** 7 (24), 14461-14465.

127. N. Holten-Andersen, M. J. Harrington, H. Birkedal, B. P. Lee, P. B. Messersmith, K. Y. C. Lee and J. H. Waite, pH-induced Metal-ligand Cross-links Inspired by Mussel Yield Self-healing Polymer Networks with Near-covalent Elastic Moduli. *Proc. Natl. Acad. Sci. U. S. A.* **2011,** 108 (7), 2651-2655.

128. Q. Li, D. G. Barrett, P. B. Messersmith and N. Holten-Andersen, Controlling Hydrogel Mechanics via Bio-Inspired Polymer–Nanoparticle Bond Dynamics. *ACS Nano* **2016,** 10 (1), 1317-1324.

129. D. E. Fullenkamp, L. He, D. G. Barrett, W. R. Burghardt and P. B. Messersmith, Mussel-inspired Histidine-based Transient Network Metal Coordination Hydrogels. *Macromolecules* **2013,** 46 (3), 1167-1174.

130. S. C. Grindy, R. Learsch, D. Mozhdehi, J. Cheng, D. G. Barrett, Z. Guan, P. B. Messersmith and N. Holten-Andersen, Control of Hierarchical Polymer Mechanics with Bioinspired Metal-coordination Dynamics. *Nat. Mater.* **2015,** 14 (12), 1210-1216.

131. S. V. Wegner, F. C. Schenk, S. Witzel, F. Bialas and J. P. Spatz, Cobalt Cross-Linked Redox-Responsive PEG Hydrogels: From Viscoelastic Liquids to Elastic Solids. *Macromolecules* **2016,** 49 (11), 4229-4235.

132. S. C. Grindy and N. Holten-Andersen, Bio-inspired Metal-coordinateHydrogels with Programmable Viscoelastic Material Functions Controlled by Longwave UV Light. *Soft Matter* **2017,** 13 (22), 4057-4065.

133. M. A. Gonzalez, J. R. Simon, A. Ghoorchian, Z. Scholl, S. Lin, M. Rubinstein, P. Marszalek, A. Chilkoti, G. P. López and X. Zhao, Strong, Tough, Stretchable, and Self-Adhesive Hydrogels from Intrinsically Unstructured Proteins. *Adv. Mater.* **2017,** 29 (10), 1604743.

134. N. Kong, L. Fu, Q. Peng and H. Li, Metal Chelation Dynamically Regulates the Mechanical Properties of Engineered Protein Hydrogels. *ACS Biomater. Sci. Eng.* **2017,** 3 (5), 742-749.

135. R. Selegård, C. Aronsson, C. Brommesson, S. Dånmark and D. Aili, Folding Driven Self-Assembly of a Stimuli-Responsive Peptide-Hyaluronan Hybrid Hydrogel. *Sci. Rep.* **2017,** 7.

136. O. Rifaie-Graham, E. A. Apebende, L. K. Bast and N. Bruns, Self-Reporting Fiber-Reinforced Composites That Mimic the Ability of Biological Materials to Sense and Report Damage. *Adv. Mater.* **2018,** 30 (19), 1705483.

137. D. A. Davis, A. Hamilton, J. Yang, L. D. Cremar, D. Van Gough, S. L. Potisek, M. T. Ong, P. V. Braun, T. J. Martínez, S. R. White, J. S. Moore and N. R. Sottos, Force-induced Activation of Covalent Bonds in Mechanoresponsive Polymeric Materials. *Nature* **2009,** 459 (7243), 68-72.

138. S. Karthikeyan and R. P. Sijbesma, Probing Strain in Thermoplastic Elastomers Using Fluorescence Resonance Energy Transfer. *Macromolecules* **2009,** 42 (14), 5175-5178.

139. Z. Wang, Z. Ma, Y. Wang, Z. Xu, Y. Luo, Y. Wei and X. Jia, A Novel Mechanochromic and Photochromic Polymer Film: When Rhodamine Joins Polyurethane. *Adv. Mater.* **2015,** 27 (41), 6469-6474.

140. S. K. Park, I. Cho, J. Gierschner, J. H. Kim, J. H. Kim, J. E. Kwon, O. K. Kwon, D. R. Whang, J.-H. Park, B.-K. An and S. Y. Park, Stimuli-Responsive Reversible Fluorescence Switching in a Crystalline Donor–Acceptor Mixture Film: Mixed Stack Charge-Transfer Emission versus Segregated Stack Monomer Emission. *Angew. Chem. Int. Ed.* **2016,** 55 (1), 203-207.

141. Y. Sagara, M. Karman, E. Verde-Sesto, K. Matsuo, Y. Kim, N. Tamaoki and C. Weder, Rotaxanes as Mechanochromic Fluorescent Force Transducers in Polymers. *J. Am. Chem. Soc.* **2018,** 140 (5), 1584-1587.

142. J. M. Clough, J. van der Gucht and R. P. Sijbesma, Mechanoluminescent Imaging of Osmotic Stress-Induced Damage in a Glassy Polymer Network. *Macromolecules* **2017,** 50 (5), 2043-2053.

143. L. Wang, W. Zhou, Q. Tang, H. Yang, Q. Zhou and X. Zhang, Rhodamine-Functionalized Mechanochromic and Mechanofluorescent Hydrogels with Enhanced Mechanoresponsive Sensitivity. *Polymers* **2018,** 10 (9), 994.

144. P. B. Rapp, A. K. Omar, J. J. Shen, M. E. Buck, Z.-G. Wang and D. A. Tirrell, Analysis and Control of Chain Mobility in Protein Hydrogels. *J. Am. Chem. Soc.* **2017,** 139 (10), 3796-3804.

145. H. J. Kong, C. J. Kim, N. Huebsch, D. Weitz and D. J. Mooney, Noninvasive Probing of the Spatial Organization of Polymer Chains in Hydrogels Using Fluorescence Resonance Energy Transfer (FRET). *J. Am. Chem. Soc.* **2007,** 129 (15), 4518-4519.

146. J. W. Neubauer, N. Hauck, M. J. Männel, M. Seuss, A. Fery and J. Thiele, Mechanoresponsive Hydrogel Particles as a Platform for Three-Dimensional Force Sensing. *ACS Appl. Mater. Interfaces* **2019,** 11 (29), 26307-26313.

147. M. Taki, T. Yamashita, K. Yatabe and V. Vogel, Mechano-chromic Protein–polymer Hybrid Hydrogel to Visualize Mechanical Strain. *Soft Matter* **2019,** 15 (46), 9388-9393.

148. N. Bruns, K. Pustelny, L. M. Bergeron, T. A. Whitehead and D. S. Clark, Mechanical Nanosensor Based on FRET within a Thermosome: Damage-Reporting Polymeric Materials. *Angew. Chem. Int. Ed.* **2009,** 48 (31), 5666-5669.

149. J. N. Brantley, C. B. Bailey, J. R. Cannon, K. A. Clark, D. A. Vanden Bout, J. S. Brodbelt, A. T. Keatinge-Clay and C. W. Bielawski, Mechanically Modulating the Photophysical Properties of Fluorescent Protein Biocomposites for Ratio- and Intensiometric Sensors. *Angew. Chem. Int. Ed.* **2014,** 53 (20), 5088-5092.

150. R. Merindol, G. Delechiave, L. Heinen, L. H. Catalani and A. Walther, Modular Design of Programmable Mechanofluorescent DNA Hydrogels. *Nat. Comm.* **2019,** 10 (1), 528.

151. X. Wang and T. Ha, Defining Single Molecular Forces Required to Activate Integrin and Notch Signaling. *Science* **2013,** 340 (6135), 991-994.

152. Y. Zhang, C. Ge, C. Zhu and K. Salaita, DNA-based Digital Tension Probes Reveal Integrin Forces During Early Cell Adhesion. *Nat. Comm.* **2014,** 5 (1), 5167.

153. F. Chowdhury, I. T. S. Li, B. J. Leslie, S. Doğanay, R. Singh, X. Wang, J. Seong, S.-H. Lee, S. Park, N. Wang and T. Ha, Single Molecular Force Across Single Integrins Dictates Cell Spreading. *Integr. Biol.* **2015,** 7 (10), 1265-1271.

154. M. K. Lee, J. Park, X. Wang, M. Roein-Peikar, E. Ko, E. Qin, J. Lee, T. Ha and H. Kong, Rupture Force of Cell Adhesion Ligand Tethers Modulates Biological Activities of a Cell-Laden Hydrogel. *Chem. Comm.* **2016,** 52 (26), 4757-4760.

155. W. J. Polacheck and C. S. Chen, Measuring Cell-generated Forces: A Guide to the Available Tools. *Nat. Methods* **2016,** 13, 415.

156. I. Schoen, B. L. Pruitt and V. Vogel, The Yin-Yang of Rigidity Sensing: How Forces and Mechanical Properties Regulate the Cellular Response to Materials. *Annu. Rev. Mater. Res.* **2013,** 43 (1), 589-618.

157. M. Goktas and K. G. Blank, Molecular Force Sensors: From Fundamental Concepts toward Applications in Cell Biology. *Adv. Mater. Interfaces* **2017,** 4 (1), 1600441.

158. A. Bauer, L. Gu, B. Kwee, W. A. Li, M. Dellacherie, A. D. Celiz and D. J. Mooney, Hydrogel Substrate Stress-Relaxation Regulates the Spreading and Proliferation of Mouse Myoblasts. *Acta Biomater.* **2017,** 62, 82-90.

159. O. Chaudhuri, L. Gu, D. Klumpers, M. Darnell, S. A. Bencherif, J. C. Weaver, N. Huebsch, H.-p. Lee, E. Lippens, G. N. Duda and D. J. Mooney, Hydrogels with Tunable Stress Relaxation Regulate Stem Cell Fate and Activity. *Nat. Mater.* **2016,** 15 (3), 326-334.

160. J. Lou, R. Stowers, S. Nam, Y. Xia and O. Chaudhuri, Stress Relaxing Hyaluronic Acid-Collagen Hydrogels Promote Cell Spreading, Fiber Remodeling, and Focal Adhesion Formation in 3D Cell Culture. *Biomaterials* **2018,** 154, 213-222.

161. N. E. Zhou, C. M. Kay and R. S. Hodges, Synthetic model proteins. Positional effects of interchain hydrophobic interactions on stability of two-stranded alpha-helical coiled-coils. *J. Biol. Chem.* **1992,** 267 (4), 2664-2670.

162. M. M. Harding, The Geometry of Metal-ligand Interactions Relevant to Proteins. *Acta Crystallogr., Sect. D: Biol. Crystallogr.* **1999,** 55, 1432-1443.

163. E. H. C. Bromley, K. J. Channon, P. J. S. King, Z. N. Mahmoud, E. F. Banwell, M. F. Butler, M. P. Crump, T. R. Dafforn, M. R. Hicks, J. D. Hirst, A. Rodger and D. N. Woolfson, Assembly Pathway of a Designed α-Helical Protein Fiber. *Biophys. J.* **2010,** 98 (8), 1668-1676.

164. S. Schmidt, A. Reinecke, F. Wojcik, D. Pussak, L. Hartmann and M. J. Harrington, Metal-Mediated Molecular Self-Healing in Histidine-Rich Mussel Peptides. *Biomacromolecules* **2014,** 15 (5), 1644-1652.

165. A. Reinecke, L. Bertinetti, P. Fratzl and M. J. Harrington, Cooperative Behavior of a Sacrificial Bond Network and Elastic Framework in Providing Self-healing Capacity in Mussel Byssal Threads. *J. Struct. Biol.* **2016,** 196 (3), 329-339.

166. A. Mordvinkin and K. Saalwächter, Microscopic Observation of the Segmental Orientation Autocorrelation Function for Entangled and Constrained Polymer Chains. *J. Chem. Phys.* **2017,** 146 (9), 094902.

167. F. Lange, K. Schwenke, M. Kurakazu, Y. Akagi, U.-i. Chung, M. Lang, J.-U. Sommer, T. Sakai and K. Saalwächter, Connectivity and Structural Defects in Model Hydrogels: A

Combined Proton NMR and Monte Carlo Simulation Study. *Macromolecules* **2011,** 44 (24), 9666-9674.

168. R. B. Merrifield, Solid Phase Peptide Synthesis. I. The Synthesis of a Tetrapeptide. *J. Am. Chem. Soc.* **1963,** 85 (14), 2149-2154.

169. R. Sheppard, The Fluorenylmethoxycarbonyl Group in Solid Phase Synthesis. *J. Pept. Sci.* **2003,** 9 (9), 545-552.

170. R. Behrendt, P. White and J. Offer, Advances in Fmoc Solid-Phase Peptide Synthesis. *J. Pept. Sci.* **2016,** 22 (1), 4-27.

171. G. Wang, Post-translational Modifications of Natural Antimicrobial Peptides and Strategies for Peptide Engineering. *Curr. biotechnol.* **2012,** 1 (1), 72-79.

172. M. Amblard, J.-A. Fehrentz, J. Martinez and G. Subra, Methods and Protocols of Modern Solid Phase Peptide Synthesis. *Mol. Biotechnol.* **2006,** 33 (3), 239-254.

173. R. Ramage, L. Jiang, Y.-D. Kim, K. Shaw, J.-L. Park and H.-J. Kim, Comparative Studies of Nsc and Fmoc as Nα-protecting Groups for SPPS. *J. Pept. Sci.* **1999,** 5 (4), 195-200.

174. K. A. Dave, M. J. Headlam, T. P. Wallis and J. J. Gorman, Preparation and Analysis of Proteins and Peptides Using MALDI TOF/TOF Mass Spectrometry. *Curr. Prot. Protein Sci.* **2011,** 63 (1), 16.13.11-16.13.21.

175. F. Hillenkamp, M. Karas, R. C. Beavis and B. T. Chait, Matrix-Assisted Laser Desorption/Ionization Mass Spectrometry of Biopolymers. *Analyt. Chem.* **1991,** 63 (24), 1193A-1203A.

176. S. M. Kelly, T. J. Jess and N. C. Price, How to Study Proteins by Circular Dichroism. *Biochim. Biophys. Acta* **2005,** 1751 (2), 119-139.

177. J. W C Johnson, Secondary Structure of Proteins Through Circular Dichroism Spectroscopy. *Annu. Rev. Biophys. Biophys. Chem.* **1988,** 17 (1), 145-166.

178. N. J. Greenfield, Using Circular Dichroism Collected as a Function of Temperature to Determine the Thermodynamics of Protein Unfolding and Binding Interactions. *Nat. Protoc.* **2006,** 1 (6), 2527-2535.

179. N. E. Zhou, C. M. Kay and R. S. Hodges, The Role of Interhelical Ionic Interactions in Controlling Protein Folding and Stability. De novo Designed Synthetic Two-stranded alpha-helical Coiled-coils. *J. Mol. Biol.* **1994,** 237 (4), 500-512.

180. S. Y. Lau, A. K. Taneja and R. S. Hodges, Synthesis of a Model Protein of Defined Secondary and Quaternary Structure. Effect of Chain Length on the Stabilization and Formation of Two-stranded alpha-helical Coiled-coils. *J. Biol. Chem.* **1984,** 259 (21), 13253-13261.

181. M. J. Pandya, G. M. Spooner, M. Sunde, J. R. Thorpe, A. Rodger and D. N. Woolfson, Sticky-end Assembly of a Designed Peptide Fiber Provides Insight into Protein Fibrillogenesis. *Biochemistry* **2000,** 39 (30), 8728-8734.

182. S. A. Potekhin, T. N. Melnik, V. Popov, N. F. Lanina, A. A. Vazina, P. Rigler, A. S. Verdini, G. Corradin and A. V. Kajava, De novo Design of Fibrils Made of Short α-helical Coiled Coil Peptides. *Chem. Biol.* **2001,** 8 (11), 1025-1032.

183. AppliedPhotophysics, User Manual Global 3 Analysis Software. **2018**, 1-25.

184. D. K. Lee, J. In and S. Lee, Standard Deviation and Standard Error of the Mean. *Korean J. Anesthesiol.* **2015,** 68 (3), 220-223.

185. C. V. Raman and K. S. Krishnan, A New Type of Secondary Radiation. *Nature* **1928,** 121 (3048), 501-502.

186. Z. Movasaghi, S. Rehman and D. I. U. Rehman, Raman Spectroscopy of Biological Tissues. *Appl. Spectrosc. Rev.* **2007,** 42 (5), 493-541.

187. P. Larkin.Infrared and Raman Spectroscopy,**2011**, Elsevier.

188. J. Bandekar, Amide Modes and Protein Conformation. *Biochim. Biophys. Acta, Protein Struct. Mol. Enzymol.* **1992,** 1120 (2), 123-143.

189. A. V. Mikhonin, Z. Ahmed, A. Ianoul and S. A. Asher, Assignments and Conformational Dependencies of the Amide III Peptide Backbone UV Resonance Raman Bands. *J. Phys. Chem. B* **2004,** 108 (49), 19020-19028.

190. G. Zhu, X. Zhu, Q. Fan and X. Wan, Raman Spectra of Amino Acids and Their Aqueous Solutions. *Spectrochim. Acta, Part A* **2011,** 78 (3), 1187-1195.

191. T. Miura, T. Satoh, A. Hori-i and H. Takeuchi, Raman Marker Bands of Metal Coordination Cites of Histidine Side Chains in Peptides and Proteins. *J. Raman Spec.* **1998,** 29 (1), 41-47.

192. L. T. C. França, E. Carrilho and T. B. L. Kist, A Review of DNA Sequencing Techniques. *Q. Rev. Biophys.* **2002,** 35 (2), 169-200.

193. C. J. Wienken, P. Baaske, U. Rothbauer, D. Braun and S. Duhr, Protein-binding Assays in Biological Liquids Using Microscale Thermophoresis. *Nat. Comm.* **2010,** 1 (1), 100.

194. G.-J. Kremers, S. G. Gilbert, P. J. Cranfill, M. W. Davidson and D. W. Piston, Fluorescent Proteins at a Glance. *J. Cell Sci.* **2011,** 124 (Pt 2), 157-160.

195. J. R. Lakowicz.Principles of Fluorescence Spectroscopy. Baltimore, USA, **2006**, Springer

196. S. Smith, L. Finzi and C. Bustamante, Direct Mechanical Measurements of the Elasticity of Single DNA Molecules by Using Magnetic Beads. *Science* **1992,** 258 (5085), 1122-1126.

197. A. Ashkin, Optical Trapping and Manipulation of Neutral Particles Using Lasers. *Proc. Natl. Acad. Sci. U. S. A.* **1997,** 94 (10), 4853-4860.

198. E. Florin, V. Moy and H. Gaub, Adhesion Forces Between Individual Ligand-Receptor Pairs. *Science* **1994,** 264 (5157), 415-417.

199. A. Engel, Biological Applications of Scanning Probe Microscopes. *Annu. Rev. Biophys. Biophys. Chem.* **1991,** 20 (1), 79-108.

200. M. L. Hughes and L. Dougan, The Physics of Pulling Polyproteins: A Review of Single Molecule Force Spectroscopy Using the AFM to Study Protein Unfolding. *Rep. Prog. Phys.* **2016,** 79 (7), 076601.

201. J. L. Hutter and J. Bechhoefer, Calibration of Atomic-Force Microscope Tips. *Rev. Sci. Instrum.* **1993,** 64 (7), 1868-1873.

202. J. N. Milstein and J.-C. Meiners (2013). Worm-Like Chain (WLC) Model. Encyclopedia of Biophysics. G. C. K. Roberts. Berlin, Heidelberg, Springer Berlin Heidelberg**:** 2757-2760.

203. F. Oesterhelt, Rief, M., Gaub, H.E., Single Molecule Force Spectroscopy by AFM Indicates Helical Structure of Poly(ethylene-glycol) in Water. *New J. Phys.* **1999,** 1 (6), 6.1-6.11.

204. K. J. Laidler and M. C. King, Development of Transition-State Theory. *J. Phys. Chem.* **1983,** 87 (15), 2657-2664.

205. H. A. Kramers, Brownian Motion in a Field of Force and the Diffusion Model of Chemical Reactions. *Physica* **1940,** 7 (4), 284-304.

206. M. Guthold, R. Superfine and R. M. Taylor, The Rules are Changing: Force Measurements on Single Molecules and How They Relate to Bulk Reaction Kinetics and Energies. *Biomed. Microdevices* **2001,** 3 (1), 9-18.

207. G. I. Bell, Models for the Specific Adhesion of Cells to Cells. *Science (New York, N.Y.)* **1978,** 200 (4342), 618-627.

208. J. L. Zimmermann, T. Nicolaus, G. Neuert and K. Blank, Thiol-based, Site-specific and Covalent Immobilization of Biomolecules for Single-molecule Experiments. *Nat. Protoc.* **2010,** 5 (6), 975-985.

209. E. Evans, Probing the Relation between Force, Lifetime and Chemistry in Single Molecular Bonds. *Annu. Rev. Biophys. Biomol. Struct.* **2001,** 30, 105-128.

210. T. G. Mezger.The Rheology Handbook, 4th edition. Hannover, Germany, **2014**, Vincentz Network.

211. C. Yan and D. J. Pochan, Rheological Properties of Peptide-based Hydrogels for Biomedical and Other Applications. *Chem. Soc. Rev.* **2010,** 39 (9), 3528-3540.

212. A. Hajighasem and K. Kabiri, Cationic Highly Alcohol-Swellable Gels: Synthesis and Characterization. *J. Polym. Res.* **2013,** 20 (8), 218.

213. S. C. Grindy, M. Lenz and N. Holten-Andersen, Engineering Elasticity and Relaxation Time in Metal-Coordinate Cross-Linked Hydrogels. *Macromolecules* **2016,** 49 (21), 8306-8312.

214. R. G. Palmer, D. L. Stein, E. Abrahams and P. W. Anderson, Models of Hierarchically Constrained Dynamics for Glassy Relaxation. *Phys. Rev. Lett.* **1984,** 53 (10), 958-961.

215. H. Giesekus, Die Elastizität von Flüssigkeiten. *Rheol. Acta* **1966,** 5 (1), 29-35.

216. N. Cathébras, A. Collet, M. Viguier and J.-F. Berret, Synthesis and Linear Viscoelasticity of Fluorinated Hydrophobically Modified Ethoxylated Urethanes (F-HEUR). *Macromolecules* **1998,** 31 (4), 1305-1311.

217. C. A. Schneider, W. S. Rasband and K. W. Eliceiri, NIH Image to ImageJ: 25 years of image analysis. *Nat. Methods* **2012,** 9 (7), 671-675.

218. E. Lacroix, A. R. Viguera and L. Serrano, Elucidating the Folding Problem of α-helices: Local Motifs, Long-range Electrostatics, Ionic-strength Dependence and Prediction of NMR Parameters. *J. Mol. Biol.* **1998,** 284 (1), 173-191.

219. A. N. Lupas, J. Bassler and S. Dunin-Horkawicz, The Structure and Topology of α-Helical Coiled Coils. *Subcell. Biochem.* **2017,** 82, 95-129.

220. R. F. See, R. A. Kruse and W. M. Strub, Metal−Ligand Bond Distances in First-Row Transition Metal Coordination Compounds: Coordination Number, Oxidation State, and Specific Ligand Effects. *Inorg. Chem.* **1998,** 37 (20), 5369-5375.

221. I. Tunn, A. S. de Léon, K. G. Blank and M. J. Harrington, Tuning Coiled Coil Stability with Histidine-Metal Coordination. *Nanoscale* **2018,** 10 (48), 22725-22729.

222. F. Jehle, P. Fratzl and M. J. Harrington, Metal-Tunable Self-Assembly of Hierarchical Structure in Mussel-Inspired Peptide Films. *ACS Nano* **2018,** 12 (3), 2160-2168.

223. E. Brandenburg, H. V. Berlepsch, J. Leiterer, F. Emmerling and B. Koksch, Formation of α-helical Nanofibers by Mixing β-structured and α-helical Coiled Coil Peptides. *Biomacromolecules* **2012,** 13 (11), 3542-3551.

224. H. Dong, S. E. Paramonov and J. D. Hartgerink, Self-Assembly of α-Helical Coiled Coil Nanofibers. *J. Am. Chem. Soc.* **2008,** 130 (41), 13691-13695.

225. K. Pagel, T. Seri, H. von Berlepsch, J. Griebel, R. Kirmse, C. Böttcher and B. Koksch, How Metal Ions Affect Amyloid Formation: Cu2+- and Zn2+-Sensitive Peptides. *ChemBioChem* **2008,** 9 (4), 531-536.

226. I. Tunn, M. J. Harrington and K. G. Blank, Bioinspired Histidine–Zn2+ Coordination for Tuning the Mechanical Properties of Self-Healing Coiled Coil Cross-Linked Hydrogels. *Biomimetics* **2019,** 4 (1), 25.

227. H. Zheng, M. Chruszcz, P. Lasota, L. Lebioda and W. Minor, Data Mining of Metal Ion Environments Present in Protein Structures. *J. Inorg. Biochem.* **2008,** 102 (9), 1765-1776.

228. G. Zhang, L. Senak and D. J. Moore, Measuring Changes in Chemistry, Composition, and Molecular Structure within Hair Fibers by Infrared and Raman Spectroscopic Imaging. *J. Biomed. Opt.* **2011,** 16 (5), 056009.

229. C. P. Lindsey and G. D. Patterson, Detailed Comparison of the Williams–Watts and Cole–Davidson Functions. *J. Chem. Phys.* **1980,** 73 (7), 3348-3357.

230. D. L. Daugherty and S. H. Gellman, A Fluorescence Assay for Leucine Zipper Dimerization: Avoiding Unintended Consequences of Fluorophore Attachment. *J. Am. Chem. Soc.* **1999,** 121 (18), 4325-4333.

231. C. A. M. Seidel, A. Schulz and M. H. M. Sauer, Nucleobase-Specific Quenching of Fluorescent Dyes. 1. Nucleobase One-Electron Redox Potentials and Their Correlation with Static and Dynamic Quenching Efficiencies. *J. Phys. Chem.* **1996,** 100 (13), 5541-5553.

232. M. Merzlyakov and K. Hristova, Forster Resonance Energy Transfer Measurements of Transmembrane Helix Dimerization Energetics. *Methods Enzymol.* **2008,** 450, 107-127.

233. W. D. Kohn, C. M. Kay, B. D. Sykes and R. S. Hodges, Metal Ion Induced Folding of a de Novo Designed Coiled-Coil Peptide. *J. Am. Chem. Soc.* **1998,** 120 (6), 1124-1132.

234. M. Conti, G. Falini and B. Samorì, How Strong Is the Coordination Bond between a Histidine Tag and Ni – Nitrilotriacetate? An Experiment of Mechanochemistry on Single Molecules. *Angew. Chem. Int. Ed.* **2000,** 39 (1), 215-218.

235. F. Kienberger, G. Kada, H. J. Gruber, V. P. Pastushenko, C. Riener, M. Trieb, H.-G. Knaus, H. Schindler and P. Hinterdorfer, Recognition Force Spectroscopy Studies of the NTA-His6 Bond. *Single Mol.* **2000,** 1 (1), 59-65.

236. P. López García, A. D. De Araujo, I. Tunn, A. E. Bergues-Pupo, D. Fairlie and K. G. Blank, Fortified Coiled Coils: Enhancing Mechanical Stability with Lactam or Metal Staples. *Angew. Chem. Int. Ed., accepted,* **2020**.

237. C. N. Z. Schmitt, A. Winter, L. Bertinetti, A. Masic, P. Strauch and M. J. Harrington, Mechanical Homeostasis of a DOPA-enriched Biological Coating from Mussels in Response to Metal Variation. *J. R. Soc., Interface* **2015,** 12 (110), 20150466.

238. T. L. Coombs and P. J. Keller, Mytilus Byssal Threads as an Environmental Marker for Metals. *Aquat. Toxicol.* **1981,** 1 (5), 291-300.

239. S. S. Nabavi, M. J. Harrington, P. Fratzl and M. A. Hartmann, Influence of Sacrificial Bonds on the Mechanical Behaviour of Polymer Chains. *Bioinspired, Biomimetic Nanobiomater.* **2014,** 3 (3), 139-145.

240. M. K. Gupta, K. A. Becknell, M. G. Crosby, N. M. Bedford, J. Wright, P. B. Dennis and R. R. Naik, Programmable Mechanical Properties from a Worm Jaw-Derived Biopolymer through Hierarchical Ion Exposure. *ACS Appl. Mater. Interfaces* **2018,** 10 (38), 31928-31937.

241. P. M. A. Gadsby and A. J. Thomson, Identification of the Imidazolate Anion as a Ligand in Metmyoglobin by Near-infrared Magnetic Circular Dichroism Spectroscopy. *FEBS Letters* **1982,** 150 (1), 59-63.

242. C. Johnson, R. Shepherd, B. Marr, S. O'Donnell and W. Dressick, Affinities of Imidazolate and Imidazole Ligands for Pentacyanoiron(III). *J. Am. Chem. Soc.* **1980,** 102, 20, 6227–6235.

243. A. Trapaidze, M. D'Antuono, P. Fratzl and M. J. Harrington, Exploring Mussel Byssus Fabrication with Peptide-Polymer Hybrids: Role of pH and Metal Coordination in Self-Assembly and Mechanics of Histidine-rich Domains. *Eur. Polym. J.* **2018,** 109, 229-236.

244. T. Miura, K. Suzuki, N. Kohata and H. Takeuchi, Metal Binding Modes of Alzheimer's Amyloid β-peptide in Insoluble Aggregates and Soluble Complexes. *Biochemistry* **2000,** 39 (23), 7024-7031.

245. S. Lin and L. Gu, Influence of Crosslink Density and Stiffness on Mechanical Properties of Type I Collagen Gel. *Materials* **2015,** 8 (2), 551-560.

246. J. Wątły, A. Hecel, M. Rowińska-Żyrek and H. Kozłowski, Impact of Histidine Spacing on Modified Polyhistidine Tag – Metal Ion Interactions. *Inorg. Chim. Acta* **2018,** 472, 119-126.

247. A. Reinecke, G. Brezesinski and M. J. Harrington, pH-Responsive Self-Organization of Metal-Binding Protein Motifs from Biomolecular Junctions in Mussel Byssus. *Adv. Mater. Interfaces* **2017,** 4 (1), 1600416.

248. K. Zhang, W. Yuan, K. Wei, B. Yang, X. Chen, Z. Li, Z. Zhang and L. Bian, Highly Dynamic Nanocomposite Hydrogels Self-Assembled by Metal Ion-Ligand Coordination. *Small* **2019,** 15 (15), 1900242.

249. L. Nian, Y. Hu, C. Fu, C. Song, J. Wang and J. Xiao, Fluorescence Self-Quenching Assay for the Detection of Target Collagen Sequences Using a Short Probe Peptide. *Talanta* **2018,** 176, 492-498.

250. H. Gradišar and R. Jerala, De Novo Design of Orthogonal Peptide Pairs Forming Parallel Coiled-coil Heterodimers. *J. Pept. Sci.* **2011,** 17 (2), 100-106.

251. R. O. Crooks, A. Lathbridge, A. S. Panek and J. M. Mason, Computational Prediction and Design for Creating Iteratively Larger Heterospecific Coiled Coil Sets. *Biochemistry* **2017,** 56 (11), 1573-1584.

252. I. Drobnak, H. Gradišar, A. Ljubetič, E. Merljak and R. Jerala, Modulation of Coiled-Coil Dimer Stability through Surface Residues while Preserving Pairing Specificity. *J. Am. Chem. Soc.* **2017,** 139 (24), 8229-8236.

253. A. E. Bergues-Pupo, K. G. Blank, R. Lipowsky and A. Vila Verde, Trimeric Coiled Coils Expand the Range of Strength, Toughness and Dynamics of Coiled Coil Motifs Under Shear. *Phys. Chem. Chem. Phys.* **2018,** 20, 29105.

254. B. C. Root, L. D. Pellegrino, E. D. Crawford, B. Kokona and R. Fairman, Design of a Heterotetrameric Coiled Coil. *Protein Sci.* **2009,** 18 (2), 329-336.

255. R. Fairman, H.-G. Chao, T. B. Lavoie, J. J. Villafranca, G. R. Matsueda and J. Novotny, Design of Heterotetrameric Coiled Coils: Evidence for Increased Stabilization by Glu-−Lys+ Ion Pair Interactions. *Biochemistry* **1996,** 35 (9), 2824-2829.

256. A. S. de Leon, C. Huster, P. Lopez-Garcia, I. Tunn, M. Goktas, E. M. Grad, K. Kroy and K. G. Blank, Fracture behavior of dynamically crosslinked starPEG networks. *in preparation* **2020**.

257. B. L. LeSavage, N. A. Suhar, C. M. Madl and S. C. Heilshorn, Production of Elastin-like Protein Hydrogels for Encapsulation and Immunostaining of Cells in 3D. *J. Visualized Exp.* **2018,** (135), 57739.

258. Y.-N. Zhang, R. K. Avery, Q. Vallmajo-Martin, A. Assmann, A. Vegh, A. Memic, B. D. Olsen, N. Annabi and A. Khademhosseini, A Highly Elastic and Rapidly Crosslinkable Elastin-Like Polypeptide-Based Hydrogel for Biomedical Applications. *Adv. Funct. Mater.* **2015,** 25 (30), 4814-4826.

List of figures

List of tables

Appendix

Table of contents

Supplementary figures

Supplementary tables

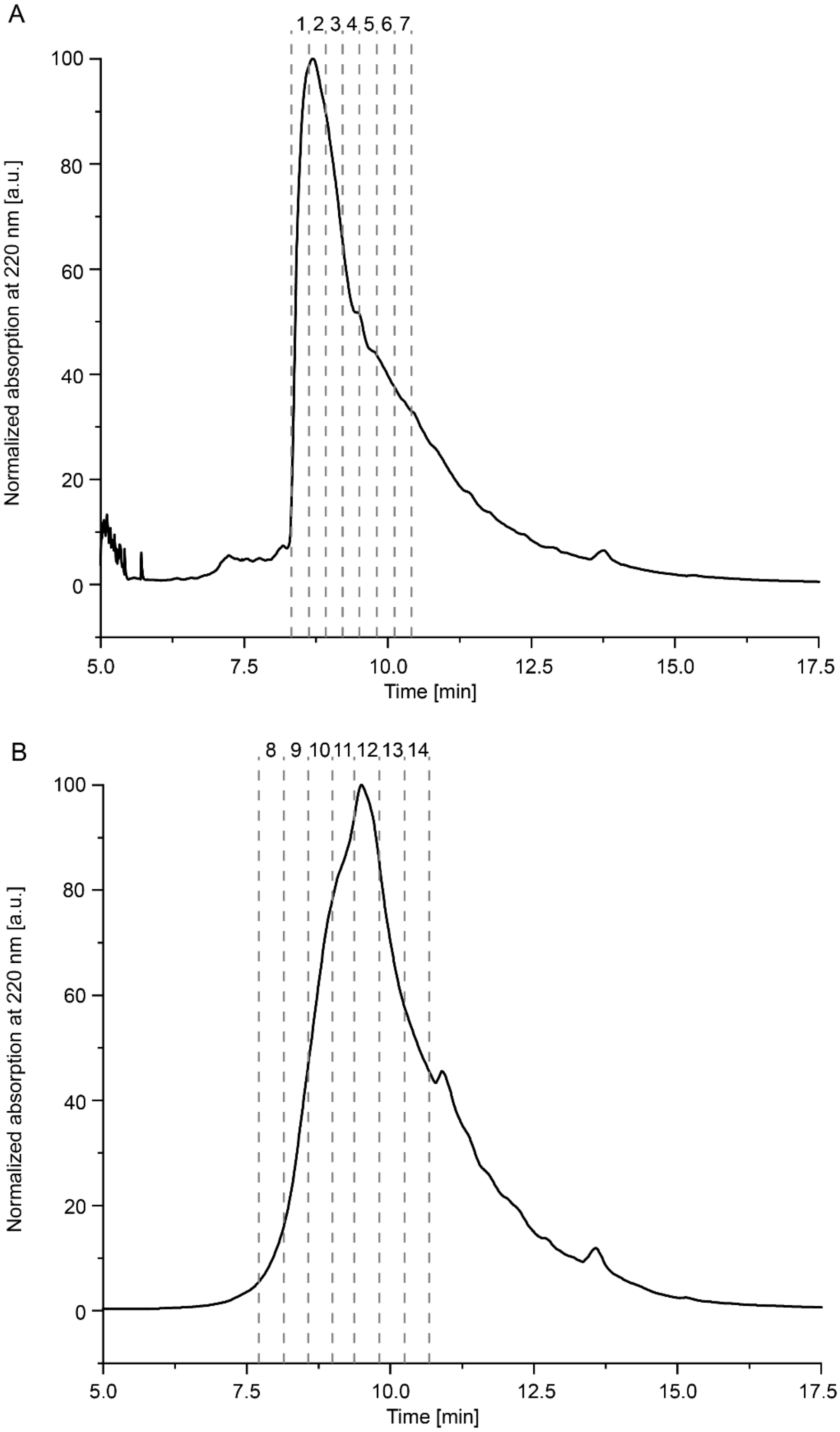

Figure S1: Preparative HPLC chromatograms of $A_{4H\perp}$. A) Preparative run 1 with the fractions 1-7. B) Preparative run 2 with the fractions 9-14. A gradient from 20 % ACN with 0.1 % TFA to 100 % ACN with 0.1 % TFA was applied over 30 min with a flow rate of 25 ml min^{-1}. The absorbance at 220 nm was monitored and fractions of 3 ml were collected. Fraction 1, 4, 5, 6, 10 and 11 were used for the measurements.

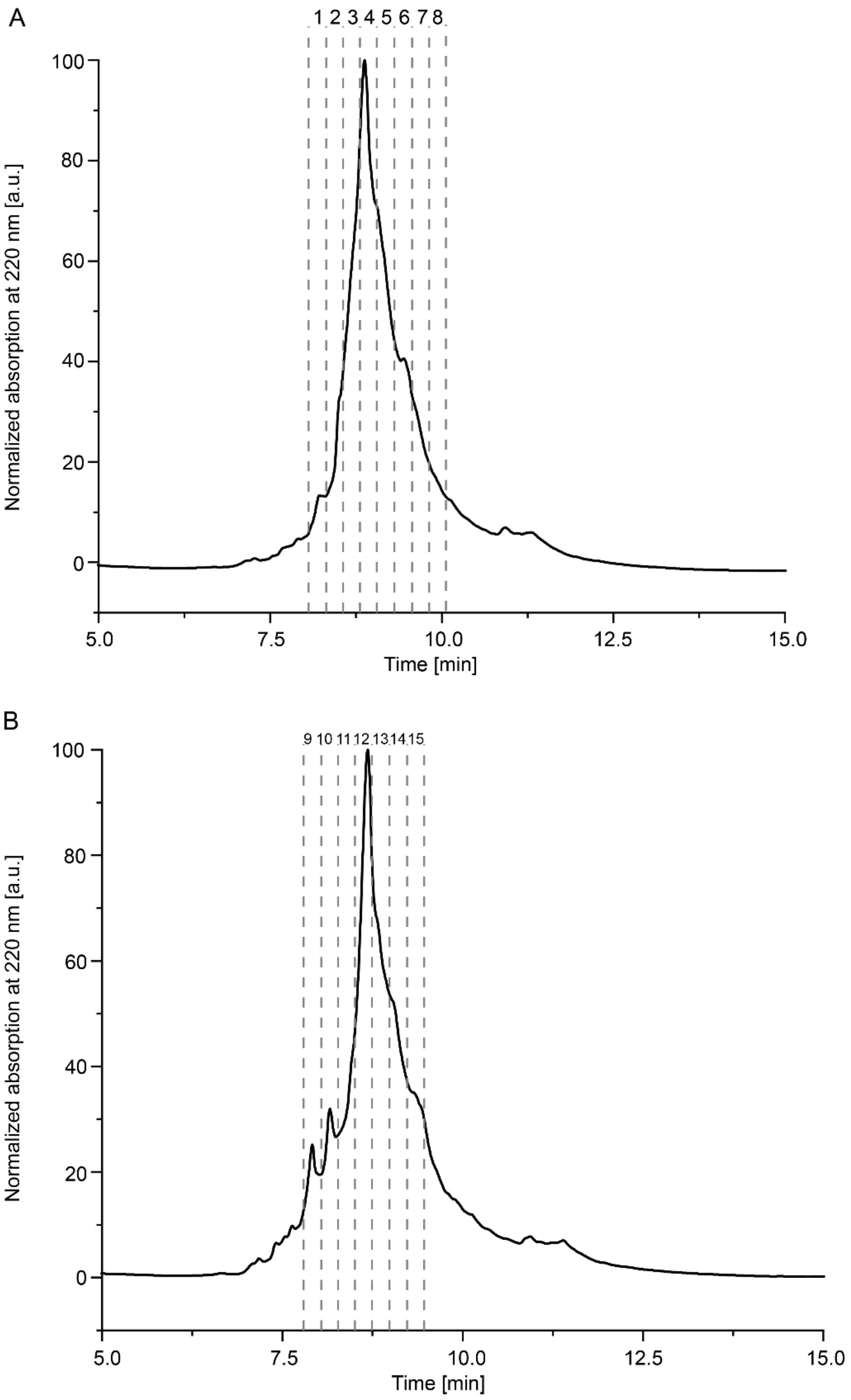

Figure S2: Preparative HPLC chromatograms of $\mathbf{B_{4H\perp}}$. A) Preparative run 1 with the fractions 1-8. B) Preparative run 2 with the fractions 9-18. A gradient from 10 % ACN with 0.1 % TFA to 100 % ACN with 0.1 % TFA was applied over 30 min with a flow rate of 25 ml min^{-1}. The absorbance at 220 nm was monitored and fractions of 3 ml were collected. Fraction 4, 6, 12 and 13 were used for the measurements.

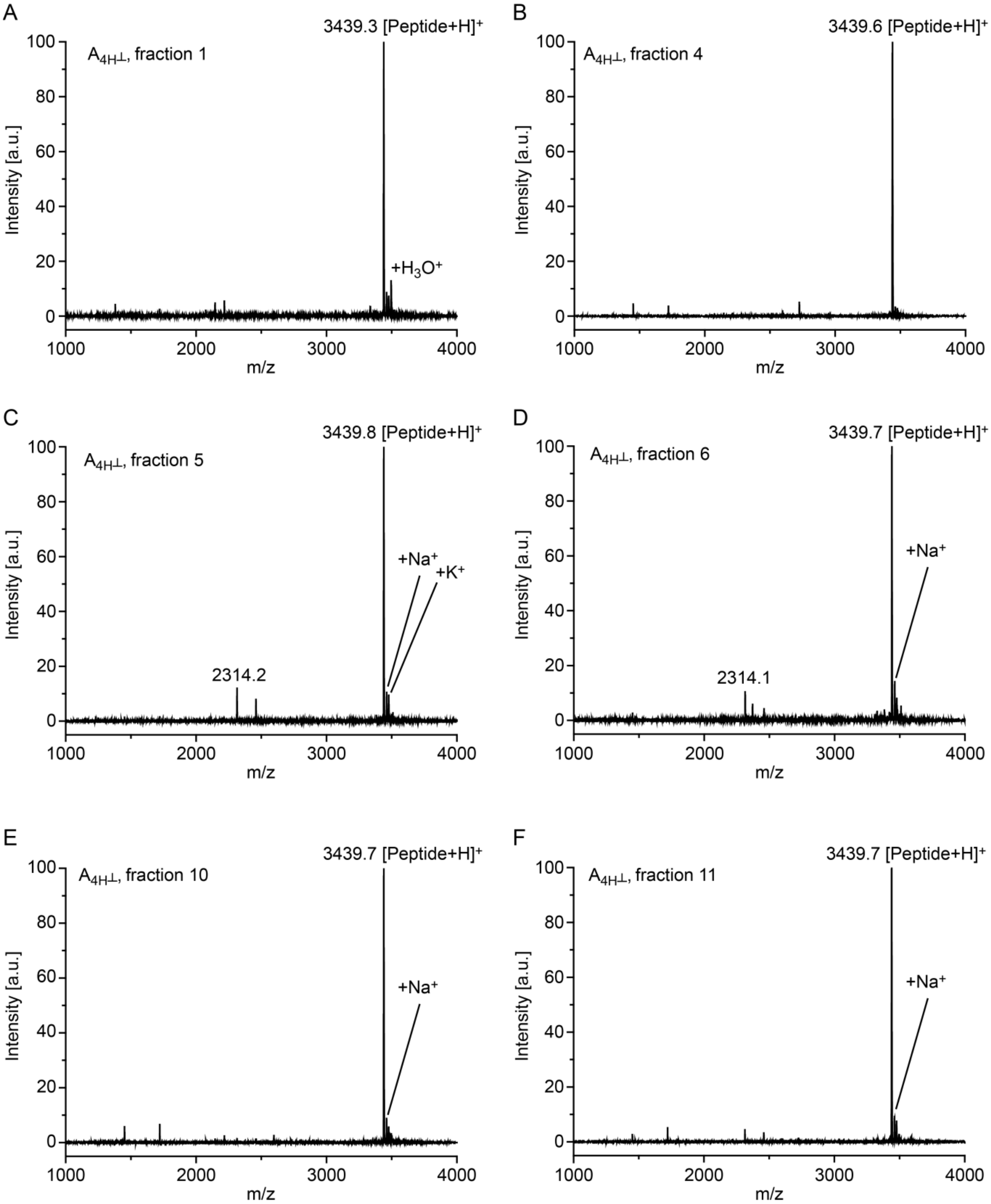

Figure S3: MALDI spectra of the peptide $A_{4H\perp}$ fractions used (A – F). As matrix, 2,5-dihydrobenzoic acid (DHB) was used. The measurements were performed in the positive mode and the spectra were normalized from 0 to 100 (maximum intensity). The theoretical mass of $A_{4H\perp}$ is 3437.8 g mol^{-1}. Sodium adduct: Na^+; potassium adduct: K^+; hydronium adduct: H_3O^+. (This figure was adapted and reproduced from ref. [226].)

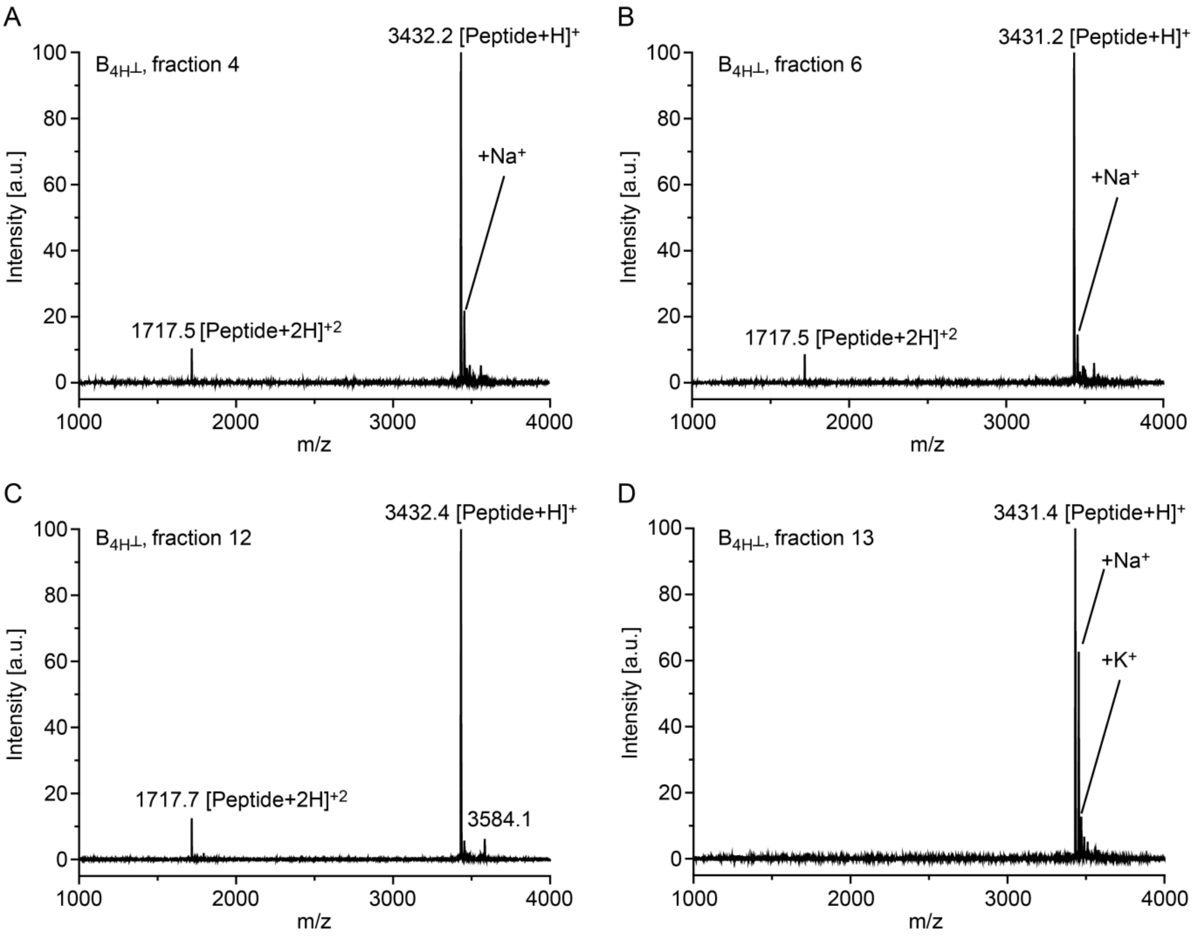

Figure S4: MALDI spectra of the peptide $B_{4H\perp}$ fractions used (A – D). As matrix, 2,5-dihydrobenzoic acid (DHB) was used. The measurements were performed in the positive mode and the spectra were normalized from 0 to 100 (maximum intensity). The theoretical mass of $B_{4H\perp}$ is 3430.2 g mol^{-1}. Sodium adduct: Na$^+$; potassium adduct: K$^+$.(This figure was adapted and reproduced from ref. [226].)

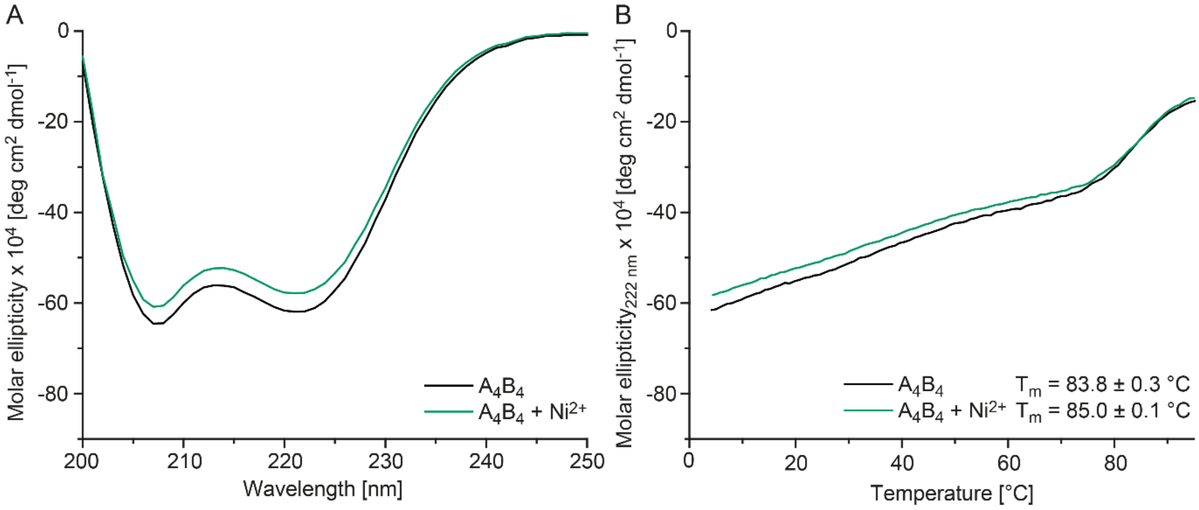

Figure S5: Circular dichroism spectra of the reference CC A_4B_4. A) Spectra of the CC, measured in the presence and absence of Ni^{2+} (3:1 Ni^{2+}:His) at 20 °C in PIPPS buffer. B) Thermal unfolding of the CC followed at 222 nm. The peptide concentration was 50 µM. The molar ellipticity was calculated using **Equation 1**. The CC data is the average of three measurements. (Reproduced with permission from ref. [221], published in 2018 by the Royal Society of Chemistry.)

Table S1: Cantilever calibration data for the dynamic SMFS experiment, performed with $A_{4HII}B_{4HII}$. The spring constant k_s of the cantilevers was determined using the thermal noise method [201].

Sample	**$A_{4HII}B_{4HII}$**		**$A_{4HII}B_{4HII}$ + 1 mM $NiCl_2$**	
Parameter	Sensitivity [nm V^{-1}]	k_s [N m^{-1}]	Sensitivity [nm V^{-1}]	k_s [N m^{-1}]
Cantilever 1	44.80	0.0170	46.42	0.0175
Cantilever 2	43.50	0.0155	43.92	0.0190
Cantilever 3	52.42	0.0142	45.85	0.0250

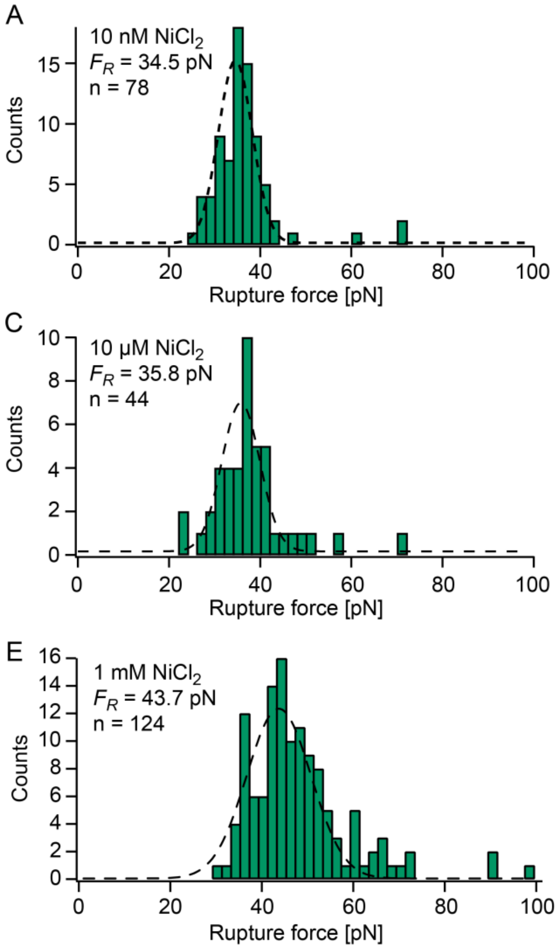

Figure S6: Single molecule force spectroscopy of $A_{4HII}B_{4HII}$ performed with different concentrations of Ni^{2+}. The following concentration were used: A) 10 nm, B) 1 µM, C) 10 µM, D) 100 µM, E) 1 mM and F) 10 mM $NiCl_2$. For all measurements, the retract speed was 400 nm s^{-1}. The most probable rupture force F_R was obtained from the Gaussian fit to the histogram.

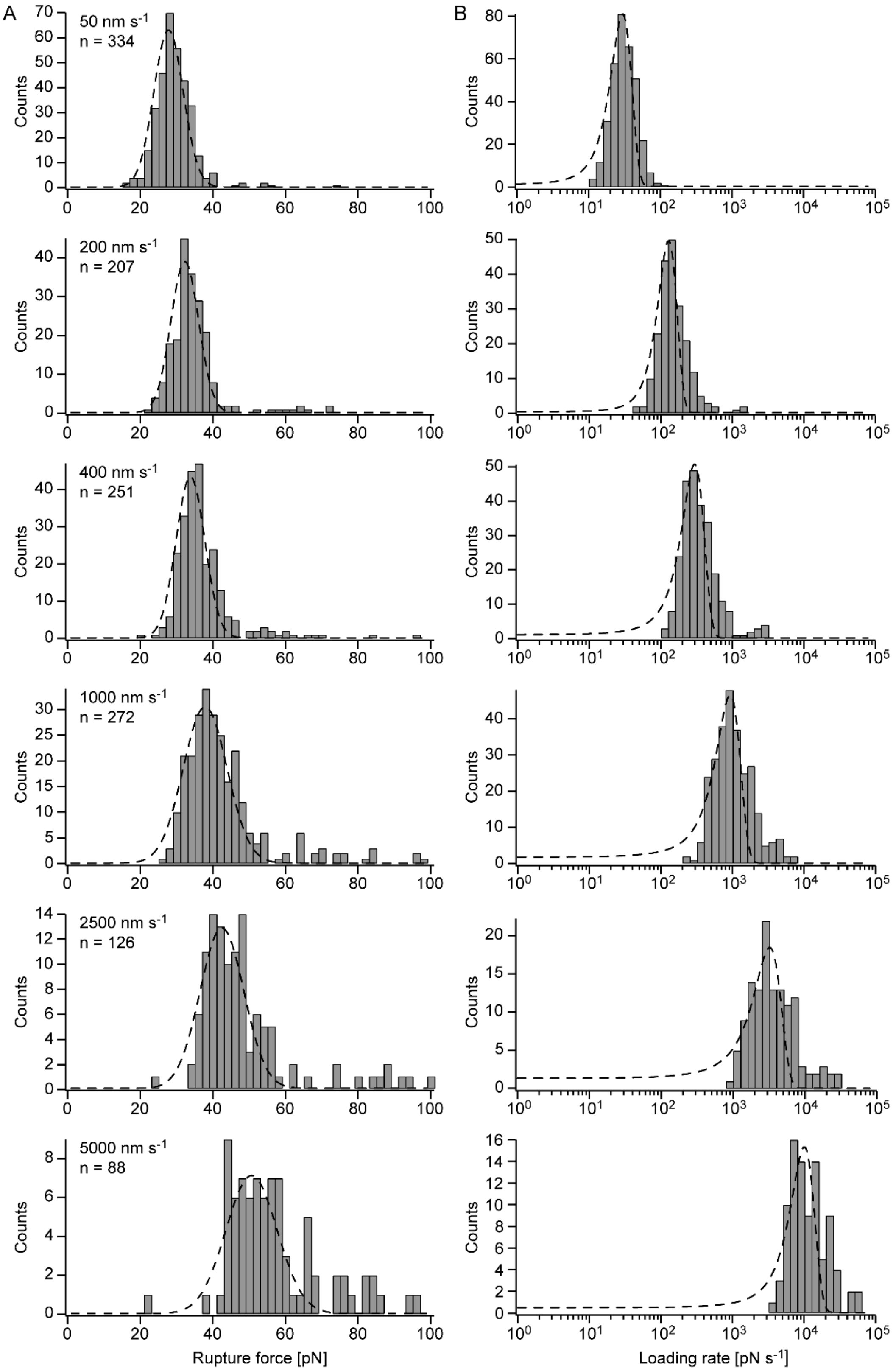

Figure S7: Representative data set of a dynamic SMFS measurement of $A_{4HII}B_{4HII}$, performed in the absence of $NiCl_2$. A) Rupture force histograms obtained at the indicated retract speeds. B) Corresponding loading rate histograms (plotted logarithmically). The dashed line represents a Gaussian fit to the histograms to obtain the most probable rupture force and loading rate; n represents the number of force-extension curves included in each histogram. (Reproduced with permission from ref. [221], published in 2018 by the Royal Society of Chemistry.)

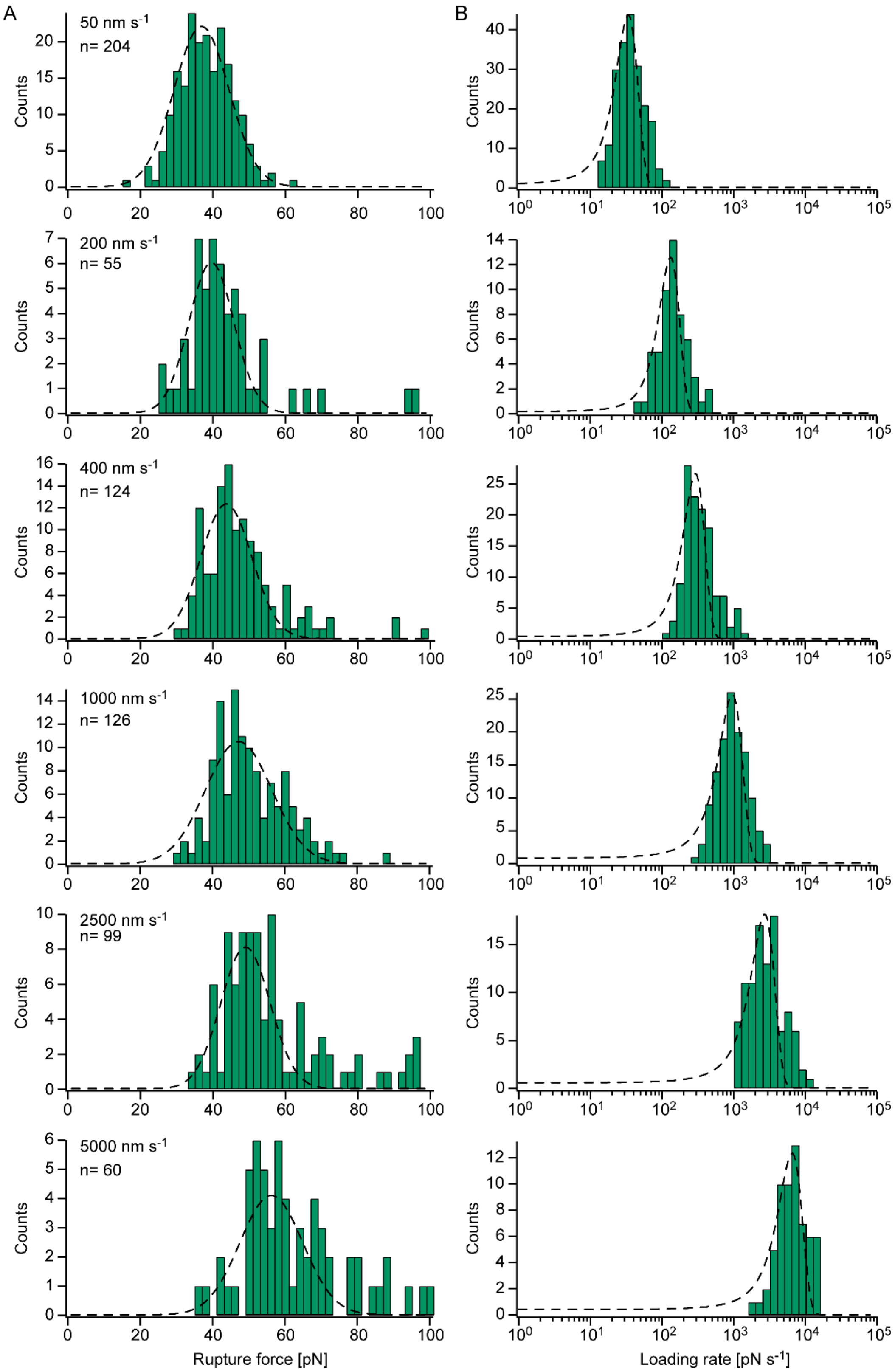

Figure S8: Representative data set of a dynamic SMFS measurement of $A_{4HII}B_{4HII}$, performed in the presence of 1 mM $NiCl_2$. A) Rupture force histograms obtained at the indicated retract speeds. B) Corresponding loading rate histograms (plotted logarithmically). The dashed line represents a Gaussian fit to the histograms to obtain the most probable rupture force and loading rate; n represents the number of force-extension curves included in each histogram. (Reproduced with permission from ref. [221], published in 2018 by the Royal Society of Chemistry.)

Table S2: Summary of the dynamic SMFS data of $A_{4HII}B_{4HII}$, obtained without and with 1 mM $NiCl_2$. Data shown in **Figure S7** and **Figure S8** are marked in bold. (Reproduced with permission from ref. [221], published in 2018 by the Royal Society of Chemistry.)

Cantilever		**1**			**2**			**3**		
Sample	Speed [nm s^{-1}]	F_R [pN]	$\dot{F}$ [pN s^{-1}]	*n*	F_R [pN]	$\dot{F}$ [pN s^{-1}]	*n*	F_R [pN]	$\dot{F}$ [pN s^{-1}]	*n*
$A_{4HII}B_{4HII}$	50	**27.8**	**30**	**334**	28.7	49	145	24.7	32	164
	200	**32.3**	**129**	**207**	31	202	95	28.1	134	92
	400	**33.8**	**298**	**251**	31.7	461	230	32.3	317	170
	1000	**37.9**	**924**	**272**	36.2	1606	63	34.1	926	254
	2500	**42.5**	**3231**	**126**	40.8	5006	54	42.8	3047	72
	5000	**50.7**	**10051**	**88**	49.4	11715	33	-	-	-
$A_{4HII}B_{4HII}$ + Ni^{2+}	50	34.4	32	341	32.9	34.4	132	**36.8**	**33.8**	**204**
	200	38.5	159	172	43.6	190	150	**39.7**	**133**	**55**
	400	41.4	351	227	44.4	431	131	**43.6**	**295**	**124**
	1000	43.4	1084	232	50.7	1281	122	**47.2**	**953**	**126**
	2500	54.6	4037	76	53.1	4134	154	**49**	**2691**	**99**
	5000	56.4*	4513*	28*	**-**	**-**	**-**	**56.2**	**6488**	**60**

*Data measured at a retract speed of 4000 nm s^{-1}.

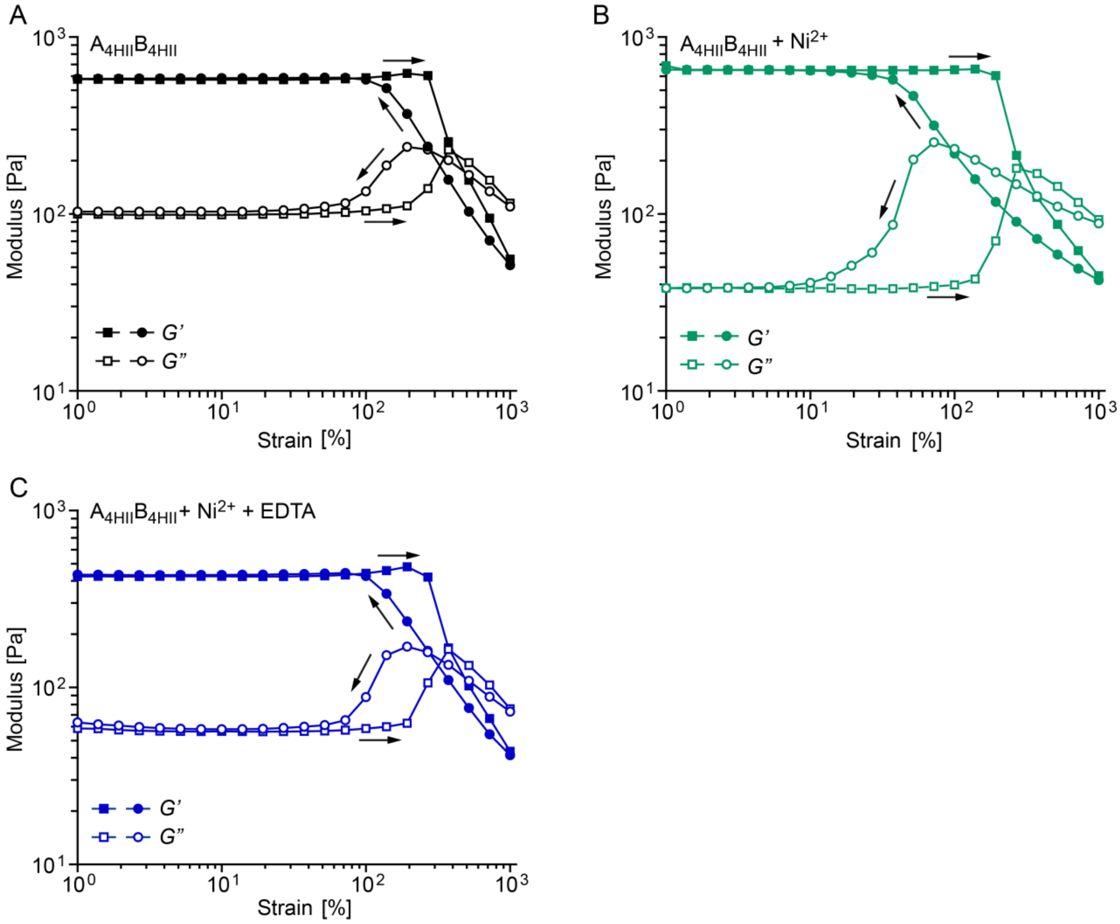

Figure S9: Amplitude sweeps of $A_{4HII}B_{4HII}$ cross-linked hydrogels. A) Measurement performed in the absence of Ni^{2+}. B) Measurement performed in the presence of 1:1 Ni^{2+}:His (4 mM $NiCl_2$). C) Measurement performed in the presence of 1:1 Ni^{2+}:His and 10 mM EDTA. All measurements were performed at 25 °C in PIPPS buffer. The amplitude sweeps were conducted at a constant angular frequency of 10 rad s^{-1}, changing the strain amplitude from 1 % to 1000 % stain and back from 1000 % to 1 %. (Reproduced with permission from ref. [221], published in 2018 by the Royal Society of Chemistry.)

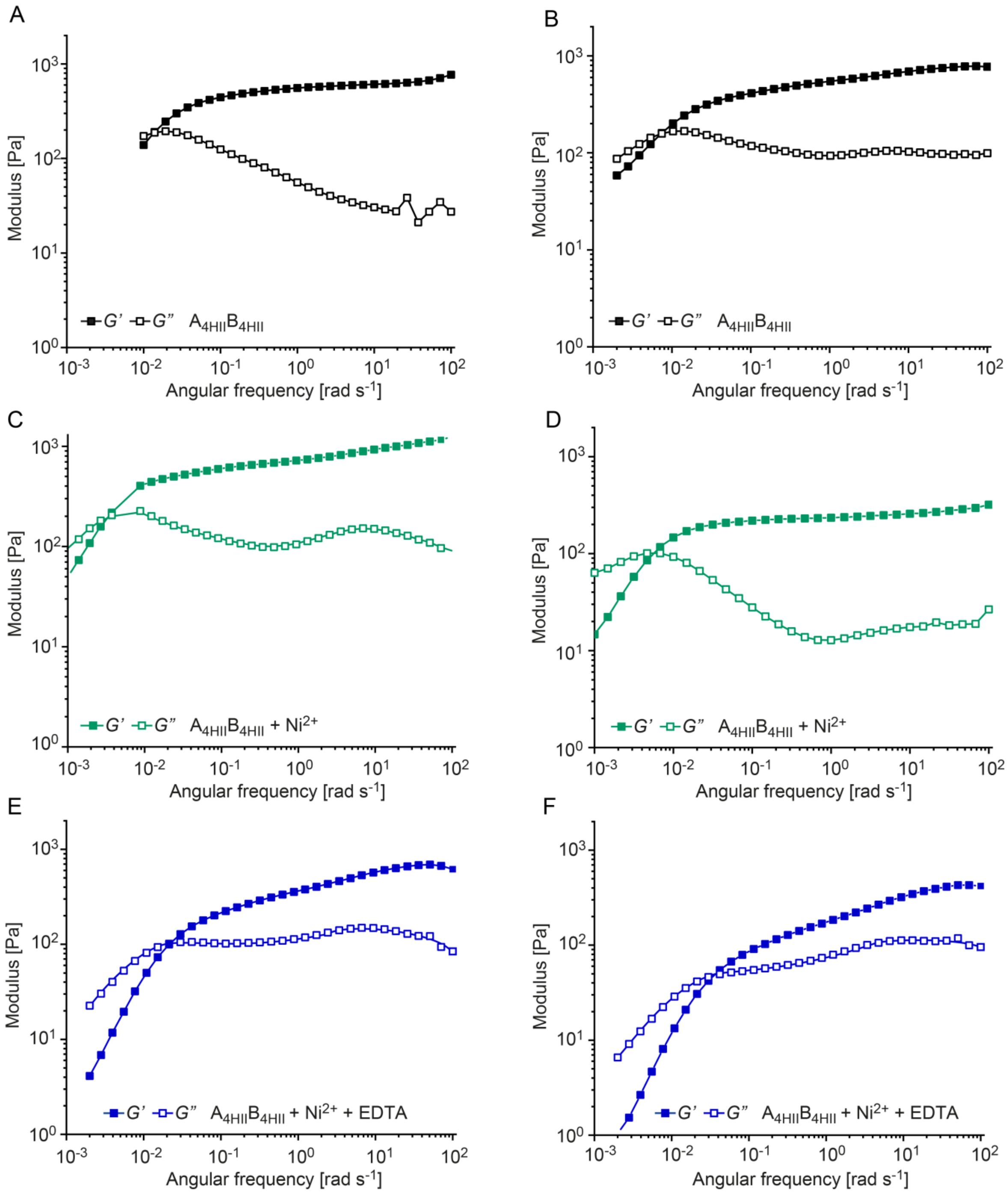

Figure S10: Additional frequency sweeps of $A_{4HII}B_{4HII}$ cross-linked hydrogels. Measurements were performed in at 25°C in PIPPS buffer in A, B) the absence of metal ions, C, D) the presence of 1:1 Ni^{2+}:His and E, F) with 1:1 Ni^{2+}:His + 10 mM ethylenediaminetetraacetate (EDTA). A stain amplitude of 1 % was used. The relaxation time τ was calculated from the crossover frequency (ω_c) where the elastic storage modulus *G'* and the viscous loss modulus *G''* intersect ($\tau = \omega_c^{-1}$).The relaxation times are reported in **Table 5.**

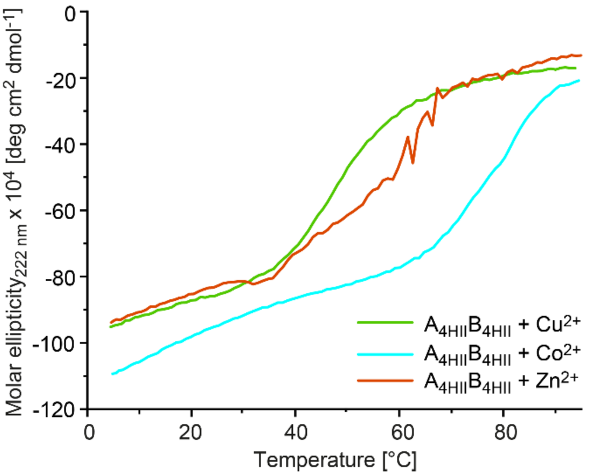

Figure S11: Thermal unfolding curves of $A_{4HII}B_{4HII}$, measured in the presence of Cu^{2+}, Co^{2+} and Zn^{2+}. The samples were heated from 4-95 °C and the signal intensity was followed at 222 nm. The peptide concentration was 50 µM in PIPPS buffer and metal ions were added in a ratio of 3:1 M^{2+}:His. The molar ellipticity was calculated using equation 1. The melting temperatures T_m were obtained using the fitting procedure in Global3 (see chapter 3.3.1). The T_m is 41.0 °C in the presence Zn^{2+}, 47.9 °C in the presence of Cu^{2+}., and 78.9 °C in the presence of Co^{2+}.

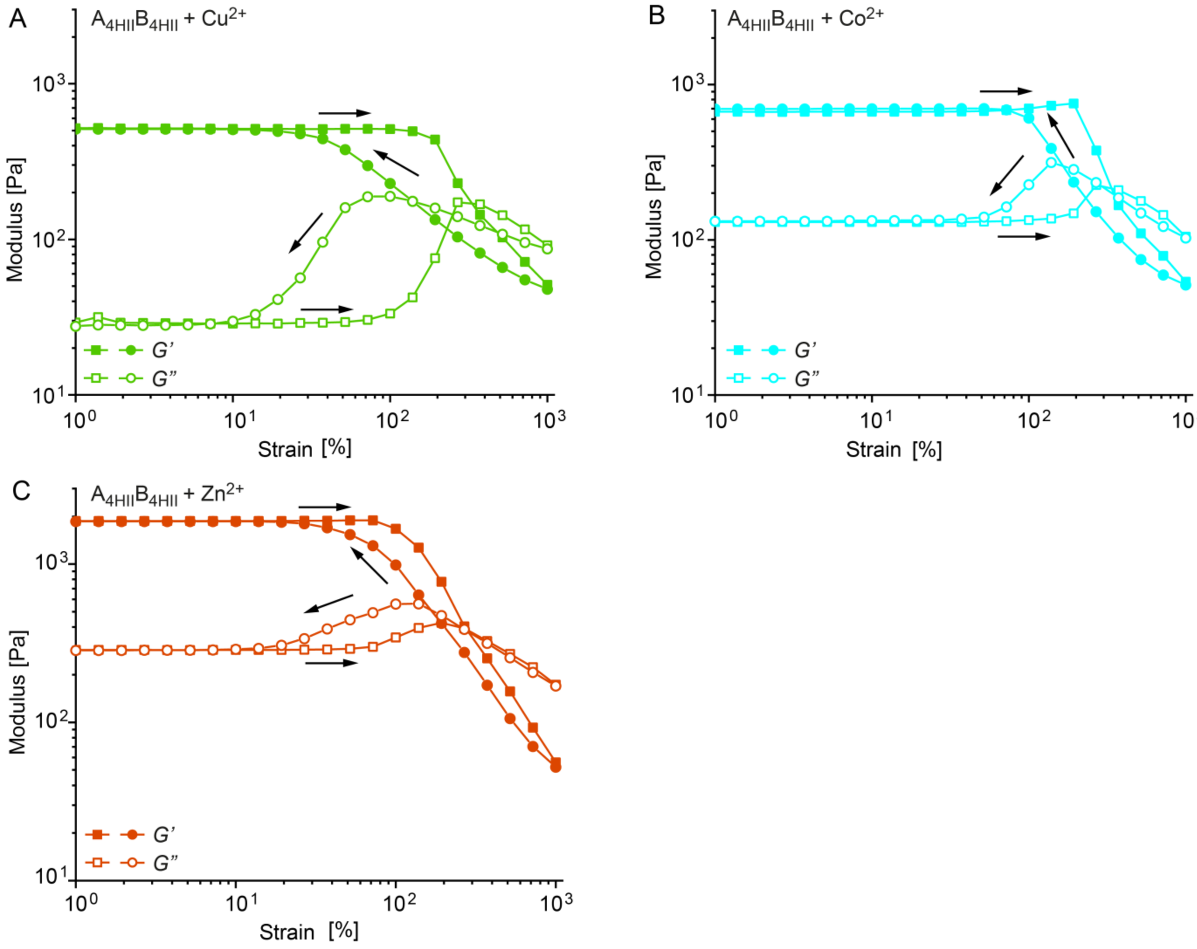

Figure S12: Amplitude sweeps of $A_{4HII}B_{4HII}$ cross-linked hydrogels, measured in the presence of Cu^{2+}, Co^{2+} and Zn^{2+}. A) Measurement performed in the presence of 1:1 Cu^{2+}:His $^+$ (4 mM $CuCl_2$). B) Measurement performed in the presence of 1:1 Co^{2+}:His (4 mM $CoCl_2$). C) Measurement performed in the presence of 1:1 Zn^{2+}:His (4 mM $ZnCl_2$). All measurements were performed at 25 °C in PIPPS buffer. The amplitude sweeps were conducted at a constant angular frequency of 10 rad s^{-1}, changing the strain amplitude from 1 % to 1000 % and back from 1000 % to 1 %.

Table S3: Melting temperatures of $A_{4H\perp}B_{4H\perp}$, determined in the absence and the presence of Zn^{2+} or Ca^{2+}. The melting temperature [°C] was obtained from the thermal unfolding curves using Global3. The standard error of the mean (SEM) was calculated using **Equation 8**.

Sample	**$A_{4H\perp}B_{4H\perp}$**	**$A_{4H\perp}B_{4H\perp}$ + 1:1 Zn^{2+}:His**	**$A_{4H\perp}B_{4H\perp}$ + 1:1 Ca^{2+}:His**
1	62.7	38.0	63.1
2	64.0	45.6	-
3	67.5	49.6	-
Mean ± SEM	64.7 ± 1.4	44.4 ± 3.4	-

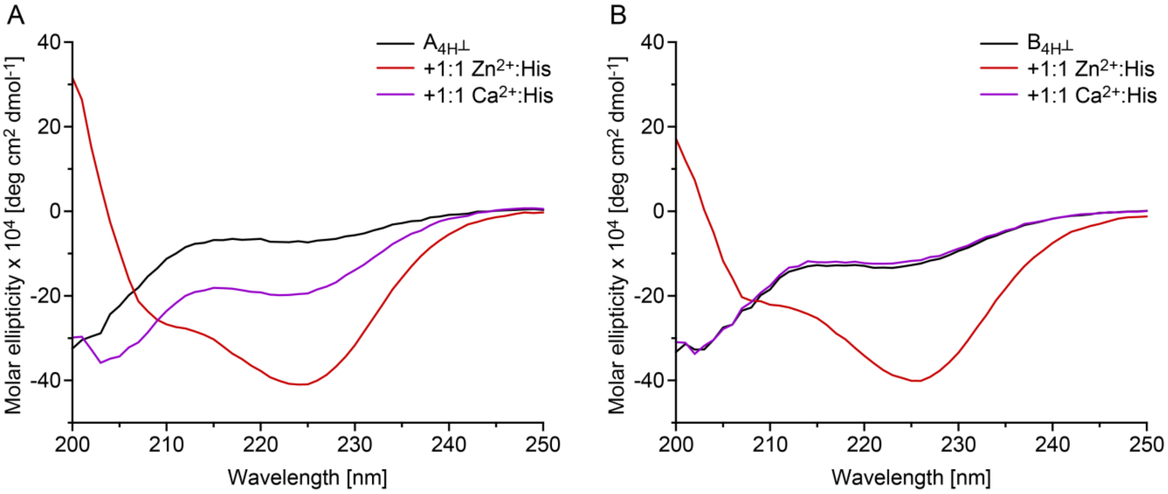

Figure S13: Circular dichroism spectra of $A_{4H\perp}$ and $B_{4H\perp}$. A) Spectra of the $A_{4H\perp}$-peptide measured in the presence and absence of Zn^{2+} or Ca^{2+} (1:1 M^{2+}:His). B) Spectra of the $B_{4H\perp}$-peptide measured in the presence and absence of Zn^{2+} or Ca^{2+} (1:1 M^{2+}:His). The peptide concentration was 50 µM. All measurements were performed at 20 °C in PIPPS buffer. The molar ellipticity was calculated using **Equation 1**. The mean melting temperature can be found in **Table S3**. (This figure was adapted and reproduced from ref. [226].)

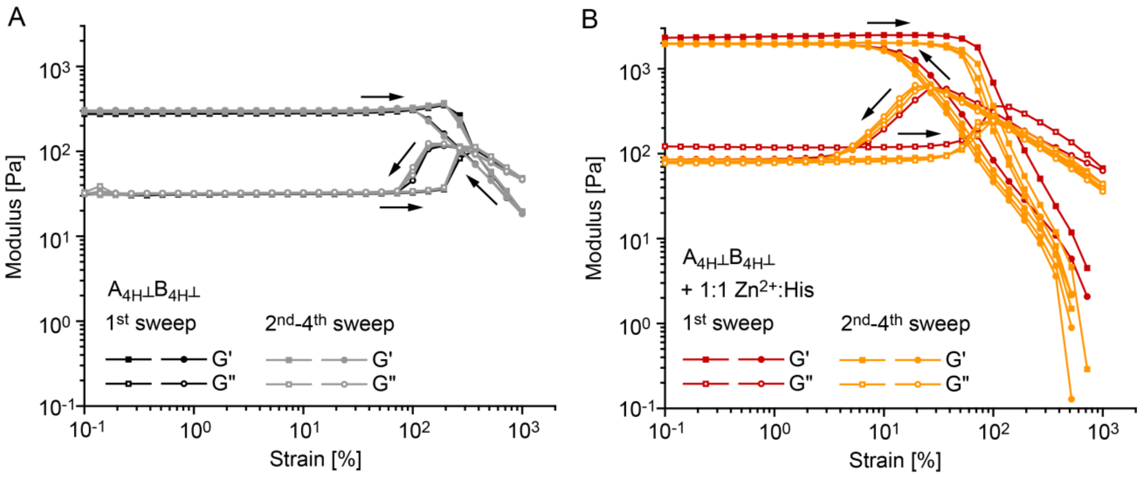

Figure S14: Strain amplitude sweeps of $A_{4H}\perp B_{4H}\perp$, measured in the presence and absence of Zn^{2+}. A) Measurement without metal ions or B) with 1:1 Zn^{2+}:His. All measurements were performed at 25 °C in PIPPS buffer. Four amplitude sweeps were performed at a constant angular frequency of 10 rad s^{-1}, changing the strain amplitude from 0.1 to 1000 % and back from 1000 % to 0.1 %. (This figure was adapted and reproduced from ref. [226].)

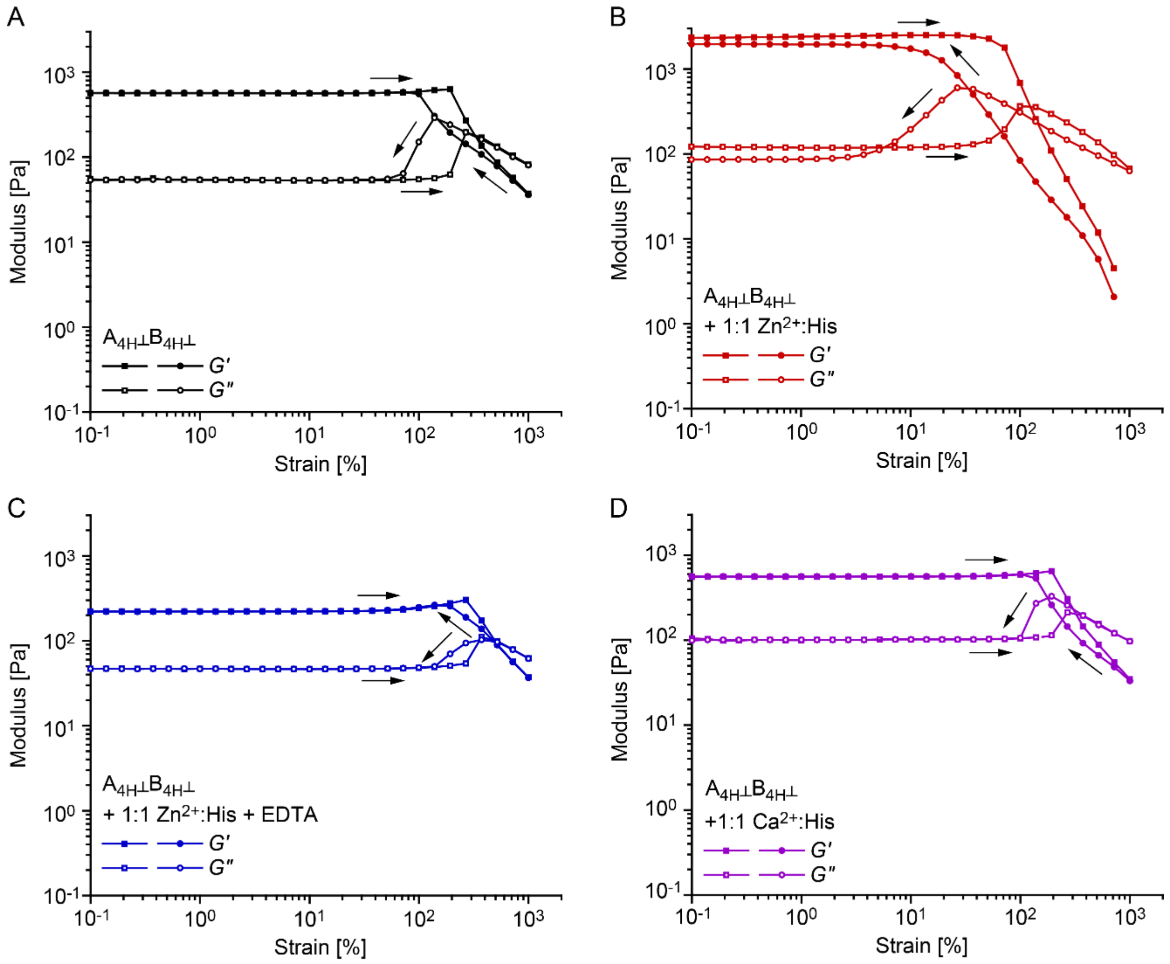

Figure S15: Strain amplitude sweep of $A_{4H}\perp B_{4H}\perp$ cross-linked hydrogels. A) Measurement performed without metal ions, B) with 1:1 Zn^{2+}:His (6 mM $ZnCl_2$), C) with 1:1 Zn^{2+}:His and 25 mM EDTA or D) with 1:1 Ca^{2+}:His (6 mM $CaCl_2$). All measurements were performed at 25°C in PIPPS buffer. Four amplitude sweeps were performed at a constant angular frequency of 10 rad s^{-1}, changing the strain amplitude from 0.1 to 1000 % and back from 1000 % to 0.1 %. (This figure was adapted and reproduced from ref.[226].)

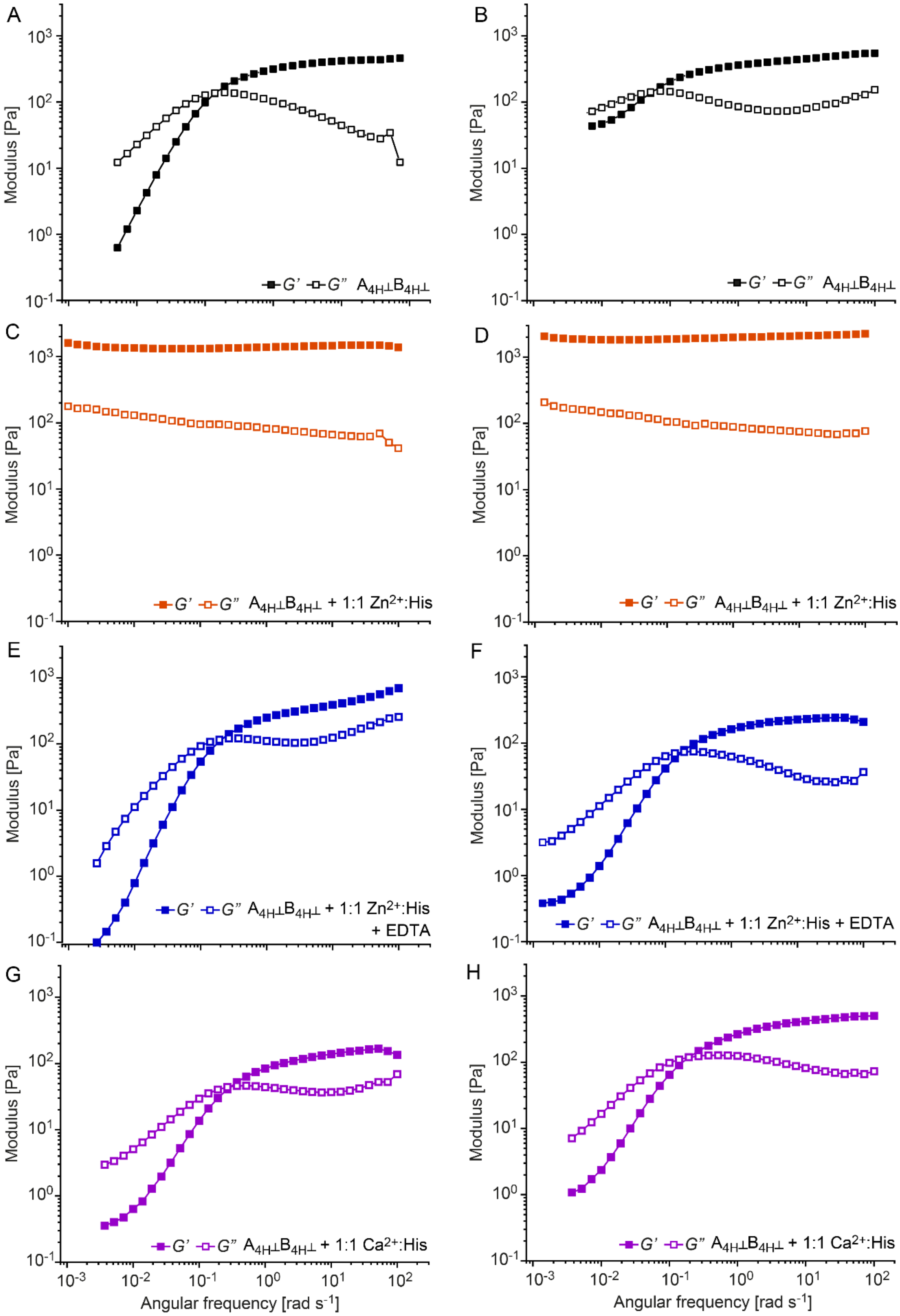

Figure S16: Additional frequency sweeps of $A_{4H\perp}B_{4H\perp}$ cross-linked hydrogels. The measurements were performed at 25 °C in PIPPS buffer A, B) without metal ions, C, D) with 1:1 Zn^{2+}:His, E, F) with 1:1 Zn^{2+}:His and EDTA and G, H) with 1:1 Ca^{2+}:His. A strain amplitude of 1 % was used. The relaxation time τ was calculated from the crossover frequency (ω_c) where *G'* and *G''* intersect ($\omega_c = \tau^{-1}$). The relaxation times are reported in **Table 6**.

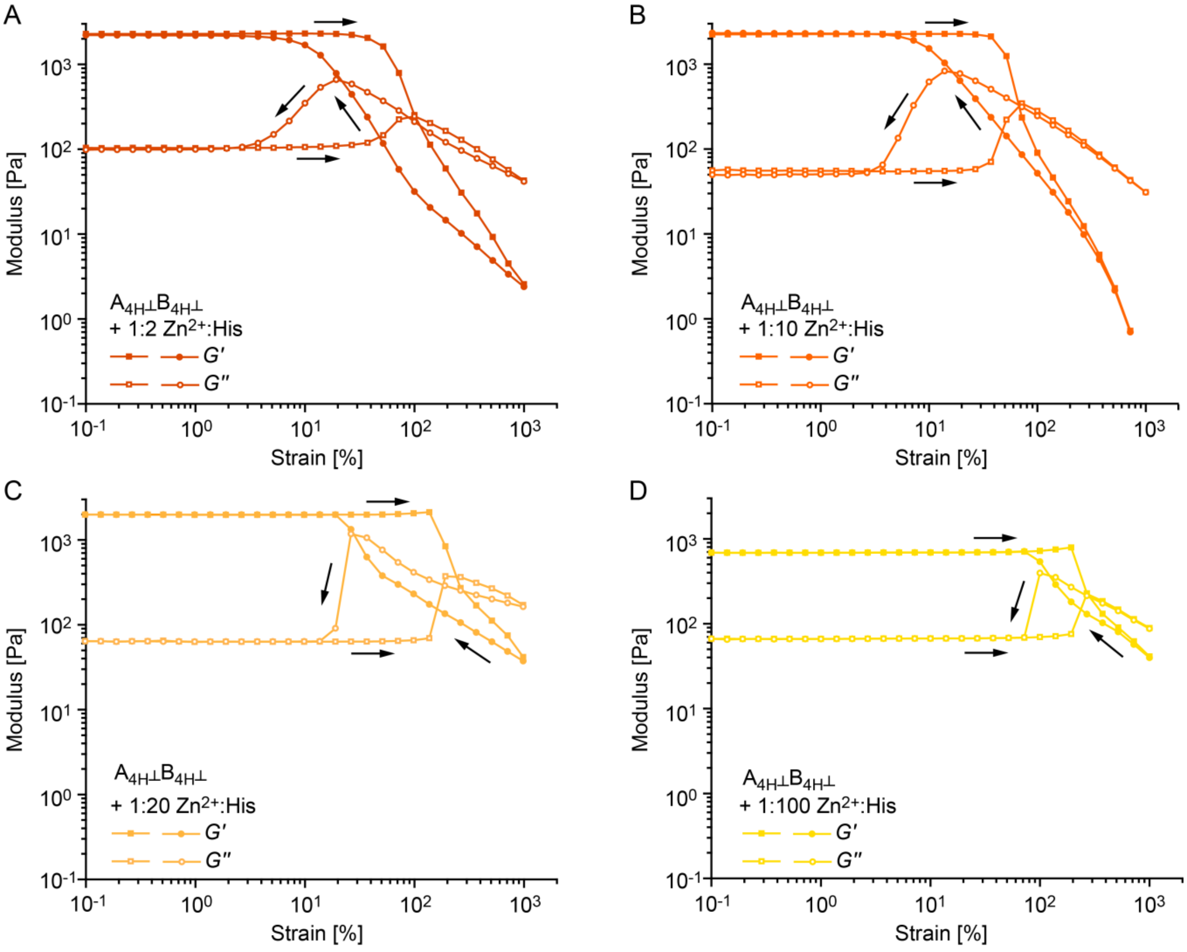

Figure S17: Strain amplitude sweeps of $A_{4H\perp}B_{4H\perp}$ cross-linked hydrogels, measured in the presence of different Zn^{2+}:His ratios. Measurements with a ratio of A) 1:2, B) 1:10, C) 1:20 and D) 1:100 Zn^{2+}:His. All measurements were performed at 25 °C in PIPPS buffer. A constant angular frequency of 10 rad s^{-1} was used and the strain amplitude was changed from 0.1 to 1000 % and back from 1000 % to 0.1 %. (This figure was adapted and reproduced from ref. [226].)

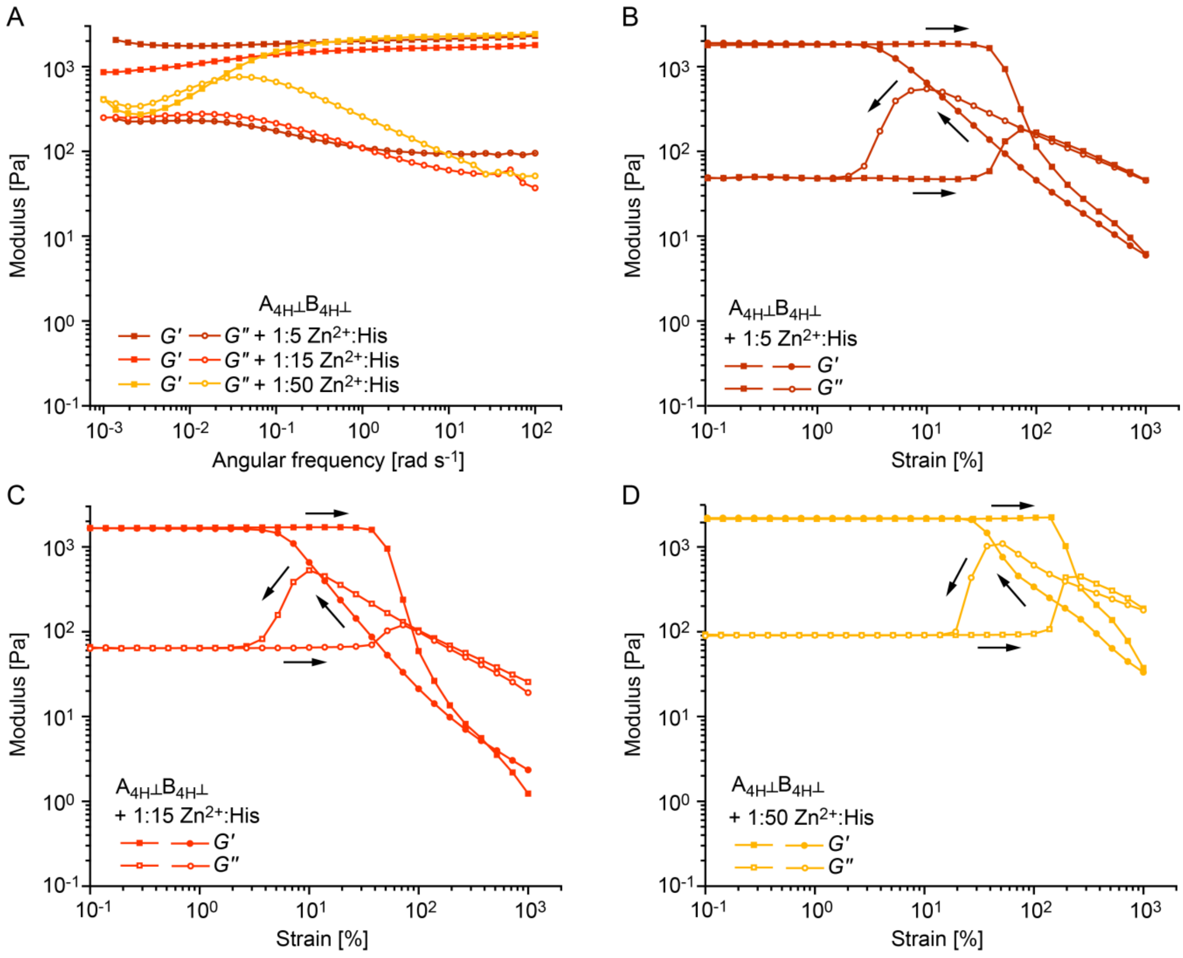

Figure S18: Additional frequency and amplitude sweeps of $A_{4H\perp}B_{4H\perp}$ cross-linked hydrogels, measured in the presence of different Zn^{2+}:His ratios. A) Frequency sweeps were performed from 100 to 0.001 rad s^{-1} at a constant strain amplitude of 1 %. B-D) Amplitude sweeps in the presence of B) 1:5, C) 1:15 and D) 1:50 Zn^{2+}:His were performed at a constant angular frequency of 10 rad s^{-1}, changing the strain amplitude from 0.1 to 1000 % and back from 1000 % to 0.1 %. All measurements were performed at 25 °C in PIPPS buffer. (This figure was adapted and reproduced from ref. [226].)

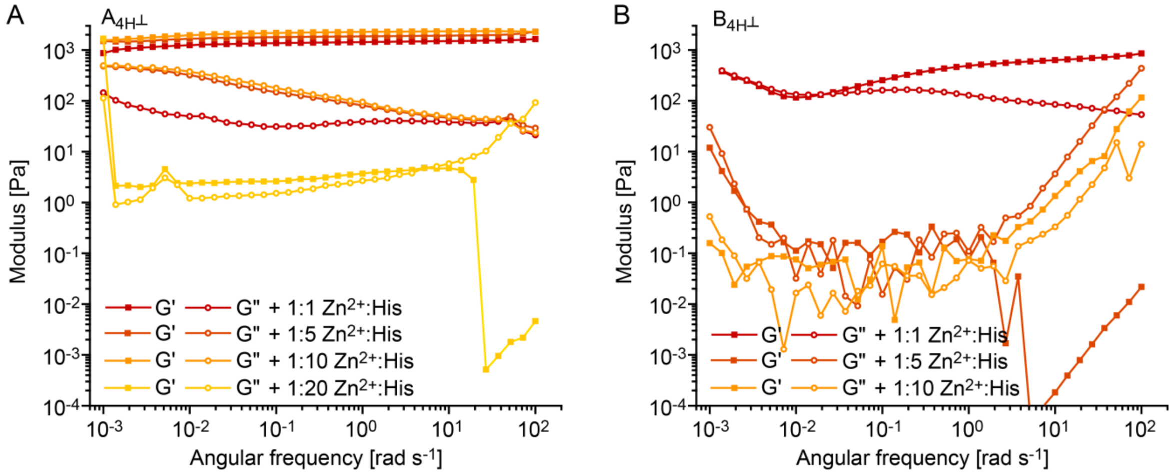

Figure S19: Frequency sweeps of the individual star-PEG-peptide conjugates, measured with different ratios of Zn^{2+}:His. A) Individual star-PEG-$A_{4H\perp}$ conjugate. B) Individual star-PEG-$B_{4H\perp}$ conjugate. The measurements were performed at 25 °C in PIPPS buffer, using Zn^{2+}:His ratios down to 1:20 (star-PEG-$A_{4H\perp}$) or down to 1:10 (star-PEG-$B_{4H\perp}$). The frequency was changed from 100 to 0.001 rad s^{-1} at a constant strain amplitude of 1 %. (This figure was adapted and reproduced from ref. [226].)

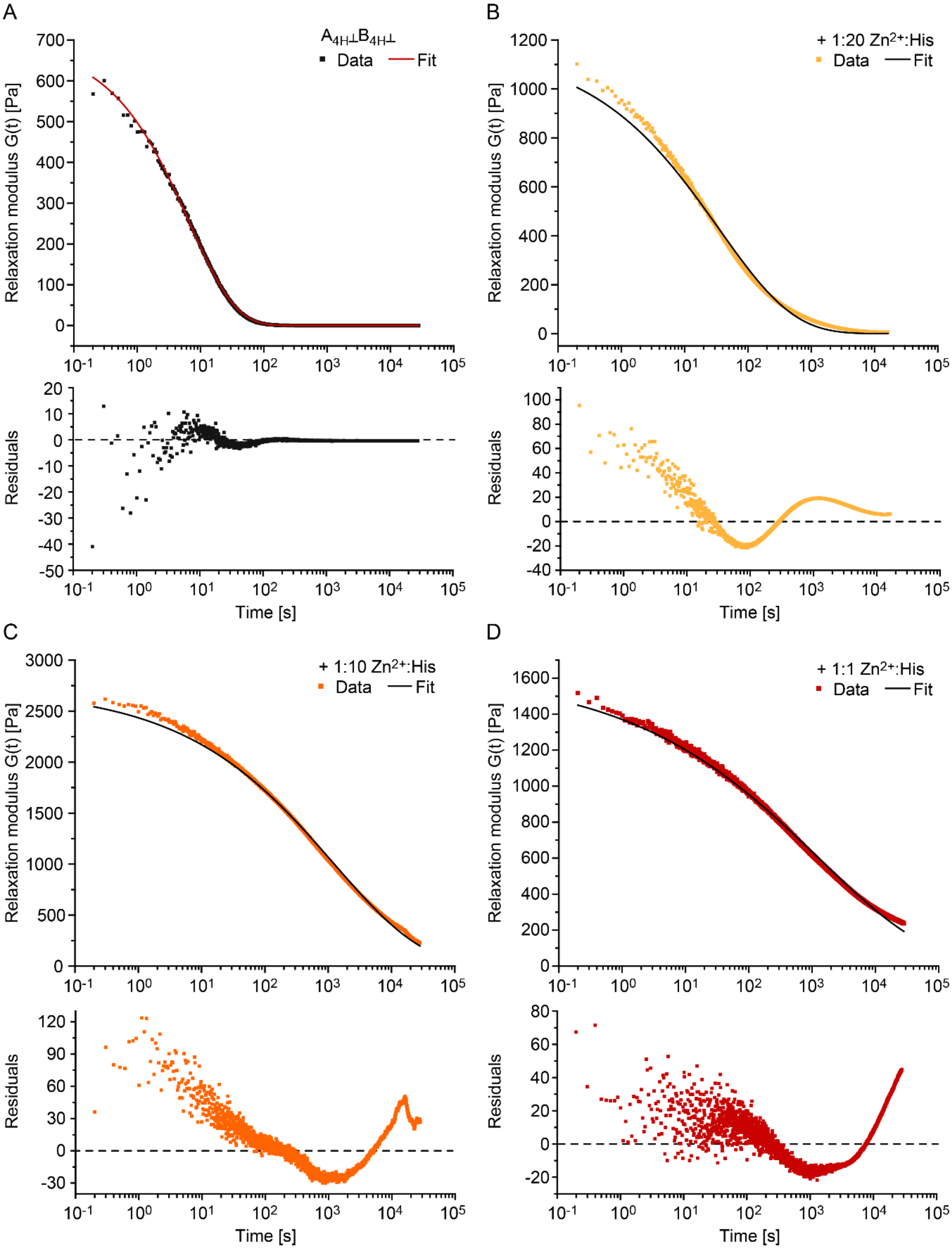

Figure S20: Stress relaxation of $A_{4H\perp}B_{4H\perp}$ cross-linked hydrogels. Measurements A) without metal ions and with B) 1:1, C) 1:10, D) 1:20 Zn^{2+}:His. All measurements were performed at 25 °C in PIPPS buffer. Stress relaxation was monitored after applying a step strain of 10 %. The relaxation modulus G(t) was fitted to Kohlrausch's stretched-exponential relaxation model (**Equation 30**). The fit parameters can be found in **Table S4**. The fit residuals are shown below the fit of the corresponding relaxation data. (This figure was adapted and reproduced from ref. [226].)

Table S4: Relaxation times of $A_{4H}{\perp}B_{4H}{\perp}$ hydrogels, obtained from frequency sweeps or stress relaxation experiments. The relaxation times at different His-Zn^{2+} ratios were obtained from the crossover of *G'* and *G"* in the frequency sweeps (τ_{fs}) or from the stress relaxation experiments (τ_{sr}). The stress relaxation curves were fitted to Kohlrausch's stretched exponential relaxation model to obtain the relaxation time τ_{sr}. G_0 is the initial plateau modulus and *α* is the fitting parameter. G_0 was fixed to the value of *G'* in the linear viscoelastic region of an amplitude sweep of the same hydrogel, which was performed before the relaxation experiment. (This table was adapted and reproduced from ref. [226]).

Hydrogel	**τ_{fs} [s]**	**τ_{sr} [s]**	***α***	**G_0 [Pa]**
$A_{4H}{\perp}B_{4H}{\perp}$	11.2	6.6	0.59	690
+ 1:20 Zn^{2+}:His	51.8	34.4	0.37	1170
+ 1:10 Zn^{2+}:His	> 1000	1244.0	0.31	2720
+ 1:1 Zn^{2+}:His	> 1000	1272.0	0.24	1630

Table S5: Melting temperature and FRET efficiency of $A_{4CF}B_{4TR}$. The melting temperature was obtained from temperature-ramp experiments with CD spectroscopy at a peptide concentration of 50 µM in PBS at 25 °C. The FRET efficiency was determined using a fluorescence spectrometer with a sample concentration of 5 µM $A_{4CF}B_{4TR}$ in PBS. The measurements were performed in triplicate and the mean and the standard error of the mean (SEM) were determined.

$A_{4CF}B_{4TR}$	**T_m [°C]**	**FRET efficiency E [%]**
1	80.1	79
2	79.4	81
3	80.6	71
Mean ± SEM	80.0 ± 0.4	77 ± 3

Table S6: Determination of the FRET efficiency in $A_{4CF}B_{4TR}$ containing hydrogels. Mean intensity of carboxyfluorescein obtained from the green channel of the CCD camera. Mean values over the entire image were obtained using imageJ [217]. The images were taken at the initial height of the hydrogels (1 mm) and after compressing the hydrogels to 0.1 mm. The FRET efficiency was calculated using **Equation 10** ($E = 1-(I_{A4CFB4TR} / I_{A4CF})$) with the mean intensity of the A_{4CF} hydrogel normalized to 100 % donor fluorescence. The mean and the standard error of the mean (SEM) were determined.

Mean intensity	**1 mm $A_{4CF}B_{4TR}$**	**1 mm A_{4CF}**	**FRET efficiency E [%]**	**0.1 mm $A_{4CF}B_{4TR}$**	**0.1 mm A_{4CF}**	**FRET efficiency E [%]**
1	20.4	77.0	74	8.7	14.5	40
2	22.9	81.6	72	8.8	14.5	39
3	19.6	77.7	75	8.7	14.7	41
4	22.0	52.6	58	8.9	14.1	37
5	22.6	77.3	71	8.9	14.9	40
6	23.6	63.1	63	8.8	14.3	38
7	19.5	69.9	72	8.7	15.2	43
8	18.0	55.4	68	8.7	13.8	37
9	18.0	55.2	67	8.7	13	33
10	19.6	34.7	44	8.8	10.3	15
Mean ± SEM			**66 ± 3**			**36 ± 3**

Table S7: Tetramethylrhodamine intensity in $A_{4CF}B_{4TR}$ and B_{4TR} containing hydrogels. The mean intensity of tetramethylrhodamine was obtained from using imageJ [217]. The images were taken at the initial height of the hydrogels (1 mm). The mean and the standard error of the mean (SEM) were determined.

Mean intensity	**1 mm $A_{4CF}B_{4TR}$**	**1 mm B_{4TR}**
1	100.1	79.2
2	102.5	87.7
3	60	80.3
4	97.8	73.9
Mean ± SEM	**90.1 ± 10**	**80.3 ± 2.8**

Acknowledgements

First of all, I would like to thank my supervisors Dr. Kerstin G. Blank and Dr. Matthew J. Harrington for their scientific and non-scientific support and guidance during the last 4 years. Thank you for the great opportunity to work on this interdisciplinary project. I would also like to thank my mentor Prof. Dr. Peter Fratzl for helpful and inspiring discussions.

I would especially like to acknowledge the International Max Planck Research School (IMPRS) on Multiscale Bio-Systems for opportunities to conduct my doctoral research in such an interdisciplinary and international research institute with excellent researchers. Furthermore, I would like to acknowledge funding from the Deutsche Forschungsgemeinschaft (DFG, German Research Foundation) – Project-ID 189853844 – TRR 102.

A big thank you goes to everyone in the Mechano(bio)chemistry research group for providing such a warm and welcoming working atmosphere. Thank you for countless scientific discussions, help with instrument trouble-shooting, extended lunch breaks with cake in the coffee corner, great restaurant and international dinner evenings and an amazing trip to Canada. Particularly, I would like to thank the technicians of the group, Anne Heilig, Reinhild Dünnebacke and Margit Rößner. Without your continuous efforts to organize everything effectively in order to keep the lab running smoothly, my daily research life would not have been so pleasant.

Besides the above mentioned, I would like to thank Dr. Daniel Varón Silva for his helpful discussions in terms of peptide synthesis and MALDI.

Last but not least, many thanks to my husband for all the chocolate, love and unexpected surprises. Without the constant love and moral support of my family and friends, I would not have managed to reach this goal.

Isabell